Andreia Arrimar Duarte

Graduated in Biology - Educational field

Storage of Water Molecules into Biomimetic Heterostructures: The Role of Roughness

Dissertation to obtain the PhD Degree in Biomedical Engineering

Supervisor: Maria de Fátima Guerreiro da Silva Campos Raposo,
Assistant Professor, Universidade Nova de Lisboa

Co-supervisor: Pedro António de Brito Tavares,
Assistant Professor, Universidade Nova de Lisboa

Júri:

Presidente: Prof. Doutor António Manuel Dias de Sá Nunes dos Santos
Arguente(s): Prof. Doutor João Filipe Colardelle da Luz Mano
Prof. Doutora Ana Maria da Conceição Ferraria

Vogais: Prof. Doutora Maria Adelaide de Almeida Pedro de Jesus
Prof. Doutora Ana Margarida Madeira Viegas de Barros Timmons
Prof. Doutora Maria de Fátima Guerreiro da Silva Campos Raposo
Prof. Doutor Paulo António Martins Ferreira Ribeiro
Prof. Doutora Quirina Alexandra Tavares Ferreira

FACULDADE DE CIÊNCIAS E TECNOLOGIA
UNIVERSIDADE NOVA DE LISBOA

December 2014

Storage of Water Molecules into Biomimetic Heterostructures: The Role of Roughness

Don´t get set into one form,

adapt it and build your own,

and let it grow, be like water.

Bruce Lee

To My Grandparents Rosindo, Maria and Virgínia

In Memory of my Grandfather Manuel

Acknowledgements

I would like to express my sincere gratitude to my supervisor *Prof. Dr. Maria Raposo* for her support, understanding, generosity and encouragement that were of great value while pursuing this work. Her perseverance and assertiveness allowed good personal and professional relationships. I certainly appreciate the prolific scientific guidance and the opportunity of being part of a research group.

I would like to thank *Prof. Dr. Pedro Tavares* for accepting to be my co-supervisor. I am very grateful for his comprehension, patience and scientific cooperation during this period.

I acknowledge both *Prof. Dr. Ana Barros* and *Prof. Dr. Maria Adelaide de Jesus* for accepting to be part of the monitoring committee, and for their precious advice that helped the progress of this research work.

I warmly thank to *Doctor Paulo Gomes* for his many years of friendship and for the fruitful challenge of joining science and education, but also for the Vacuum Ultraviolet spectroscopy measurements.

I am very grateful to *Prof. Dr. Paulo Ribeiro* for reading drafts, helpful asking, insightful questions, and his spontaneous good mood.

Special thanks to *Mestre Luís Abegão* for technical support in quartz crystal microbalance measurements implementation, for the extended scientific discussions, but above all for his optimism and willingness.

I am very grateful to *Doctor João Lourenço* for the support and technical advices and to *Eng. Jorge Ribeiro* for the precious technical designs and I would like to extend my sincere thanks to all of the other members that have been part of the Sistemas Moleculares Funcionais research group, for the opportunities over the years, the provided and developed support.

I would like to thank the entire research staff and students with whom I've worked with, mainly *Francisco Brasil, João Lourenço, Sérgio Filipe and Tiago Valente* for their continuous help in daily laboratory life.

I thank *Dr. Cristina Cordas* and *Dr. Filipe Folgosa* from Departamento de Química of FCT-UNL, for their helpful assistance, sympathy and collaboration.

I want to thank *Dr. Joana Pinto and Mestre Tomás Calmeiro* from CENIMAT of FTC-UNL for the atomic force microscopy *ex situ* measurements.

I want to thank *Prof. Dr. António Lopes* from ITQB-UNL for DLS measurements.

I would also like to thank *Prof. Dr. Ana Viana and Doctor Joaquim Marquês* from Centro de Química e Bioquímica, Faculdade de Ciências, Universidade de Lisboa, for their fruitful collaboration and atomic force microscopy *in situ* and ellipsometry measurements.

I want to thank *Prof. Dr. Ana Botelho do Rego* from Centro de Química Física Molecular, Instituto Superior Técnico, Universidade de Lisboa, for her collaboration and discussion with the measurements made on the x-ray photoelectron spectroscopy facility.

I want to thank *Doctor Søren Vrønning Hoffmann* from Institute for Storage Ring Facilities, University of Aarhus, Denmark, for providing the facilities to carry out VUV measurements.

I want to thank *Prof. Dr. Benachir Bouchikhi* from Sensor Electronic & Instrumentation Group, Moulay Ismaïl University, Faculty of Sciences, Physics Department of Morocco for application of the Layer-by-layer films in an electronic tongue sensor.

I want to thank to *Dr. Marco Salerno* from Istituto Italiano di Tecnologia of Italy for his help in statistical analysis of atomic force microscopy images.

I also thank *Prof. Dr. Osvaldo Novaes Jr. and Dr. Marli Moraes* from Grupo de Física de Polímeros do Instituto de Física São Carlos for collaboration on several developed projects.

I want to acknowledge *Mestre Ana Carapeto* for the valuable suggestions in quartz crystal microbalance technique.

Many thanks to all, *Mr. Arez, Mrs. Fátima, Mrs. Helena, Mrs. Ana Cruz* and *Mrs. Luiza Oliveira,* from *Physics Department and CeFiTec,* for their help in my administrative adventures.

Special thanks to all elements that belong to *Novo Núcleo Teatro* from FCT-UNL, for the contribution in my personal and interpersonal development, for the fantastic opportunities experienced in the university theater world, but above all for their dedication and friendship.

To my friends, I will not point names but you know who you are, who accompanied me throughout these years thanks for being part of my journey.

Naturally and not less important, I must thank my parents *Carlos Duarte* and *Rosinda Arrimar* for their constant support and encouragement who selflessly supported me during my graduate education and my entire life.

I want to express my gratitude to my sister *Neuza Arrimar Duarte* for being an example of dedication and perseverance and for the scientific and artistic inputs.

I also thank to Departamento de Física, Universidade Nova de Lisboa, for providing the logistic conditions.

I acknowledge funding from the Portuguese research Grant No. PEst-OE/FIS/UI0068/2011 through FCT-MEC and the fellowship SFRH/BD/62229/2009.

Abstract

The development of devices based on heterostructured thin films of biomolecules conveys a huge contribution on biomedical field. However, to achieve high efficiency of these devices, the storage of water molecules into these heterostructures, in order to maintain the biological molecules hydrated, is mandatory. Such hydrated environment may be achieved with lipids molecules which have the ability to rearrange spontaneously into vesicles creating a stable barrier between two aqueous compartments. Yet it is necessary to find conditions that lead to the immobilization of whole vesicles on the heterostructures. In this work, the conditions that govern the deposition of open and closed liposomes of 1.2-dipalmitoyl-*sn*-Glycero-3-[Phospho-*rac*-(1-glycerol)] (sodium Salt) (DPPG) onto polyelectrolytes cushions prepared by the layer-by-layer (LbL) method were analyzed. Electronic transitions of DPPG molecules as well as absorption coefficients were obtained by vacuum ultraviolet spectroscopy, while the elemental composition of the heterostructures was characterized by x-ray photoelectron spectroscopy (XPS). The presence of water molecules in the films was inferred by XPS and infrared spectroscopy. Quartz crystal microbalance (QCM) data analysis allowed to conclude that, in certain cases, the DPPG adsorbed amount is dependent of the bilayers number already adsorbed. Moreover, the adsorption kinetics curves of both adsorbed amount and surface roughness allowed to determine the kinetics parameters that are related with adsorption processes namely, electrostatic forces, liposomes diffusion and lipids re-organization on surface. Scaling exponents attained from atomic force microscopy images statistical analysis demonstrate that DPPG vesicles adsorption mechanism is ruled by the diffusion Villain model confirming that adsorption is governed by electrostatic forces. The power spectral density treatment enabled a thorough description of the accessible surface of the samples as well as of its inner structural properties. These outcomes proved that surface roughness influences the adsorption of DPPG liposomes onto surfaces covered by a polyelectrolyte layer. Thus, low roughness was shown to induce liposome rupture creating a lipid bilayer while high roughness allows the adsorption of whole liposomes. In addition, the fraction of open liposomes calculated from the normalized maximum adsorbed amounts decreases with the cushion roughness increase, allowing us to conclude that the surface roughness is a crucial variable that governs the adsorption of open or whole liposomes. This conclusion is fundamental for the development of well-designed sensors based on functional biomolecules incorporated in liposomes. Indeed, LbL films composed of polyelectrolytes and liposomes with and without melanin encapsulated were successfully applied to sensors of olive oil.

KEYWORDS: Layer-by-layer films; Surface Roughness; Quartz Crystal Microbalance; DPPG; Liposomes; Kinetic Adsorption; Atomic Force Microscopy; Scaling Laws; Power Spectral Density; Vacuum Ultraviolet Spectroscopy; X-ray Photoelectron Spectroscopy, Sensor.

Resumo

A criação de dispositivos baseados em filmes finos heteroestruturados de biomoléculas podem contribuir em larga escala para o desenvolvimento da área da biomedicina. No entanto, a eficácia destes dispositivos está dependente das condições que permitem manter as moléculas biológicas hidratadas e, portanto, é necessário que estas heteroestruturas armazenem água. Um ambiente hidratado pode ser obtido a partir de moléculas lipídicas que têm a capacidade de se reorganizar espontaneamente em vesículas criando uma barreira estável entre dois compartimentos aquosos. Contudo, é necessário encontrar as condições que levam à imobilização de vesículas intactas sobre heteroestruturas. Neste trabalho foram analisadas as condições que levam à deposição de lipossomas abertos e fechados de 1.2-dipalmitoyl-*sn*-Glycero-3-[Phospho-*rac*-(1-glycerol)] (sal de sódio) (DPPG) em almofadas de polieletrólitos, preparados pelo método de camada-sobre-camada (LbL). As transições eletrónicas das moléculas de DPPG bem como os coeficientes de absorção foram obtidos por espectroscopia de ultravioleta de vácuo (VUV), enquanto a composição elementar das heteroestruturas foi caracterizada por espectroscopia de fotoeletrão de raios-X (XPS). A presença de moléculas de água nos filmes foi inferida por XPS e espectroscopia de infravermelho. A análise de dados obtidos por microbalança de cristal de quartzo (QCM) permitiu deduzir que, em alguns casos, a quantidade de DPPG adsorvida depende do número de bicamadas previamente absorvidas. Além disso, as curvas de cinética de adsorção, tanto da quantidade adsorvida como da rugosidade da superfície, permitiram determinar os parâmetros de cinética relacionados com os processos de adsorção em causa, ou seja, forças electrostáticas, difusão de lipossomas e reorganização dos lípidos sobre a superfície. Os expoentes de escala calculados a partir da análise estatística de imagens obtidas por microscopia de força atómica demonstraram que a adsorção das vesículas de DPPG é regida pelo modelo de difusão de Villain confirmando que a adsorção é regida por interações eletrostáticas. O tratamento da densidade espectral de potência permitiu uma descrição minuciosa da superfície das amostras, bem como das suas propriedades estruturais internas. Estes resultados provaram que a rugosidade da superfície influencia a adsorção dos lipossomas de DPPG em superfícies cobertas por uma camada de polieletrólito. Assim, uma baixa rugosidade provoca a ruptura dos lipossomas originando uma bicamada lipídica, enquanto uma elevada rugosidade induz à adsorção de lipossomas inteiros. Mais ainda, a quantidade máxima adsorvida normalizada obtida por QCM, uma medida de fracção de lipossomas abertos, mostra um decréscimo com o aumento da rugosidade, permitindo concluir que a rugosidade da superfície é uma variável crucial que regula a absorção de lipossomas abertos ou inteiros. Esta conclusão é de interesse fundamental no desenvolvimento de sensores com base em biomoléculas funcionais incorporadas em lipossomas. De facto, filmes LbL compostos por polieletrólitos e lipossomas com e sem melanina encapsulada foram aplicadas com sucesso para sensores de azeite.

PALAVRAS-CHAVE: Filmes de Camada-sobre-camada; Rugosidade da superfície; Microbalança de Cristal de Quartzo; DPPG; Lipossomas; Cinética de adsorção; Microscopia de Força Atómica; Leis de escala; Densidade Espectral de Potência; Espectroscopia de ultravioleta de vácuo; Espectroscopia fotoeletrão de Raio-X; Sensor.

CONTENTS

FIGURES

TABLES

Acronyms

ACS	Acoustic Vibration
AFM	Atomic Force Microscope
ASTRID	Institute For Storage Ring Facilities
BE	Binding Energy
CEC	Capillary electrochromatography
CEFITEC	Centro de Física e Inovação Tecnológica
CV	Cyclic voltammetry
CVC	Continuous Vertical Closed
Df	Fractal Dimension
DLS	Dynamic Light Scattering
DMPC	1.2-dimyristoyl-sn-glycero-3-phosphocholine
DNA	Deoxyribonucleic acid
DPPG	1.2-dipalmitoyl-sn-Glycero-3-[Phospho-rac-(1-glycerol)] (Sodium Salt)
EDS	Energy Dispersive X-ray Spectroscopy
EL	Electronic language
ESCA	Electron Spectroscopy for Chemical Analysis
EW	Edwards-Wilkinson
FAT	Fixed Analyzer Transmission
FCT	Faculdade de Ciências e Tecnologia
FTIR	Fourier Transform Infrared
FWHM	Full Width at Half Maximum
GC-MS	Gas chromatography coupled with mass spectroscopy
HA	Hyaluronic acid
HD	Hydrodynamic Diameter
HE-tongue	Hybrid Electronic Tongue
HVE-tongue	Hybrid Voltammetric Electronic Tongue
HPLC	High performance liquid chromatography
IR	Infrared
IUPAC	International Union of Pure and Applied Chemistry
JMA	Johnson-Mehl-Avrami
KPZ	Kardar-Parisi-Zhang
LB	Langmuir-Blodgett
LbL	Layer-by-layer
LCD	Liquid crystal display
LUV	Large Unilamellar vesicles
MLV	Multilamellar Vesicles
MVS	Mechanical Vibration Sensitivity
PAH	Poly(allylamine hydrochloride)
PC	Phosphatidylcholine

PC	Principal components
PCA	Principal component analysis
PEI	Poly(ethyleneimine)
PEM	Polyelectrolyte multilayer
PG	Phosphatidylglycerol
PSL	Polymer-supported liposomes
PLB	Polymer-supported phospholipid bilayer
PLL	Poly-L-lysine
POPC	1-Palmitoyl-2-oleoyl-*sn*-glycero-3--phosphocholine
PSD	Power Spectral Density
PSD_{ABC}	ABC or K-correlation model
$PSD_{fractal}$	Fractal model
PSD_{sh}	Superstructures model
PSL	Polymer-supported liposome
PSS	Poly(sodium 4-styrenesulfonate)
QCM	Quartz Crystal Microbalance
RDS	Respiratory Distress Syndrome
RNA	Ribonucleic acid
SAM	Self-assembled monolayer
SEM	Scanning Electron Microscope
SFM	Scanning Force Microscopy
SHC	Stationary Horizontal Closed
SHO	Stationary Horizontal Open
SLB	Supported lipid bilayer
SPB	Solid-supported phospholipid bilayer
SPM	Scanning Probe Microscopy
SPR	Surface Plasmon Resonance
SR	Synchrotron radiation
SRS	Stanford Research Systems
STM	Scanning Tunneling Microscopy
SUV	Small Unilamellar Vesicles
SVC	Stationary Vertical Closed
SVM	Support vector machines
SVO	Stationary Vertical Open
TVS	Thermal Vibrations
UNL	Universidade Nova de Lisboa
UV	Ultraviolet
UV-Vis	Ultraviolet-visible
VUV	Vacuum Ultraviolet
XPS	X-ray photoelectron spectroscopy

Symbology

A	Absorbance
Abs	Absorbance
Abs_{168nm}	Absorbance at 168 nm of wavelength
Abs_{p138nm}	Partial Absorbance at 138 nm of wavelength
A_1	Peak 1 area, fitted with Gaussian curve
α	Roughness exponent
b	Optical path
β	Growth exponent
c	Concentration
c	Vacuum speed light
CC	Correlation coefficient
ξ	Correlation length
D_T	Coefficient difusion
Δ	Phase difference
ΔE	Adsorbed energy
Δf	Frequency shift
ΔI	Current change
Δm	Adsorbed amount
ρ_q	Quartz density
ρ_f	Film density
ε	Absorption/extinction coefficient
ε_p	Partial absorption coefficient
ε_{p138nm}	Partial absorption coefficient at 138 nm of wavelength
$\varepsilon_{DPPG168nm}$	DPPG Absorption coefficient at 168 nm of wavelength
$\varepsilon_{PAH168nm}$	PAH Absorption coefficient at 168 nm of wavelength
F	Average number of particles that deposit on the surface
F_{ol}	Fraction of open liposomes
f	Frequency
f_q	Quartz fundamental resonant frequency
f_t	Transition frequency
γ	Fit linear slope
h	Surface grains height
h	Planck constant
I_{max}	Maximum current
I_{min}	Minimum current
I_0	Intensity of the incident light
I_s	Intensity of the scattered light
η	Viscosity

η_i	Noise
L	Length scale
λ	Wavelength
K	Spectral strength
k_B	Boltzmann constant
ξ	Correlation Length
M	Matrix columns
M_f	Film mass
Mw	Molecular weight
N	Matrix lines
n	Bilayers number
n_{JMA}	Exponent of the JMA equation
$n - \pi^*$	Electronic transition from an orbital n to an orbital π^*
$n_O - \pi^*_{CO}$	Electronic transition from the lone-pair of the carbonyl group to the antibonding π_{CO}- valence orbital
$n'_O - \pi^*$	Electronic transition from the second lone-pair of the carbonyl group to the orbital π^*
$n_O - \sigma^*$	Electronic transition from the carboxyl group of the atomic orbital *n* to the orbital σ^*
N	Constant frequency of the specific crystal cut
ν	Spectral index
P_1	Gaussian position of the peak 1
pk	Dissociation constant
Ψ	Amplitude angle
$\pi - \pi^*$	Electronic transition from an orbital π to an orbital π^*
Ra	Average roughness
R_H	Hydrodynamic radius
Rku	Kurtosis
Rms	Root-mean-square roughness
R_p	Parallel reflection coefficient
Rpm	Average maximum profile peak height
Rq	Root-mean-square roughness
R_s	Perpendicular reflection coefficient
Rsk	Skewness
Rt	Maximum height of the profile
Rtm	Average maximum height of the profile
Rv	Maximum profile valley depth
Rvm	Average maximum profile valley depth
S	Surface area of the deposited film

S_{ox}	Maximum slope of the current curve in the oxidation phase
S_{red}	Maximum slope of the current curve in the reduction phase
t	time
T	Absolute temperature
τ	Characteristic time
τ_{sh}	Lateral size of surface aggregates
Γ	Adsorbed amount per unit area
Γ_{DPPG}	DPPG adsorbed amount per unit area
Γ_{max}	Maximum adsorbed amount per unit area
Γ_{PAH}	PAH adsorbed amount per unit area
V	Particle volume
W_1	Gaussian width of peak 1
z	Dynamic exponent

1 INTRODUCTION

The growing interest in developing molecular devices for electronics, photonics and sensors based on biological molecules is due essentially to their ability to interact with dedicated and located chemical species. The creation of devices can be achieved condensing biomolecules in heterostructured thin films assembled onto solid supports making sure that these molecules have an adequate environment in order to maintain its specificity. Among others, the main factors that influence biomolecules functionality are ionic strength, pH, ionization degree, hydrogen bonds and especially water content. However, at room conditions, thin films lose water molecules that are bound to the biological molecules, the so-called structural water, compromising the biomolecular structure and stability, and consequently its own functionality. Therefore, it is mandatory an aqueous environment inside these heterostructures in order to provide well-designed biomimetic supramolecular devices. Such environment may be achieved with lipid molecules, which are the building blocks of all living cells, representing 50% of mass of the cell membranes. Lipids can be used to prepare simplified membrane models intra-layered with biomolecules or to obtain "water bags", liposomes, due to their poor solubility in water which causes a spontaneous rearrangement into vesicles creating a stable barrier between two aqueous compartments. Both, lipid membrane models or liposomes immobilized on surfaces, allow the creation of a biological compatible environment.

The deposition of lipids on solid supports can be achieved by Langmuir-Blodgett (LB) and Layer-by-Layer (LbL) techniques [1]. LB technique allows the deposition of sequences of lipid monolayers inter or intra-layered with functional biological molecules, e.g. proteins or DNA. However, this technique excludes the possibility of intact liposomes being deposited on a support. On the other hand, the LbL method, originally applied to the physical adsorption of oppositely electrical charged polyelectrolyte layers from aqueous solutions, has been extended to prepare lipid bilayers [2, 3] and, in certain cases, to adsorb whole liposomes that, in a proper way, can be assembled with encapsulated biological molecules [4, 5]. Immobilization of intact liposomes can be achieved with unprotected vesicles, i.e., vesicles with no polymer protective shell or biomolecules, but only under experimental conditions with a suitable combination of surfaces and liposomes. Consequently, the adhesion and stabilization of intact liposomes layers requires a strategy to avoid the vesicles rupture. In addition, recent research on polyelectrolytes LbL films composition reveal that when adsorption parameters are adequately controlled during layers assembly, water molecules remain in these films even when samples are submitted to high vacuum for several hours [6]. Therefore, the LbL technique seems to be an excellent approach to incorporate water molecules into these supramolecular heterostructures aiming a successful maintenance of the biological molecules functionality. Nevertheless, the conditions that define the deposition of open or whole liposomes onto solid supports are not well established in literature, so it is necessary to find these conditions in order to store water molecules into LbL films.

The main goal of this work is to evaluate and optimize the conditions for water molecules storage into functional supramolecular heterostructures, with the ability to mimic membranes or rudimentary cells, obtained from polyelectrolytes and biomolecules, by using the LbL method. Owing that LbL technique is based on physical adsorption phenomena both adsorbate and adsorbent should be considered.

Besides other physicochemical surface properties which are determinants for the adsorption of biomolecules and the conformational state of the adsorbent, such as chemical nature, charge, hydrophilicity, or structure; the role of the surface roughness in the adsorption phenomena is poorly characterized. Roughness imposes local geometrical constraints on the adsorbents that can be crucial for self-assembly processes, particularly when the sizes of self-assembled domains exceed the characteristic dimensions of the surface features. Thus, roughness is expected to influence the formation and organization of the self-assembled biomolecules.

As a first approach, the adsorption phenomena should be characterized in order to find the adequate parameters that lead to liposomes immobilization on surfaces. One of the main parameters to be exploited, e.g. by Quartz Crystal Microbalance (QCM) or by spectrophotometries, is the mass per unit area of the adsorbed layers on solid supports as a function of different adsorption parameters.The measurements with QCMs at the solid-liquid interface was introduced in the eighties when a suitable oscillator circuit for operation in liquids was developed [7] and it is often used to discriminate between systems with a low amount of water, e.g., supported-lipid bilayers (SLBs), in opposition to those with higher volume of water storage such as liposomes. However, *in situ* QCM measurements require improvements in order to overcome limitations associated to experimental setups configurations. In order to improve the QCM technique at solid/liquid interface a homemade cell was designed and implemented, providing a new successful experimental setup. Since lipids absorb in the ultraviolet region, the vacuum ultraviolet (VUV) spectroscopy technique, available in Synchrotron Radiation facilities and vastly used for macromolecules characterization which allows identifying their electronic transitions, was found to be an adequate method to analyse the amount of lipid bilayers or liposomes adsorbed onto solid supports.

The surface morphology characterization of the heterostructures can provide information about the liposomes immobilization mechanism on a surface. The surface analysis is usually associated to the concept of surface roughness which has a huge influence on many physical phenomena acting with higher effectiveness as the size of the objects decreases (to microscale). The present reduction of the devices, e.g., microelectromechanical systems, requires an improved grasp of the role of surface roughness, e.g., in contact mechanics and adhesion. Surface roughness is also of great importance for the function of many biological systems as cell adhesion in different microorganisms [8] and tumor growth [9]. Some animal species such as flies, bugs, crickets and lizards are able to attach and move on both very smooth and rough vertical solid walls, e.g. stone walls or leaves, due to the presence of very soft layers on their feet. On the other hand, plant surfaces developed non-wetting coatings, based on surface roughness on many different length scales, the so-called *lotus effect*, in order to reduce water losses as an adaptation to terrestrial environment. Currently, surface morphologies can be probed by atomic force microscopy (AFM) technique. Because of its ability to provide nanometer-scale images of biological samples, AFM is a powerful method used in biology and in membrane biophysics. It is known that for randomly rough surfaces, the function surface roughness power spectrum, inferred from the measured height profile, allows to determine the growth mechanisms based on scaling exponents as well as the mean grain size of the surfaces. Thus, the study and characterization of the

surface roughness is important to understand the adsorption mechanisms as well as the inner structure of the films.

Bearing in mind the goal of this work, the presence of water molecules inside the heterostructures can be analyzed by infrared (IR) and X-ray photoelectron (XPS) spectroscopies. IR spectroscopy is a method used to determine the fundamental vibrations and the associated rotational-vibrational structures of the molecules and XPS probes the surface region allowing the chemical qualitative and quantitative characterization of the heterostructures.

Therefore to achieve the proposed main goal, this work is focused on LbL films composed by polyelectrolytes such as poly(ethylenimine) (PEI), poly(allylamine hydrochloride) (PAH) and poly(sodium 4-styrenesulfonate) (PSS) and by the synthetic lipid 1.2-dipalmitoyl-sn-Glycero-3-[Phospho-rac-(1-glycerol)] (Sodium Salt) (DPPG). This lipid is widely studied since the natural phosphatidylglycerol (PG) is present in biological membranes of many organisms showing a crucial role in vital functions, e.g., induction of DNA replication in *E. coli* [10] and increase of the gases diffusion efficiency in pulmonary alveolus [11]. Melanin was used to be incorporated in DPPG liposomes and was selected to this work since is an important bio-macromolecule present in different organs of animals and plants [12-14], but also because it has different physicochemical properties including piezoelectricity and photoconduction being its main functions: photoprotection, photosensitization and thermoregulation [15]. Different types of supramolecular heterostructures were produced using the Layer-by-Layer technique such as: i) LbL films composed by polyelectrolytes interspersed with whole liposomes or lipid bilayers; ii) LbL films composed by a cushion of polyelectrolyte multilayers with intact liposomes and/or lipid bilayers adsorbed on top; iii) in certain cases, LbL films composed by polyelectrolytes interspersed with liposomes having melanin encapsulated or with lipid bilayers intra-layered with melanin. The adsorbed layers growth processes were monitored by the QCM technique *in situ* and by VUV spectroscopy. Kinetic characteristic parameters as a function of adsorption time and layers number were extracted by fitting the data with the Johnson-Mehl-Avrami equation [16]. The surface morphology of the LbL films was characterized by AFM imaging *ex situ* and *in situ* before and after polyelectrolytes multilayers assembly and lipid vesicles immobilization. Roughness amplitude parameters and dynamic scaling exponents were obtained from AFM data treatment. QCM and AFM imaging were combined to gather information of the layers growth mechanisms. Spectroscopic techniques, such as FTIR, VUV and XPS were used to find the composition, ionization and vibrational energy states of the organic molecules, but also to validate QCM and AFM interpretations.

This thesis is divided into 5 chapters. Chapter 2 describes cell membrane models and the techniques used to produce supramolecular heterostructures based on biological molecules onto solid supports. Chapter 3 presents the experimental section, such as the materials and the methods used to prepare the thin films, as well as the techniques used to characterize the heterostructures. The results and the discussion of the work are present in chapters 4 and 5. The characterization of DPPG liposomes suspension and DPPG cast films; the advances in instrumentation and experimental details developed for measurements *in situ* with a Quartz Crystal Microbalance; as well as the growth analysis of PEI/DPPG and PAH/DPPG LbL films can be found in chapter 4. Chapter 5 discusses the storage of

water molecules on LbL films, by creating planar lipids bilayers or depositing intact vesicles, through DPPG liposomes adsorption onto smooth and rough polyelectrolytes multilayers and solid supports. This chapter also presents a multisensory system using the produced LbL films for classification of olive oils collected from different Moroccan and Portuguese regions. Finally, the conclusions of the developed work and the future perspectives are present in Chapter 6.

2 LIPID BARED HETEROSTRUCTURES

An overview of the cell membranes models and the techniques used to produce supramolecular structures with biological molecules immobilized onto solid supports is presented in this chapter. Furthermore, a review of the experimental conditions that lead to adsorption of intact liposomes on solid supports or formation of lipid bilayers is also reported.

2.1 Cell membrane

In a sense, life is defined by membranes, because they delimit the barrier between the living cells and its surroundings. The cell membrane structure model currently accepted, *fluid mosaic model,* was proposed by Singer and Nicholson [17] in 1972. According to this model, see figure 2.1, the biological membrane is a dynamic and fluid structure whose basic constitution is a phospholipid bilayer (lipid bilayer) with incorporated proteins. The hydrophilic polar heads of the phospholipids bilayer are outer disposed occupying the two surfaces (intra and extracellular) and the hydrophobic tails are thus oriented to each other. The lipids of the bilayer are movable, often changing their position within a layer [18].

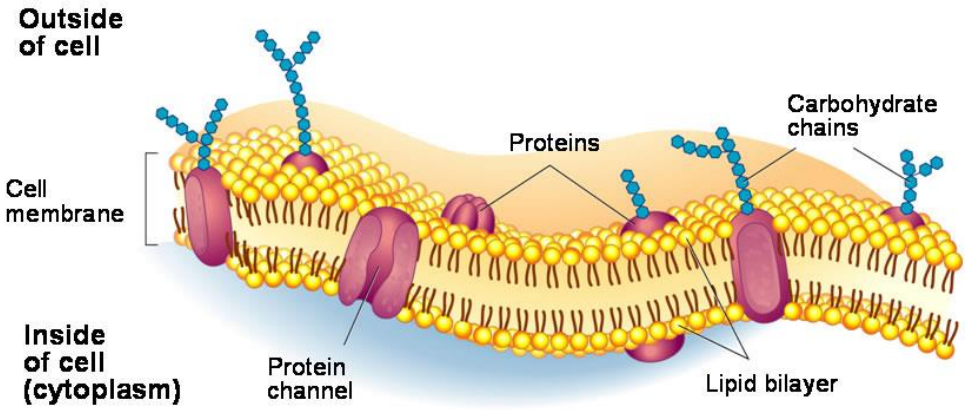

Figure 2.1. Schematic representation of a cell membrane [19].

On the external face of the cell membrane, carbohydrates are linked to phospholipid heads (glycolipids) or to proteins (glycoproteins), which are believed to be important to substances recognition. The biomembrane's ultrastructure presents an asymmetric arrangement, because it has some proteins linked to the membrane surface (extrinsic proteins) and others partially or wholly embedded in the bilayer (intrinsic proteins). These proteins may work as enzymes, substances transporters or signals receptors of the external environment. The relative proportions of proteins and lipids vary with the type of cell membrane and with its function. Besides, this model proposes that lipids and proteins diffuse freely in the plane of the cell membrane [20].

Lipid membranes structures are extremely difficult to study because of the polymorphic nature of the lipid arrangement, which presents a considerable variety of lipids, with different physical properties such as cross section, fluidity, electrical charge, molecular weight, among others. Furthermore, the covalent bonds of proteins and carbohydrates increases the complexity of the membrane structure [21]. The *in vivo* lipids role extends beyond structural division, involving also those molecules in cell signaling pathways [21] and in maintenance of the differences in electrolyte concentration and electrical field gradient between the extracellular environment and the cytoplasm. Biomembranes are essential to life mechanisms of regulation throughout many interfaces of the cell. Moreover, cell membranes composition can change quickly to respond to environmental stimuli [22]. Due to the complexity and heterogeneity of cell membranes, mechanisms and functions of lipid-biomolecule interactions have been often investigated using simplified models called biomimetic systems.

2.2 Cell membrane models

2.2.1 Phospholipids

The plasma membrane of a cell is composed by a bilayer of glycerophospholipid molecules. A single glycerophospholipid molecule is composed of two major regions: a hydrophilic head and a hydrophobic tail. Figure 2.2 shows the subregions of a glycerophospholipid molecule, in this case a phosphatidylcholine. The hydrophilic head is composed of a choline structure and a phosphate which is connected to a glycerol with two hydrophobic tails called fatty acids.

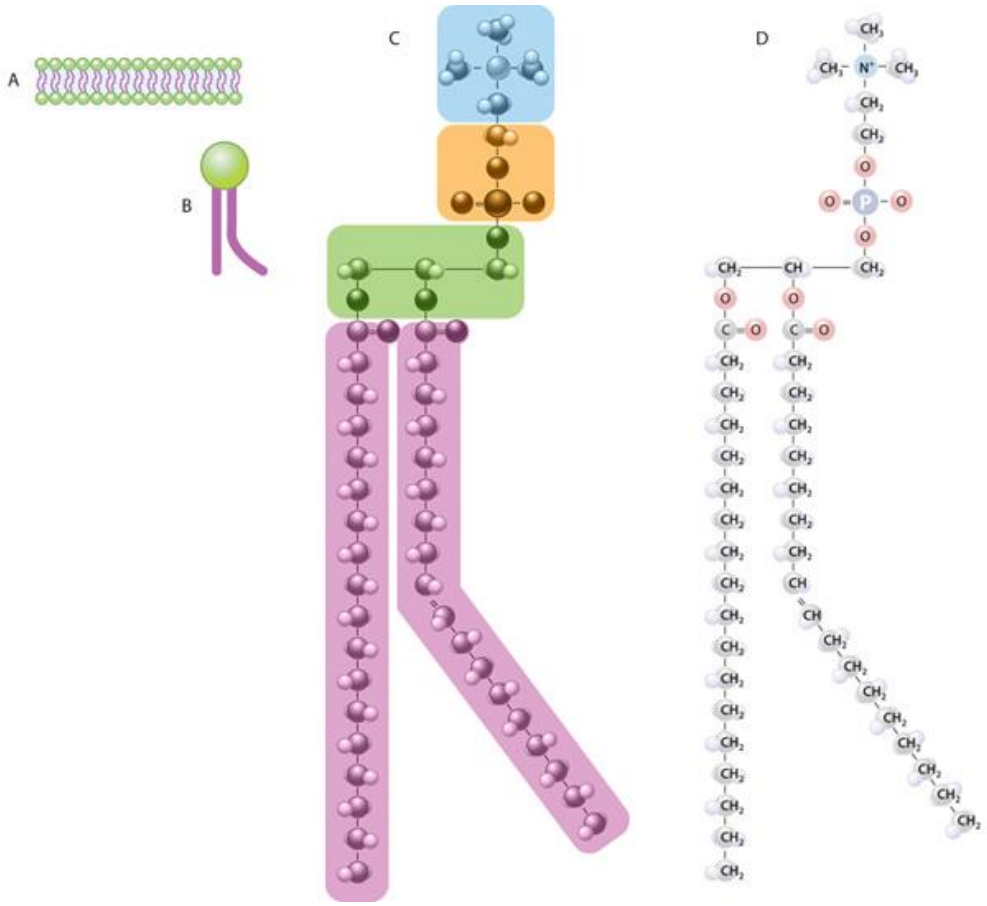

Figure 2.2. The lipid bilayer (A), structure (B and C) and composition (D) of a phosphatidylcholine molecule is shown as example of a glycerophospholipid. As shown in (C), the hydrophilic head is composed of a choline structure (blue) and a phosphate (orange); this polar head is connected to a glycerol (green) with two hydrophobic tails (purple) called fatty acids. View (D) shows the specific atoms within the various subregions of the phosphatidylcholine molecule. Note that a double bond between two of the carbon atoms in one of the hydrocarbon (fatty acid) tails causes a slight kink on this molecule, so it appears bent [23].

When phospholipids are mixed with water, a self-organization of the molecules occurs, where the hydrophobic portion is directed toward the center and may form various types of systems, as disposed on figure 2.3, including:

i) Micelles: aggregates with hydrophobic chains oriented inwards and the remaining hydrophilic groups at the surface in contact with water molecules, creating an environment without water. Essentially spherical, micelles can be also disc-shaped, cylindrical, ellipsoidal, among others;

ii) Liposome: vesicles obtained from phospholipids dispersion in an aqueous environment; they may comprise one or more lipid bilayers interspersed with aqueous surroundings.

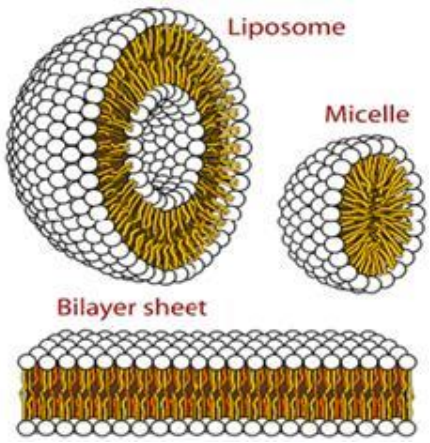

Figure 2.3. Schematic illustration of liposome, micelle and lipid bilayer sheet [24].

These features can be used to mimic biological membranes that are present in the organelles of living cells, e.g. mitochondria, golgi apparatus, nucleus cell, lysosomes, endoplasmic reticulum, amongst others.

2.2.2 Liposomes

Liposomes can be formed by sonication or mechanical dispersion of phospholipids in an aqueous solution and may be composed of one or more concentric lipid bilayers separated by an aqueous medium. These systems are often used to encapsulate active drugs or to incorporate proteins [25-27] and have proved to be useful as controlled models increasing the knowledge of the permeability properties of biological membranes [28]. Phospholipid vesicles were first described in 1965 by Alec Bangham and coworkers [27]. Immediately after the Bangham work, liposomes showed up as simplified systems for biological membranes research. Since Gregory Gregoriadis studies, in 1971, liposomes have been widely investigated [26, 29-31] in what concerns their physical properties [32-34], preparation [35, 36], formation and fusion mechanisms [37, 38], membrane transport [39] and characterization methods. Apart from its utility in physical chemistry, these biomimetic models have been extended to the medicine field [40, 41], such as for encapsulate bioactive agents [42] or to interact with living cells [43], for vaccines [44] and for veterinary goods [45] production, for erythrocytes substitution [46, 47] and for cosmetic applications [48]. The liposomes may also be used as pharmaceutical transporters, e.g. in cancer therapy [25], by introducing exogenous molecules which are carried in their “water bags” or within the lipid bilayer, into living cells, i.e., liposomes containing soluble molecules that after fusion with the cell membrane release their contents into the cell cytoplasm [49]. In 2005, Michel *et al.* have successfully assembled intact vesicles interlayered with polyelectrolytes layers onto solid supports, extending these models’ ability to be used as drug reservoirs and for advances in well-designed sensors and devices [50].

Liposomes can be prepared from natural or synthetic phospholipids. The first can be extracted from biological material of living cells; e.g. phosphatidylcholine (lectin) phospholipid can be removed from egg yolk or soybeans. These natural phospholipids are used as the main lipid components for the production of liposomes because they are quite abundant in cell membranes. They may vary concerning the length, composition and saturation of the hydrocarbon chains. Synthetic lipids, despite having a well-defined lipid composition of their hydrocarbon chains, may have greater or lesser number of carbon atoms, equal or different and saturated or unsaturated fatty acid chains. Besides, they possess a greater homogeneity allowing a better understanding, characterization and manipulation of their behavior in opposition to natural phospholipids.

Currently, liposomes are not only applied to the biomedical field (e.g. diagnostic tests, blood transfusion in the absence of an appropriate donor, or detoxification through the use of chelating agents), but their applications have been extended to industry, cosmetics, agriculture (fertilizer stabilization), livestock (dairy maturation of milk), purification, recovery, catalysis and energy conversion processes [51].

Summarizing, liposomes can be defined as a colloidal association of amphipathic lipids that spontaneously organize themselves in closed concentric structures or vesicles. They can be extracted from natural lipid mixtures or extracted and purified from synthetic lipids that are commercially available. These vesicles can be classified by their size, *lamellae* number, lipid formation, stability and preparation mode [31]. Figure 2.4 depicts liposomes types that are commonly used as membrane model systems, namely multilamellar vesicles (MLV), small unilamellar vesicles (SUV) and large unilamellar vesicles (LUV). SUVs are usually obtained by extrusion of multilamellar liposomes through porous polycarbonate membranes at high pressure or by sonication of lipid aqueous suspensions [52]. The liposome category is essentially determined by their preparation method which should always be selected carefully, since its composition, number of layers, size distribution and encapsulated volume influence considerably the liposomes applications.

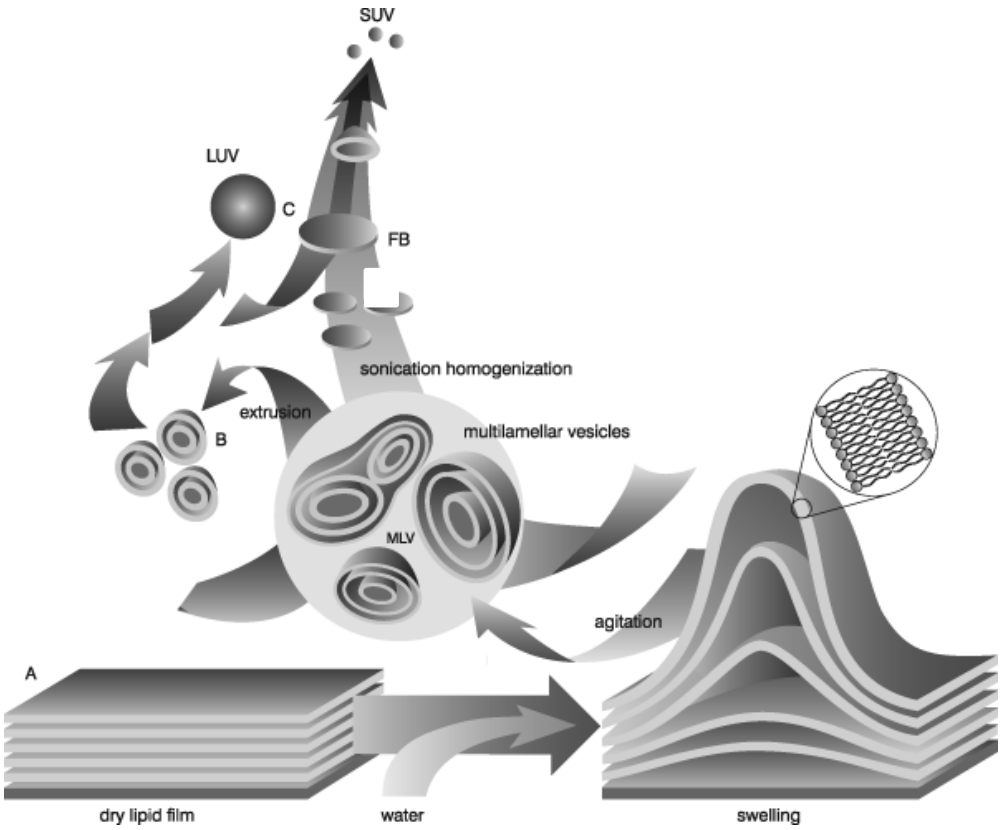

Figure 2.4. Schematic representation of multilamellar vesicles (MLV), small unilamellar vesicles (SUV) and large unilamellar vesicles (LUV) preparation methodologies [53].

The key factors for vesicles' characterization are size, *lamellae* number and lipid bilayers constitution. Various parameters such as charge, stability, curvature of the bilayer or bilayers, phase membrane and formation of lipid domains depend on the phospholipid composition, the presence of sterols, the proportion of these components and the insertion of exogenous molecules into their bilayers [51]. The true conformation of the liposomes may be crucial for specific applications.

2.3 Supramolecular structures production techniques

Nanostructured thin films based on organic and inorganic compounds, are systems that can act as simplified models of the cell membrane and have been widely exploited in different fields, from physics to medicine, for example in the development of molecular devices and sensors and in pharmaceutical research, respectively. Their potential applications in biology and medicine have been highlighted in the second half of the twentieth century, when these supramolecular heterostructures were combined with biological materials at a molecular level. The methods most commonly used for thin film deposition on solid substrates are the Langmuir-Blodgett (LB) and Layer-by-Layer (LbL) techniques [54].

2.3.1 Langmuir-Blodgett technique

Langmuir-Blodgett technique was designed in the 30s by Irving Langmuir and Katharine Blodgett. Langmuir was responsible for the equipment development of monomolecular films adsorbed at the air-water interface and also for their theoretical models. Katherine Blodgett contributed primarily for the film's transfer methods from the water surface to a solid substrate. The films adsorbed onto solid surfaces are named Langmuir-Blodgett (LB), while films spread on water are called Langmuir [55]. A schematic representation of these techniques is displayed in figure 2.5. Molecules used to manufacture Langmuir and LB films are amphiphilic, generally having a hydrophilic head and a hydrophobic apolar tail [56]. Due to its polar head the molecules have affinity for water, spreading out the surface without dissolving due to the presence of a nonpolar tail. These materials are immiscible with water and can only be dissolved in volatile solvents which evaporate rapidly, leaving the amphiphilic molecules dispersed over the water surface. Examples of amphiphilic materials are fatty acids, such as stearic acid, and esters and ethers with long hydrocarbons chains. The steps to produce Langmuir and LB films are the following: i) a small amount of solution containing amphiphilic molecules is spread on the water surface, allowing the formation of a monomolecular film; ii) thereafter, movable barriers are used to compress the monolayer, causing rearrangement of the molecules with their heads anchored on the aqueous surface and the tails facing the air; iii) at maximum packing, molecules reach a condensed state, and if the compression continues the film collapses [55]; iv) this monolayer can be transferred to a solid substrate by dipping through it. Each dipping cycle transfers two additional monolayers to the substrate.

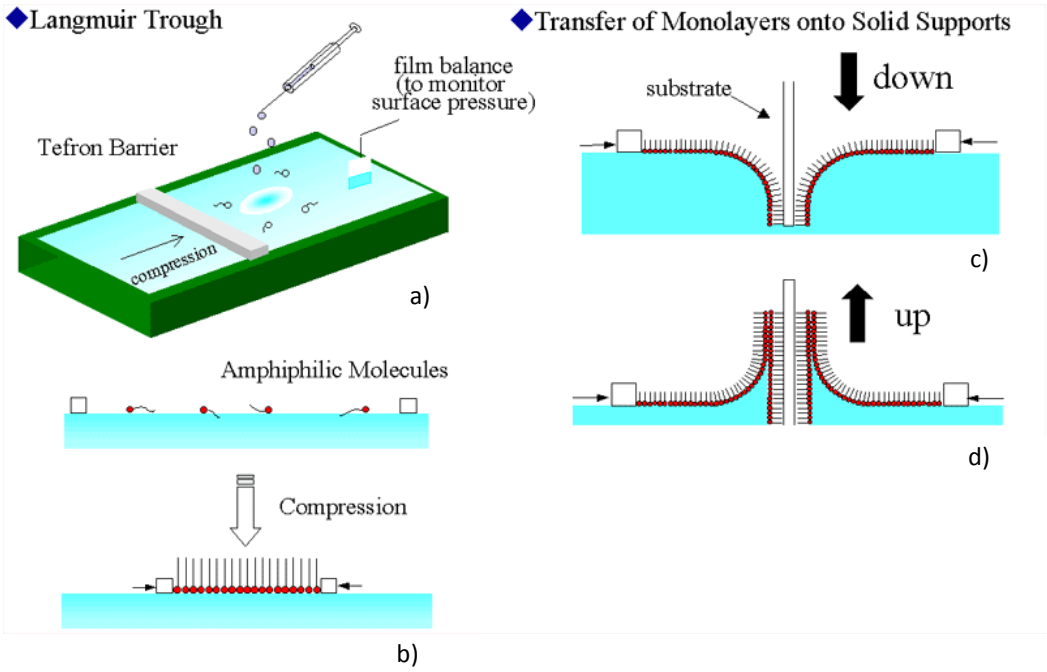

Figure 2.5. Schematic diagram of Langmuir and Langmuir-Blodgett films procedures: a) a small amount of a suspension with amphiphilic molecules is spread on the water surface and a monomolecular film is formed; b) movable barriers compress the monolayer, leading to rearrangement of the molecules, with their heads anchored on the aqueous surface and the tails facing the air, until a maximum packing is reached and the condensed state is attained; c) the condensed monolayer can be transferred into a solid substrate by dipping through it; d) another monolayer can be added by pulling the solid surface from water. This process can be repeated in order to obtain various multimolecular layers [57].

2.3.2 Layer adsorption techniques

2.3.2.1 Self-assembled monolayers

Self-assembly monolayer (SAM) technique is a process used to produce well-organized structures obtained from the spontaneously adsorption of molecules onto solid supports or substrates (polymers, metals, semiconductors, ceramics) upon chemical interactions (see figure 2.6). In 1978, Sagiv reported the first results of irreversible adsorption of organic solutions on solid surfaces through covalent bonding as a method to produce monolayers holding a controllable in-plane molecular organization [58, 59]. SAM is a model system used to investigate organic and biological interfaces comprising a technical interest for the fabrication of sensors, transducers and protective layers for lubrication and is a pattern able for lithography applications with nanometer precision. For example, SAM arrays of immobilized single-stranded deoxyribonucleic acid (DNA), the so-called DNA chips, have revolutionized the genetic analysis for disease detection, toxicology, forensics, industrial processing and environmental monitoring [60].

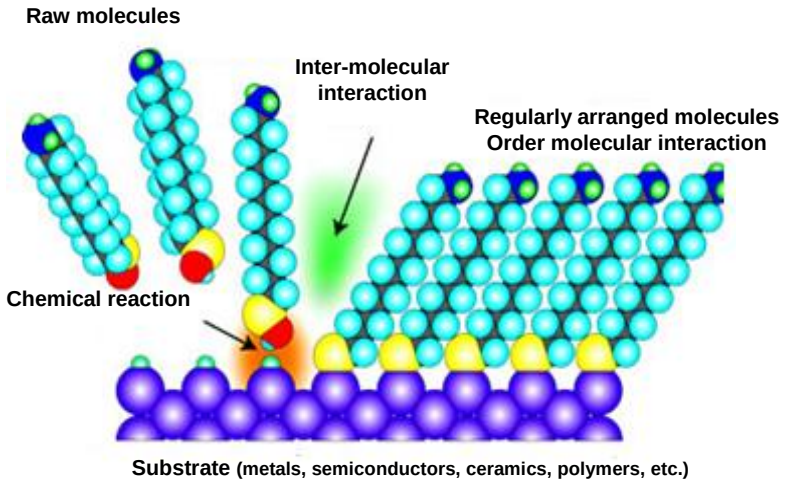

Figure 2.6. Scheme of the self-assembly monolayer technique. Due to chemical interactions the molecules are spontaneously adsorbed on a substrate resulting in a well-organized structure [60].

2.3.2.2 Layer-by-layer technique

An alternative method to produce functional biomolecular heterostructures was developed in 1992, by Decher *et al.* [61], named the layer-by-layer (LbL) technique [1] and is based on the electrostatic interactions between oppositely charged molecules. The experimentally procedure to produce the LbL films is shown in figure 2.7, where a negatively charged solid substrate is immersed, for example, in a cationic solution, until a polycationic layer is adsorbed on the substrate surface. Then, the sample is immersed in an anionic solution, promoting the adsorption of the polyanionic layer onto the polycationic layer previously adsorbed, creating a bilayer. The desired number of bilayers is achieved by repeating the explained method [62]. After each layer deposition the sample is washed in order to remove any weakly adsorbed molecules. Finally, the LbL films can be dried with a nitrogen flow or at

room temperature. This technique allows the assembly of alternately cationic and anionic species on solid substrates of any shape or size. Regarding to LbL films growth, it is known that the major driving forces are the ionic attraction between the electrically charged layers, although other interactions such as hydrogen bonding and hydrophobic interactions can also conduce the LbL films assemblage [16].

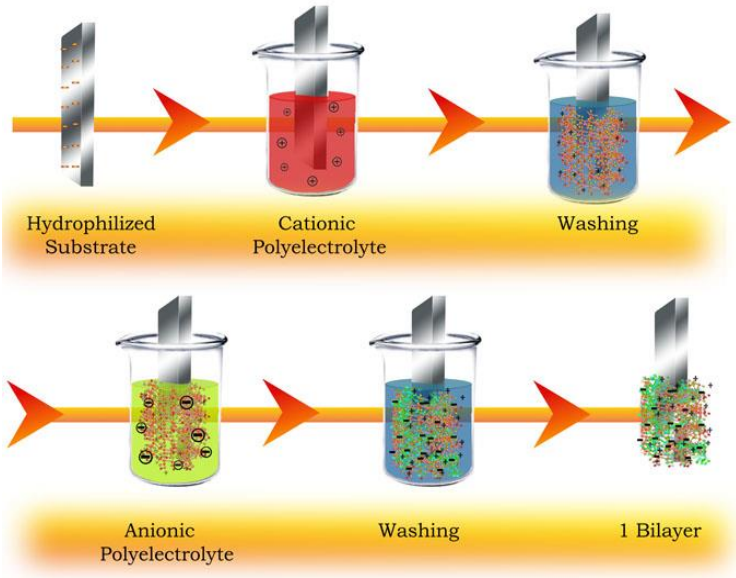

Figure 2.7. Scheme LbL technique procedure. The desired number of bilayers is achieved by repeating the method represented.

The LbL technique offers experimental simplicity, it is a low cost method and is suitable for aqueous solutions [1]. Furthermore, the absorption of each layer is dependent on the following parameters: polyelectrolyte solution molarity, pH of the polyelectrolyte and washing solutions, ionic strength, room temperature, adsorption time, substrate affinity, surface roughness, polyelectrolyte volume solution with respect to substrate area, and drying procedures. All these variables can contribute to adsorption or desorption phenomena of the layers when immersed in a solution or subjected to vacuum [1]. Studies done by Lourenço *et al.* [6, 63] allowed to verify that the amount of water molecules in LbL thin films is influenced by the salt concentration in the solution, drying procedures, as well as the type of materials used in the heterostructures assembly.

The creation of molecular heterostructures is governed by the variables described above, but the surface roughness is an important parameter that must be highlighted. Furthermore, the number and diameter of the molecular aggregates, called "particles", strongly depend on the adsorption time, as well as the number of layers already adsorbed and rinsing and drying procedures [1]. Moreover, we have to consider the different types of interactions between biological molecules, deeming it a challenge not only due to molecules complexity, but also because different non-covalent bonds to which molecule is subjected.

2.4 Liposomes immobilization onto solid supports

Liposomes formed from self-assembly of lipids are important cell membrane models since lipids are the basic building blocks of the living cells, representing approximately 50% of their membrane mass. The liposomes immobilization on LbL films is suitable to exploit important characteristics of these heterostructures when functional biological materials are combined, especially the ability to preserve bioactivity and to serve as template for surface functionalization, e.g. in tissue engineering. In fact, the effectiveness of LbL assemblies has been proved for several other biological materials such as proteins, enzymes, DNA and viruses [54]. Aiming to mimic cell membranes, liposomes have been immobilized on solid supports, called supported-lipid bilayers (SLB). However, during liposome adsorption three situations may occur, as explained in figure 2.8: they may adsorb as intact vesicles (C); or the vesicles can adhere, break and spread creating a planar lipid bilayer (A and B); or adsorption could not occur at all (D) [64].

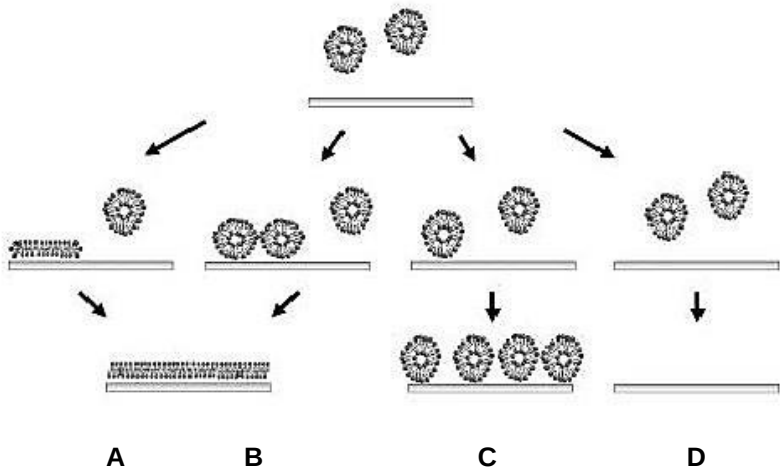

Figure 2.8. Schematic representation of the pathways of vesicle deposition and SLB formation: (A) Formation of an SLB generated at low vesicular coverage; (B) Formation of an SLB produced at high vesicular coverage; (C) Formation of a liposome layer; (D) Inhibited adsorption [64].

When liposomes are adsorbed on polyelectrolyte multilayers obtained by the LbL technique they may remain intact creating a polymer-supported liposomes (PSLs) [61, 65] or suffer rupture followed by their spreading throughout the surface producing bilayers, named polymer-supported phospholipid bilayers (PLBs) [3, 64, 66]. These systems have been widely used as well-defined model systems to study biomembranes' properties, particularly structures and functions, e.g. to understand cells adhesion and protein interactions [67], as well as to design biosensors [68]. A crucial example is the interaction between beta-amyloid peptides and lipid membranes working as trigger agents in Alzheimer's disease [69]. Also, negatively charged liposomes keep their integrity when adsorbed on highly curved surfaces [70]. Vesicles immobilization onto surfaces and the factors responsible for

creating conditions for liposome rupture must be analyzed in order to increase vesicles half-life and to activate a controlled drug release using an external stimulus [71].

2.4.1 Solid-supported phospholipid bilayers

Solid-supported phospholipid bilayers (SPBs) were introduced in the eighties by Tamm and McConnell [72, 73] and can be easily formed by the SUVs adsorption and fusion onto solid supports. Adsorption kinetic processes underlying SPB formation are dependent on the liposomes composition, size, osmotic pressure and ionic strength, pH of the solution and charge and roughness of the surface [74]. Phospholipid liposomes easily disperse and self-assemble in a reproducible way to form bilayers on hydrophilic solid supports, such as glass [70], silica (SiO_2) [75] and mica [76] surfaces.

A number of studies have identified some of the critical stages of vesicles adsorption (adhesion), fusion, deformation, rupture, and spreading of the lipid bilayer. The most promising conditions required for attaining homogeneous single bilayers from adsorption of neutral lipids onto charged surfaces are displayed in table 2.1, namely: vesicle-support electrostatic interactions; high liposome concentration ($>$0.1 mg/mL); edges vesicle-bilayer interactions; vesicle composition; temperature above the chain melting point; presence of calcium ions; and polyelectrolytes multilayers cushions [77].

Table 2.1. Conditions for liposome rupture during adsorption.

Conditions for liposome rupture during adsorption	Literature
High ionic strength (vesicle-support electrostatic interactions)	[77] Anderson et al, Langmuir, 2009, 25 (12), 6997. [78] Faiss et al, Eur Biophys J, 2004,33, 555. [64] Richter et al, Biophys J, 2003, 85, 3035.
Critical vesicular surface coverage	[64] Richter et al, Biophys J, 2003, 85, 3035. [77] Anderson et al, Langmuir, 2009, 25 (12), 6997. [75] Reimhult et al, Langmuir, 2006, 22, 3313. [79] Stroumpoulis et al, AIChE J, 2006, 52 (8), 2931. [66] Richter et al, Langmuir, 2006, 22, 3497.
Edges vesicle-bilayer interactions	[77]Anderson et al, Langmuir, 2009, 25 (12), 6997. [67] Weirich et al, Biophys J, 2010, 98, (1)85. [75] Reimhult et al, Langmuir, 2006, 22, 3313. [79] Stroumpoulis et al, AIChE J, 2006, 52 (8), 2931. [64] Richter et al, Biophys J, 2003, 85, 3035. [66] Richter et al, Langmuir, 2006, 22, 3497.
Vesicle composition	[78] Faiss et al, Eur Biophys J, 2004,33, 555. [64] Richter et al, Biophys J, 2003, 85, 3035.
Temperature above the chain melting point	[77] Anderson et al, Langmuir, 2009, 25 (12), 6997.
Calcium Ions	[80] Marquês et al, Biochim Biophys Acta, 2011, 1808,405. [64] Richter et al, Biophys J, 2003, 85, 3035. [66] Richter et al, Langmuir, 2006, 22, 3497.
Polyelectrolyte Multilayers (PEMs)	[2] Haas et al, Biophys J (Annual Meeting Abstracts), 2001, 80 (1):100 Part 2. [81] Kohli et al, J Colloid Interface Sci, 2006, 301, 461. [3] Gromelski et al, Colloids Surf B Biointerfaces, 2009, 74, 477.

Formation of SPBs can be described in different stages, displayed in figure 2.9 [72, 75, 82, 83]: 1) Initially some whole liposomes populate the surface (A and B); 2) At a critical coverage, liposomes start to break, fuse and form bilayer islands (C to E), coexisting both liposomes and a bare surface (F); 3) Finally, a coherent SPB is formed, covering the whole surface (H). Additionally, Tang *et al.* [84] demonstrated that the ionization degree of the polymers-cushions and the phospholipid composition can also influence the liposomes kinetics adsorption and the bilayer formation.

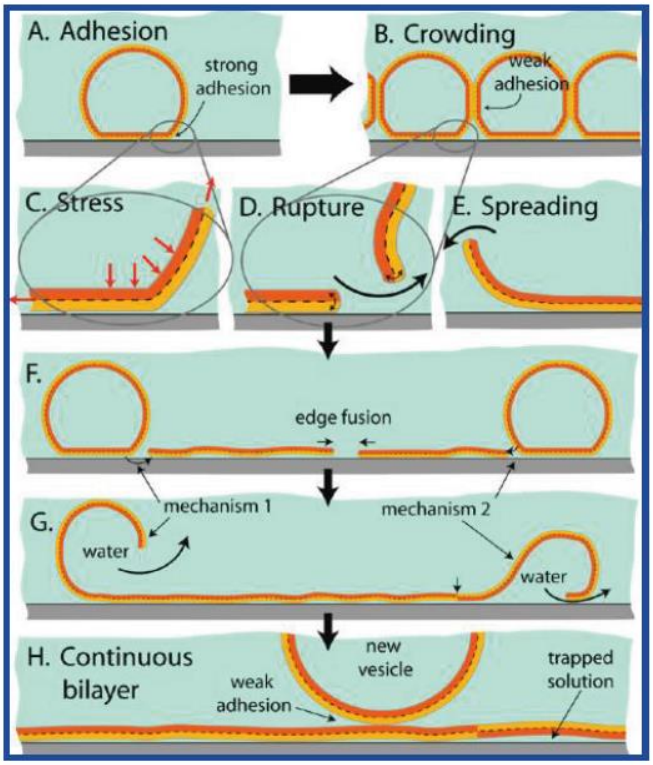

Figure 2.9. Different stages of vesicle adsorption: (A) adhesion, (B) crowding, (C, D, E) stress-induced rupture and spreading of bilayer patches that can expose leaflets either by mechanism 1 or 2 (F, G), coalescence of high energy edges and expulsion of water and excess of lipid and (H) growth of patches into a continuous bilayer; further adsorption of vesicles to the bilayer is weak and does not lead to their rupture or spreading [77].

2.4.2 Polymer-supported liposomes

Polymer-supported liposomes (PSLs) obtained by the LbL technique offer key advantages over the direct use of liposomes [61, 85] and may find several applications, including the modeling of cell membranes and the incorporation of pharmaceutical drugs or biomolecules for drug delivery [4, 5]. Recently, it was demonstrated [86-91] that using the LbL technique based on the adsorption of oppositely charged materials [1, 61, 92, 93], also called the self-assembly technique, liposomes can be adsorbed without rupture and consequently permitting the creation of heterostructures based on whole liposome layers alternated with polyelectrolytes. Adsorption of intact liposomes embedded in

polyelectrolyte multilayers (PEMs) greatly enhances the capabilities of liposomes towards dedicated biosensors, namely for the development of new functionalized surfaces or drug release systems for biomolecules encapsulation allowing the preservation of their activity [94]. Tanaka and Sackmann [95] used the LbL method to investigate the properties of membranes and membrane-associated proteins, while Yamauchi *et al.* [96] prepared lipid/DNA LbL films for stent-assisted gene transfer. Until now it was demonstrated that a controlled adsorption of vesicles containing a small fraction of charged lipids allows their adsorption without rupture and their subsequent embedding in PEM films, meaning that vesicles may be immobilized in an intact or slightly deformed state, turning them suitable to act as drug reservoirs [3, 64, 90, 97, 98]. Table 2.2 presents an overview from literature of works related to conditions for closed vesicles adsorption.

Table 2.2. Intact vesicles adsorption conditions.

Conditions for intact vesicles adsorption	Literature
Gold surface (hydrophobic surface)	[83] Keller and Kasemo, Biophys J, 1998, 75, 1397. [75] Reimhult et al, Langmuir, 2006, 22, 3313. [99] Morita et al, J Colloid Interface Sci 2006, 298, 672.
Polyelectrolyte Multilayers (PEMs)	[100] Moraes et al, Mater Sci Eng C Mater Biol Appl, 2008, 28, 467. [3] Gromelski et al, Colloids Surf B Biointerfaces, 2009, 74, 477. [90] Volodkin et al, Soft Matter, 2009, 5 1394. [94] Michel et al, Langmuir, 2004, 20, 4835.

Due to the low stability of a lipid bilayer on solid supports, studies have been done to immobilize liposomes in LbL heterostructures. In studies performed by Moraes *et al.,* they used surface plasmon resonance (SPR) to confirm liposomes' integrity of interspersed layers in dendrimer/liposome produced by the LbL technique [100]. Delajon *et al.* [101] employed neutron reflectivity to study the charge effects on adsorption processes of LbL films. Volodkin and coworkers produced LbL films with liposomes coated with two biocompatible polyelectrolytes (Hyaluronic acid (HA) and poly-L-lysine (PLL)) and proved the structural integrity of the liposomes. In another study [4], fluorescence measurements, showed that melanin activity was preserved when encapsulated in liposomes interspersed in polymer layers produced by the LbL method. On the other hand, in LbL films containing melanin adsorbed on polyelectrolyte layers, degradation of melanin was found, which proves that liposomes are crucial in maintaining an environment close to physiological, thus preserving melanin integrity and enabling their application in biological systems [4].

2.5 Water

Covering 70% of the surface, water is the most abundant molecule on Earth, responsible for the existence of life in our planet and it can be found in three physical states: solid, liquid and gaseous. Interactions with water are part of our world, existing both in a large scale of as in ice, snow and rain, and at a molecular scale, playing an important role in the macromolecular conformation of the biological molecules.

Thus, water can be found in cells, having the ability of hydrating membranes and large biomolecules. In geology, interfacial water molecules can control mineral dissolution and ion adsorption. In chemistry, water is an important polar solvent that is often in contact with interfaces. Different hydration water orientations are assumed to occur in the first solvation shell on anions and cations: (A) an anion orients the OH bond toward it, whereas (B) a cation orients the water dipole moment vector away from it [102]. Although, water is a very small molecule with a radius of 1.4 Å [103], it can form a rather extended hydrogen bond networks.

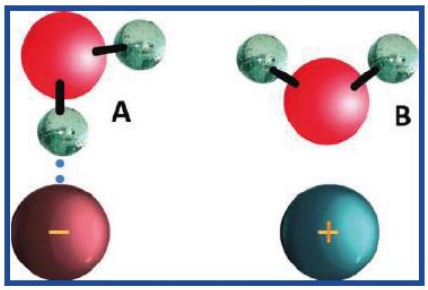

Figure 2.10. Different hydration water orientations are assumed to occur in the first solvation shell on anions and cations: (A) an anion orients the OH bond toward it, whereas (B) a cation orients the water dipole moment vector away from it [102].

A large number of experimental [104-106], computational [103, 106] and theoretical studies [107, 108] have revealed how the properties of water molecules and ionic aqueous solutions change due to neighborhood membranes and, in turn, how the membranes properties strongly depend on properties of aqueous solutions at the membrane boundary. The importance of incorporating a molecular-level description of water into the study of biomembrane surfaces can be demonstrated by the examination of the interaction within the phospholipid bilayers, that can serve as biological membrane models. Berkowitz and Vácha described the interaction of pure water and also of aqueous ionic solutions with model membranes and explained the origin of the hydration force, the structural properties at interface water-phospholipid bilayers, and the influence of phospholipid headgroups on water dynamics [109].

Works accomplished by Israelachivili *et al.* [77] showed that when phospholipid bilayers are deposited on solid surfaces, a presence of a thin layer with 0.6-0.9 nm of thickness can be found between the lipid bilayer and the silica substrate. Recent experimental advances in vibrational spectroscopy allowed to investigate the interface water-reverse micelles depicted in figure 2.11 [110]. This study

showed that at low hydration levels, all water molecules penetrate deeply into the headgroup region, except for zwitterionic phosphatidylcholine lipids, thus interacting favorably with phosphate and carbonyl groups, which are, in fact, 5-10 Å from the headgroup surface.

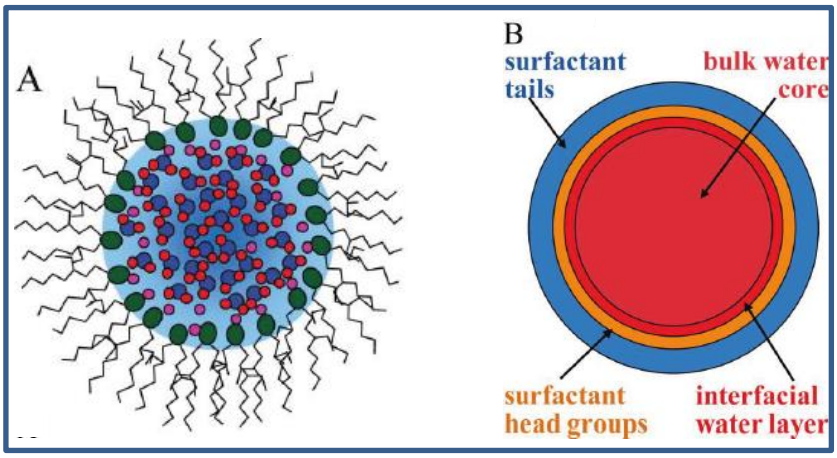

Figure 2.11.(A) Diagram of a reverse micelle with water trapped. (B) Schematic showing the various regions of the reverse micelle structure [104].

3 EXPERIMENTAL SECTION AND CHARACTERIZATION TECHNIQUES

This chapter describes the experimental procedures used to prepare thin films and the techniques employed to characterize the samples.

3.1 Materials

This sub-chapter describes the materials used to prepare supramolecular heterostructures.

3.1.1 Organic polyelectrolytes

The polycations used to assemble supramolecular heterostructures were the poly(allylamine hydrochloride) (PAH; average Mw = 50,000–65,000 $gmol^{-1}$) whose monomer has an ionic group NH_3^+ with a Cl^- counterion and the poly(ethyleneimine) (PEI; average Mw = 60,000 $gmol^{-1}$). The polyanion used was poly(sodium 4-styrenesulfonate) (PSS; average Mw = 70,000 $gmol^{-1}$) whose monomer has an ionic group SO_3^- with a Na^+ counterion. LbL films preparation was done using aqueous polyelectrolyte solutions with a monomeric concentration of 10 mM, and pH~4, pH~8 and pH~6 for PAH, PEI and PSS solutions, respectively. Under these conditions, PAH and PEI are positively charged and PSS is negatively charged. PEI, PAH and PSS polyelectrolytes were purchased from Sigma–Aldrich and their molecular structures are depicted in figure 3.1. All chemicals were used as received and solutions were prepared using ultrapure water (Milli-Q, Millipore GmbH) with a resistivity of 18.2 MΩ.cm and pH~5.7. These solutions were chosen due to their well-known assembly characteristics, namely growth features and adsorption kinetics [111, 112].

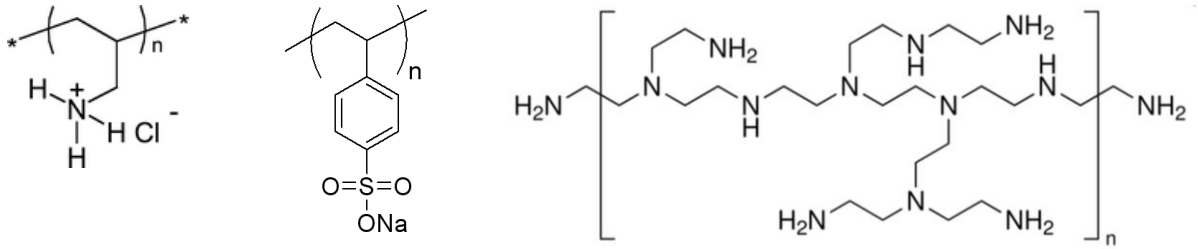

Figure 3.1.Polyelectrolytes molecular structures used in LbL self-assembly technique.

Regarding LbL self-assembly technique, these polyelectrolytes allow incorporation of molecules intercalated between layers, as a method for immobilizing inorganic nanoparticles or colloids, DNA, proteins, viruses and dyes. The main requirement to achieve a proper configuration is that *pK* values of the polyelectrolyte molecules must be known and the pH value at which the assembly occurs must be controlled. The advantage of using PSS, PAH and PEI polyelectrolytes interspersed, for example, with proteins, is their ability to provide a flexible arrangement acting as a cushion for the adsorbed layer [113].

3.1.2 Lipid

Highly pure (>99%) synthetic 1.2-dipalmitoyl-sn-Glycero-3-[Phospho-rac-(1-glycerol)] (Sodium Salt) (DPPG), with a molecular weight of 744.96 $gmol^{-1}$ was purchased from Avanti Polar Lipids and its chemical structure is shown in figure 3.2. The fact that DPPG liposomes are negatively charged at pH~5.7 allows its use in LbL films' assembly. In addition, it is one of the most common lipids in model membranes.

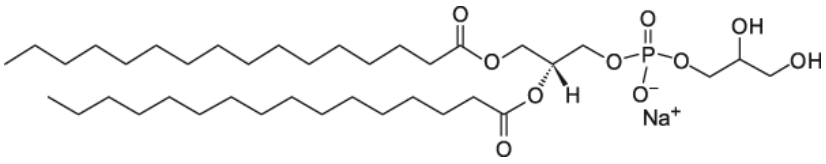

Figure 3.2. Chemical structure of 1.2-dipalmitoyl-sn-Glycero-3-[Phospho-rac-(1-glycerol)] (Sodium Salt) (DPPG).

Natural phosphatidylglycerol (PG) is an ubiquitous phospholipid in biological membranes of many organisms. It is found in all bacterial membranes as well as in the mitochondrial inner membranes of eukaryotic cells. The PG constitutes about 15-20% of the total phospholipids in *Escherichia coli* bacteria. Owing to its simple lipid composition, *E. coli* serves as a useful model organism for understanding the primary roles played by PG in membranes [114]. *In vivo* evidences have shown that the presence of anionic phospholipids is essential for the initiation of DNA replication in *E. coli* [10]. In plants, PG is mainly present in thylakoid membranes and it has been suggested to play specific roles in photosynthesis [115]. Small quantities of PG are found in almost animal tissues, but it is particularly abundant in the surfactant pulmonary mixture which has the function of reducing the pulmonary alveolus surface tension in order to improve gases diffusion efficiencies [11]. It is well established that PG concentration increases during fetus development. Respiratory distress syndrome (RDS) is the major cause of neonatal mortality and affects about 1 % of all newborns. The RDS is caused by the structural immaturity of the lungs and the inadequate levels of surfactant in the alveoli. The PG test measures these phospholipid levels in the amniotic fluid in order to know the lung maturity of the fetus. This test is done between 34 and 38 weeks of pregnancy and can be used to determine the appropriate course of action if the baby is at risk of being born prematurely [116].

3.1.3 Melanin

Melanin belongs to an important class of bio-macromolecules and it is observed in different organs of living organisms. This protein can be found in various regions of the human body and animals [12, 13], such as skin, hair, eyes, inner ear and brain and in plants, such as black tea leaves, amongst others [14]. There are four main categories of melanins: eumelanin, pheomelanin, allomelanin and neuromelanin [117]. The eumelanin has been widely studied for decades, it can be found in animals and it contains both brown and black pigments [117]. These bio-macromolecules have different physicochemical properties including piezoelectricity and photoconduction and their main functions are photoprotection, photosensitization and thermoregulation [15]. They can absorb a broad UV-visible range and can act as antioxidants [14]. Due to their diverse functions and physical properties, these macromolecules have been used in diseases' treatment [118] and in electronics, biosensors and photoactive devices [119]. Melanin's immobilization and manipulation onto solid substrates is interesting for technological applications because of its electronic properties; however it is very difficult to preserve melanin's functionality [48], due to its low solubility and chemical stability in aqueous solution. However, it was demonstrated that melanin incorporated into liposomes exhibit better solubility and stability than free melanin in an aqueous solution [4].
Synthetic melanin was purchased from Sigma–Aldrich (product number M8631) and incorporated into DPPG liposomes (see section 3.2.1) and its chemical structure is shown in figure 3.3.

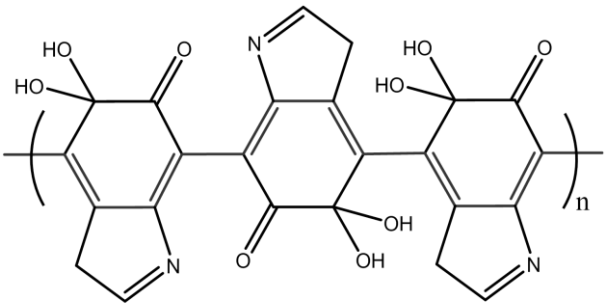

Figure 3.3. Chemical structure of melanin.

3.1.4 Olive oils

Olive oil is a highly appreciated food product not only in the Mediterranean basin's countries, where there is intense olive oil production [120], but all over the world due to its owing nutritional properties [121], remarkable digestibility, high oxidative stability even after being cooked, strong capacity to prevent heart and vascular diseases [122]. Geographical origin is one of the most important factors involved in olive oil quality. In fact, there are many different varieties of olive, each one with a

particular flavor, texture, and shelf-life that make them more or less suitable for different applications such as direct and indirect human consumption. For example, Cobrançosa and Gallo olives are two famous varieties cultivated in Portugal, on the other hand, Picholine olive is largely grown in Morocco, France, Italy, United States of America and other places around the world [123, 124]. The relationship between geographical area and quality as well as chemical composition of different olive oil varieties has been studied by several authors using different techniques. Indeed, several techniques were used to determine geographical origin of olive oils, namely: high performance liquid chromatography (HPLC) [125], gas chromatography coupled with mass spectroscopy (GC-MS) [126], capillary electrochromatography (CEC) with UV–Vis detection [127]. Most of these methods are based on conventional analytical techniques that require complex instruments and qualified personnel. It is therefore of great interest to develop a simple and reliable method that may characterize and classify olive oil geographical origins. In this context, the use of electrochemical sensors can be considered as an interesting alternative tool to assess the quality of olive oil and their application in classification or authentication trials [128].

In this study a total of 11 olive oil samples from Portugal and Morocco were analyzed: 6 samples came from six different commercial Portuguese olive oils and the other five came from Moroccan olive oils namely, Gallo Classico, Fio Dourado, Oliveira da Serra, Paladin, Gallo Reserva and SOS Pobreza; and Moulay Idriss, M'rirt, Ouarzazate, Ouazzane and Taounate, respectively. For electrochemical measurements, 15 ml of olive oil of each sample were dissolved in 45 ml of dichloromethane (CH_2Cl_2) and tetrabutyl-ammonium tetraphenylborate ($C_{40}H_{56}BN$) (70 mg) was used as a supporting electrolyte, solutions were magnetically stirred and thermostatically controlled using a water bath of ~30 °C. Results and discussion can be found in section 5.6.

3.1.5 Solid supports

According to the suitable characterization technique different solid supports or substrates were used to prepare thin films. Calcium fluoride and silicon substrates were previously washed with detergent, followed by immersion in a 7:3 H_2SO_4/H_2O_2 "piranha" solution for about 5 minutes in an ultrasound bath, and then washed with ultrapure water. The gold-quartz crystal substrate was cleaned in an ultrasound bath at 60°C during 15 min in a 2 % Mucasol solution, followed by rinsing with ultrapure water, ethanol and ultrapure water again. Thereafter the substrate received a UV/Ozone treatment during one hour and finally was washed with ultrapure water. The voltammetry (interdigitate) electrodes were cleaned successively in acetone, "piranha" solution for 1 min and rinsed with distilled water. After the cleaning steps all substrates went through a final wash with ultrapure water and then were dried with a nitrogen stream before thin films assembly.

3.2 Methods

This sub-chapter describes the methods used to prepare DPPG liposomes suspensions and polyelectrolyte solutions used to create thin films. Some experimental details of the characterization techniques used are introduced in this sub-chapter, but a detailed description can be found in section 3.3.

3.2.1 DPPG Liposomes suspension

Small unilamellar vesicles (SUV) were obtained by starting to dissolve DPPG in methanol:chloroform (2:8); after solvent evaporation, using a gentle stream of nitrogen, the lipid film was hydrated for 2 h in ultrapure water supplied by a Millipore system; this dispersion was vortexed intermittently leading to multilamellar vesicles (MLVs); then an ultrasonic processor UP50H from Hielscher Ultrasonics (GmbH, Germany) was used to sonicate the MLVs suspensions at 30 kHz of working frequency, in an ice bath, during 30 seconds. This procedure was repeated 15 times with 1 minute delay between cycles. In other experiments, the SUV suspensions were obtained by the MLVs suspension extrusion in a mini-extruder, purchased at Avanti Polar Lipids, plugged with polycarbonate membranes containing 0.1 μm pores diameter. All the liposomal suspensions were stored in the fridge at 6°C. Figure 3.4 represents schematically SUVs suspension procedure. The size distribution of DPPG liposomes obtained by sonication and extrusion methods were analyzed by Dynamic Light Scattering (DLS) and results are shown in section 4.1.

To encapsulate melanin into SUVs, a methanol solution containing 0.16 mg/mL of melanin was mixed with DPPG in a methanol:chloroform (2:8) solution. The following steps are the same as those described above to produce DPPG SUVs liposomes by the sonication procedure.

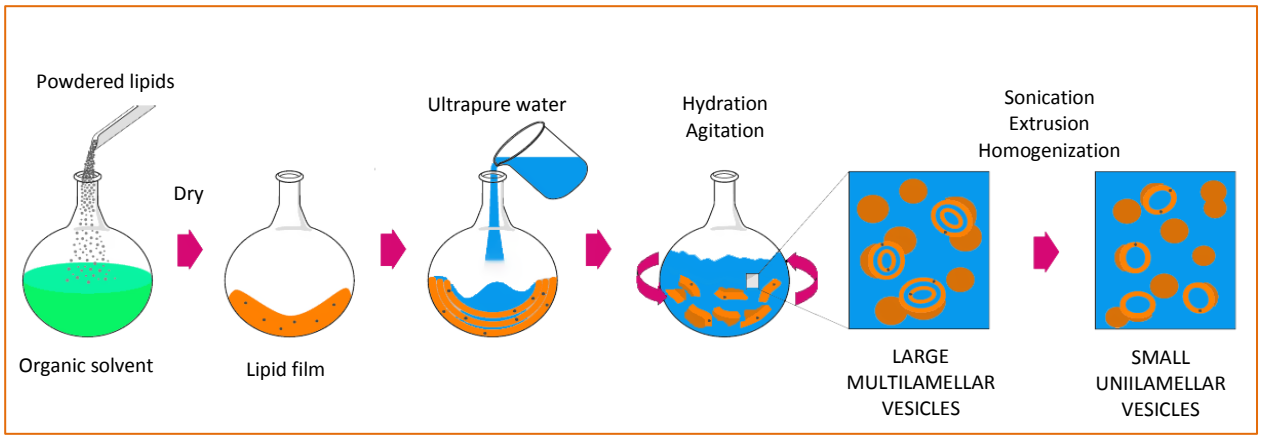

Figure 3.4. Schematic representation of MLVs and SUVs preparation by the lipid film hydrating method. 1) Lipids dissolution into a suitable organic solvent. 2) Lipid film formation on the walls of the flask by evaporation of the organic solvent. 3) Film hydration by adding an aqueous solution. 4) Agitation and obtaining of MLVs. 5) SUVs or LUVs obtained by sonication or extrusion (adapted from [53]).

3.2.2 Thin films preparation

In this subsection it is explained the different experimental procedures performed to create the thin films. It is also introduced the characterization techniques used to analyzed each sample.

3.2.2.1 Cast films

This technique consists in the injection, with the aid of a micropipette, of the solution under study over a substrate. Cast films of extruded SUVs were obtained by casting 5mM of DPPG SUV suspension onto a calcium fluoride substrates for Fourier transform infrared spectroscopy (FTIR) measurements and onto silicon supports to be analyzed by atomic force microcopy (AFM), scanning electron microscope (SEM), energy dispersive X-ray spectroscopy (EDS) and X-ray photoelectron spectroscopy (XPS) techniques. The PAH cast films were obtained by casting the polycationic solution onto quartz substrates. The water solvent was removed by submitting the samples to primary vacuum during 12 h. The DPPG cast films characterization is provided in section 4.2 and 4.5 and for the PAH cast films is presented in section 4.5.

3.2.2.2 LbL films

This subsection presents all LbL films produce throughout the work. Although the LbL technique is generally defined by adsorption of solutions oppositely charged, depending on the characterization techniques used, different methods were performed in order to get more reliable results.

3.2.2.2.1 PEI/DPPG

Kinetic growth of PEI/DPPG bilayers, i.e. DPPG layer adsorbed onto a PEI layer, was monitored using a quartz crystal microbalance (QCM), explicitly QCM 200 from Standford Research Systems, disposed in five different arrangements: Stationary Horizontal Open (SHO), Stationary Horizontal Closed (SHC), Stationary Vertical Open (SVO), Continuous Vertical Closed (CVC) and Stationary Vertical Closed (SVC). These five different QCM experimental configurations for *in situ* measurements, i.e. at solid-liquid interface, were compared. The constraints related to mechanical and acoustic vibrations and the liquid-quartz crystal interface fluctuation temperature were studied. LbL films' growth based on cationic polyelectrolyte PEI and anionic DPPG liposomes, obtained by sonication and adsorbed onto Au-quartz crystal resonator in aqueous solutions were characterized. Monomeric concentrations of 10 mM and 1.5 mM, respectively. The kinetics curves attained in each procedure were analyzed to infer about the adequate configuration that will improve QCM measurements in liquid phase. For experimental details please access section 3.3.1. Topographic images of the PEI cushion and the PEI/DPPG LbL film were obtained by atomic force microscopy (AFM), in non-contact mode, using an Asylum MFP3D. Section 4.3 displays the obtained results and respective discussion.

3.2.2.2.2 $(PAH/PSS)_{10}$ cushion and $(PEI/DPPG)_{10}$

Assembly of ten PEI/DPPG bilayers adsorbed onto a cushion prepared with common polyelectrolytes was monitored *in situ* by QCM using the SHC system described in section 4.3. The $(PAH/PSS)_{10}$ cushion was adsorbed onto Au-quartz crystal by the LbL method, via sequential adsorption of oppositely charged PAH and PSS polyions solutions. The polyelectrolytes solutions and the DPPG suspension's adsorption time were 3 minutes and 15 minutes, respectively. The $(PEI/DPPG)_{10}$ LbL films prepared from cationic aqueous solutions of PEI polyelectrolyte and anionic DPPG liposomes, obtained by extrusion, with 10 mM and 5 mM, respectively, were assembled onto the $(PAH/PSS)_{10}$ LbL film. To infer about the adsorption processes, the kinetics curves were analysed and the obtained findings are discussed in section 4.4.

3.2.2.2.3 PAH/DPPG and $(PAH/DPPG)_{10}$

LbL films build up with ten PAH/DPPG bilayers were deposited onto calcium fluoride, quartz and silicon substrates for spectroscopy studies. LbL films were obtained by immersing the substrates in a PAH solution during 3 min, followed by rinse with ultra-pure water. Then the substrate was immersed in a DPPG suspension for 30 min, followed by another rinse with water. Timepoints for adsorption were chosen based on adsorption kinetics studies [129, 130]. After each bilayer deposition samples were dried with a gentle nitrogen flow. This adsorption procedure was repeated to obtain the desired number of bilayers. Film growth was monitored with vacuum ultraviolet (VUV) spectroscopy measurements. Surface morphology of a PAH/DPPG LbL film deposited onto silicon substrate was characterized by AFM technique in non-contact mode using a Nanoscope III microscope (Digital Instruments, Veeco). Results and discussion are presented in section 4.5.

3.2.2.2.4 $(PAH/DPPG)_5$ and $(PEI/DPPG)_5$

$(PAH/DPPG)_5$ and $(PEI/DPPG)_5$ LbL films prepared for XPS measurements were assembled by immersing a silicon substrate in PAH or PEI solution during 3 min, followed by rinse with ultrapure water. Then the substrates were dipped in DPPG suspensions, obtained by sonication, for 10 min, followed by wash process again. This adsorption procedure was repeated in order to obtain the number of bilayers desired. The achieved results are presented and discussed in subsection 4.5.5.

3.2.2.2.5 $PEI/(PSS/PAH)_5$ and $PEI/(PSS/PAH)_5/DPPG$

$PEI/(PSS/PAH)_5$ polyelectolyte multilayer (PEM) was assembled *ex situ* onto a gold-quartz crystal resonator via LbL technique. NaCl salt concentration of PAH and PSS solutions was 1 M. The adsorption times for the polyelectrolytes solutions were 30 min and 20 min, for PEI layer and PAH and PSS layers, respectively. Between each adsorption step the crystal/PEM was rinsed with ultrapure water. At the end, the LbL film was dried at room temperature. The adsorption of a layer of DPPG liposomes, obtained by sonication, was performed using the SVC setup by placing the quartz/PEM in a holder QCM cell, filled with ultrapure water (for more details please access section 4.3), reaching a

stagnation point volume of 6 ml. After ultrapure water injection in the QCM cell, the capacitance was cancelled. Then, a certain quantity of DPPG solution was injected into the cell in order to obtain 1 mM as final concentration. The frequency shift was recorded during 300 minutes at 20°C. Both PEM and DPPG surface topographies were imaged by a MFP-3D (Asylum Research, USA) AFM apparatus in non-contact mode and the DPPG kinetic curves were obtained by QCM (using the SVC system). Obtained data are shown and debated in section 5.1.

3.2.2.2.6 Au/DPPG, Au/PAH/DPPG and PEI/(PSS/PAH)$_4$/DPPG

Preparation of Au/PAH and Au/PEI/(PSS/PAH)$_4$ polymers-supported surfaces were performed *ex situ.* In the first case, the Au-quartz crystal resonator was dipped in a PAH solution for 3 minutes, followed by a washing process with ultra-pure water. The second LbL film was executed using the same immersion times for each polyelectrolyte solution which then were sequentially adsorbed until reaching the desired number of layers. In this case, NaCl salt concentration of PAH and PSS solutions was 1 M. Finally, the polymers-supported surfaces were dried at room temperature.

Surface morphologies of Au-quartz crystal, polymers-supported surfaces and DPPG liposomes, obtained by sonication, adsorbed onto Au and different polymers were investigated by AFM *in situ* measurements, *i.e*., the sample was immersed into a liquid cell with ultrapure water. Au and polymers-supported surfaces were initially covered with 40 µL of ultra-pure water followed by the injection of 60 µL of DPPG suspension. Imaging was performed using a Multimode Nanoscope IIIa Microscope (Digital Instruments, Veeco).

The amount of DPPG layer assembled onto PAH was monitored *in situ* via QCM using the SVC experimental configuration. Prior to QCM measurements, the Au-quartz crystal/PAH was plugged in the crystal holder and then the liquid cell was attached to it. The frequency shift was recorded during 70 minutes. All QCM measurements were made at 20°C with a fundamental frequency of 5 MHz.

LbL films of Au/(PAH/DPPG)$_4$ were obtained by immersing the Au-quartz crystal substrate in a PAH solution during 3 minutes, afterwards it was washed with ultrapure water, then it was immersed in the DPPG dispersion, obtained by sonication, for 10 minutes, followed by another rinsing process. This procedure was repeated four times. The film was dried at room temperature. Optical characterization of the gold substrates before and after (PAH/DPPG)$_4$ LbL film adsorption was done with an ellipsometer (SENTECH Instruments GmbH, Berlin).

The outcomes are displayed and discussed in sections 5.2 and 5.3.

3.2.2.2.7 PEI/(PSS/PAH)b/DPPG and PAH/DPPG

PEI/(PSS/PAH)b heterostructures with different number of bilayers, n ($1 \leq b \leq 4$), were prepared *ex situ* from PEI, PSS and PAH polyelectrolyte solutions. These polyelectrolytes solutions were adsorbed sequentially using the LbL technique onto Au-quartz crystal resonator. The heterostructure preparation method started with the immersion of the Au-quartz crystal in an aqueous PEI polycationic solution for 3 minutes, followed by a rinse process with ultrapure water. Afterwards, the PEI/quartz crystal was dipped in a PSS polyanionic solution for 3 minutes, followed by a wash process. The previous steps

were repeated using PAH as polycationic solution. In this case a PEI/$(PSS/PAH)_1$ heterostructure was created. PSS/PAH assembly was repeated until the LbL film attained the desired number of bilayers. NaCl salt concentration of PAH and PSS solutions was 1 M. To produce a sample with a single PAH layer, the Au-quartz crystal support was dipped for 3 minutes in a PAH solution, followed by washing with ultrapure water. This Au/PAH sample was prepared without salt in order to reduce the roughness. pH of both PAH solutions, with and without salt, is similar in order to guarantee the same ionization degree of the outer PAH layers. All samples were left to dry under ambient conditions. Prior to QCM measurements, using the SVC setup, the quartz crystal/PEM was plugged to the crystal holder and the liquid cell attached to it, giving rise to a volume stagnation point of 6 mL. For operation in liquids, after ultrapure water injection in the QCM cell the capacitance cancellation was carried out. Then a certain volume of DPPG suspension, obtained by sonication, was injected into the cell in order to attain 1.47 mM as final concentration. All QCM measurements were recorded during 900 minutes at 20°C with a fundamental frequency of 5 MHz. The findings are presented and discussed in sections 5.4 and 5.5.

Surface morphology of DPPG liposomes adsorbed onto the Au-quartz crystal/PAH and Au-quartz crystal/PEI$(PSS/PAH)_4$ obtained with different adsorption times, namely 5, 30, 60, 300, 900 and 1800 seconds, was investigated *ex situ* using the AFM MFP-3D (Asylum Research, USA) , in non-contact mode. The achieved results are available and discussed in section 5.4.

PEI/(PSS/PAH)b heterostructures, before and after DPPG liposomes adsorption, as produced with the QCM, were imaged *ex situ* using the AFM MFP-3D (Asylum Research, USA), in non-contact mode. PEI/$(PSS/PAH)_4$ and PEI/$(PSS/PAH)_4$/DPPG LbL films were analyzed by XPS technique. Obtained data are accessible and debated in section 5.5.

3.2.2.2.8 $(PAH/DPPG)_3$, $(PEI/DPPG)_3$ and $(PEI/(DPPG+melanin))_3$

$(PAH/DPPG)_3$, $(PEI/DPPG)_3$ and $(PEI/(DPPG+melanin))_3$ LbL films were prepared onto glass substrates with interdigitated electrodes deposited on it. Adsorption time used for both PAH and PEI polyelectrolytes solutions was 3 minutes. For the DPPG and DPPG+melanin suspensions, obtained by sonication, with 1 mM of monomeric concentration, the interaction time was 10 minutes. DPPG+melanin designation refers to melanin encapsulated into DPPG liposomes. The results are accessible and discussed in section 5.6.

3.3 Characterization techniques

The following section describes the experimental techniques used to obtain a detailed characterization of the prepared thin solid films.

3.3.1 Quartz Crystal Microbalance

Nowadays, Quartz Crystal Microbalance (QCM) is a fundamental instrument used to measure the mass of the nanomaterials assembled on solid surfaces. The QCM concept first developed by Sauerbrey [131, 132] is based on the quartz crystal piezoelectric properties [133]. Currently, AT-cut quartz crystals with a thickness shear mode vibration [134] are most commonly used as QCM sensors because of their superior mechanical and piezoelectric properties [135]. The QCM operation is based on placing the crystal in resonance, at a frequency proportional to the mass uptake on the crystal, according with the relation:

$$\Delta f = -\frac{{f_q}^2 M_f}{N\rho_q S} = -\frac{{f_q}^2 m_f}{N\rho_q} \tag{3.1}$$

where f_q is the fundamental resonant frequency of the quartz crystal, *N* is the frequency constant of the specific crystal cut, AT-cut or BT-cut ($N_{AT} = 1.67 \times 10^5 Hz \cdot cm$; $N_{BT} = 2.5 \times 10^5 Hz \cdot cm$), $\rho_q = 2.65\ Kg \cdot dm^{-3}$ is the quartz density; *S* is the surface area of deposited film and M_f is the mass of the film. When the deposited films covers the whole sensitive area of the quartz resonator it is easier to use the real areal density, $m_f = M_f/S$, to further calculate the film thickness, $l_f = m_f/\rho_f$, where ρ_f is the deposited film density. A typical quartz resonator is shown in figure 3.5. The quartz crystal is usually covered by gold or silver keyhole-shaped electrodes on both major faces, with approximately 150 nm of thickness, deposited by vacuum evaporation. The central part of the resonator brings up the mass-sensitive area, covering the area where the two electrodes overlap. Equation 3.1 shows that the QCM mass sensitivity, $\Delta f/M_f$, is proportional to the square of the quartz resonator frequency [136].

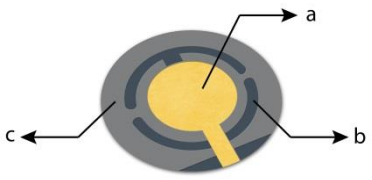

Figure 3.5.Typical quartz resonator (a) front gold and (b) back gold electrodes, (c) quartz crystal.

QCM200 system acquired from Stanford Research Systems (SRS), California, was used to carry out the experiments. This model is a stand-alone instrument with a built-in frequency counter and resistance meter which includes a controller, an electronic crystal oscillator, a crystal holder and a quartz crystal double coated with chromium and gold. The crystal holder can be electrically connected to the QCM25 crystal oscillator that operates with a QCM200 controller. The crystal probe connector is an RJ-45 receptacle used to connect the QCM200 controller to the QCM25 crystal oscillator. The standard sensor crystal used by the QCM200 system consists of a thin disk, with a nominal output frequency of 5 MHz, AT-cut, α-quartz with circular electrodes patterned on both sides. The crystal holder is rugged, compact and easy to operate and may be used in liquid or gas environments.
This instrument is stand-alone type with a frequency counter and a resistance meter, where the resonance frequency and the resistance are measured and displayed on the LCD panel, although the software control allows the data real-time reading, this also enables data acquisition connected via RS-232 to a computer. Figure 3.6 shows the digital controller and the crystal oscillator.

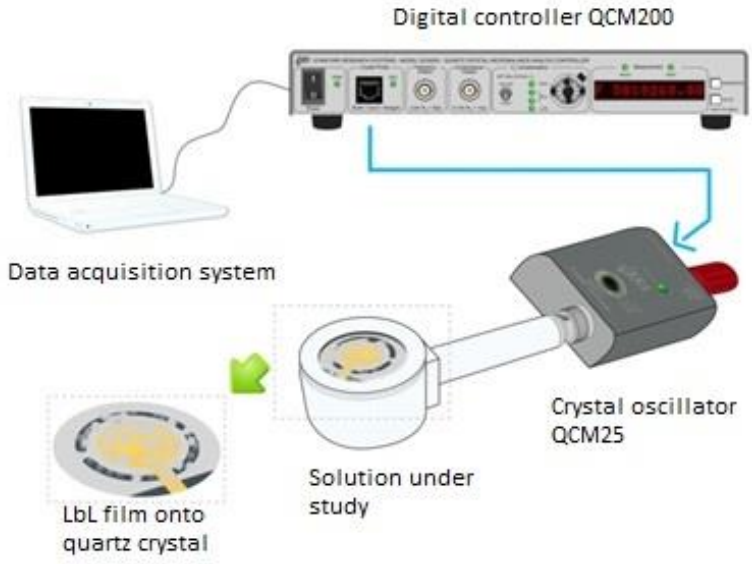

Figure 3.6. Scheme illustrating the experimental procedure for measuring the mass variation analysis of the solutions using a QCM200 (adapted from [137]).

For many years, QCMs were regarded as just gas-phase mass detectors [138], however, the work produced by Nomura and Okuhara (1982) showed that they can be operated in contact with liquids and viscoelastic deposits [7]. Currently, there is a large variety of QCM applications such as, immunosensors [139], sorption sensors [140], moisture analyzers [141], particulate monitors [142], contamination monitors [143], electrovalency measurements [144], hydrogen absorption on metal films [145], bubble formation [146], redox and conductive polymer research [147], double-layer characterization [148], corrosion studies [149], surface oxidation [150], DNA and RNA hybridization studies [151], antigen-antibody reactions [152], protein adsorption [153], detection of virus capsids [154], bacteria [155] and mammalian cells [156], protein-protein interactions [157], self-assembled

monolayers [158], molecularly imprinted polymers [159], Langmuir/Langmuir-Blodgett films [160], laser ablation [161], desorption and breakdown studies [162] and intelligent biomaterials [163], amongst other applications.

Given the great variety of applications described above it is essential to underline that the major QCM advantage is its high mass sensitivity *in situ* measurements, associated to its weightless that turns the equipment portable and its moderate cost compared with other measuring mass techniques. In addition, is a nondestructive technique so the thin films can be further analyzed using different techniques, e.g. atomic force microscopy, scanning electron microscopy or X-ray photoelectron spectroscopy. QCM can be a very useful tool for suspended particles measurements as long as the operational limitations are acknowledged, such as the particle size, concentration, humidity, temperature, molecules physical/chemical properties, or quartz crystal position angle [164].

The QCM technique allows differentiating between intact and disrupted liposomes adsorbed on the quartz crystal resonator. Usually, the immobilized liposomes tend to i) keep an intact structure, ii) form lipid bilayers or iii) monolayers, depending on the solid surfaces, properties of the modified surface, immobilization methods and liposome properties. Also, other experimental parameters as temperature, size, surface nature and osmotic pressure have been studied on supported phospholipid bilayers (SPB) build-up using the QCM technique [165-167]. Israelachvilli and collaborators [168] used a QCM to study the influence of salt and liposome concentration of 1.2-dimyristoyl-sn-glycero-3-phosphocholine (DMPC) vesicles on silica. Reimhult *et al* observed vesicles adsorption on gold (Au) surfaces [75] and vesicles adsorption followed by SPB formation on silicon dioxide supports using the QCM technique [169].

Although this technique is strongly disseminated for liquid measurements, it is common to obtain kinetic curves with noise and instabilities and, in certain cases, non-reproducible data specifically due to different experimental procedures carried out by the operator. So, in order to study these and other limitations such as mechanical and acoustic vibrations and liquid-quartz crystal interface temperature fluctuation, different QCM experimental configurations were tested and compared using the LbL assembly [170] onto a quartz crystal resonator from aqueous solutions of PEI polyelectrolyte and DPPG liposomes. The kinetics curves attained by each QCM setup (see section 4.3) were analyzed to infer about its suitability for mass uptake measurements in liquid phase.

Five different experimental configurations were developed, three with the quartz crystal vertically positioned and in the other two horizontally placed. The horizontal modes were called the Stationary Horizontal Closed (SHC) and the Stationary Horizontal Open (SHO) as shown in figure 3.7 a) and b), respectively and the vertical setups were named the Continuous Vertical Closed (CVC), the Stationary Vertical Closed (SVC) and the Stationary Vertical Open (SVO) as shown in figure 3.7 c), d) and e), respectively. A flow cell, shown on figure 3.7 (c), was acquired from SRS to test a closed system with a continuous liquid flux. The liquid flux was provided by a peristaltic pump purchased from ISMATEC, model ISM795C (1.00 REGLO ANALOG MS-2/12-160 EA) connected to two-stop tubes IDEX Tygon LfL with an internal diameter of 1.6 mm. An inject cell, represented in figure 3.7 d), was designed and produced to test a stationary closed system.

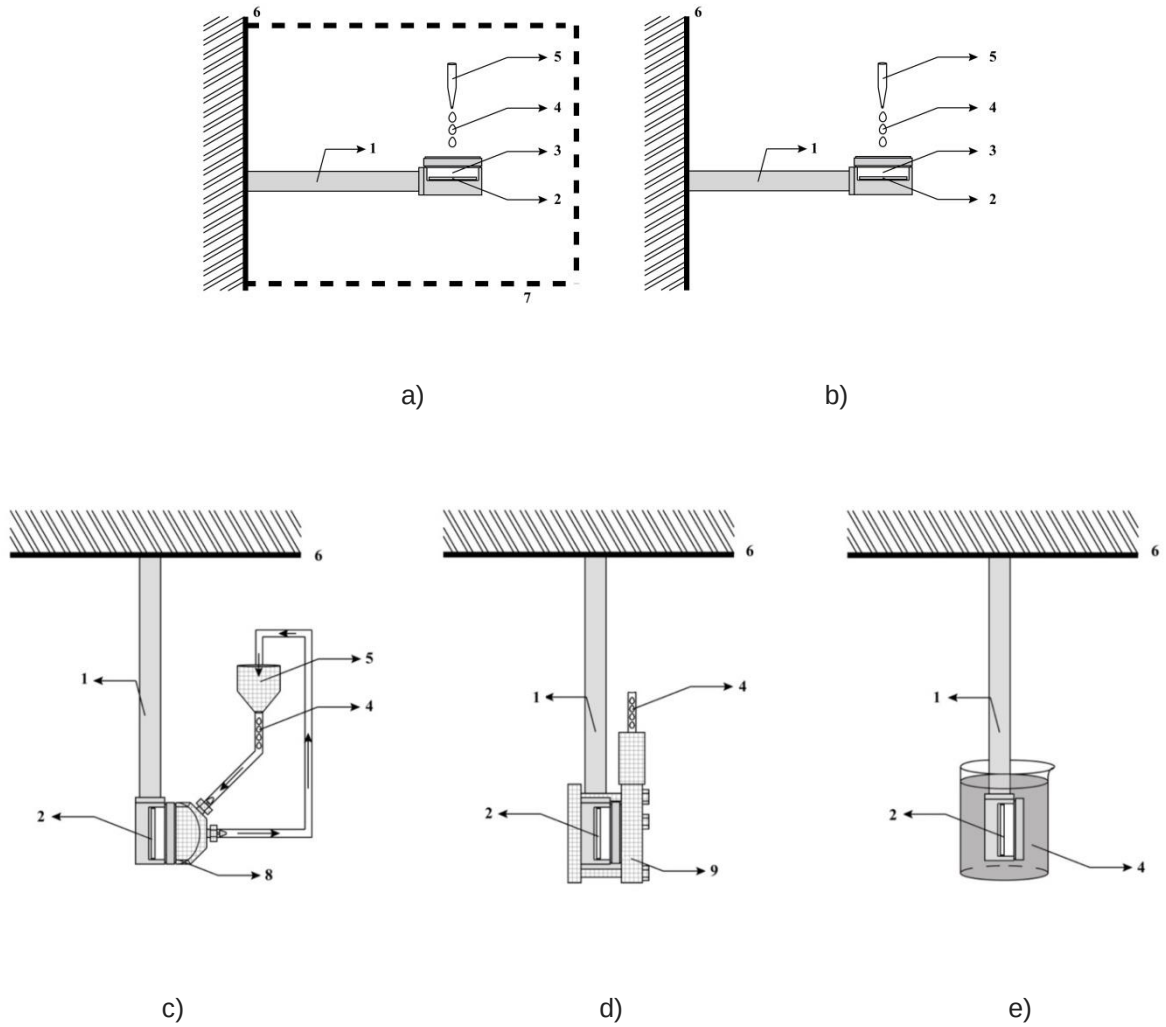

Figure 3.7. (a) Stationary Horizontal Closed (SHC), (b) Stationary Horizontal Open (SHO), (c) Continuous Vertical Closed (CVC), (d) Stationary Vertical Closed (SVC) and (e) Stationary Vertical Open (SVO) experimental configurations. 1 – crystal holder; 2 – quartz crystal; 3 – crystal holder head; 4 – solution; 5 – Pasteur *pippete*; 6 – support; 7 – acrylic protection chamber; 8 – flow cell; 9 – inject cell.

In order to monitor the buildup of a PEI/DPPG bilayer with monomeric concentrations of 10 mM and 1.5 mM for PEI and DPPG, respectively, the QCM was attuned by the following method. The dry operation was achieved by switching the C_o compensation to HOLD and the ten-turn dial to 8.0. The OSC led from the QCM controller turns on as soon as proper quartz oscillation is established in the dry crystal. After a short initialization period, an absolute frequency very close to 5 MHz (nominal dry frequency) should be presented on the front panel measurement display. The PARAMETER key was pressed to display the absolute resistance and a value less than 75 Ohms should appear at this time. The frequency should stabilize in approximately 2 hours. Subsequently, the frequency stabilization in liquid was performed by injecting ultra-pure water into the crystal holder head and then the controller was switched to ADJUST mode for nulling C_o. The frequency stabilization time depends on the temperature gradient between the quartz crystal and the liquid. When the liquid stabilization frequency was achieved the injection of the PEI and DPPG solutions could be initiated.

For SHO and SHC experimental configurations, PEI/DPPG assembly begins with the PEI solution injection using a Pasteur *pipette* onto the crystal holder head horizontally positioned. After 3 minutes, the PEI solution was removed using a Pasteur *pippete*, followed by a wash process with ultrapure water. Next the phospholipid suspension was injected onto the crystal holder head followed by a rinse process after 10 minutes of DPPG deposition.

The SVO is the simplest setup tested and consists in dipping the crystal holder head into the solution with an adsorption time of 3 and 10 minutes for PEI and DPPG solutions respectively, with an ultra-pure water rinse process between adsorptions.

The CVC system is the most complex system, because its continuous flux needs a flow cell coupled to a peristaltic pump. The main drawback is that the solution volume needed to perform the measurements is considerably larger than the other experimental configurations. The liquid operation started by filling the two-stop connecting tubes with ultra-pure water after switching to ON the peristaltic pump. A frequency decrease of 700 Hz should be displayed on the front panel when the ultra-pure water filled the flow cell chamber. After the frequency stabilization, the pump is stopped, the tube switched from the ultra-pure water to the PEI solution and the pump is switched ON again. The same process is repeated for the DPPG suspension adsorption and for the rinse processes. The adsorption time for both solutions was 10 minutes.

The SVC system procedure started by attaching the inject cell to the crystal holder head (see figure 3.8) and then, with the help of a syringe, the chamber is filled with 6 ml of ultra-pure water until covering the quartz crystal. The PEI solution was introduced into the inject cell, followed by a resting time of 10 minutes. Care must be taken when the operator is filling the crystal holder cell in order to avoid the formation of microbubbles. After the PEI solution was removed and a rinse process with ultrapure water was performed. The same procedure was repeated for the DPPG suspension with a resting time of 15 minutes, followed by a rinsing process.

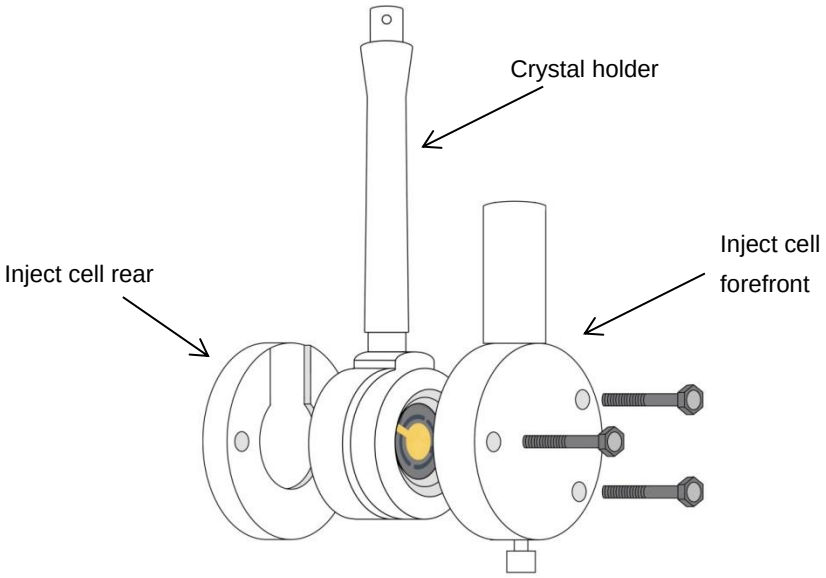

Figure 3.8. Schematic representation of the inject cell apparatus.

The five different experimental configurations were used with the intent to detect, understand and overcome weaknesses found during adsorption kinetics curves in liquid QCM measurements, taking into account parameters such as mechanical vibration, acoustic vibrations and thermal fluctuations. After a detailed analysis of the five QCM obtained data, discussed in section 4.3, the SVC system proved to be the more reliable method, and therefore was the most used experimental configuration throughout this work. Nevertheless, the SHC system was selected to grow LbL films with a large number of layers because small amounts of solution are required; on the other hand, it is less expensive and has low time consumption.

3.3.2 Atomic Force Microscopy

Binnig and Rohrer, in 1981 developed a technique known as Scanning Tunneling Microscopy (STM) [171], and since then the nanometric techniques have emerged. STM can produce images of conductive surfaces. Based on this idea, Binnig, Quate and Gerber invented in 1986 [172], the Atomic Force Microscope (AFM) also known as Scanning Force Microscopy (SFM), which can produce images of conductive and non-conductive surfaces. These techniques (STM and AFM) and their various operating modes are a new class of instruments belonging to a microscopy group called Scanning Probe Microscopy (SPM).

AFM involves the use of a cantilever bearing a tip at its end, which can be used to scan or probe surfaces. When the tip approach a solid surface, attraction and repulsion forces between the tip and the sample lead to a deflection of the cantilever [173]. Typically, the deflection is measured by using a laser spot which is reflected from the cantilever top surface into an array of photodiodes whose output signal is collected by a differential amplifier. In figure 3.9, it is illustrated a schematic representation of the atomic force microscope technique.

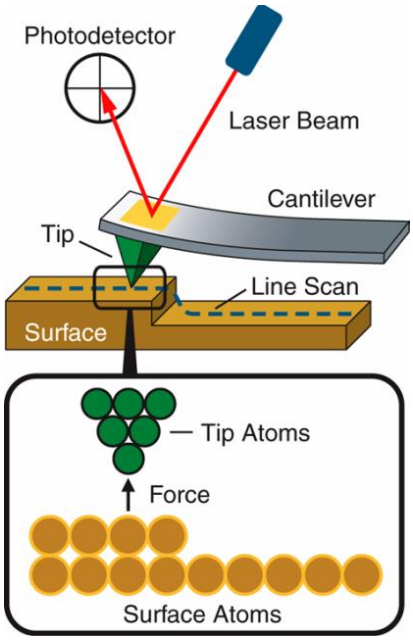

Figure 3.9. Schematic representation of the atomic force microscope (AFM) technique. The tip is fixed under a cantilever focused by a light beam which is reflected and is used to detect the cantilever movement across the four quadrant photodetector [174].

AFM technique can be used either to image surface topographies or to obtain forces profiles of the tip-sample interactions as a function of the gap between the tip and the sample. Thus, during the imaging procedure, AFM can be operated in a number of modes, depending on the application, such as contact mode and non-contact mode [175]. In contact mode, the cantilever tip scans across the surface. A feedback loop maintains a constant ‘‘setpoint’’ deflection between the cantilever and the surface while the scanner is moving across the surface area. The force between the tip and the surface is kept constant during this operation. In the non-contact mode, the cantilever tip is oscillating while is scanning the surface. A feedback loop maintains a constant ‘‘setpoint’’ oscillation amplitude while the scanner is moving across the surface area. So, AFM can be used either to image surfaces, e.g. with liposomes immobilized, or to carry out force measurements giving information about their rigidity and stability [173].

3.3.2.1 Surface morphology

The surface morphology of an interface is usually described by statistical parameters based on a topographic function normally involving a large amount of data.

A surface is formed by aggregates with different heights distributed over a certain area and the AFM image is formed by *x* and *y* points and height, *z*, distributed in a given area, *A,* with a matrix whose elements are the height *z(x,y)*. The mean height of an image, with *N* lines and *M* columns, can be calculated by the following expression [176]:

$$z_{med}\,(N,M) = \frac{1}{NM}\sum_{x=1}^{N}\sum_{y=1}^{M} z(x,y) \tag{3.2}$$

The main statistical amplitude parameter used to characterize the smoothness of a surface is the root-mean-square roughness (Rq) and it is expressed by the equation [176]:

$$R_q\,(N,M) = \sqrt{\frac{1}{NM}\sum_{x=1}^{N}\sum_{y=1}^{M}[z(x,y) - z_{med}\,(N,M)]^2} \tag{3.3}$$

Average roughness (Ra) and root-mean-square roughness (Rq) are the most used amplitude parameters. Particularly, the latter is used to study temporal changes during the growth surface and spatial differences when the surface feature has different scales because this parameter is more sensitive to large deviations with respect to the mean line.

The amplitude distribution function also allows determining skewness (Rsk) and kurtosis (Rku) parameters. Rsk is a measure of asymmetric distribution of a particular frequency. This parameter measures the symmetry of the profile at a mean line. A symmetric distribution of the heights' peaks means that the number of peaks and valleys is the same and consequently Rsk=0. If the profile has more peaks than valleys than Rsk>0, and if it has more valleys than peaks than Rsk<0. Rku measures the surface sharpness. When Rku is equal to 3 it indicates a gaussian amplitude distribution and the surface is called Mesokurtic, but if Kurtosis is smaller than 3 the surface is flat and it is called Platykurtic. Finally, in case of Kurtosis being higher than 3, the surface has more peaks than valleys and is named Leptokurtic [177].

The one-dimensional roughness amplitude parameters used to characterize the surface topographies of the images acquired to execute this work were attained by the *Gwyddion* software and are listed in table 3.1. The texture is split to waviness (the low-frequency components defining the overall shape) and roughness (the high-frequency components) at the cut-off frequency.

Table 3.1. One-dimensional roughness amplitude parameters used to characterize the AFM topography surfaces.

Parameters	Description
Roughness Average (Ra)	Arithmetical mean deviation. The average deviation of all points roughness profile from a mean line over the evaluation length: $$R_a = \frac{1}{N}\sum_{j=1}^{N}\left\|r_j\right\|$$
Root Mean Square Roughness (Rq)	The average of the measured height deviations taken within the evaluation length and measured from the mean line: $$R_q = \sqrt{\frac{1}{N}\sum_{j=1}^{N} r_j^2}$$
Maximum Height of the Profile (Rt)	Maximum peak-to-peak-valley height. The absolute value between the highest and lowest peaks: $$R_t = \left\|\min_{1\le j\le N} r_j\right\| + \left\|\max_{1\le j\le N} r_j\right\|$$
Maximum Profile Valley Depth (Rv)	Lowest valley. There is the depth of the deepest valley in the roughness profile over the evaluation length: $$R_v = \left\|\min_{1\le j\le N} r_j\right\|$$
Average Maximum Height of the Profile (Rtm)	Mean peak-to-valley roughness. It is determined by the difference between the highest peak ant the lowest valley within multiple samples in the evaluation length: $$R_{tm} = R_{vm} + R_{pm}$$
Average Maximum Profile Valley Depth (Rvm)	The mean valley depth based on one peak per sampling length. The single deepest valley is found in five sampling lengths (m = 5) and then averaged: $$R_{vm} = \frac{1}{m}\sum_{i=1}^{m} R_{vi}$$ where, $$R_{vi} = \left\|\min r_j\right\| \qquad for \qquad (i-1)\frac{N}{m} < j < i\frac{N}{m}$$
Average Maximum Profile Peak Height (Rpm)	The mean peak height based on one peak per sampling length. The single highest peak is found in five sampling lengths (m = 5) and then averaged: $$R_{pm} = \frac{1}{m}\sum_{i=1}^{m} R_{pi}$$ where, $$R_{vi} = \left\|\max r_j\right\| \qquad for \qquad (i-1)\frac{N}{m} < j < i\frac{N}{m}$$
Skewness (Rsk)	Skewness is a parameter that describes the shape of the Amplitude Distribution Function (ADF). Skewness is a simple measure of the asymmetry of the ADF, or, equivalently, it measures the symmetry of the variation of a profile about its mean line: $$R_{sk} = \frac{1}{NR_q^3}\sum_{j=1}^{N} r_j^3$$
Kurtosis (Rku)	Kurtosis is the ADF shape parameter considered. Kurtosis relates to the uniformity of the ADF or, equivalently, to the spikiness of the profile: $$R_{ku} = \frac{1}{NR_q^4}\sum_{j=1}^{N} r_j^4$$

Despite that the statistical parameters listed in table 3.1 only give vertical information, both longitudinal and lateral information can be obtained by spectral and correlation techniques based on Fourier transformation [178]. The Power Spectral Density (PSD) provides a more detailed description of surface topography, including fractal geometry, scaling concepts and film properties [179]. The characterization of LbL films [180, 181] polymeric blends [182], field-effect transistors [183] and biological samples [182] were accomplished by dynamic scaling analysis. For example, Buchko *et al.* have used PSD analysis to measure the different length scales of a neuron corresponding to its cell body, axon and fillipodia [184].

PSD function offers a representation of the space periodicity and the roughness amplitude, because such method decomposes the surface profile into spatial wavelengths, and consequently compares different roughness values attained in several spatial frequency ranges. Accordingly, PSD functions provide information about height deviations from a mean plane and lateral distance over which this variation happens [185]. Briefly, PSD may provide quantitative information about spatial periodicity, roughness, growth regime, grain size and correlation length [186, 187], describing a surface much better than roughness parameters.

Grain size can be estimated using PSD function defined by [176]:

$$P\ (u,v) = \ |F(u,v)|^2 \tag{3.4}$$

where $F(u,v)$ is the Fourier Transform of the matrix of the heights $z(x,y)$ obtained from the AFM images, given by:

$$F(u,v) = \frac{1}{N^2}\sum_{x=0}^{N-1}\sum_{y=0}^{N-1} z(x,y)\ exp\left[-j2\pi\ \frac{(ux+vy)}{N}\right] \tag{3.5}$$

It represents a function in the reciprocal space if *k*, defined by $k^2 = u^2 + v^2$, is the wavelength.

However, this two-dimensional information is complex and therefore interpretation of the measurements is difficult. In order to simplify the analysis concepts, we will take into account only the surface profiles measured along the AFM fast-scan direction.

3.3.2.2 Power spectral density analysis

Typically, PSD plots present three regions: (i) the plateau height at low frequencies, which is related to the height of the rough surface. This section has an absence of correlation (it does not change with the scale) and of any characteristic length; (ii) the region of the medium frequencies gives the correlation length, which defines the lateral extent of the rough surface, this section is strongly frequency dependent and it represents the power-law decay; and (iii) the section of large frequencies gives the nature of roughness [188]. PSD analysis de-convolutes roughness as a function of surface lateral length scales, correlates vertical amplitude with spatial frequency of surface features and may

also reveal characteristics of the surface microstructure [189]. Variation of height fluctuations of the structures can be represented through PSD spectra where singularities can characterize the evolution of the surface during particles' assembly. So, power spectrum of the surface morphology shows not only the growth process and the microstructure of thin film but also characterizes the dynamic scaling behavior related to the surface roughness and correlation. This allows us to treat the entire surface deposit as a self-affine fractal structure. Analysis of the PSD curves becomes much easier if models are applied to extract information retained in these curves. An overview of models applied in surface characterization can be found in ref. [190].

The scaling behavior of surfaces can be analyzed from 1D PSD. In a finite frequency range, a self-affine structure exhibits a power–law decay [191],

$$1D\ PSD\ (f_s) = K_0 f_s^{-\gamma} \tag{3.6}$$

where k_0 is a constant dependent on the systems and γ is related to the roughness exponent (α) by $\alpha = (\gamma - j)/2$, where the line scan dimension *j*=1. In a limited length scale, real surfaces, occasionally, also show fractal behavior, called fractal dimension, which can be described by the roughness exponent.

Experimental PSD plots are relatively constant at low frequencies and exhibit an exponential dependence at high frequencies. Frequently thin film surfaces are found to be self-affine fractals over a considerable length scale. Such surface growth can be due to both layer-by-layer assembly and unstable growth [192]. Thus, thin film morphology can be quantitatively characterized by fractal strengths and fractal dimensions which allow acquiring useful information about thin film structure, making this approach considerably more suitable when compared to other common conventional analyses.

Scaling laws can be applied to describe the surface topography [130],

$$PSD(f) = \begin{cases} K f_s^{-\gamma}, & 1/f < \xi \\ A, & 1/f > \xi \end{cases} \tag{3.7}$$

where K and *A* are constants, γ is the roughness related exponent and ξ is the correlation length. The conventional method for determine the correlation length (ξ) is to calculate the inverse of the transition frequency between two regions ($\xi = 1/f_t$), e.g. the transition between the low-frequency level and the high-frequency self-affine section, which defines f_t. Generally, the correlation length reports progressions between physical processes that occur during surface growth. Regarding nanocrystalline films the correlation length is the minimum distance between two points that are not affected by each other, i.e. the mean distance between two grains. But for dense features the correlation length expresses the mean grain diameter [185].

Generally, for high spatial frequencies PSD function reflects the roughness contribution from all features of the surface which can be described by the inverse power law decay as follows [179]:

$$PSD_{fractal}(f, K, \nu) = \frac{K}{f^{\nu+1}} \tag{3.8}$$

where *f* is the spatial frequency, *K* is the spectral strength and ν is the spectral index.

This index allows to determine the fractal dimension, Df, which in turn can be used to quantify the surface morphology. The Df values can be calculated, in the case of PSD at one dimension, by the equation:

$$Df = \frac{1}{2}\big(7 - (\nu + 1)\big) = \frac{1}{2}(6 - \nu) \tag{3.9}$$

The dimension value determinates the relative amounts of the surface irregularities at different distance scales. If *Df* = 3 it is called the extreme fractal; *Df* = 2.5 it is named the Brownian fractal; and if *Df* = 2 is called the marginal fractal.

For medium spatial frequencies, PSD plots can be characterize by the k-correlation or ABC model (PSD_{ABC}), which is a generalization of the fractal model presenting a flat response below a cut-off frequency followed by a decrease of the PSD values with the increase of spatial frequency, and is represented by the equation [193]:

$$PSD_{ABC} = \frac{A}{(1 + B^2 f^2)^{\frac{(C+1)}{2}}} \tag{3.10}$$

where *A*, *B* and *C* are the functional parameters. *A* parameter describes the low frequency limit of the spectrum meaning there is no significant deviation in the height value across these dimensions in real space. *B* parameter determines the transition between the low-frequency plateau and the sloped part of PSD indicating the position of the curve “knee” which is related to the correlation length and represents the mean grain size. *C* parameter is the inverse slope at high spatial frequency range, which gives the nature of roughness and is related to different growth mechanisms; it is a constant greater than 1. This parameter explains film growth in terms of: viscous flow (C = 1), evaporation and condensation (C = 2), bulk diffusion (C = 3) and surface diffusion (C = 4). The fractal dimension which determines the relative amounts of the surface irregularities at different distance scales, can be obtained from the *C* parameter of the k-correlation model by the relation,

$$Df = \frac{(7 - C)}{2} \tag{3.11}$$

However, if we are dealing with surfaces with clusters or aggregates on the top, the ABC model cannot characterize such superstructures. It should be necessary to consider the superstructure PSD model (PSD_{sh}) which makes possible the characterization of the aggregates or superstructures formed on the surface [194]. This model is represented by the following equation:

$$PSD_{sh} = K_{sh} exp[-\pi^2 \tau_{sh}^2 (f - f_{sh})^2] \tag{3.12}$$

where τ_{sh} represents the lateral size of the features on the surfaces, K_{sh} is associated to the volume of the features and f_{sh} is the spatial frequency of the superstructures of the surface.

There are several ways to define a fractal. Perhaps the simplest manner regards to the geometric invariance condition of an object when observed on different scales. These objects are called self-similar fractals because they magnify (or shrink) in an isotropic order. Strictly, we can say that self-similarity is a symmetry property which makes the fractal invariable under an isotropic geometric transformation. While mathematical fractals are generally statisticians, many natural fractals are random (e. g. the coast of a country) and their self-similarity should be observed from the statistical point of view; i.e. these fractals maintain a statistical correlation when observed in different scales. There are fractals which are also formed by mini-prints, but these do not maintain fixed the original proportions, i.e., they are invariant under anisotropic transformations. In this case they are called self-affine fractals, for example the morphology of a cauliflower [192].

Using fractal analysis it is possible to extract varied information from measured textures and it is a very useful approach to describe surface characteristics of thin films [185]. Because particle deposition is a far-from-equilibrium process, growth of an interface can be characterized quantitatively using different growth models which can explain the observed morphology. The complexity of thin film morphology and the growth process at an interface is mainly governed by the interaction of deposition, desorption and surface diffusion (relaxation) of atoms or molecules when arriving on the surface [192]. Thus, fractal theories have been used to provide a new quantitative method to describe particle aggregates structures in many water systems. Previous research in this area includes fractal characterization of particles produced from wastewater treatment [195], bacterial and yeast aggregates from laboratory batch experiments [196], and phytoplankton aggregates in a simulated oceanic system [196]. So, it is now believed that most particle aggregates in nature and engineered systems are fractal in their morphological structure [197]. Recent researches proved that fractal geometry and scaling concepts can describe the morphology of a rough surface by the fact that its symmetry do not change at different scales. Therefore, the surface morphology is governed by scaling laws [193, 194].

3.3.2.3 Surface growth

Surface temporal evolution can be obtained by *Rq* behavior as function of the surface growth time. Surface growth usually has two phases; first a strong surface roughness variation occurs as a function of time, followed by a stabilization stage which corresponds to a saturation time - crossover time. For time values below the saturation point the roughness can be defined by the scaling law,

$$Rq\ (L,t) \propto t^{\beta} \tag{3.13}$$

where *L* is the scan length, *t* the time and β the growth exponent which represents the temporal dependence of the surface formation process. When time is larger than saturation time roughness depends on the scan length, *L*, which may be expressed as follows:

$$Rq\ (t) \propto L^{\alpha} \tag{3.14}$$

where α is called the critical exponent which characterizes the roughness of a saturated interface.

Saturation time depends on the size of the systems analyzed according to the expression:

$$t_x(L) \propto L^z \tag{3.15}$$

where *z* is the dynamic exponent. This exponent is associated to α and β by the following relation:

$$z = \frac{\alpha}{\beta} \tag{3.16}$$

Determination of the scaling exponents is important because there are empirical models that describe phenomena which are associated with morphological changes during growth of thin films. The most important models are listed in table 3.2, with typical values for the respective critical exponents.

Table 3.2. Critical exponents values of different surface growth models.

Models	$\boldsymbol{\alpha}$	$\boldsymbol{\beta}$	$\boldsymbol{z}$
Random deposition [198]	-	0.5	-
Edwards-Wilkinson [199]	0	0	2
Villain [200]	0.667	0.2	3.33
Villain (with diffusion) [192]	1	0.25	4
Kardar-Parisi-Zhang [192]	0.38	0.24	1.58

The models mentioned in table 3.2 describe the height growth of a film based on an asymptotic stochastic differential equation of Langevin type:

$$\frac{\partial h\,(x,t)}{\partial t} = A_i\,\{h\} + \eta_i\,(x,t) + F \tag{3.17}$$

where i represents a particular class, $A_i\,\{h\}$ a function that can depend on the spatial derivatives of $h(x,t)$, $\eta_i(x,t)$ noise that may exist in random fluctuations of the deposition process and F average number of particles that deposit on the surface. Random deposition model is based on the particle deposition on top of a randomly selected column which is the simplest case of all growth processes, and it is described by the equation:

$$\frac{\partial h\,(x,t)}{\partial t} = \eta_i\,(x,t) + F \tag{3.18}$$

The characteristic roughness parameters for random deposition are β = ½ and α = 0, because there is an absence of a correlation between the different columns that constitute the system. The Edwards-Wilkinson (EW) model complements the random deposition model adding the relaxation mechanism, i.e., the particle that is deposited can spread to a local with a minimum height, Figure 3.10.

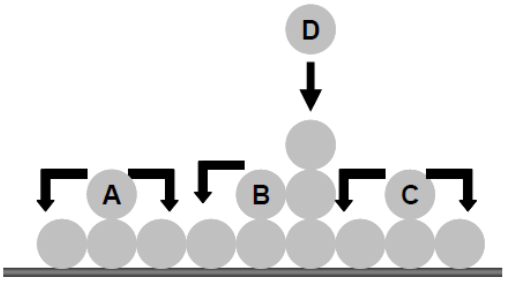

Figure 3.10. Schematic representation of the Edwards-Wilkinson model. It is possible to observe the random diffusion of particles *A* and *C* to a local with a minimum height that can be either to the left or to the right. The particle *B* can spread only to one side, since it has only a minimum location [201].

For the EW model the equation 3.18 takes the following form:

$$\frac{\partial h\,(x,t)}{\partial t} = \nu\nabla^2 h(x,t) + \eta(x,t) + F \tag{3.19}$$

where ν is the surface tension and the term $\nu\nabla^2 h(x,t)$ is related with the surface smoothing, i.e., it describes the irregular redistribution of the interface. Roughness parameters that characterize this model are both zero, α = 0 and β = 0, because they characterize very smooth surfaces.

The Kardar-Parisi-Zhang (KPZ) model is based on particles aggregation. When a particle reaches the surface containing aggregates, a link occurs and it becomes part of it. This type of growth may lead to empty spaces inside the film, Figure 3.11.

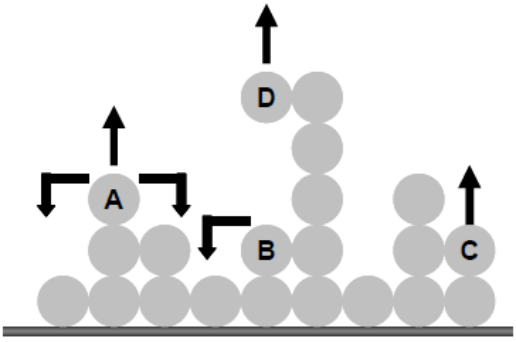

Figure 3.11. Schematic representation of the Kardar-Parisi-Zhang (KPZ) model. The particles *A* and *B* can spread to its local minimum, the particle *D* can adhere laterally to the column without having to have a position immediately below, thereby forming an aggregate. Any particle may be subjected to desorption [201].

The model can be described by the KPZ equation:

$$\frac{\partial h\,(x,t)}{\partial t} = \nu\nabla^2 h(x,t) + \frac{\lambda}{2}(\nabla h(x,t))^2 + \eta(x,t) + F(x,t) \tag{3.20}$$

where a non-linear $\frac{\lambda}{2}(\nabla h(x,t))^2$ term appears, referring to the lateral growth of an interface.

Villain model takes into account the number of neighboring bonds rather than its height, i.e., when the particle reaches the surface it will preferentially choose a position with the highest possible number of connections, figure 3.12.

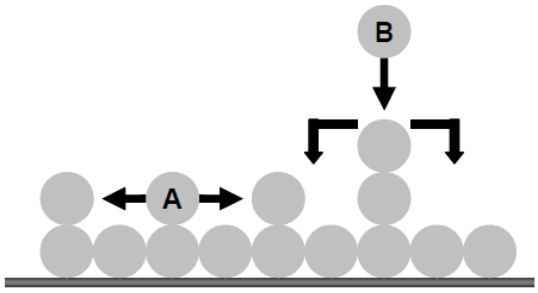

Figure 3.12. Scheme of the deposition of particles by the Villain model. The particle *A* will connect to one of its neighboring particles and the particle *B* will connect with the particle which is at the top of the column or with the particles of the base. In this model the bonds do not depend of the height but the place where they can make the largest number of connections [201].

The equation that describes the Villain model is the following:

$$\frac{\partial h\,(x,t)}{\partial t} = \nu\nabla^2 h(x,t) - \Omega\nabla^4 h(x,t) + \eta(x,t) + F(x,t) \qquad (3.21)$$

where the term $\Omega\nabla^4 h$ corresponds to the particles diffusion at certain correlation length, L_x. Correlation length corresponds to the average diameter of the grain saturation. When $L \leq L_x$ diffusion of particles occurs, meanwhile $L \geq L_x$ the particles aggregate.

Three types of AFM equipments were used in this work to image surface morphologies of the thin films as described below.

Topographic images of PAH and PAH/DPPG LbL films deposited onto silicon substrates, were acquired by Nanoscope III microscope (Digital Instruments). Commercial Si cantilevers with a spring constant between 20 and 100 N/m and free oscillation interval between 250 and 300 Hz were used. The topographic images were obtained using the non-contact mode and are shown and discussed in section 4.5.

Surface morphologies of Au-quartz crystal support and PAH, PEI and PEMs heterostructures before and after adsorption of DPPG liposomes were also characterized by AFM. Measurements were made in non-contact mode *ex situ* at room temperature using an MPF-3D (Asylum Research, USA). Silicon probes OMCL-AC160TS (Olympus, Japan), with nominal spring constant and resonance frequency of ~26 N/m and ~300 kHz, respectively, were used. Images of topography with 512×512 pixels each were obtained at a scan rate of 1 Hz on scan areas of either 0.5×0.5 and 2×2 μm^2, giving a maximum single pixel spacing of ~ 3.9 nm in the latter case. Surface roughness of each sample has been evaluated as the root mean square of the distribution of heights in the AFM topographical images. All measurements were taken in Height Mode with display of amplitude and/or phase.

Surface morphologies *in situ* of Au quartz crystal, Au/PAH and Au/PEI/$(PSS/PAH)_4$ and of DPPG liposomes being adsorbed onto these surfaces were investigated using AFM measurements at room

temperature using a Multimode Nanoscope IIIa Microscope (Digital Instruments, Veeco). Samples were initially covered with 40 μL of ultra-pure water followed by injection of 60 μL of DPPG suspension. Topographic images were taken with a scan rate of ca. 2 Hz in non-contact mode. Use of an oscillating probe drastically reduces the force applied to the sample during scanning as compared to measurements performed in contact mode, since the cantilever only touches the surface after one oscillation cycle. Images were recorded with 256×256 pixels on height and phase modes. Before each experiment, the glass block holding the cantilever was washed several times with water and ethanol. Cantilevers used were made of silicon nitride (NPS, ca. 0.58 N/m of spring constant, Veeco) with a resonance frequency in liquid of about 9 kHz.

The row/column statistics tool of *Gwyddion* software was used to calculate the standard deviation of Rq of all individual row/column values and the obtained values were used as roughness error bars.

AFM experiments were performed to identify the best scan area to perform roughness comparisons among different samples. Roughness of surfaces or layers formed in random processes are usually scale invariant, at least over some regions of scale, and this must be reflected in the mathematical description inherent to the kinetic growth models employed to explain the data.

3.3.3 Dynamic Light Scattering

Dynamic Light Scattering (DLS), also called Photon Correlation Spectroscopy, is a spectroscopic technique used in Chemistry, Biochemistry and Physics mainly to characterize the hydrodynamic radius of polymers, proteins, and colloids in solution. DLS is a useful technique that allows to determine the size distribution of nanoparticles in a suspension, but also to detect small amounts of high mass species in protein samples.

In a typical DLS experiment, presented in figure 3.13, a solution/suspension of analytes is irradiated with a monochromatic laser light and the intensity fluctuations of the diffracted light are measured as a function of time. Intensity data is then collected using an autocorrelator to determine the size distribution of particles or molecules in a sample.

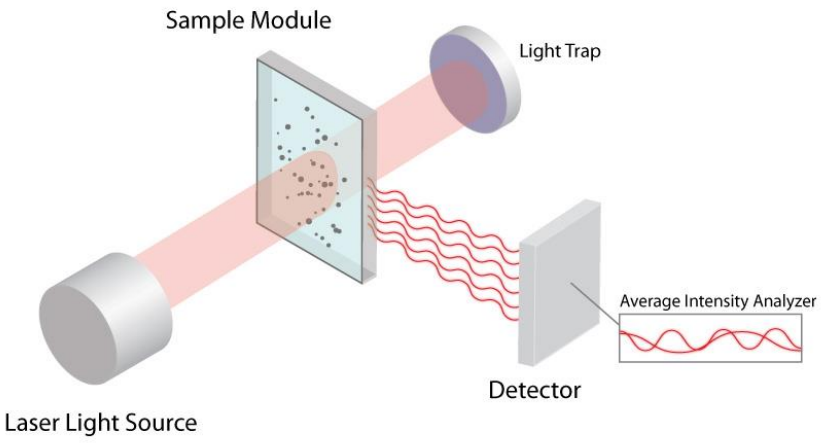

Figure 3.13. Scheme illustrating the experimental procedure of DLS [202].

In practice, particle samples are typically not stationary because they are suspended in a solution and as a result they are moving randomly due to collisions with solvent molecules. The hydrodynamic radius of the particle (particle hydrated radius) can be calculated by the Stokes-Einstein equation [203, 204] that describes the motion for spherical particles and is given by the following equation:

$$R_H = \frac{k_B T}{6\pi\eta D_T} \tag{3.22}$$

where, R_H is the hydrodynamic radius, k_B Boltzmann constant, *T* the absolute temperature, η viscosity and D_T diffusion coefficient which is inversely proportional to the particle radius, demonstrating that small particles should diffuse faster than large ones [60].

The fundamental distribution generated by the DLS device is an intensity distribution that can be converted into a volume distribution and thus converted into a number distribution. However, the number distributions are of limited use because small errors collected during the correlation function generate large errors. To notice that although equation 3.22 is valid for monodispersed suspensions of particles it cannot be applied for populations with different sizes, i.e. polydisperse systems. Methods of analysis of polydisperse samples require higher resolution and an additional mathematical algorithm for correlation function treatment. The resulting correlation of this type of populations consists of a mixture of exponential decays, each one with a different relaxation time related to the particle size. Each different size contributes in a different way with its exponential to the total scattered light. In addition, the smaller the particle size the smaller the intensity of scattered light. This relation is given by the equation:

$$\frac{\mathrm{I_s}}{\mathrm{I_o}} \propto \mathrm{V}^2 \tag{3.23}$$

where I_s is the scattered light intensity, I_o the incident light intensity and *V* the particle volume. According to this equation and considering spherical particles, a difference of one order of magnitude in the particles radius leads to a difference of three orders of magnitude in the percentage of volume and six orders of magnitude in the scattered light intensity value.

In this work two different DLS equipments were used to analyse the DPPG liposomal suspensions. The mean hydrodynamic diameter of the extruded DPPG liposomal suspension was measured using a DLS particle size analyser Model BI-90 (Brookhaven Instruments Corp., Holtsville, NY). One drop of the nanoparticle suspension, 80 μl, was added to the cuvette with 3 ml of ultrapure water, and the contents were mixed by gentle shaking, followed by measurement at 25 °C. Measured values are given as mean volume-average; dispersion from the mean value is described as the full-width half maximum in square brackets [FWHM]; both values are given in nanometers. For further information see section 4.1.

The DLS Zetasizer Nano-ZS Series ZEN3600 device (Malvern Instruments Ltd., UK) equipped with a 4 mW He-Ne Laser (633 nm), using a 1x1 cm^2 polystyrene latex cuvette was used to find the average hydrodynamic diameter of the sonicated DPPG liposomes in an aqueous solution. For additional information see section 4.1.

3.3.4 Ultra-Vacuum Ultraviolet Spectroscopy

Ultra-vacuum ultraviolet absorption spectroscopy is a technique that allows characterization of materials and is based on the electronic states of molecules obtained from interaction between ultraviolet radiation and matter. Absorption spectra can be acquired by setting a sample between the radiation source and the detector. Thus, the radiation absorbed by the sample leads to an increase of its internal energy that can rise to values equal to the absorbed photon energy and it is expressed using the Planck relation [205]:

$$\Delta E = h\nu = \frac{hc}{\lambda} \tag{3.24}$$

where h is the Planck's constant, c is the speed of light in vacuum and $\Delta\mathrm{E}$ is the absorbed energy per each molecule in an electronic transition from the fundamental state to a high-energy state , i.e. excited state [206]. Spectroscopic classification of molecules can be obtained because each molecule will absorb characteristic energy levels that correspond to specific electronic transitions. Typically, electronic transitions are situated in the ultraviolet or visible region in two different ranges of wavelengths (λ): visible and ultraviolet. Table 3.3 lists the different absorption regions and their radiation wavelength ranges.

Table 3.3. Visible and Ultraviolet subregions and the respective radiation wavelength ranges.

Region	Subregions	Range (wavelength)
Visible	Red	770 nm – 622 nm
	Orange	622 nm – 597 nm
	Yellow	597 nm – 577 nm
	Green	577 nm – 492 nm
	Blue	492 nm – 455 nm
	Violet	455 nm – 390 nm
Ultraviolet	UVA	390 nm – 320 nm
	UVB	320 nm – 290 nm
	UVC	290 nm – 200 nm
	Vacuum UV	200 nm – 10 nm

In polyatomic molecules three types of electrons may be considered: those which form simple chemical bonds (σ electrons), the responsible for double bonds (π electrons) and the nonbonding or unshared that do not participate in chemically bond (*n* electrons). The *p* or *s* atomic orbitals which are projected in the bond direction are named σ orbitals, and the resultant ligand orbitals that are overlap are called σ bonds. π orbitals are obtained through the perpendicular projection of the atomic orbitals *p* in the bond direction. Typically, in unsaturated systems, i.e. containing double bonds, the π electrons

predominate and determine the energy states of the valence electrons which are excited by absorption of visible and ultraviolet radiation.

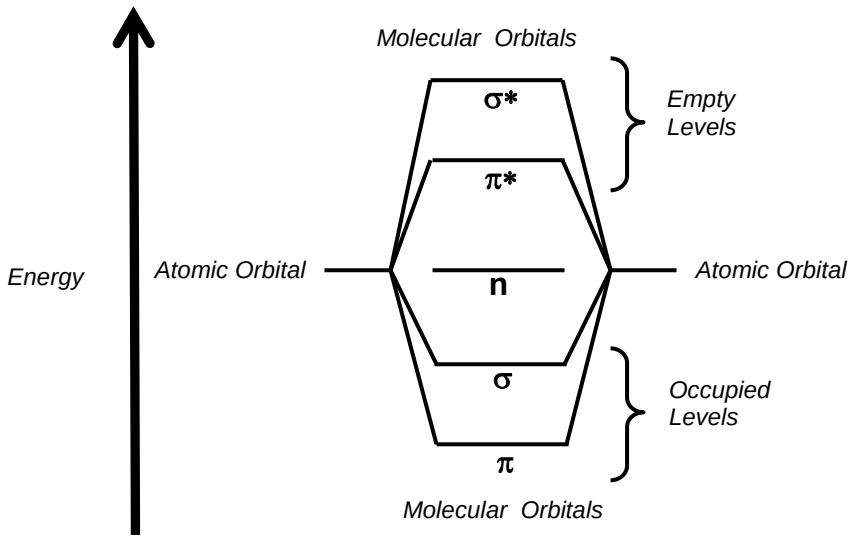

Figure 3.14. Schematic representation of the energy levels. Adapted from [205].

In polyatomic systems, such as in organic molecules, three main groups of electron transitions can occur: i) transitions from a stationary state orbital to a higher energy orbital, which means, $\pi \rightarrow \pi^*$ transitions and $\sigma \rightarrow \sigma^*$ transitions; ii) transitions from an unshared atomic orbital to a higher energy molecular orbital, named, $n \rightarrow \pi^*$ transitions and $n \rightarrow \sigma^*$ transitions and; iii) transitions from a stationary state orbital to higher energy orbitals, towards molecule ionization, that are designated Rydberg orbitals.

Table 3.4. Electronic transitions for each region of the electromagnetic spectrum. Adapted from [205].

Electronic Transitions	Electromagnetic Spectrum Regions
$\sigma \rightarrow \sigma^*$	Vacuum Ultraviolet
$\pi \rightarrow \pi^*$	Ultraviolet
$n \rightarrow \pi^*$	Near Ultraviolet
$n \rightarrow \sigma^*$	Far Ultraviolet or Near Ultraviolet (exceptionally)
Rydberg	Vacuum Ultraviolet

The majority of the absorption spectra of the organic molecules are located in the near UV zone and in the visible region and are owed to $\pi \rightarrow \pi^*$ or $n \rightarrow \pi^*$ transitions. The first ones are much more intense then the latter since, in this case, the unfavorable spatial orientation between n and π^* orbitals gives

place to low intensity transitions. On the other hand, bands observed in the vacuum ultraviolet region are owed to $\sigma \rightarrow \sigma^*$ and $n \rightarrow \sigma^*$ transitions.

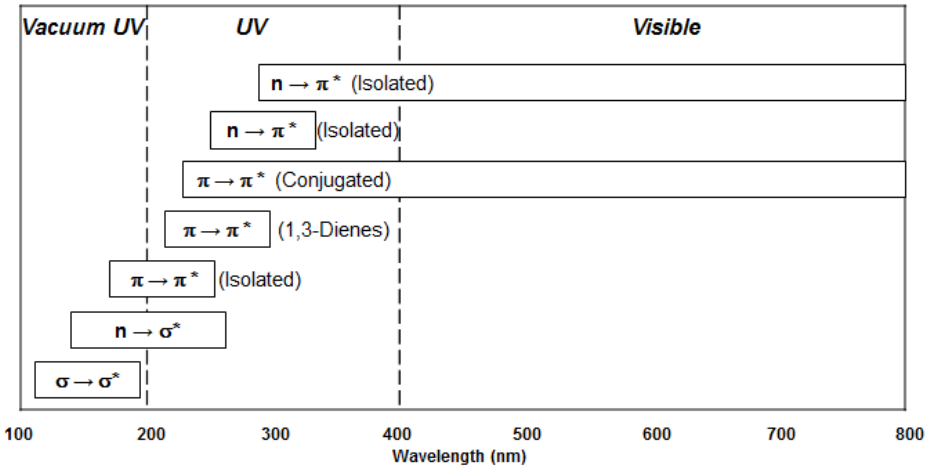

Figure 3.15. Schematic representation of the energy levels. Adapted from [207] .

The occurred transitions from radiation and matter interactions are usually represented using an absorbance spectrum in which absorbance is plotted against incident beam wavelength. This function is given by the Lambert-Beer Law defined as:

$$A = \varepsilon\, bc = log\left(\frac{I_0}{I}\right) \tag{3.25}$$

where *A* is the absorbance, ε is the extinction coefficient, *c* is the concentration (g/l) of the solution under study, *b* is the optical path (cm), I_0 is the radiation intensity of the incident beam and *I* is the radiation intensity of the emerging beam. The energy absorption quantity treatment depends on the Lambert-Beer law where for a given substance and a given wavelength, absorbance is directly proportional to the concentration of the absorbing species. This is a basic law for all types of absorption of the electromagnetic radiation applied to solutions, gases and solids.

High resolution vacuum ultraviolet (VUV) photo-absorption spectra of LbL films were recorded at the ultraviolet beam line (UV1) [208] in the ASTRID Synchrotron Radiation facilities at Aarhus University, Denmark. The synchrotron radiation allows high spectral resolution because it is characterized by high intensity and collimated beam, and may be highly polarized. When the high intensity and the broad spectrum space are combined with other properties, such as polarization control and collimation, the synchrotron radiation is a powerful tool in diverse fields as physics, materials, chemistry, biology, medicine, among others. The setup depicted in figure 3.16 consists of a vacuum chamber containing up to three CaF_2 sample disks and one reference disk mounted on a MDC SBLM-266-4 push-pull linear motion. The VUV beam light passed through the disks and the transmitted intensity is measured at 1.0 nm intervals using a photomultiplier detector (Electron Tubes Ltd., UK). The transmitted light intensity and the synchrotron beam ring current are measured at each wavelength, with a typical

resolution better than 0.08 nm. The sample chamber has a LiF entrance window and a MgF_2 exit window in front of the photomultiplier. The minimum wavelength is determined by the CaF_2 substrates so that the lowest wavelength at which reliable data could be collected was ~125 nm. In order to avoid absorption from molecular oxygen in air for wavelengths below 190 nm, the small gap between the sample chamber exit window and the photo multiplier detector was flushed with He gas.

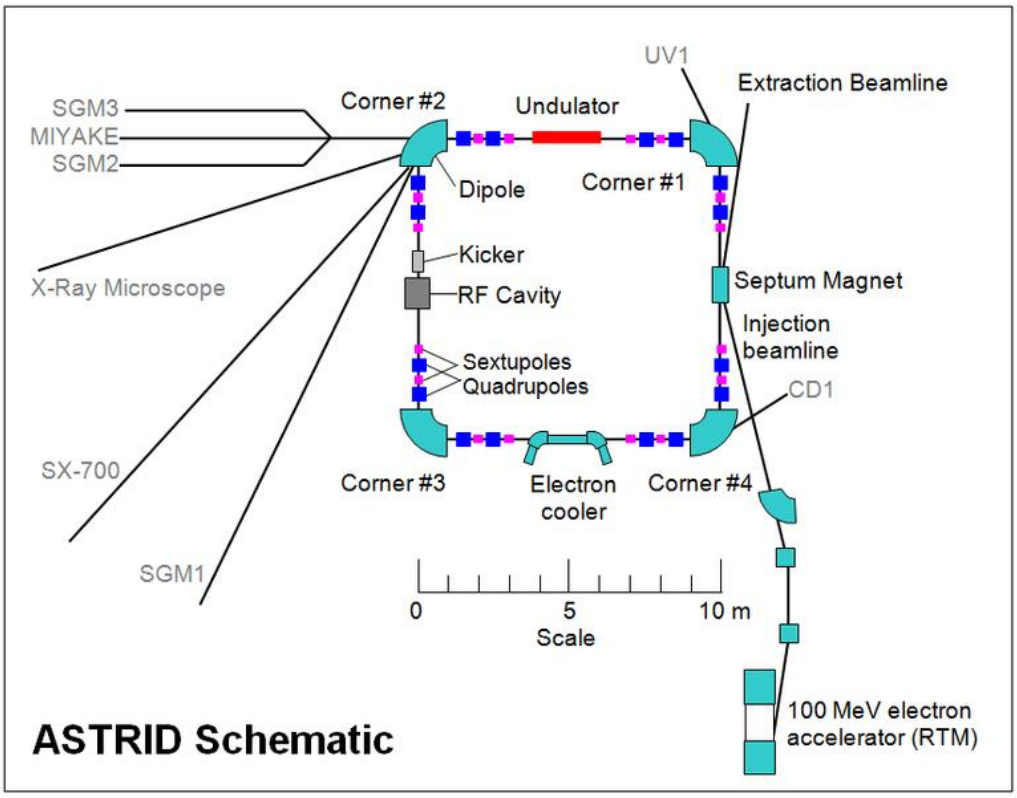

Figure 3.16. Scheme ASTRID synchrotron accelerator [209].

The obtained VUV spectrum is the sum of the absorption bands with a maximum absorbance at wavelengths where the electronic transitions are observed. Afterwards, such spectrum is deconvoluted, using specific software, to several peaks and the transitions associated to the obtained energy values are assigned, allowing the characterization of the material under study. VUV spectra were obtained using the following protocol: (i) radiation intensity transmitted by the substrate is measured (I_0); (ii) radiation intensity transmitted by the substrate with the film absorbed on it is determined (I); (iii) radiation intensity transmitted by the substrate is measured again ($I`_0$). This last step is required because there is an intensity decay of the beam throughout time which consequently leads to a transmitted radiation intensity decrease caused, not by the film absorption, but by the characteristic beam decay. In this case, Lambert-Beer law must be adjusted as follows:

$$Absorbance = -\log\left(\frac{I}{(0.5I_0)+(0.5I_0')}\right) \tag{3.26}$$

The spectroscopic characterization of LbL films containing liposomes is essential not only to determine the precise film architecture but also to guide the design of drug delivery systems. In this study we provide the first report of vacuum ultraviolet spectroscopy characterization of LbL films made with liposomes from DPPG alternated with PAH. Measurements in the 6.0–9.5 eV range allowed us to identify the electronic transitions responsible for the spectra. To calculate the absorbance, light intensity spectra of the CaF_2 disc/or quartz cuvette were measured before and after measuring the spectrum of the disc covered with LbL film or DPPG dispersion or PAH solution. The average of those two spectra and the spectrum of the coated solid support (with film, dispersion or solution) were used to calculate the absorbance using the Lambert-Beer equation. Surface mass density of LbL films could be determined. Damage of UV irradiation in vacuum of DPPG liposomes during the course of VUV measurements was inferred. Discussion of the results and respective treated data are presented in section 4.4.

3.3.5 X-Ray Photoelectron Spectroscopy

X-ray photoelectron spectroscopy (XPS) is a surface-specific spectroscopic technique and is based on X-ray irradiation of the surface under study, followed by analysis of the emitted electrons kinetic energies [210]. The depth of analysis does not go beyond 10 nm. This technique allows determining the oxidation state of an element and infers the type of chemical species to which is connected to. For each element, there is a characteristic binding energy associated to each photoelectron in a given orbital, i. e. each element will give rise to a characteristic set of peaks in the XPS spectrum. The photoelectron kinetic energy is equal to the incident photons energy minus the photoelectron binding energy. Manifestation of specific energy peaks indicates presence of a specific element in the sample. Furthermore, the intensity of the peaks is related to the atomic concentration in the sample. Thus, the XPS technique, also known by the alternative acronym ESCA (Electron Spectroscopy for Chemical Analysis) permits both qualitative and quantitative analysis of the surface composition. Based on this technique it is possible to obtain a quantitative elemental chemical analysis, oxidation states, functional groups presence and ligands, as well as the nature of the connections (ionic and covalent). The sensitivity of the technique is about 0.1 % to all elements of the periodic table, except for H and He. It can be used for all solid materials stable at high vacuum, conductors such as metals, or insulators such as ceramics, polymers, glass and others. Figure 3.17 outlines the typical experimental arrangement of the XPS technique.

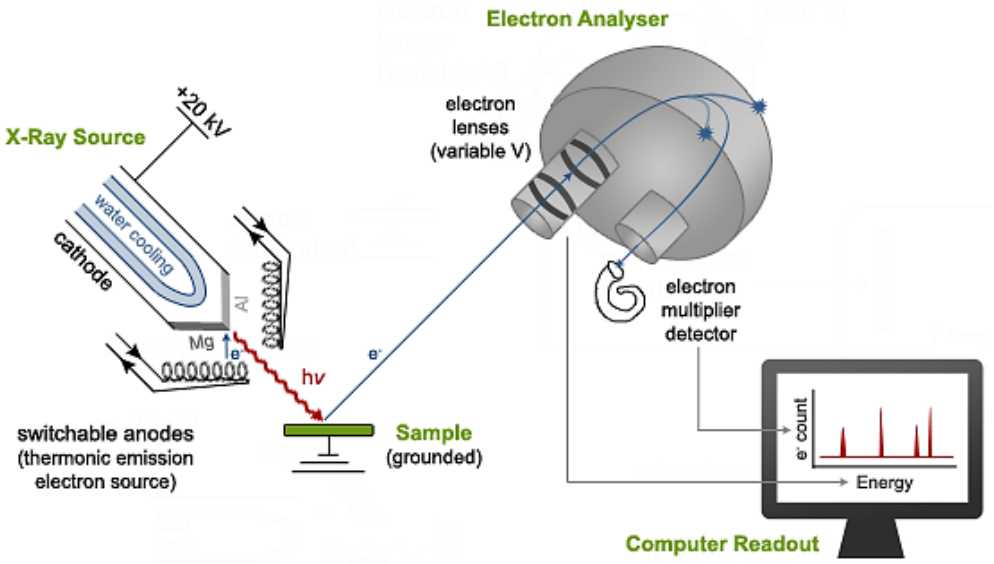

Figure 3.17. The typical experimental arrangement of the XPS technique [211].

XPS technique instrumentation consists in a X-ray source, with or without a coupled monochromator, an electron energy analyzer and an electron detector. The sample needs to be placed on a high vacuum chamber in order to perform analysis. The X-ray source is composed by a heated filament (cathode) electron emitter; these electrons are accelerated to the anode, usually cooled with water. Due to the electron bombardment, it creates holes in the innermost levels of the anode atoms, which are filled by electronic transitions from the higher levels L (n = 2) to the lowest K (n = 1) emitting X radiation. The X-ray sources most used are the Mg Kα photons beam with primary energy of 1253.6 eV and the Al Kα photons beam with primary energies of 1486.6 eV. A X-ray monochromator allows narrowing of the line widths with 0.2 eV, which improves the signal lines by eliminating the satellites that confound the spectra interpretation.

XPS characterization has grown significantly in the recent decades, especially in multidisciplinary fields of science, such as biomaterials, composites, nanotechnology and others. Typically, this technique is used in semiconductor, electronic materials, biomedical applications materials, polymers and plastics industries.

In this work the XPS spectrometer used was a XSAM800 (Kratos) non-monochromated comprising a dual anode source, with one of the anodes covered with magnesium and the other with aluminum which emit photons, respectively, with 1253.6 eV (Mg Kα) and 1486.6 eV (Al Kα). The apparatus was operated in FAT (Fixed Analyzer Transmission) mode [212], in which the electrons are accelerated or delayed in order to always be conducted at the same pass energy. The advantage of this mode is the constant analyzer resolution in the whole energy range. The current and voltage used were 10 mA and 13 kV, respectively. Samples were analyzed at room temperature in ultra-high vacuum pressures of the order of 10^{-7} Pa. All samples were analyzed in their central part, in an area of 3x1 mm^2 at a take-off angle of 0° relatively to the sample's normal, using the high mode amplification. Spectra were recorded with a Sun SPARC Station 4 with Vision software (Kratos) using a step of 0.1 eV. X-ray source satellites were subtracted; Shirley background and pseudo-Voigt profiles (Gaussian and

Lorentzian products) were fitted to each region using a non-linear least-squares algorithm. No flood-gun charge compensation was used. Binding energies (BE) were corrected setting C 1s BE lowest energy to 284.7 eV, corresponding to a C sp^2, in the sample with the PEM cushion and to 285 eV, corresponding to C sp^3, in the samples with DPPG [213]. For quantification purposes, sensitivity factors were 0.66 for O 1s, 0.25 for C 1s, 0.42 for N 1s, 0.29 for P 2p, 0.54 for S 2p, 2.3 for Na 1s, and 0.73 for Cl 2p as supplied by Kratos.

3.3.6 Fourier Transform Infrared Spectroscopy

Absorption spectroscopy in the infrared region is based on the fact that chemical bonds have specific frequencies of vibration which correspond to energy levels of the molecule (in this case called vibrational levels) [210]. Thus, this spectroscopy detects radiation that is absorbed by the molecular vibrational bonds. The infrared regions of the electromagnetic spectrum ranges between the visible and microwaves, and is subdivided into near (4000 - 12500 cm^{-1}), medium (400 - 4000 cm^{-1}) and far (10 - 400 cm^{-1}) infrared. Thus, the near infrared spectral region comprises the interval between 800 and 2500 nm for wavelengths lectures corresponding to 4000 - 12500 cm^{-1} for measurements in wave numbers [214]. The chemical bonds of the substances have specific frequencies of vibration which correspond to vibrational levels of the molecule. Radiation absorption in the infrared region is due to the electrical dipole moment variation of the molecule as a result of its vibrational movement. There are two types of molecular vibrations: stretching and bending. Stretching vibrations consist in the rhythmic movement along the bond axis giving rise to interatomic distances that increase or decrease. Figure 3.18 schematizes the two modes of stretching vibrations: antisymmetric and symmetric.

(A) (B)

Figure 3.18. Stretching vibration modes: (A) antisymmetric and (B) symmetric.

Bending vibrations are defined as an angle change between bonds with a shared atom or as the movement of a group of atoms which move in relation to one part of the molecule, but not considering the remaining atoms of the other part of the molecule. For example, rotational vibrations of balance and wagging, involve bond angle changes considering a set of arbitrary coordinates inside the molecule. Figure 3.19 depicts four modes of bending vibrations, namely: scissoring, twisting, rocking and wagging.

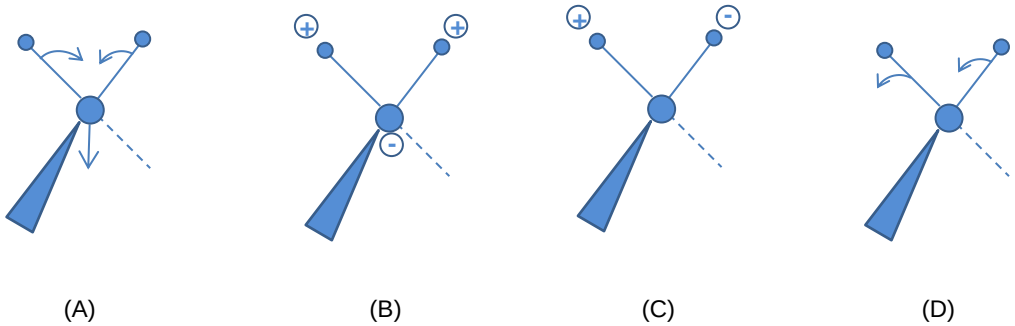

Figure 3.19. Schematic representation of the four modes of bending vibrations: (A) scissoring, (B) twisting, (C) rocking and (D) wagging.

Fourier Transform Infrared (FTIR) spectrophotometers are based on the Michelson interferometer. In this system the radiation of the light source is split into two equal beams by a beamsplitter, as shown in figure 3.20. One of the beams follows toward a fixed position mirror which reflects back to the beamsplitter and here again split up and part of this goes to the detector. The other beam leaves the beamsplitter towards a movable mirror, this mirror also reflects, a division of the radiation occurs and a portion of this is received by the detector. As the moving mirror travels a certain distance from the interferogram, a recombination of the two beams occurs. Thus, the interferogram is formed by the sum of all the waves of different frequencies and amplitudes that arrives at the interferometer. However, despite the interferogram contain all the information provided by the spectrophotometer this way is not very useful, and this information must be converted into a spectrum that relates the intensities with respective frequencies via Fourier transform [215].

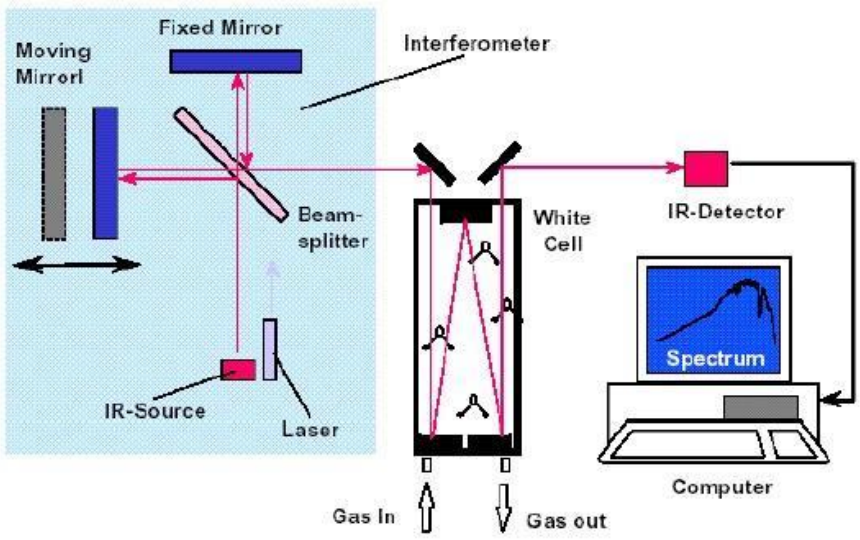

Figure 3.20. Schematic representation of a FTIR spectrometer [216].

The main advantages of the FTIR technique are the accuracy, simplicity and rapid interpretation of the data, it does not need qualified personnel to perform and can be directly used on the local production, as well as is a non-destructive method. Therefore, this methodology has applications in various types of industry, such as food, agricultural, pharmaceutical, textile, oil, cosmetics, among others [217].
FTIR measurements of DPPG cast films deposited on calcium fluoride were obtained with a spectrophotometer Thermo Scientific Nicolet-model 530 (Waltham, MA, USA).

3.3.7 Scanning electron microscope

The first high-resolution Scanning Electron Microscope (SEM) with a sub-micron probe was developed by Manfred von Ardenne, in 1937. However, the major impulse in materials characterization using the electronic microscope occurred in the 50s [218-220] . An account of the early history of SEM has been presented by McMullan [221].
SEM is a powerful tool used to support scientific research, as well as the development and quality control of materials and it is applied to domains extended from microstructural characterization (metals, ceramics, composites, biomaterials, coatings) to applications in geology, biology and medicine, powder characterization, etc. This technique can be applied to thin films in order to determine heterostructures' thicknesses, to analyze microstructures, to identify defects and impurities, and to perform adherence, corrosion and fracture studies. SEM achieve similar pictures to those obtained by reflection optical microscope, but in a range of magnification dramatically higher (from 10x to 18000x) with a field depth of 30 μm. This technique is generally associated to Energy Dispersive X-ray Spectroscopy (EDS), which allows a semi-quantitative analysis of the chemical elements of the materials surface.
The operational principle is based on the incidence of an electron beam to a point on the surface of the target sample and subsequent collection of electronic signals sent by the target material, as displayed in figure 3.21. Samples are sequentially scanned by an electron beam accelerated by a voltage which varies between 0 and 40 kV, finely focused through an electromagnetic lens system. Interaction of the electronic beam with the sample results in emission of various types of radiation like electrons, including secondary electrons used in the formulation of the sample image (with energies less than 50 eV). Secondary electrons are electrons suffering excitation and "escaping" from the sample's surface. Back-scattered electrons allow discrimination of regions of the sample under analysis using light and heavy atoms. Secondary electrons are generated by inelastic interaction processes of primary and back-scattered electrons with higher energy bonding electrons. The electrons depth does not exceed a few dozens of nanometers. The images obtained by detecting secondary electrons have a strong topographic contrast being the contrast a consequence of the emission of back-scattered electrons, whose intensity increases with the atomic number. The fact that the secondary electrons come from a small volume makes it possible to obtain excellent images, allowing visualization of the topographic contrast.

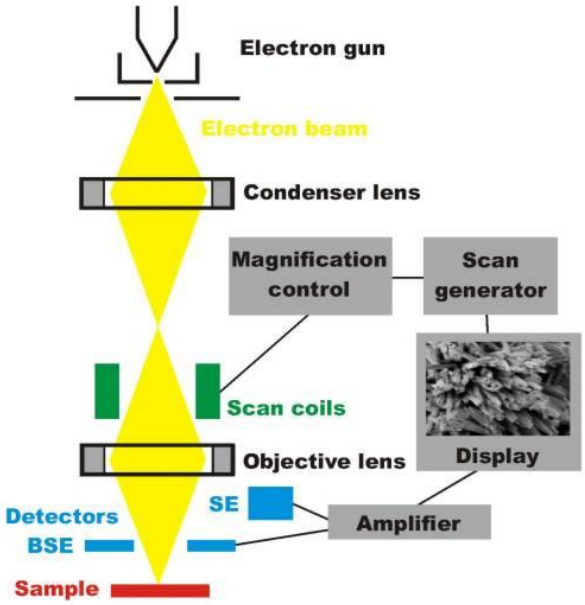

Figure 3.21. Schematic representation of the SEM technique [222].

Substrate surface of DPPG cast films deposited on silicon was analyzed on a ZEISS Auriga CrossBeam model DSM 962 SEM focused ion beam setup. To increase the surface sensitivity, SEM images were typically obtained at a low acceleration voltage of 2 kV. Semi-quantitative analysis of the cast films was obtained by energy-dispersive x-ray spectroscopy (EDS) integrated in the same Zeiss Auriga platform using an Oxford INCA x-act silicon drift detector and an Oxford INCA microanalysis software. Analysis was performed at 15 keV, with an aperture size of 30 µm, a magnification of 1000× and an acquisition time of 120 s for each sample.

3.3.8 Ellipsometry

Ellipsometry is an optical technique sensitive to changes occurring on the surface, based on the fact that the polarization state of the light changes when a light beam is reflected by a surface. Indeed, when a substrate is covered by a thin film, the optical system comprising the film and the substrate causes a change in light polarization. It is thus possible to deduce information on the properties of the films, especially thickness and refractive index. Polarization state is characterized by amplitude (Ψ) and phase difference (Δ) of the two components of the polarized light: parallel (P) and perpendicular (S) to the plane of incidence. A schematic illustration of the principle of ellipsometry is shown in figure 3.22.

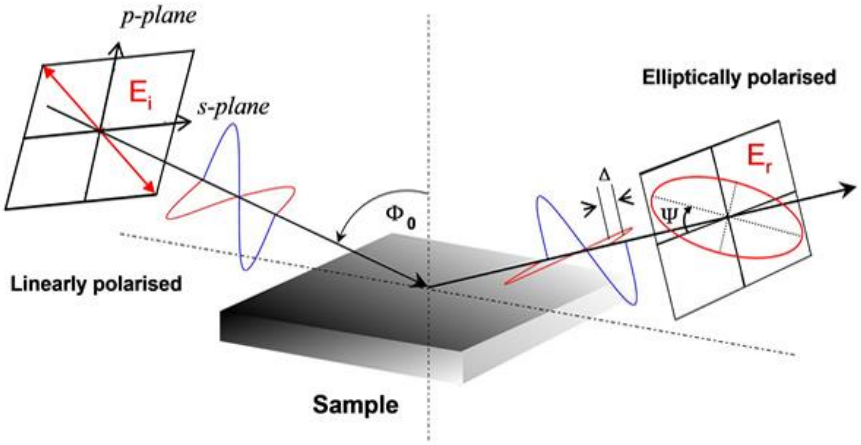

Figure 3.22. Schematic illustration of the principle of ellipsometry, from [223].

Ellipsometry measurements allow determining the angles, ψ , and variations, Δ. The total effect caused by the reflection is described by the ellipsometry fundamental equation [223]:

$$\rho = \frac{R_p}{R_s} = \tan(\psi)^{(j\Delta)} \tag{3.27}$$

where ρ is the ratio between the reflection coefficients of the parallel and perpendicular components, R_p and R_s. These coefficients depend on the wavelength of light, incidence angle and optical properties of the system (layers thickness and their refractive indices).

Thickness of a PAH/DPPG bilayer after adsorption onto Au-quartz crystal surface, see section 4.6, was recorded using an ellipsometer (SENTECH Instruments GmbH, Berlin) fitted with a He–Ne laser (632.8 nm). Data was processed and fitted using the software provided by SENTECH (SE 400). Measurements were carried out at an angle of incidence of 70°.

3.3.9 Voltammetric electronic tongue

According to the International Union of Pure and Applied Chemistry (IUPAC) [224] an electronic language (EL) is a multi-system sensor composed of chemical sensors with reproducible response, high stability and cross-sensitivity to different species in solution and therefore provide signals profiles that translate global information about the samples. Multivariate statistical methods are used to processing the signals profiles in order to achieve the analysis main goal, which may be the recognition of the qualitative composition (samples classification and discrimination), the quantitative analysis of chemical multi-species and the evaluation of the samples taste. ELs are systems with earned interest because they allow acquiring global information on complex samples which cannot be

possible with other analytical methodologies, mostly mimicking the human tongue in flavors appreciation. This information varies according to the characteristics of the EL used.

Electronic tongues are defined as an array of non-specific (electro) chemical sensors with cross-sensitivity to different species in a solution combined with an appropriate chemometric tool for the data processing. A huge effort has been devoted to the development of innovative sensors with improved characteristics. The sensors used in the electronic tongue may use several measurement principles, including mass detection quartz microbalances [225], optical transduction [226] and electrochemical measurements. In particular, electrochemical sensors (voltammetric, impedimetric, or potentiometric) are the most widely used in electronic tongue technology. Electronic tongues are usually applied to give qualitative information about the studied samples, but they can also predict the concentration of individual species in the product. More recently, voltammetric electronic tongues associated with chemometrics data analysis have been proposed for the olive oil characterization using the chemical composition responsible for the delicate taste [227, 228]. Up to now, electronic tongue systems have proved their reliability and versatility in a wide range of fields, such as agro-food analysis [229], environmental monitoring [230], clinical diagnostic [231] and pharmaceutical analysis [232]. In this work, a hybrid voltammetric electronic tongue (HVE-tongue) is applied to classify a set of olive oil samples coming from different Moroccan and Portuguese regions. Indeed, HVE-tongues can include two or more sensor families. Usually, it is a combination of potentiometric, voltammetric and/or conductimetric sensors. After getting signals from all types of sensors, data processing is performed by means of chemometric methods to extract useful information. The HVE-tongue allows obtaining more diverse information about the sample. This gives the opportunity for better, more reliable and more accurate characterization of the sample and increases the probability of correct samples classification [233] .

3.3.9.1 HE-tongue set-up measurement

The voltammetric measurement cell was formed by two kinds of working electrodes, Ag/AgCl as a reference electrode and platinum plate as a counter electrode, which was housed inside a stainless steel cylinder as the body of the devise.

Fig. 3.23 shows a schematic representation of the experimental set-up used in the measurements. Sensors were assembled in a homemade glass backer. Working electrodes were connected to a relay box, enabling each of them to be connected separately to a standard three electrodes configuration. Current responses were measured by a portable potentiostat (PalmSens BV, The Netherlands). Electrochemical experiments were performed at a room temperature. Several tests were carried out on olive oil samples for each working electrode, in order to optimize the electrochemical window range. Cyclic voltammetry (CV) was recorded in a range of varying potentials from -700 to 1300 mV at scan rate of 20 mVs^{-1} [234].

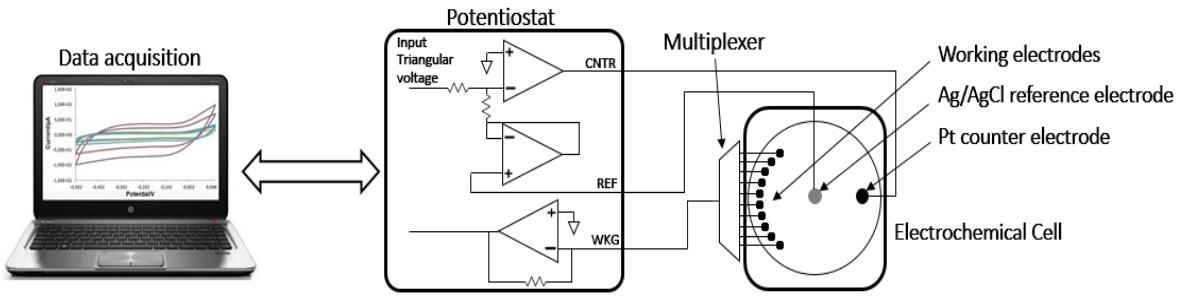

Figure 3.23. Portable HE-tongue setup for the evaluation of olive oils [235].

3.3.9.2 Features extraction

Extraction of features from voltammograms is an essential pre-processing issue towards pattern recognition. The goal of this procedure is to determine the values of the variables which characterize a certain category of very similar products. This is seeking for the discriminative features that are invariant to irrelevant transformations of a final HE-tongue database. In this study, in order to fully exploit the maximum information existing in the response, features were directly extracted from the responses of each sensor of the array, as follows:

- $\Delta I = I_{max} - I_{min}$: current change calculated as the difference between maximum and minimum values of the current, were I_{max} is the maximum value of the current measured in the final potential range and I_{min} is the minimum value of the current measured in the initial potential.
- S_{ox}: maximum slope of the current curve in the oxidation phase.
- S_{red}: maximum slope of the current curve in the reduction phase.

These features were the ones which give a better discrimination of the analyzed products according with previous works from others [234, 236]. Features obtained from the voltammograms of HE-tongue were gathered in a dataset and used to build a model to classify olive oils samples. In total, each olive oil measurement was characterized by thirty features (i.e., 10 sensors × 3 features per sensor). These variables were organized in a rectangular matrix as a database.

3.3.9.3 Principal Component Analysis

Data contained in the dataset was analyzed by using Principal Component Analysis (PCA). The aim of using this pattern recognition method in this study is to estimate the performance of HE-tongue in identifying and classifying the geographical origin of different olive oils samples. PCA is a linear and unsupervised technique that is useful for the compression and classification of data [21, 23]. The purpose is to reduce the dimensionality of a data set by finding a new set of variables, smaller than the original set of variables that nonetheless retains most of the sample's information. PCA summarizes

variation in a correlated multi-attribute to a set of uncorrelated components, each of which is a particular linear combination of the original variables. Extracted uncorrelated components are called principal components (PCs) and are estimated from the eigenvectors of the covariance or correlation matrix of the original variables.

A HVE-tongue was developed by combining two electrochemical sensors types, such as: i) three LbL films based on PAH and PEI common polyelectrolytes, the synthetic phospholipid DPPG, and the biopolymer melanin and ii) seven voltammetric sensors: Copper (Cu), Glassy Carbon (GC), Gold (Au), Nickel (Ni), Palladium (Pd), Platinum (Pt) and Silver (Ag). Advantages that make these sensors well suited for this application are the small size, low cost, reproducibility and easy integration into the measurement system in the same platform. Therefore, they can be integrated in a portable and a miniaturized analytical system to achieve rapid and in-field measurements. The data treatment was carried out by Principal Component Analysis (PCA). In this study, a total of eleven olive oil samples were analyzed: six commercials Portuguese olive oils, namely Gallo Classico, Fio Dourado, Oliveira da Serra, Paladin, Gallo Reserva and SOS Pobreza and other five commercials Moroccan olive oils, specifically Moulay Idriss, M'rirt, Ouarzazate, Ouazzane and Taounate. Results and discussion are shown in section 5.6.

4 IMMOBILIZATION OF LIPOSOMES ON SURFACES

This chapter reports the characterization of the DPPG small unilamellar vesicles (SUVs) suspension, obtained by extrusion and sonication procedures, immobilized on flat solid supports and on rough polyelectrolyte multilayers (PEMs). A detailed and comparative kinetic study of the assembly of PEI/DPPG LbL films by five different experimental configurations using a quartz crystal microbalance (QCM) *in situ*, i.e. at solid-liquid interface, is also reported. Furthermore, the growth of $(PEI/DPPG)_{10}$ self-assembled films using the layer-by-layer (LbL) technique based on the adsorption of oppositely charged materials of DPPG SUVs layers alternated with polyelectrolytes onto a PEM surface, was monitored by QCM and the calculated mass amounts of the layers as well as the adsorption kinetic processes are presented. Also, the growth of $(PAH/DPPG)_{10}$ LbL film onto a smooth solid surface was examined by vacuum ultraviolet (VUV) spectroscopy. The electronic transitions and functional groups assignments and the mass surface density are described. Besides, statistical analysis of the PAH/DPPG surface topographies imaged by atomic force microscopy (AFM) is also presented.

4.1 DPPG suspension analysis

The size distribution by intensity of DPPG liposomes suspension produced by the extrusion method was determined by dynamic light scattering (DLS) using the model BI-90 equipment and is shown in figure 4.1. These values were fitted and a Gaussian curve with a single peak centered at 169±3 nm was obtained, showing a monomodal distribution. The polydispersity of the solution was 0.179 revealing the homogeneity of the liposomal suspension because it presents a value below 0.3. However, it should be referred that probably the mean effective hydrodynamic radius of the particles is smaller than the achieved due to the fact that the DLS equipment is outdated and it took too much time collecting the data. Thus, and because DLS measures the Brownian movement of the particles and analyzes the fluctuations of the intensity of scattered light, it is worth to consider that the smaller particles weren't gathered during measurements.

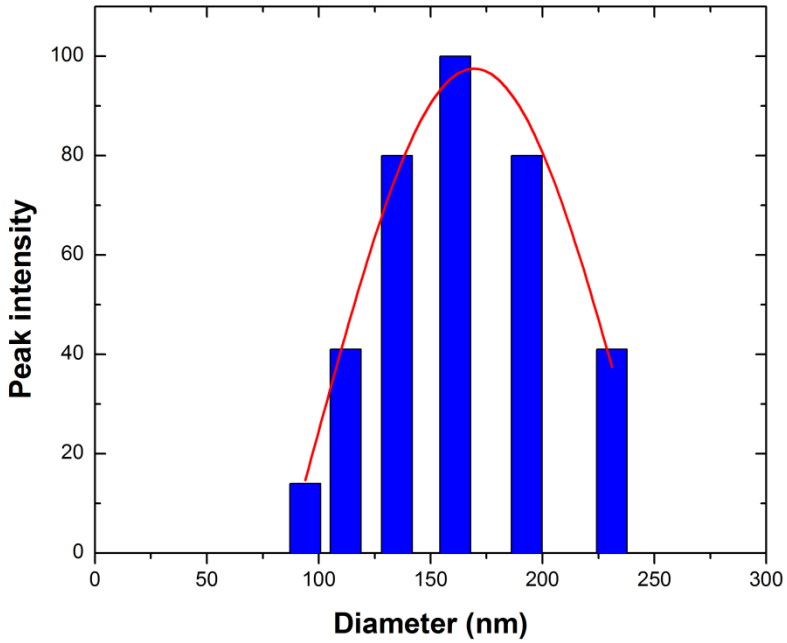

Figure 4.1. Size distribution by volume of the DPPG vesicles obtained by the extrusion method in a mini-extruder containing polycarbonate membranes with 0.1 μm pores. The Gaussian fit curve (red color) presents a single peak centered at 169±3 nm showing a monomodal distribution.

The size distribution characteristics by intensity and volume of DPPG liposomes produced by the sonication method were determined by DLS model Zetasizer Nano-ZS Series ZEN3600 (Malvern Instruments) and the obtained hydrodynamic diameters (HD) are displayed in table 4.1. The particle size shows a polymodal distribution, since the volume distribution has three maxima, centered at 25, 102 and 195 nm. The intensity distribution presents two maxima centered at 30 and 388 nm. The third peak, for higher HD, cannot be distinguished in size intensity distribution of the DPPG as it is almost constant without prominent peaks. Since scattered light is proportional to square of volume, an order of magnitude in the particles radius leads to a difference of three orders of magnitude in the volume percentage and six orders of magnitude in the scattered light intensity value. Indeed, the volume distribution HD of peak 2 is roughly 4 times the HD of peak 1, and light intensity scales as the square of volume, HD of peak 2 in light intensity distribution is expected to be approximately 16 times the HD of peak 1; in fact it is more than 13 times, showing good agreement. Regarding the intensity distribution, the presence of a peak centered at 388 nm with 92% of intensity is justified by the fact that larger particles, associated to peaks 2 and 3 of volume distribution and with a low volume percentage value (8%), are contributing strongly for the intensity of the scattered light. Consequently, despite the residual presence of larger particles in DPPG suspension, one can consider that most of the DPPG liposomes have a mean diameter size of 25 nm. The fact that the sum of percentage volume from the three peaks does not reach 100% may be related to the possible presence of titanium residues, in DPPG suspension, with micron size (see figure 4.2), released from the probe during sonication, which were not taken into account by the model.

Table 4.1. Volume and Intensity distributions characteristic of DPPG liposomes obtained from DLS measurements: HD (hydrodynamic diameter) associated with peak position, peak intensity and peak width.

Peak	Volume distribution			Intensity distribution		
	HD (nm)	Peak Intensity (%)	Peak Width (nm)	HD (nm)	Peak Intensity (%)	Peak Width (nm)
1	25	75.7	6	29	8	7
2	102	4.5	26	388	92	321
3	195	3.8	40	----	----	----

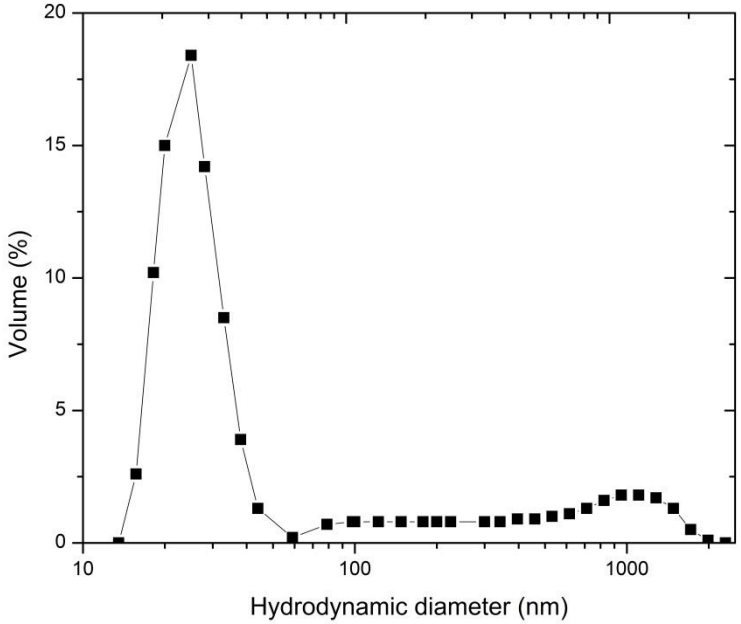

Figure 4.2. Size distribution by volume of the DPPG vesicles obtained by the sonication method using an ultrasonic processor over 30 seconds and repeated 15 times with 1 minute delay between cycles. It should be referred that the high values of hydrodynamic diameter (around 1000 nm) probably correspond to titanium particles released from the ultrasonic probe during sonication.

4.2 Characterization of DPPG cast films

Topographic images with 0.5×0.5 μm^2 of DPPG cast films produced with extruded DPPG suspensions deposited on silicon surfaces were obtained by AFM technique in non-contact mode and are shown in figure 4.3 a) (3D view) and b) (height phase). Figure 4.3 c) presents a height profile of the surface. The DPPG suspension concentration used to perform the cast films was 5 mM. On the left side of the figure 4.3 c) a profile of a DPPG vesicle with approximately 100 nm of length is displayed and, on the right side, two terraces with about 5±1 nm of height, each corresponding to the thickness of two

different supported lipid bilayers (SPBs). SPBs can be easily formed by the assembly of liposomes on considered smooth hydrophilic solid supports, such as silicon. This behavior is greatly reported in literature, for an overview see [3, 67, 75, 77, 165, 169]. Although, a greater number of studies have identified some of the critical stages of vesicle adsorption and spreading of lipid bilayer on smooth surfaces, further investigations are needed concerning rough surfaces and lipid loading a net charge. In this case, and considering the fact that the silicon is a hydrophilic substrate with a root-mean-square roughness of 0.3±0.1 nm and the DPPG liposomes are negatively charged, it's easy to realize that when the first DPPG vesicles reach on the surface, they readily start to break and spread throughout the surface forming SPB patches. Afterwards, the vesicles accumulate preferentially along the SPB patches edges, where they disrupt more quickly and fuse with the adjacent SPB islands. SPB coverage reaches a critical point, where liquid-like coalescence of patches occurs rapidly (at a constant bilayer area). Probably, due to SPB lost edges, more vesicles will bind, spread and coalesce, creating another lipid bilayer that will cover partly the underlayer SPB formed previously, as it can be seen in figure 4.3 a) and b) by the large round islands found at different heights. Then, when a critical surface coverage is attained and perhaps due to the fact that the surface has become more rough or because the interactions between DPPG liposomes and silicon substrate diminished, new liposomes attached to the SPBs surface without rupture, corresponding to the small circles domains found at high heights in figures 4.3 a) and b). The surface root-mean-square roughness (Rq) found was 11±2 nm. A statistical analysis of the intact liposomes adsorbed on the top surface reveals an average height and width of 11±3 nm and 87±9 nm, respectively, meaning that after adsorption the SUVs kept closed but with a certain flattening. These values showed that the effective mean diameter of the DPPG liposomes is lower than the obtained by DLS, due to some constrains reported in section 4.1. Israelachvilli works demonstrate the presence of a thin layer of water between 0.6 and 0.9 nm trapped between the phospholipid bilayer and the silicon surface [77]. This explains the thickness difference between SPB levels presented in figure 4.3 c), with 5 nm, and DPPG phospholipid bilayer, reported in [237], with 4.5 nm.

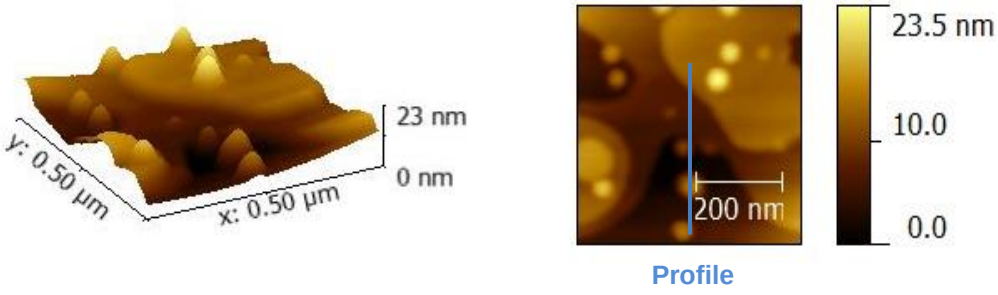

a) b)

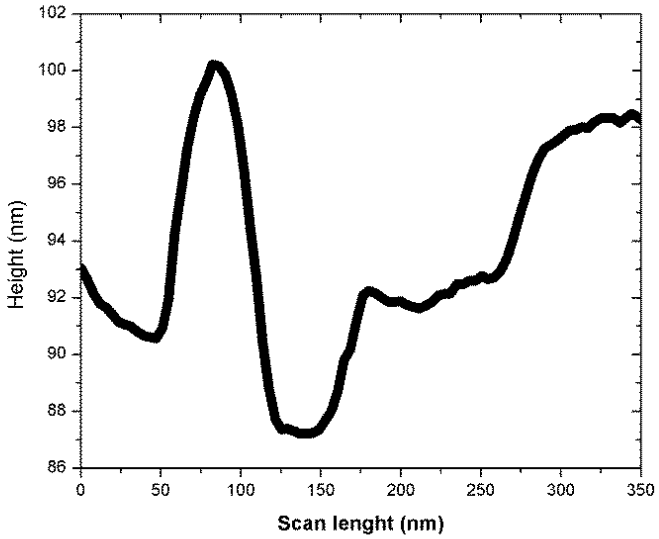

c)

Figure 4.3.Topographic AFM images a) and b) with 0.5×0.5 μm^2 area of DPPG cast films deposited onto a silica substrate. c) The height profile obtained from topographic image b) shows a liposome, on left, with a diameter of ~100 nm and two levels, on right, with about 5 nm corresponding two to DPPG lipid bilayers deposited one above the other.

In order to confirm the presence of intact liposomes and the SUVs vesicles size found in DPPG cast films, samples were imaged via SEM. Figure 4.4 shows an image obtained by this technique where it is possible to observe the presence of vesicles with a range diameter from 75 to 110 nm. Although other measurements, data none shown, revealed a presence of vesicles with lengths fluctuating between 40 to 70 nm.

Combining the AFM and SEM results with the accomplished by DLS measurements, see section 4.1, a mean diameter value of 120 nm was found and will be considered for later studies performed with DPPG suspensions attained by the extrusion method.

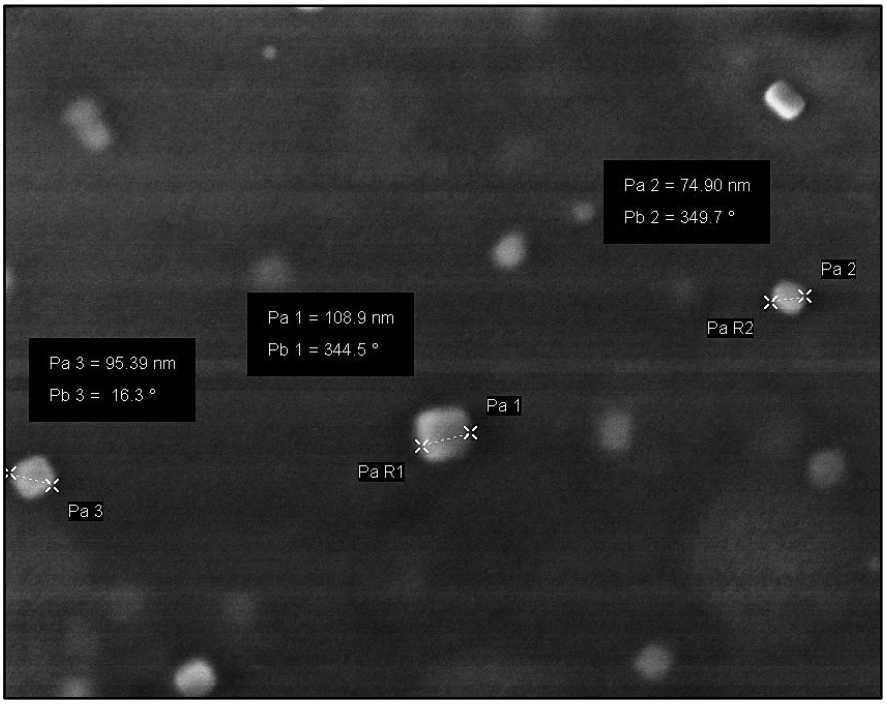

Figure 4.4. SEM image of a DPPG cast film showing vesicles with diameters between 75 and 109 nm.

A semi-quantitative analysis of DPPG cast films was performed by Energy-dispersive X-ray Spectroscopy (EDS). The obtained spectrum presented in figure 4.5 reveals the presence of carbon (C), oxygen (O), sodium (Na) and phosphorus (P) elements assigned to the DPPG liposomes and of silicon (Si) element owned to the substrate.

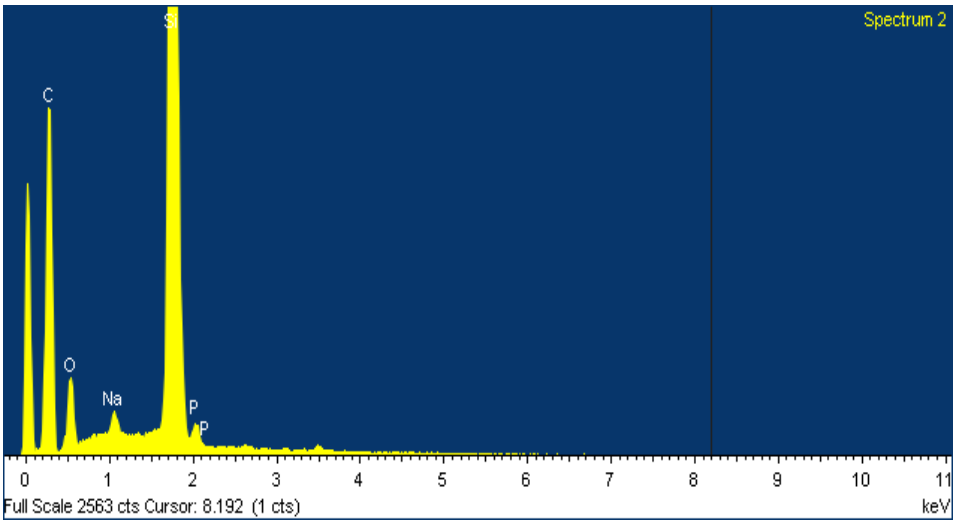

Figure 4.5. EDS spectrum of DPPG cast film with a concentration of 5mM deposited onto a silicon substrate.

Aiming to verify if DPPG vesicles adsorbed on the top of SPB, as shown by AFM topographic images (figure 4.3), have the ability to serve as water molecules reservoirs more measurements were made, specifically via spectroscopies techniques. Thus, the DPPG suspension was casted onto calcium fluoride (CaF_2) surfaces to be analyzed by Fourier transform infrared (FTIR) spectroscopy. The obtained infrared spectrum, shown in figure 4.6, reveals a major band with a peak centered at 3440 cm^{-1} which can be assigned to OH group of the glycerol and to water retained in liposomes [238]. The strong bands at 2915 and 2852 cm^{-1} corresponding to C–H stretching of the phospholipid hydrocarbon tails, namely CH_2 and CH_3 groups, respectively [4]. The peak at 1738 cm^{-1} can be assigned to stretching of carbonyl group (C=O) [239-241] while the large peak at 1638 cm^{-1} can be also associated to vibrations of C=O groups which are embedded in hydrogen bonds, taking into account Blume *et al* which observed that in presence of stronger hydrogen bonds and/or more hydrogen bond donors the vibrational frequency of the lipid ester C=O group shifts to lower wavenumbers [242, 243]. It should be also referred that Paolorossi and Montich observed that DPPG presents a band at 1643 cm^{-1} which has been associated to unfolded structure [244] while Surewicz and Mantsch observed a peak at 1649 cm^{-1} which was associated to unordered conformations [245, 246]. The peak at 1467 cm^{-1} represents the CH_2 scissoring [247, 248]. The small peak at 1414 cm^{-1} can be assigned to in-plane bending of C–O–H group. The peak at 1241 cm^{-1} is associated to antisymmetric stretching of hydrated PO_4^- group [249], while the peak at 1222 cm^{-1} is related to P=O antisymmetric stretching of PO_4^- group [247, 248]. The peaks at 1169 and 1070 cm^{-1} can be assigned, respectively, to asymmetric and symmetric stretching of CO–O–C groups [250]. Finally, the peaks at 1096, 1057 and 1047 cm^{-1} can be associated to symmetric stretching of CO–O–C, C–O–C and C–O–P groups, respectively [247, 248, 251].

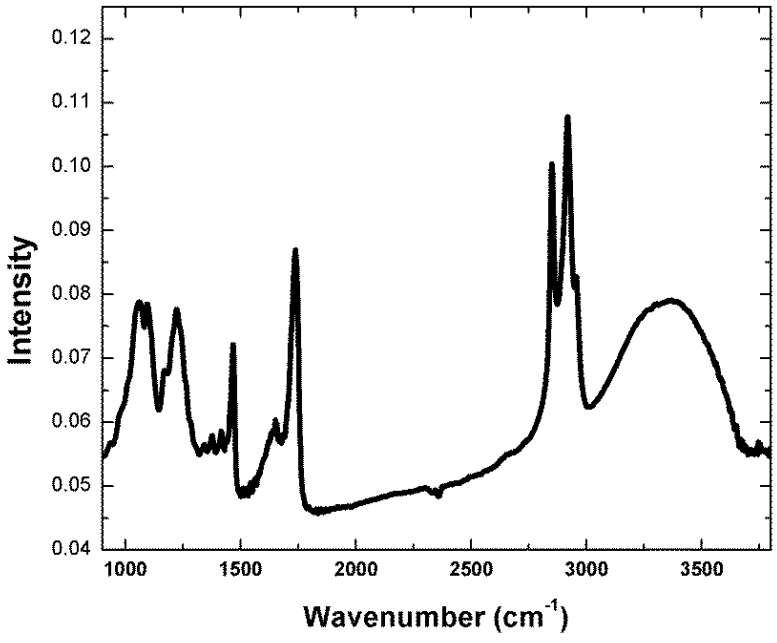

Figure 4.6. Infrared spectrum of DPPG cast film prepared onto a CaF_2 substrate.

DPPG cast films deposited on silicon surfaces were also analyzed by X-ray photoelectron spectroscopy (XPS). According to the XPS spectra of DPPG cast films, taken at take-off angle of 0° relative to the normal surface of films, it was possible to detect the following elements: carbon (C), oxygen (O), sodium (Na) and phosphorus (P). Furthermore, in table 4.2 is listed the atomic percentages, as well as the binding energies (BE) that were corrected using the aliphatic C 1s BE equal to 285.0 eV as reference. The C 1s region was fitted with four peaks. The two first peaks with low BE centered at 285.0 and 285.6 (± 0.1) eV are attributed to an aliphatic carbon and to a carbon single bonded to an oxygen (hydroxyl carbon), respectively [213]. The others two peaks with higher BE centered at 286.9 and 289.2 (± 0.1) eV are associated to a carbon double bonded to oxygen, namely a carbonyl carbon (C=O) and a carboxylate carbon (O–C=O), respectively [252]. The origin of the oxygen detected in the XPS spectra can not only be attributed to DPPG vesicles but also to the silicon substrate. At the O 1s core level binding energies region the sample exhibit three components centered at 531.4, 533.0 and 535.8 (± 0.2) eV. The first one is assignable to the oxidation from the silicon surface [213] and the third to water molecules aggregates entrapped in the film [6, 253]. The second peak can be assignable to an oxygen single bonded to a phosphate and to a carbon and the oxygen double bonded to a carbon [213]. The region of the P 2p comprises one doublet. The most intense component P $2P_{3/2}$ centered at 133.7 ± 0.2 eV is typical of a phosphorous with a neighborhood rich in oxygen [254]. The BE of 1071.4 eV corresponds to sodium DPPG counterion.

Table 4.2. Atomic Concentrations (%), Binding Energies (BE), eV, and respective assignments of the DPPG cast films deposited on silicon substrates.

	Atomic percentage (%)	**BE (eV)**	**Assignments**
C 1s 1	44.3	285.0	C-C, C-H
C 1s 2	21.0	285.6	C-O
C 1s 3	7.4	286.9	C=O
C 1s 4	3.8	289.2	O=C-O
O 1s 1	5.2	531.4	Substrate oxide
O 1s 2	13.8	533.0	$-OPO_3^-$
O 1s 3	0.8	535.8	-OH
P $2p_{3/2}$ 1	1.2	133.7	$-PO_3^-$
P $2p_{1/2}$ 2	0.6	134.6	$-PO_3^-$
Na 1s	1.8	1071.4	Na

During XPS measurements the samples are submitted to high vacuum for several hours. Consequently, water molecules present in samples that are not bounded are easily removed, while bonded water molecules, i.e. structural water, remain in the sample. As the peak obtained 535.8 eV [6] is associated to the presence of water molecules aggregates entrapped in the film, one can conclude that water is retained inside of the intact vesicles of the DPPG cast films. This finding is corroborated by AFM topographies and SEM images where it was possible to verify the presence of intact liposomes adsorbed onto a hydrophilic surface after the completely coverage by SPBs.

4.3 Improving Quartz Crystal Microbalance measurements accuracy in liquids

The accuracy of a commercial Quartz Crystal Microbalance (QCM200 from Stanford Research Systems, California) to measure the adsorbed amount of polyelectrolytes and biological molecules at solid/liquid interface was tested using different experimental configurations to conclude about the quality, stability and reproducibility of the measured data. The evaluation consisted in comparing the adsorb kinetics curves of adsorption of the cationic polyelectrolyte PEI and the anionic DPPG liposomes, obtained by sonication, when disposing the quartz crystal in five different experimental configurations, namely: Stationary Horizontal Open (SHO), Stationary Horizontal Closed (SHC), Stationary Vertical Open (SVO), Continuous Vertical Closed (CVC) and Stationary Vertical Closed (SVC). For this last configuration a new homemade cell was designed and implemented.

4.3.1 Testing QCM setups sensor

Figures 4.7 a), b) c) d) and e) show the frequency shift as a function of adsorption time of a PEI/DPPG bilayer assembled by disposing the quartz crystal resonator in five different experimental configurations, explicitly: (a) Stationary Horizontal Open (SHO), (b) Stationary Horizontal Closed (SHC), (c) Stationary Vertical Open (SVO), (d) Continuous Vertical Closed (CVC) and (e) Stationary Vertical Closed (SVC).

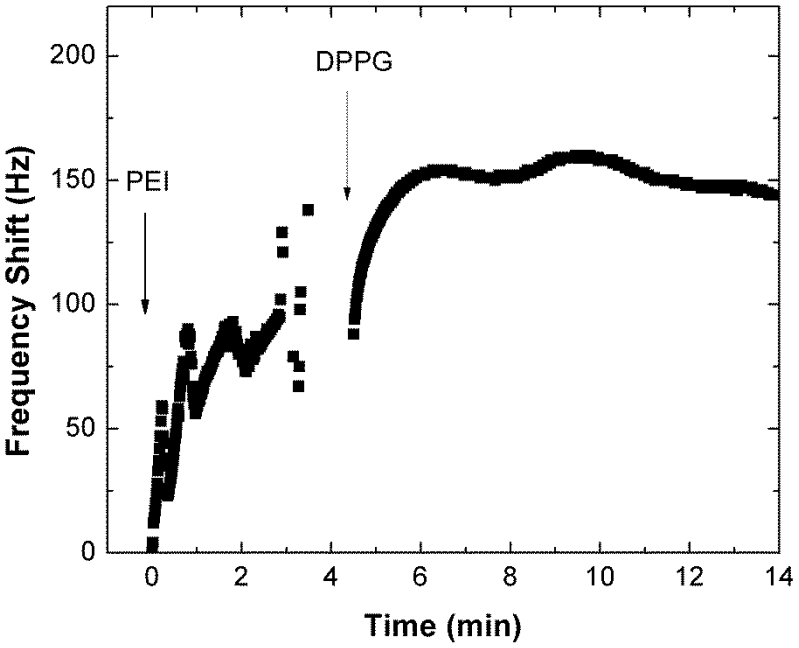
DPPG
PEI
Frequency Shift (Hz)
Time (min)
0
50
100
150
200
0
2
4
6
8
10
12
14

a)

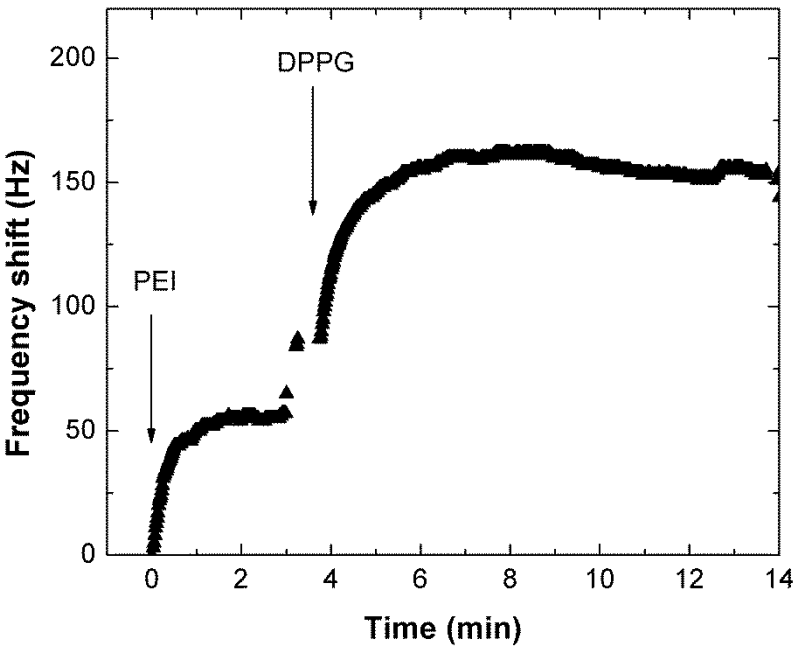
DPPG
PEI
Frequency shift (Hz)
Time (min)
0
50
100
150
200
0
2
4
6
8
10
12
14

b)

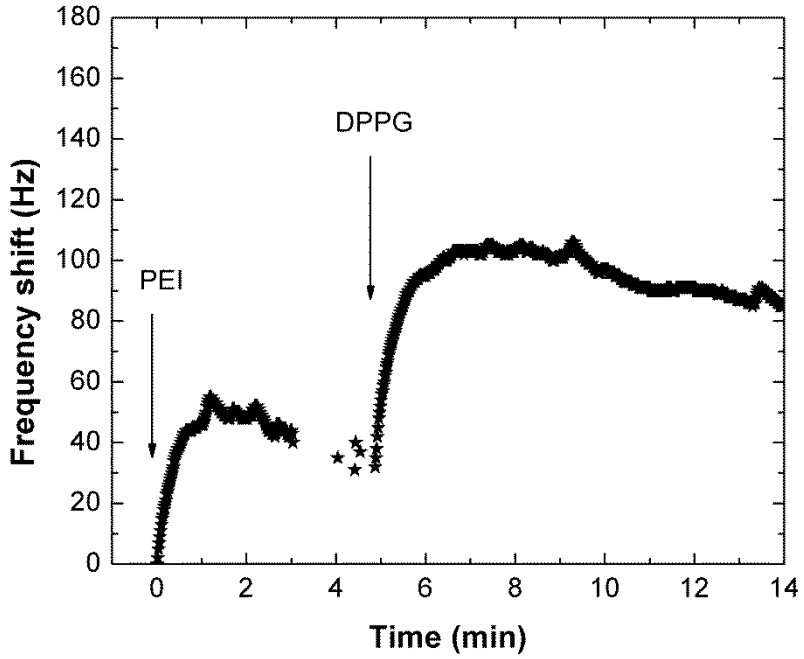
Frequency shift (Hz)
Time (min)
PEI
DPPG

c)

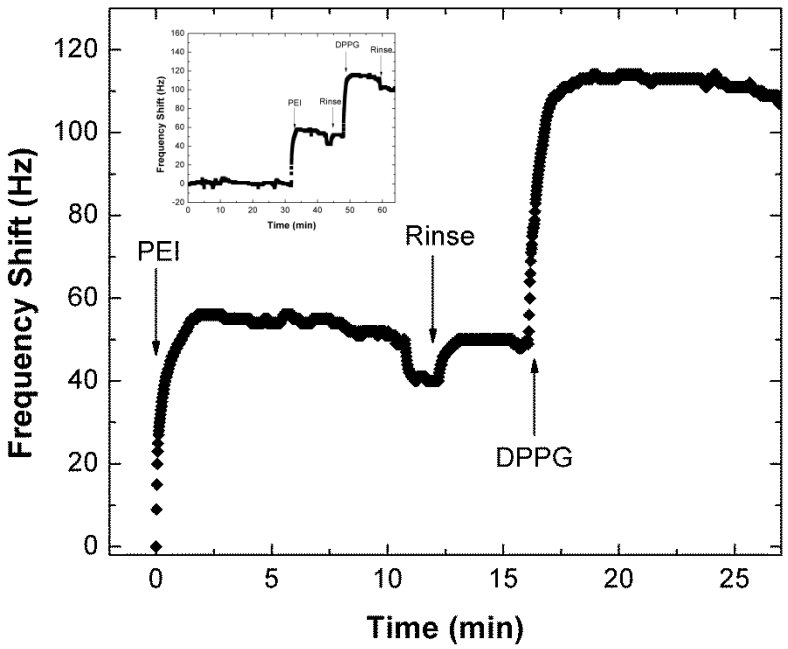
Frequency Shift (Hz)
Time (min)
PEI
Rinse
DPPG

d)

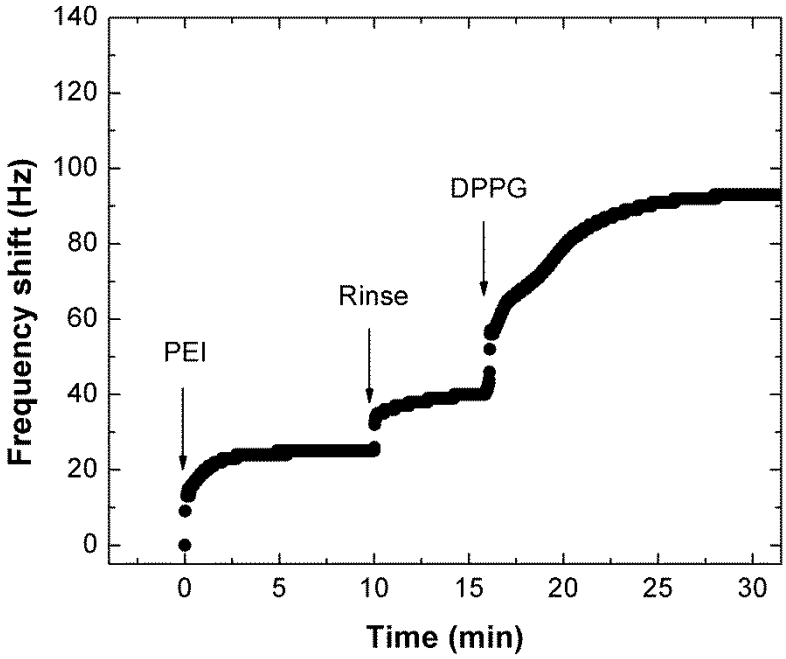

e)

Figure 4.7. Frequency shift as a function of time corresponding to PEI/DPPG bilayer assembling measured in the (a) Stationary Horizontal Open (SHO), (b) Stationary Horizontal Closed (SHC), (c) Stationary Vertical Open (SVO), (d) Continuous Vertical Closed (CVC) and (e) Stationary Vertical Closed (SVC) experimental configurations. The inset in graph d) displays the stabilization frequency in liquid before the PEI/DPPG assembly in the CVC system.

Kinetic curves obtained from five different QCM experimental configurations were analyzed in order to realize and overcome handicaps related to laboratory procedures, mechanical and acoustic vibrations.

The quartz crystal horizontal setups, SHO and SHC, proved to be more sensitive to external mechanical vibrations, see figures 4.7 a) and b), namely because the injection of solutions on the quartz crystal is handmade, using a Pasteur *pippete,* and does not allow maintain a continuous flow when the solution is being deposited. On the other hand, the main advantages of these experimental setups are the ease of use and the fact that small amounts of solution, about 1.5 ml, are required.

The SVO is the simplest setup due to the fact that the crystal holder head is vertically submerged into the solution, however this procedure is unreliable and may produce mechanical vibrations due to the crystal holder head immersion, see figure 4.7 c). In addition, this system requires a great amount of solution, of about 35 ml, per layer. Although it is an open system, the acoustic vibrations can be reduced by the high quantity of solution.

The CVC system presents some drawbacks concerning to mechanical vibrations caused by the peristaltic pump work, as revealed by the inset in figure 4.7 d), where is displayed an irregular

frequency after liquid balance operation. Note that the acquired peristaltic pump has 12 cylinders in order to reduce the noise. However, the noise reduction is not enough and more improvements concerning to peristaltic pumps must be done. Furthermore, the appearance of microbubbles inside the tubes during the solutions flow is very common and compromise severely the measurements. Also the high expense of solution and operational costs are strong limitations.

Analyzing the data acquired by the SVC system, figure 4.7 e) and comparing with the other setups, it is possible to realize that, during PEI and DPPG adsorptions, mechanical and acoustic vibrations were reduced as well as thermal variations. It seems that this system has an adequate chamber volume that supports external inputs. Nevertheless, kinetic curves displayed in figure 4.7 e) are distinct from the other setups due to solution diffusion processes [111].

Table 4.3 displays the final frequency shift achieved after the completion of a PEI/DPPG bilayer for each experimental setup. The PEI/DPPG frequency shift attained by SHO and SHC systems was 141±21 Hz and 154±23 Hz, respectively. These values are much greater than the obtained by the vertical setups, such as de SVO, CVC and SVC, with a final frequency shift of 84±13 Hz, 99±15 Hz and 93±14 Hz, respectively. Thereby, values measured with quartz crystal resonator in the horizontal position present a higher frequency shift than the ones obtained with the vertical arrangement. These results allow us to conclude that, due to gravity force, the vertical alignment of the quartz crystal reduces the measured mass since non-adsorbed molecules are not being weighted.

Table 4.3. PEI/DPPG final frequency shifts measured with Stationary Horizontal Open (SHO), Stationary Horizontal Closed (SHC), Stationary Vertical Open (SVO), Continuous Vertical Closed (CVC) and Stationary Vertical Closed (SVC) experimental configurations.

System Type	Adsorption time (min)		Frequency shift (Hz)
	PEI	DPPG	PEI/DPPG
SHO	3	10	141±21
SHC	3	10	154±23
SVO	3	10	84±13
CVC	10	10	99±15
SVC	10	15	93±14

4.3.2 QCM comparison setups summary

To systematize the comparison between the different experimental configurations setups, a set of qualitative parameters were define, namely the reproducibility, the system sensibility to mechanical and acoustic vibrations, MVS and ACS, respectively, and the influence of temperature variation (TSV). So, if during measurements the oscillator only gets interference when the user is operating the system (e.g. washing the quartz crystal support between adsorptions), the MVS parameter receives the LOW

status; but if in the same conditions, the oscillator responds to any vibration caused by managing items on the working bench, it receives the MEDIUM status; and if it responds to any mechanical vibration produced in the room, HIGH status is assumed for this parameter. The ACS parameter is related to any noise produced during measurements, for example, if the system responds to any sound noise in the room, it receives the HIGH status, but if it only responds to the sound noise near the system, the parameter is classified with MEDIUM status; and if the system does not respond to any kind of sound noise, the parameter receives the LOW status. The qualitative scale associated to temperature is based on temperature change rates, for example, if the system responds to a difference of temperature from 0.5 to 1.0 °C per hour, the TVS parameter is considered HIGH; but if the system only responds between 1.0 and 3.0 °C per hour the parameter is stated as MEDIUM; and if the system doesn't respond to temperature differences between 3.0 and 5.0 °C the parameter receives the LOW status. Reproducibility is a parameter dependent of the previous parameters, i.e., if an experimental configuration receives a HIGH status for the reproducibility parameter thus, all the previous parameters must to be LOW; a MEDIUM reproducibility means that at least two of the previous parameters does not assume the HIGH status; and a LOW reproducibility means that at least two of the previous parameters takes the HIGH status. The quantitative parameter Operational Cost is related to the volume of solution(s) used for QCM measurements and is presented in percentage, being the maximum value of reference equivalent to the adsorption of 20 layers in the SVC system, with a total volume value of 120 ml. The result of the qualitative analysis according with the described above is displayed in table 4.4.

Table 4.4. Comparison between the different tested QCM systems, namely Stationary Horizontal Open (SHO), Stationary Horizontal Closed (SHC), Stationary Vertical Open (SVO), Continuous Vertical Closed (CVC) and Stationary Vertical Closed (SVC) experimental configurations.

System Type	Reproducibility	MVS[i]	ACS[ii]	TVS[iii]	Operational Cost[iv] (%)
SHO	Low	High	High	High	10
SHC	Medium	High	Low	Medium	10
SVO	Medium	Medium	Low	Low	47*
CVC	Medium	Medium	Low	Medium	40
SVC	High	Low	Low	Low	100

[i] Mechanical Vibration Sensitivity; [ii]Acoustic Vibration; [iii]Thermal Variations; [iv] Operational Cost per 20 layers
*In the SVO system the solution change was performed only after 5 adsorbed layers.

4.3.3 Analysis of PEI and DPPG Kinetics

In order to compare the data acquired by the five different experimental setups configurations, PEI and DPPG adsorption kinetics curves were plotted together, as shown in figures 4.8 a) and b), respectively. Comparing the PEI adsorption kinetic curves between the different setups configurations, presented in figure 4.8 a), one can infer that the open systems (SVO and SHO) present larger disturbances in their kinetic curves and therefore are less reliable. In fact, these experimental setups configurations are subjected to changes in the film viscoelastic properties during PEI adsorption and are also affected by temperature fluctuations because they are open systems. PEI frequency shift results obtained by CVC and SHC setups demonstrated that those are more trustworthy systems for polyelectrolytes adsorptions, being more resilient to solutions viscoelastic properties changes, i.e. changes from rigid to soft film, because small amounts of solution to preform measurements are needed, allowing the reduction of the interactions between the adsorbent and the adsorbed. The SVC system showed a smaller PEI frequency shift (25 Hz) then the other systems due to diffusion processes inherent to polyelectrolyte solution injection [111]. After PEI adsorption the rinse procedure leads to an increase of ~10 Hz, see figure 4.7 e), suggesting entrapped water molecules in the film. PEI frequency shift average in solution obtained by Baba and co-workers after 15 minutes of adsorption time was 31.5 Hz [130]. The closed systems (SHC, SVC and CVC) also demonstrated that are less affected by mechanical and acoustic vibrations and by small temperature variations.

Figure 4.8 b) illustrates frequency shift versus time, corresponding to the growth of an adsorbed DPPG layer, obtained by the five different setups. Overall, the SVO, SHO and SHC systems revealed a decrease of the frequency shift after five minutes of DPPG absorption suggesting that desorption took place into some extent or that liposomes have disrupted releasing the entrapped water. However, Morita *et al* proved that even without liposomes volume change, a decrease of the adsorbed mass can be detected when the water sphere deforms [99]. This assumption leads us to suggest that after the adsorption of DPPG vesicles a spatial rearrangement of the vesicles took place affecting the QCM measurements. DPPG kinetic adsorption data acquired by CVC experimental configuration revealed a more stable curve without frequency shift decrease, probably due to the fact that the DPPG continuous flux through the cell gives rise to a decrease in the number of collisions between the liposomes and the PEI cushion combined with the fact that it is a closed circuit and so can avoid thermal fluctuations. In the SVC system the liposomes kinetic immobilization is mainly controlled by two processes, such as diffusion and adsorption due to electrostatic interactions and therefore the DPPG kinetic curves present two stages, as we can see in figure 4.8 b), taking longer than 10 minutes until total adsorption occurs [111]. In this setup configuration, one should take into attention that the diffusion rates increase with the reduction of the particle size increasing the number of collisions between adsorbate and adsorbent [255].

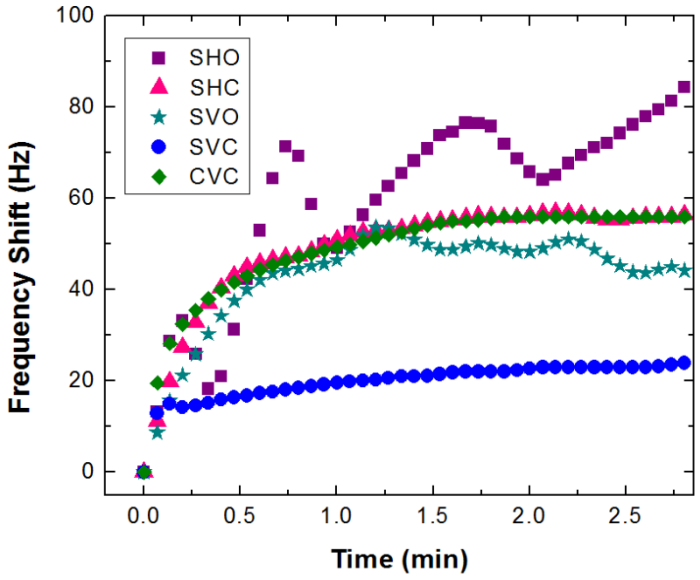

a)

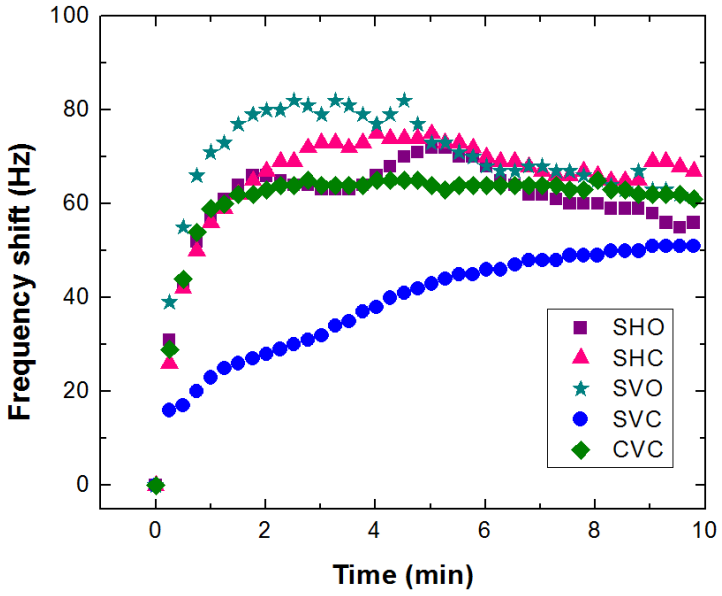

b)

Figure 4.8. Adsorption kinetics curves of a) PEI and b) DPPG measured by Stationary Horizontal Open (SHO) (squares), Stationary Horizontal Closed (SHC) (up triangles), Stationary Vertical Open (SVO) (stars), Stationary Vertical Closed (SVC) (circles) and Continuous Vertical Closed (CVC) (diamonds) systems.

The amount of DPPG adsorbed amount onto PEI polymer cushion, obtained by the SVC QCM system, was calculated from equation 3.1 and a value of 9±1 mg/m^2, corresponding to frequency shift of 53 Hz, was attained. This value is twice the one predicted for a planar DPPG bilayer [256] suggesting the presence of closed DPPG liposomes immobilized on the PEI surface. Since the first layer is the support for the liposomes adsorption, the type of polyelectrolyte used as cushion plays an important role for the anchoring of the subsequent layers and the stability of the whole film. It should be emphasized that the structure of the film is also strongly dependent on the deposition conditions, namely the ionic strength and pH of the solution [257]. At high pHs only a small fraction of amino groups of PEI is charged, approximately 5% of monomer [258, 259] and at pH 9 the PEI ionization degree is ~0.25 presenting a coiled conformation. Electrostatic interactions between the neighboring ionized groups may be disregarded at a low degree of ionization region, i.e. smaller than 0.4 [260]. LbL films assembled with PEI as a precursor layer at high pH are thicker giving a greater robustness to the heterostructure. Thus, the weakly charged PEI is more hydrophobic and promotes the formation of denser layers. It has been demonstrated that an increase of the surface hydrophobicity influences the adsorption phenomena and, consequently, avoids the liposome rupture [111].

Bearing in mind that DPPG suspension used in QCM measurements is sonicated a mean diameter of 25 nm for DPPG vesicles is expectable and a mass amount of 16 mg/m^2 for hexagonal packing vesicles adsorbed onto a flat surface was calculated. Thus a value of 9 mg/m^2 attained from equation 3.1 is smaller than the predicted, suggesting that two situations may have occurred: the PEI surface is not completely filled with intact DPPG liposomes, and/or several vesicles have disrupted releasing the entrapped water. This is in agreement with previous adsorption experiments revealing that the adsorbed amounts are dependent of the adsorbent roughness and the number of pre-adsorbed bilayers [261, 262]. In order to better understand the deposition of each layer and to compare to the obtained QCM data the surface morphology will be analyzed by atomic force microscopy (AFM).

4.3.4 Analysis of topographic surfaces

AFM topographic images with 2x2 μm^2 obtained from Au-coated quartz crystal surface and from PEI and PEI/DPPG LbL films deposited onto the crystal are shown in figure 4.9. Surface profile parameters as root-mean-square roughness (Rq) and kurtosis (Rku) values are displayed in table 4.5. Here, a meaningful difference of Rq values can be found for Au-quartz crystal surfaces before and after the adsorption of a PEI layer, namely of 1.3 nm and 0.5 nm, respectively. These results indicate that when the PEI layer is adsorbed onto the Au-quartz crystal surface, the PEI molecules fill the spaces between the peaks of the gold surface decreasing the surface sharpness, i.e. mesokurtic, with a Rku equal to 3±1. This result is in accordance with Kolasińska [257] who postulated that when the PEI is used as a first layer, it can act as a scaffold making multilayer structures thicker and more stable for treatment in environments at various pHs, with a more homogeneous electronic distribution, providing a more homogeneous and smooth surfaces than those containing strong polyelectrolytes. When the DPPG layer is adsorbed onto Au/PEI layer the Rq value increases from 0.5 to 4 nm,

revealing that liposomes have been adsorbed in an intact closed shape. Furthermore, the Rku also increased revealing a surface with more peaks than valleys [177], which in turn proves the adsorption and the integrity of the DPPG vesicles.

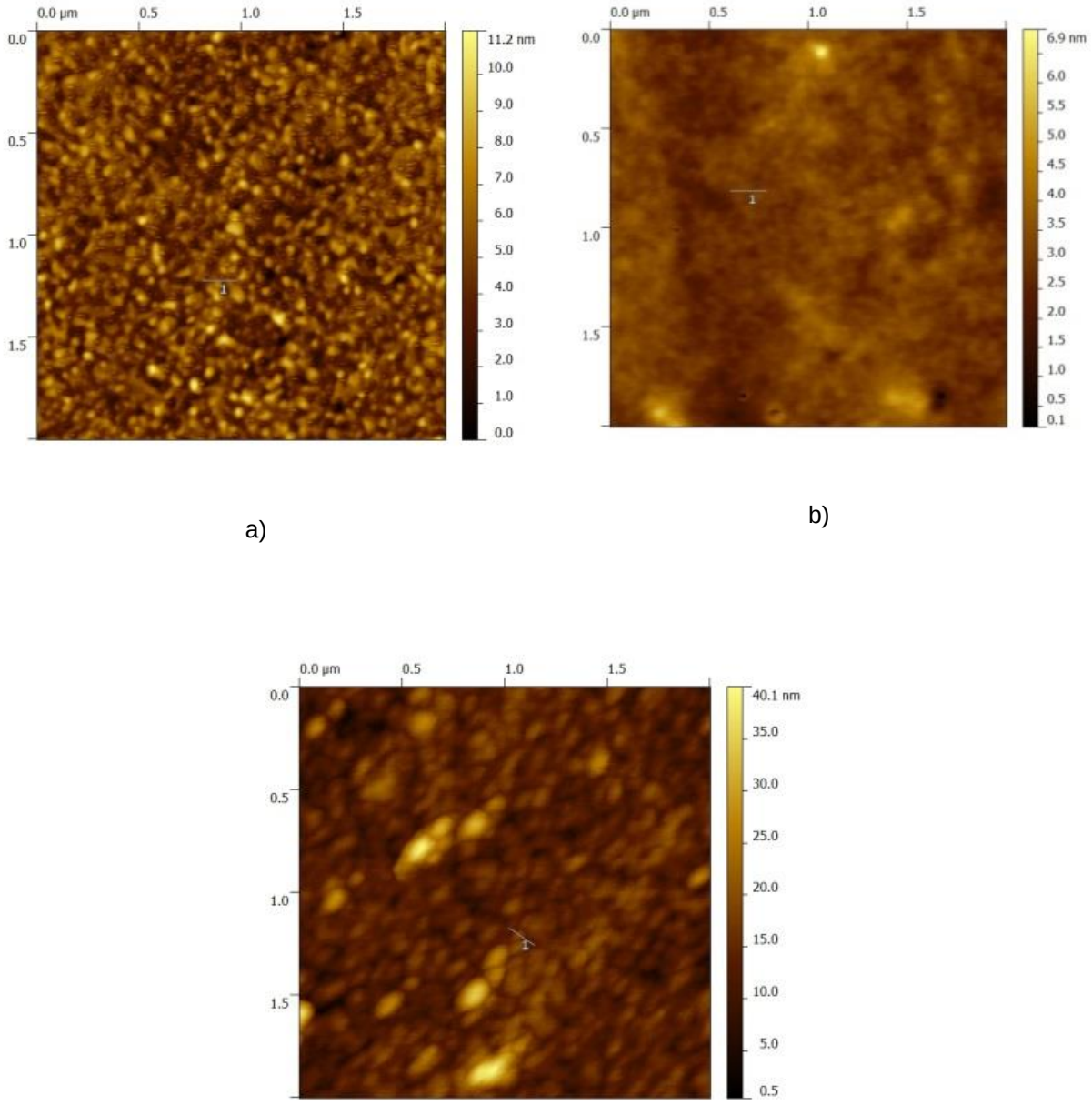

a) b)

c)

Figure 4.9. Topographic images with $2\times2\mu m^2$ area of a) Au-coated quartz crystal, b) Au/PEI and c) Au/PEI/DPPG surfaces.

Table 4.5. AFM 1D statistical parameters of Au-coated quartz crystal, Au/PEI and Au/PEI/DPPG surfaces. Topographic data were obtained from a measured area of 2×2 μm^2.

LbL films	AFM 1D Statistical parameters (rows)							
	Rq (nm)	*Rku*	*Height distribution Gaussian fit parameters*					
			P1 (nm)	*W1 (nm)*	*A1*	*P2 (nm)*	*W2 (nm)*	*A2*
Au	1.3±0.2	3.3±0.7	4.663±0.007	2.42±0.02	0.959±0.007	----	----	----
Au/PEI	0.5±0.2	3±1	3.015±0.002	0.853±0.004	0.988±0.005	----	----	----
Au/PEI/DPPG	4±1	4±2	13.01±0.02	5.73±0.04	0.90±0.02	20±2	10±2	0.09±0.03

Rq – root-mean-square roughness; Rku – Kurtosis; P1 – peak 1 position; W1 – width peak 1; A1 – peak 1 area; P2 – peak 2 position; W2 – width peak 2; A2 –peak 2 area.

The height profiles with 160 nm of scan length obtained from 2×2μm^2 surface images of Au, Au/PEI and Au/PEI/DPPG were plotted together and are displayed in figure 4.10. The profile of the DPPG layer, with a width and height values of approximately 60 nm and 30 nm respectively, presents larger roundish features than the mean diameter determined by DLS, 25 nm.

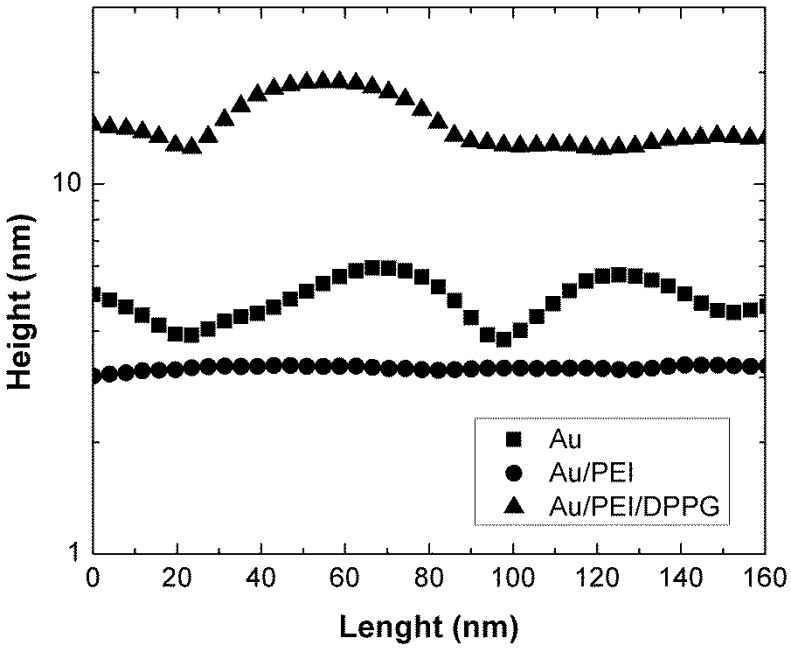

Figure 4.10. Profiles obtained from 2×2μm^2 surface images of Au (squares), Au/PEI (circles) and Au/PEI/DPPG (up triangles).

The height distribution curves achieved for the three analyzed surfaces are displayed in figure 4.11. The plots were fitted with Gaussian curves and the obtained parameters are displayed in table 4.5. Concerning to the height distributions of Au and PEI surfaces only one peak centered at 4.663±0.007 nm and 3.015±0.002 nm, respectively, was found. After the deposition of PEI onto Au substrate there

is a small reduction of the height confirming the observed Rq roughness decrease. Regarding to the height distribution of the DPPG layer, two peaks, slightly smaller than the nominal vesicles diameter, centered at 13.01±0.02 nm and 20±2 nm were obtained. This evidence suggests two situations: i) liposomes are immobilized in a close packed way, so that AFM tip is only probing the upper parts [263]; however and taking into account that the DPPG adsorption attained by the QCM data was smaller than the theoretical expected leads us to believe that a large fraction, approximately 50%, of the DPPG vesicles have disrupted, forming lipid bilayers, and thus releasing the water entrapped; ii) because the weakly PEI polyelectrolyte underlayer is hydrophobic, but also smooth, after DPPG vesicles immobilization they flattened due to nearly absence of interactions.

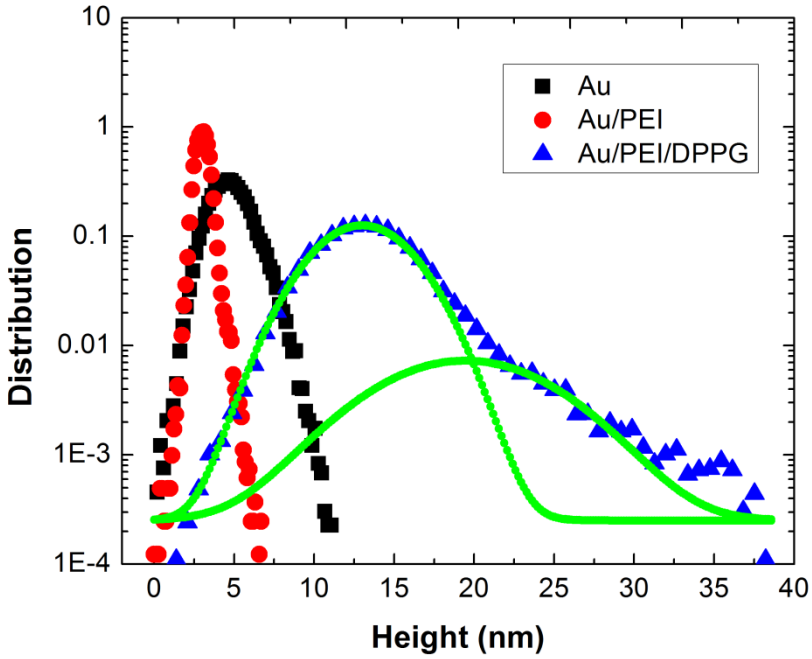

Figure 4.11. Height distribution of Au (squares), Au/PEI (circles) and Au/PEI/DPPG (triangles) obtained from the AFM images. The respective Au/PEI/DPPG height distributions Gaussian fits are represented in green.

The calculated surface statistical parameters obtained from AFM topographic images have supported the kinetics data obtained by the SVC QCM system. Summarizing, PEI and DPPG adsorptions were proved by the differences attained in Rq and Rku values before and after solutions deposition. In addition, the height distribution parameters are consistent with DPPG liposomes adsorbed on PEI surface in a close packed form. The possibility of having DPPG lipid bilayers or vesicles slightly flattened on PEI surface cannot be discarded, which explains the much lower DPPG adsorbed amount achieved during QCM measurements.

Regarding to the purpose of this study, the comparison between the five different QMC experimental configurations allowed us to conclude that both SVC and CVC systems are the more reliable setups to be use in LbL films assembly *in situ* using polyelectrolytes and liposomes aqueous solutions. Nevertheless, it must be taken into account that the SVC system has inherent diffusions processes,

precluding kinetic curves comparison between both systems. For further studies of LbL films growth with a large number of bilayers, the SHC setup will be the system selected because small amounts of solution are needed and requires less time is requirement to perform the measurements, but we cannot discard the fact that this system requires a meticulous operationalization in order to QCM measurements derive successfully.

4.4 Growth analysis of PEI/DPPG LbL films

Taking into account the previous studies where it has been suggested that the breaking of DPPG liposomes after immobilization on PEI polyelectrolyte layer is probably due to low roughness surface; the buildup of LbL films with DPPG extruded vesicles interspersed in PEI layers was implemented onto a rough polyelectrolyte multilayers (PEM) cushion in order to avoid liposomes rupture. As described above the assembly of a LbL film with a great number of bilayers, in this case $(PEI/DPPG)_{10}$, was executed using the SHC QCM system.

4.4.1 $(PAH/PSS)_{10}$ LbL Film Cushion

The analysis of QCM data cushion associated to $(PAH/PSS)_{10}$ LbL film, prepared to prevent the rupture of the extruded DPPG liposomes, revealed a frequency shift of 248 Hz. Despite the exponential build-up of this film, a mean value for the adsorbed amount per unit area per bilayer of 4.4 mg/m^2 was calculated using the equation 3.1. This value, obtained for the $(PAH/PSS)_{10}$ LbL film prepared from aqueous solutions without salt, is in accordance with literature for LbL films assembly prepared in aqueous solutions with 0.5 M of salt, where a value of 6 mg/m^2 mass amount per PAH/PSS bilayer was attained [264]; since a high salt concentration origin a high adsorbed amount. Surface topographies measured by AFM, indicate Rq values of 4±1 nm for $(PAH/PSS)_2$ LbL films [265]. Such result allows us to conclude the roughness value is relatively small when compared with the size of liposome which should take an average value of 120 nm [91].

4.4.2 Growth of the $(PEI/DPPG)_{10}$ LbL films

A $(PEI/DPPG)_{10}$ LbL film was assembled onto $(PAH/PSS)_{10}$ polyelectrolyte multilayer. The growth of the LbL heterostructure was monitored by QCM using the SHC setup and the frequency shift (ΔF) plotted as a function of time is shown in Figure 4.12 (a). LbL film growth can be characterized by plotting the accumulated ΔF as a function of the number of layers or bilayers. Figure 4.12 (b) shows the accumulated frequency for PEI, DPPG and PEI/DPPG layers during assembly. The analysis of these plots points toward a typical LbL film growth, where the roughness of the substrate has an influence in the adsorbed amounts as demonstrated by [262, 266]. In fact, the adsorbed amount increases exponentially until the 4^{th} bilayer followed by a linear growth.

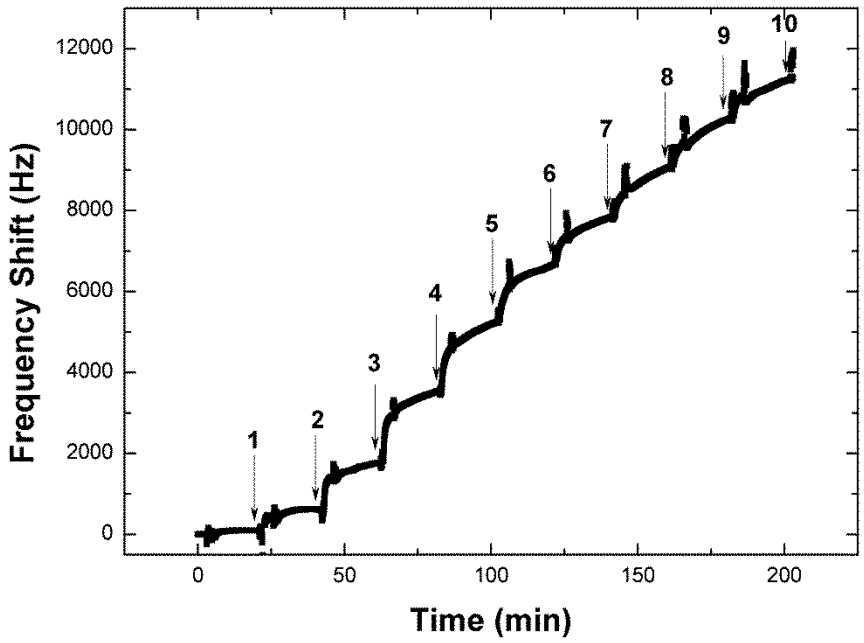

a)

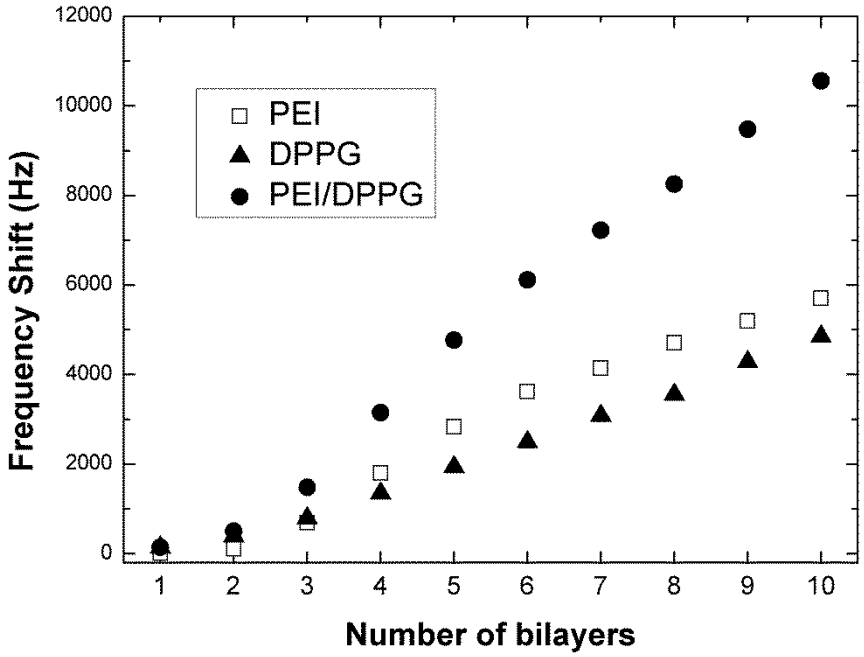

b)

Figure 4.12. a) QCM frequency shift due to the successive adsorption of PEI/DPPG bilayers with water rinsing between deposition steps. b) Accumulated frequency shift of the assembly of ten PEI (open squares), DPPG (up triangles) and PEI/DPPG layers (circles).

The adsorbed mass per unit of area for each PEI, DPPG and PEI/DPPG deposited layers was calculated using equation 3.1 and the results as a function of number of bilayers are displayed in figure 4.13. Analyzing this figure, it is found that the adsorbed amount of DPPG increases until the 4th bilayer where it reaches a saturation point, attaining to a constant value of mass adsorbed of 103±14 mg/m^2. This finding suggests that different processes occur when DPPG layers are being attached to the surface since it takes diverse adsorbed mass values until reach saturation.

The adsorbed amounts for DPPG lipid bilayer and close-packed layer with liposomes with 120 nm of diameter were calculated in order to compare with the experimental values. Assuming that one DPPG lipid bilayer is adsorbed on the crystal surface, the DPPG adsorbed amount per unit of area should take a value of 5.5 mg/m^2. This value was calculated taking into account that the DPPG molar mass is 744.96 g/mol and considering condensed lipids where the hydrophilic area of the phospholipid molecule head is ~45 Å^2 [267]. This means that about 5.9x10^{14} DPPG molecules should be adsorbed on the crystal surface which gives an adsorbed amount of 5.5 mg/m^2. Kasemo *et al* have found a value of ~5mg/m^2 for 1-Palmitoyl-2-oleoyl-*sn*-glycero-3--phosphocholine (POPC) lipid bilayers adsorbed onto silica-coated quartz crystals [268]. Considering a DPPG liposome layer immobilized on the same surface in a close-packed spheres model one can find a value of 77 mg/m^2. The experimental adsorbed amounts for each DPPG layer can now be compared with these theoretical values.

During first DPPG layer adsorption, an adsorbed amount of about 24 mg/m^2 was attained indicating a higher value than for a single lipid bilayer. Thus, two reasons can lead to this adsorbed value: i) some of DPPG liposomes adsorbed on the PEI surface disrupt and spread in the surface while others are intact increasing the surface roughness. Israelachvilli *et al.* [67] demonstrated that isolated vesicle rupture is rare. However, the coexistence of ruptured and intact liposomes adsorbed on MgF_2 was observed in [269]; ii) it was observed that after washing, the first PEI adsorbed layer, the QCM frequency increases 42 Hz indicating that PEI and cushion molecules were removed. This trend, that originated an increase of the film roughness, was already observed by Lvov *et al.* [270]. The ablation of molecules from the surface can also create both positive and negative islands, where DPPG liposomes can or cannot be adsorbed. Both reasons prompt to a roughness increase which can now create conditions to adsorb a higher amount of PEI. This sequence is repeated until the 4th bilayer, where the surface is prepared to adsorb a DPPG maximum amount due to liposomes organization. Afterwards, the structural rearrangement of liposomes creates conditions to surface roughness decrease with subsequent reduction of the PEI adsorbed amount, for the next two bilayers where the PEI mass attains to a constant value, as shown in figure. 4.13. When DPPG adsorbed amount is maximum, i.e. reaches to the saturation point, it means that liposomes are in close-packed spheres and, consequently the surface roughness becomes higher than the cushion roughness leading to a greater PEI adsorbed amount for these deposited layers. However, it is expected that after the 5th bilayer the layers become more homogeneous than the first which is in opposition with the found by Warsynski *et al.* [271]. They demonstrate that the inner structure of the LbL films formed with PEI as an anchor is more homogeneous and therefore less rough. The mass amount attained for the DPPG

after the 5th layer is higher, 103±14 mg/m^2, than the predicted theoretically, 77 mg/m^2. One of the main reasons could be the fact that QCM measurements were made using the SHC setup, in which higher values of adsorbed mass are achieved because the quartz crystal resonator is disposed at the horizontal, as already been discussed in the previously section. However, more advanced adsorption kinetic treatments need to be performed in order to find the processes that are occurring during the assembly of the $(PEI/DPPG)_{10}$ LbL film.

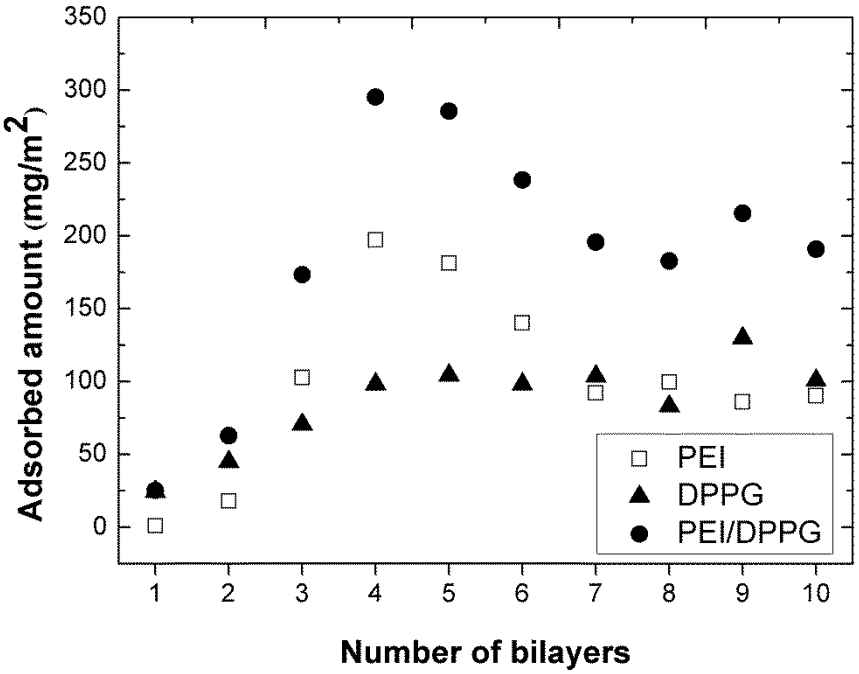

Figure 4.13. Adsorbed amount of PEI and DPPG layers and PEI/DPPG bilayers plotted as a function of the number of bilayers.

4.4.3 DPPG adsorption kinetics

In order to study DPPG adsorption kinetics, QCM frequency shifts of each DPPG layer were plotted as time function. As an example, figure 4.14 shows the kinetic curve of the first DPPG layer. This adsorption kinetic curve points to the combination of two different adsorption processes. This is in accordance with several adsorption kinetic studies on LbL films which follows the general equation [16]:

$$\Gamma = \Gamma_1\left(1 - exp(-t/\tau_1)\right) + \Gamma_2\left(1 - exp(-(t/\tau_2)^{n_{JMA}})\right) \quad (4.1)$$

where Γ is the amount adsorbed per unit area, Γ_1 and Γ_2 are constants representing the maximum amount adsorbed during each process, τ_1 and τ_2 are the characteristic times of the processes, respectively, and n_{JMA} is the exponent of the variable time value that relates to the type of adsorption that occurs in the film. The DPPG adsorption kinetic plots were fitted with this equation maintaining n_{JMA}

equal to the unit. One possible explanation for these two processes can be the adsorption of liposomes during the first stage (first process), followed by adsorption and rearrangement of the adsorbed liposomes on the surface, corresponding to the second process. The parameters obtained from fitting the DPPG kinetic curves reveal that the maximum adsorbed amount associated to the process with shorter characteristic time takes a mean value of 14±3 mg/m^2 with a mean characteristic time of 24±4 seconds. However, the process for larger times (second process) revealed that both maximum adsorbed amount and characteristic time are dependent of the number of bilayers already adsorbed.

The characteristic times behavior is easily observed by plotting τ_1 and τ_2 as a function of the number of bilayers (Inset of Fig. 4.14). As we can see in the inset of figure 4.14, the time required to the second process is lower in first and second DPPG deposition layers, greatly increasing in third and fourth layers, and then decreasing to a constant value. This variation suggests some structural rearrangement and relaxation after the liposomes adsorption in the 3rd and 4th layers.

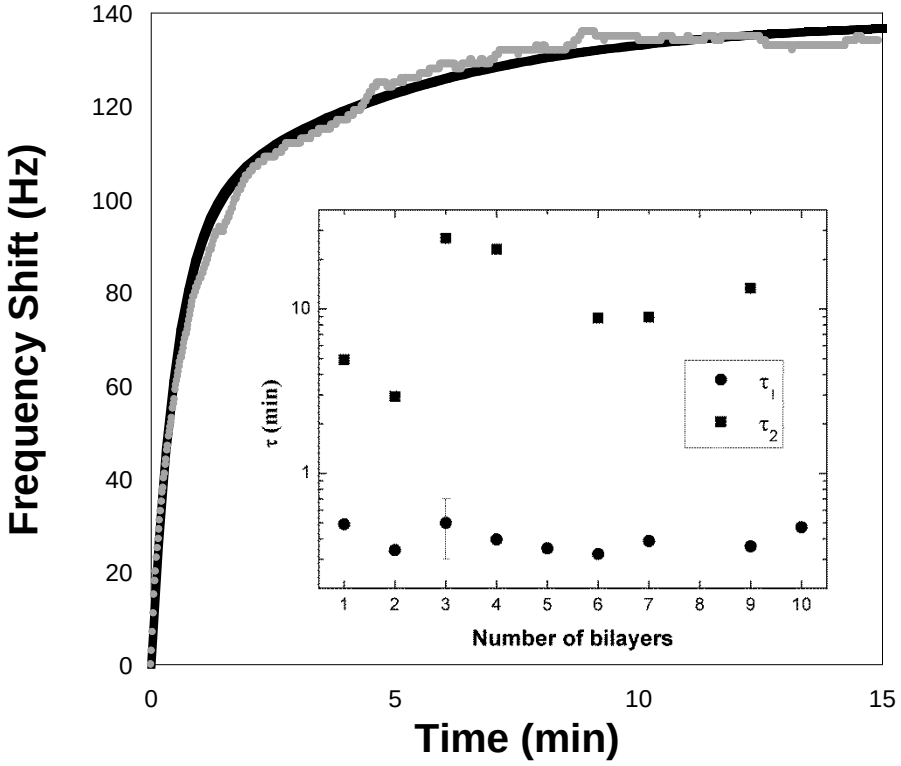

Figure 4.14. Adsorbed amount of DPPG-liposome on a LbL film $(PAH/PSS)_{10}$/PEI as a function of immersion time. The first-order kinetics showed a characteristic time of 0.49 minutes and the second process showed a characteristic time of 4.7 minutes. The inset shows τ (min) of the first (circles) and second (squares) order kinetics as a function of bilayers number.

This result is in accordance with the proposed model of adsorbed amount increase associated to surface roughness growth. However, it is difficult to define all changes that are arising, because adding a new layer onto liposomes already immobilized causes deformations in the previous one. It should be referred that the DPPG maximum adsorbed amount of 103±14 mg/m^2 is higher than the value calculated to a close-packed spheres model in somewhat due to the viscoelastic properties of liposomes, related to the fact that they are structures substantially larger and less compacted subject to greater deformation [83], and also because QCM measurements were made using the SHC setup. Figure 4.15 outlines the proposed model for the $(PEI/DPPG)_6$ LbL film adsorption onto a rough polyelectrolyte cushion.

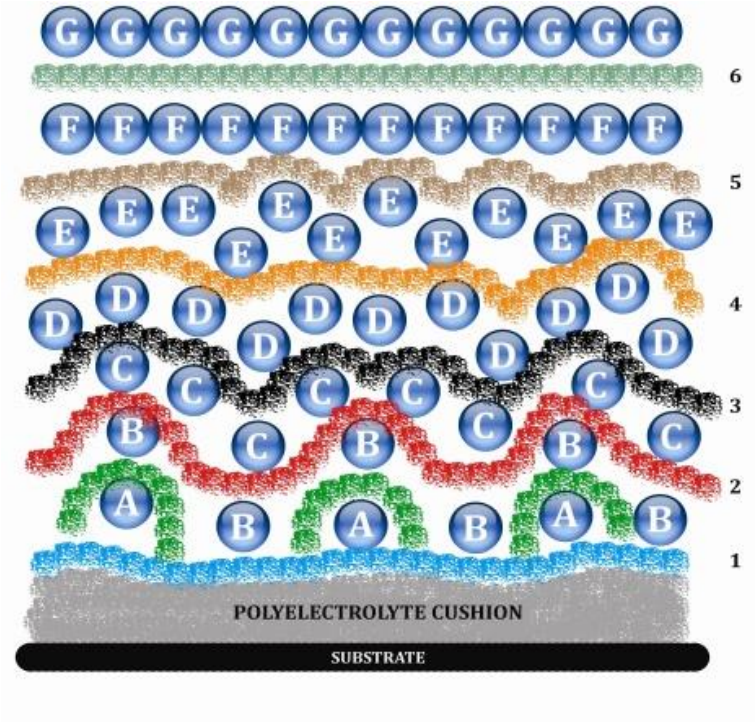

Figure 4.15. Schematic representation of the adsorption of $(PEI/DPPG)_6$ LbL film onto a rough polyelectrolytes cushion. The numbers correspond to the PEI successive layers adsorbed and the letters are concerned to the DPPG liposome layers adsorbed.

The QCM data analysis allowed to infer that DPPG adsorbed amount is dependent of the number of bilayers already adsorbed, increasing from 24 mg/m^2 in the first bilayer to a constant value of 103±14 mg/m^2 after the 4th bilayer. This dependence was interpreted by the roughness evolution with the number of bilayers which increases until a maximum and after that decreases to a constant value. Kinetic curves reveal that the DPPG adsorption is justified by two processes, one which is associated to adsorption of DPPG liposomes with a small constant time independent of the bilayers number and another depending on the number of bilayers, associated to a structural rearrangement of DPPG liposomes on surface.

4.5 Growth analysis of PAH/DPPG LbL films

In order to test the adsorption of DPPG liposomes onto a smooth planar surface a $(PAH/DPPG)_{10}$ LbL film was build-up onto a silicon surface. This assembly was monitored by vacuum ultraviolet (VUV) spectroscopy and the adsorbed amounts of DPPG and PAH layers were determined. To our knowledge this is the first report of VUV measurements for DPPG liposomes, which also served to verify possible damage of prolonged UV irradiation on DPPG-containing LbL films, with the implications for biological systems. The characterization of the PAH/DPPG LbL films was complemented by AFM. Furthermore, XPS analysis was carried to better understand the inner structure of the PAH/DPPG and PEI/DPPG LbL films.

4.5.1 VUV characterization of DPPG and PAH molecules

To our knowledge, there are no VUV studies for DPPG or any other phospholipid in condensed or gas phases. For the sake of comparison, we first obtained the VUV absorption spectra of DPPG and PAH cast films which were fitted with Gaussian curves as indicated by the solid green curves in the figures. Gaussian curves were chosen because they provide the best fits to the experimental data. The inset in Figure 4.16 a) shows an absorbance spectrum for a DPPG cast film, prepared with a suspension obtained by extrusion. The spectra of DPPG and PAH cast films are shown in Figure 4.16 b), to be used as comparison with the spectra of LbL films containing the two components. Since the PAH film was cast onto a quartz substrate, the spectrum was measured only down to 160 nm. The peak positions and Full Width at Half Maximum (FWHM) obtained in the fitting are listed in table 4.6. The error were obtained from the fitting.

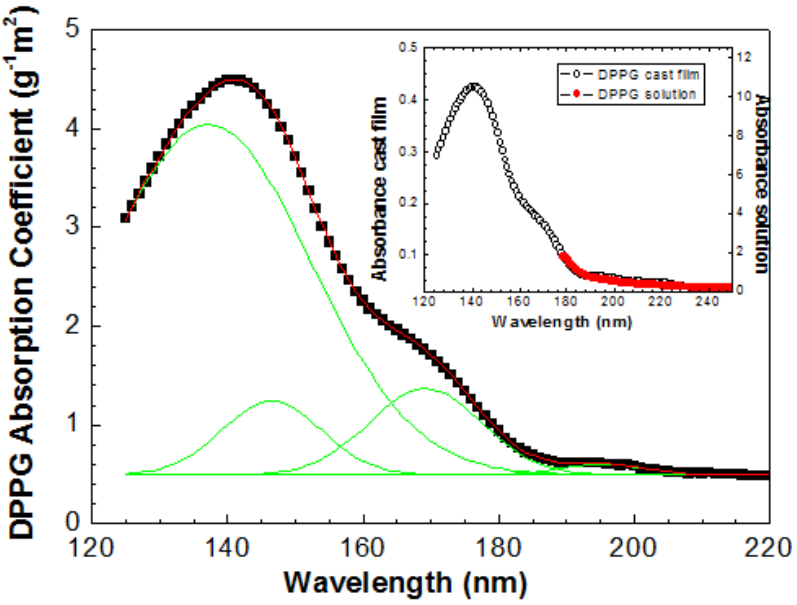

a)

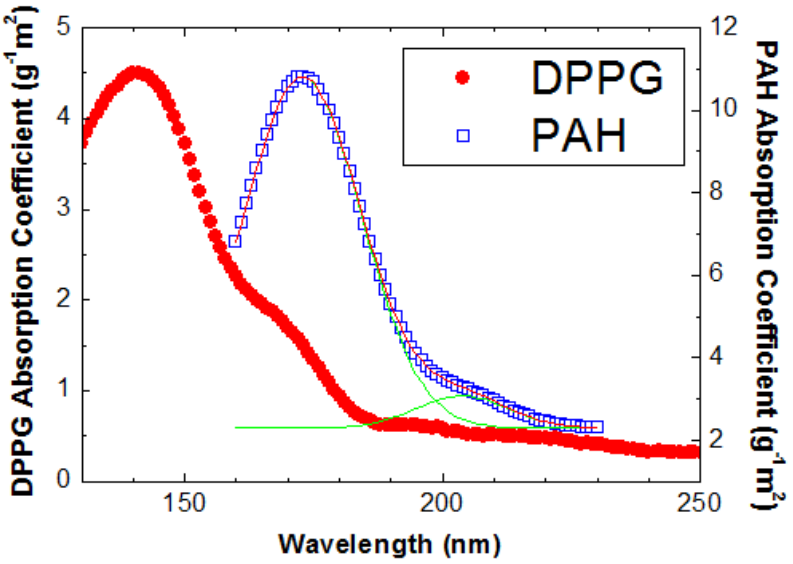

b)

Figure 4.16. a) Absorption coefficient spectrum obtained from VUV absorption measurements for a DPPG cast film. Green curves depict the fitting of the absorption spectrum with Gaussian curves with bands at 138.2±0.4 nm, 145.8±0.4 nm, 169.8±0.3 nm and 192±2 nm. In the inset is shown the VUV spectra of DPPG cast film and of DPPG dispersion. b) Absorption coefficient spectrum obtained from VUV absorption measurements for DPPG and PAH cast films. The green lines correspond to the fitting of PAH spectrum with Gaussian functions with bands at 172.9±0.1 nm and 203.8±0.8 nm.

The smallest peak for the DPPG cast film at 194.4±0.7 nm (6.38±0.04 eV) is assigned either to the $n_O \rightarrow \pi^*_{CO}$ transition from the lone-pair on the carbonyl oxygen to the antibonding π_{CO}-valence orbital [272, 273] and to the valence shell electronic excitations of hydroxyl groups [274-278]. For the peak at 168±3 nm (7.38±0.09 eV) several assignments are possible: i) $n'_O \rightarrow \pi^*$ transitions, where n'_O is the second lone pair orbital on the carbonyl group oxygen [272]. ii) $n_O \rightarrow \sigma*$ transition in the carboxyl group, from the atomic orbital n (ground state) to the antibonding σ -valence orbital [272, 273]. iii) $n_O \rightarrow \sigma^*$ transition due to the promotion of an electron from the highest filled molecular orbital to an antibonding orbital (σ^*_{O-H}), which normally appears from 165 to 200 nm (6.2-7.5 eV) [274]. iv) water dissociation [279]. The peak at 147.2±0.2 nm (8.424±0.009 eV) is assigned to the phosphate group [273, 280, 281]. The strongest peak at 138.2±0.8 nm (8.97±0.03 eV) is ascribed to $\pi_{C=O} \rightarrow \pi^*_{CO}$, where a valence transition from the bonding π orbital to the antibonding π-valence orbital occurs [272, 273]. The amount of DPPG in the film can be estimated from the VUV spectrum, but this requires a precise measurement of film thickness, which is hampered by the non-uniformity of the cast film. Therefore, in a control experiment we obtained the VUV spectrum of a 5 mM aqueous solution of DPPG. The measurement was performed only up to 170 nm owing to the use of aqueous solutions [279]. The absorption coefficients were estimated by assuming that DPPG molecules absorb similarly in the liquid and in cast films, which is justified by the similarity in the spectra for the film and solution, as shown in the inset of figure 4.16 a). Using the Lambert-Beer law, the DPPG absorption coefficient at 180 nm was calculated from DPPG solution spectra. This absorption coefficient calculated from the DPPG solutions spectra was then used for the DPPG cast films, from which the absorption coefficients could be calculated for small wavelengths, as displayed in Figure 4.16 a). DPPG absorption coefficient curve was fitted with four Gaussians which allows one to calculate the partial absorption coefficients, ε_p, at peak position by considering the maximum absorbance of the peak. These values are displayed in Table 4.6. As the PAH spectrum was not measured for small wavelengths, the partial absorption coefficient (ε_{p138nm}) of 3.7±0.4 g^{-1} m^2 calculated for the maximum absorption peak at 138 nm for DPPG allows us to determine the adsorbed amount of DPPG in LbL films. The absorption coefficients, ε, at peak position are also listed in table 4.6.

Using the VUV spectra of PAH aqueous solutions and the Lambert-Beer law, the PAH absorption coefficient spectrum was calculated and shown in Figure 4.16 b). Absorption from the nitrogen group was expected according to the literature, as excitation energies below 8 eV have been found for ammonia [282-285] and amine [283-287] molecules. The spectrum for the PAH cast film could be fitted with two Gaussian curves, as shown in figure 4.16 b), whose parameters are given in table 4.6. The more intense peak at 172.9±0.1 nm (7.172±0.004 eV) is assigned to electronic $n_N \rightarrow 3pa$ transitions from the lone-pair electrons on nitrogen to nitrogen atomic-like orbitals [283, 287]. This peak is superimposed onto another at 203.8±0.8 nm (6.08 eV) in figure 4.16 b) which can be assigned to the $n_N \rightarrow 3sa$ [283, 287, 288] transitions. The partial absorption coefficients for the peaks at 173 nm and 204 nm were estimated as 8.51±0.02 and 0.77±0.01 g^{-1} m^2, respectively, while the absorption coefficients attain 10.81±0.02 and 3.33±0.02 g^{-1} m^2 values, respectively.

Table 4.6. Peak position and FWHM parameters for the peaks obtained from fitting the VUV spectra and corresponding assignments of DPPG and PAH cast films and PAH/DPPG LbL films. The absorption coefficients (ε) and partial absorption coefficients (ε_p) were calculated for each peak position.

Peak parameters for VUV data of DPPG cast film				**Literature**	**Assignment**	
Peak Position (nm/eV)	**FWHM (nm)**	**ε_p ($g^{-1}m^2$)**	**ε ($g^{-1}m^2$)**	**Peak Position (eV)**	**Electronic Transition**	**Functional Group**
138.2±0.4 /8.97±0.03	31.8±0.3	3.7±0.4	4.42±0.02	8.4[a] 8.5[a,b]	$\pi_{C=O} \rightarrow \pi^*_{CO}$	Carboxyl
145.8±0.4 /8.50±0.02	13±1	0.50±0.05	4.24±0.02	8.5[c]	----	Phosphate
169.8±0.3 /7.30±0.01	14.5±0.6	0.66±0.07	1.70±0.02	7.7[a] 7.1[a,b] 7.4[d] 6.2-7.5[e] ;7.8[a,b]	$n'_O \rightarrow \pi^*$ ---- $n_O \rightarrow \sigma^*$	Carboxyl Hydroxyl Hydroxyl/carboxyl
192±2/6.46±0.07	34±5	0.17±0.02	0.61±0.02	5.8[a,b] 6.2-7.5[e] 6.4[f]	$n_O \rightarrow \pi^*_{CO}$ $n_O \rightarrow \sigma^*$	Carboxyl Hydroxyl
Peak parameters for VUV data of PAH cast film				**Literature**	**Assignment**	
Peak Position (nm/eV)	**FWHM (nm)**	**ε_p ($g^{-1}m^2$)**	**ε ($g^{-1}m^2$)**	**Peak Position (eV)**	**Electronic Transition**	**Functional Group**
172.9±0.1/7.172±0.004	22.9±0.2	8.51±0.02	10.81±0.02	8.19[g,h] 7.14[g] 7.01[g] 7.1[i, j] 7.0[i, j] 7.927[k]	n_N – 3pa	Amine
203.8±0.8/6.08±0.05	18±2	0.77±0.01	3.33±0.02	6.4[g] 6.51[h] 5,77[g] 5.83[g], 5.7[i] 5.8[i], 6.0[j], 6.392[k] , 6.56[l]	n_N - 3sa	Amine
Peak parameters for VUV data of DPPG/PAH LbL film				**Literature**	**Assignment**	
Peak Position (nm/eV)	**FWHM (nm)**	**ε_p ($g^{-1}m^2$)**	**ε ($g^{-1}m^2$)**	**Peak Position (eV)**	**Electronic Transition**	**Layer**
136±2/9.12±0.07	28±3	3.7±0.4	---	8.4[a] 8.5[a, b]	$\pi_{C=O} \rightarrow \pi^*_{CO}$	DPPG
147.2±0.2/8.424±0.009	13±2	0.50±0.05	---	8.5[c]	----	DPPG
168±3/7.38±0.09	18±3	---	---	7.7[a] 7.1[a, b] 7.4[d] 6.2-7.5[e] 7.8[a, b] 8.19[g,h],7.14[g] ,7.01[g] 7.1[i, j]7.0[i, j],7.927[k]	$n'_O \rightarrow \pi^*$ ---- $n_O \rightarrow \sigma *$ n_N – 3pa	DPPG PAH
194.4±0.7/6.38±0.04	15±2	---	---	5.8[a, b] 6.2-7.5[e] , 6.4[f] 6.4[g], 6.51[h] 5,77[g] 5.83[g] , 5.7[i] , 5.8[i] 6.0[j] , 6.392[k], 6.56[l]	$n_O \rightarrow \pi^*_{CO}$ $n_O \rightarrow \sigma^*$ n_N - 3sa	DPPG PAH

[a]Reference [273]. [b]Reference [272]. [c]Reference [280]. [d]Reference [279]. [e]Reference [274]. [f]Reference [275]. [g]Reference [286]. [h]Reference [282]. [i]Reference [287]. [j]Reference [283]. [k] Reference [284]. [l] Reference [288].

4.5.2 PAH/DPPG LbL Films

The VUV spectra for PAH/DPPG LbL films are shown in figure 4.17 a), which were fitted with four Gaussian curves, as indicated in the inset. Since DPPG has four and PAH has two components, these fitting points are the result of the overlapping of PAH and DPPG peaks. Taking into account the assignments above for DPPG and PAH molecules, one can assign the peaks for PAH/DPPG LbL films as follows: those at 194.4±0.7 nm and 168±3 nm are due to both types of molecules while the other peaks are only due to DPPG. With peaks associated with only one type of molecule (DPPG in this case), it is possible to use the VUV data for the films to estimate the adsorbed amount of DPPG, and then ascribe the remainder to PAH. Table 4.6 gives the parameters from these fittings and the assignment to electronic transitions in each bilayer and type of molecule.

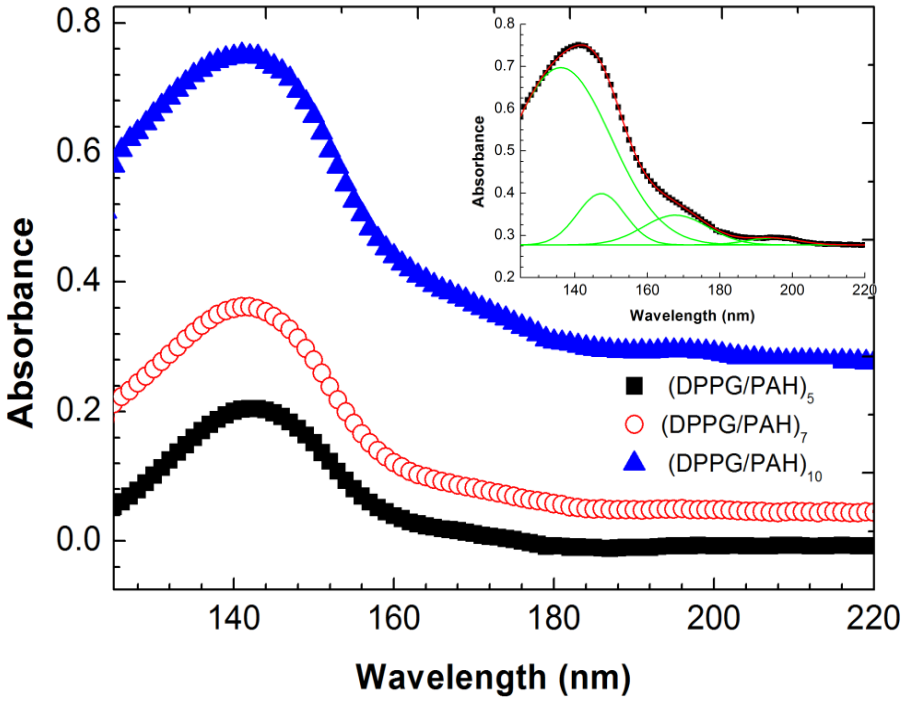

a)

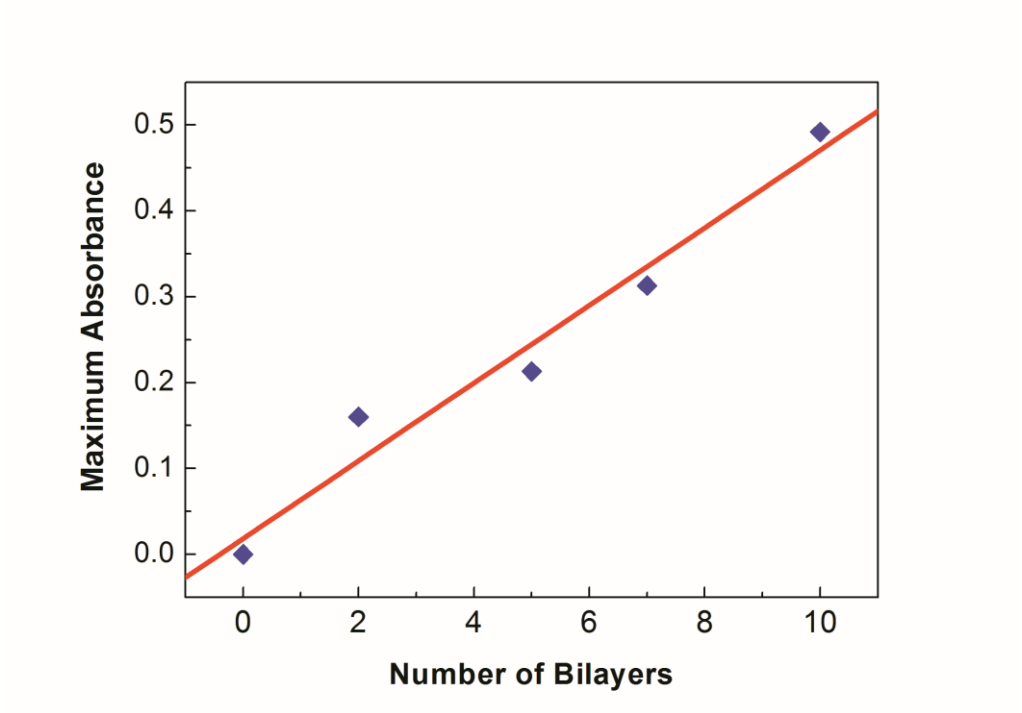

b)

Figure 4.17. a) VUV Absorption spectra for LbL PAH/DPPG films with distinct numbers of bilayers. In the inset is shown the VUV spectrum of the $(PAH/DPPG)_{10}$ film. The green lines in the inset indicate the fitting with Gaussian functions, with bands at 136±2 nm, 147.2±0.2 nm, 168±3 nm and 194.4±0.7 nm. b) Maximum absorbance (142 nm) with baseline correction versus the number of bilayers in the PAH/DPPG LbL film.

The adsorbed amount per bilayer can be estimated because the PAH/DPPG LbL films grow linearly with the number of bilayers, as indicated in Figure 4.17 b) for the maximum absorbance with baseline correction. This is in accordance with results by Constantino *et al* [289, 290] who measured the conventional UV-Vis absorption spectra of DPPG/PAH LbL films, and found that the absorbance at 200 nm increased linearly with the number of bilayers. This linear growth is due to adsorption processes governed by electrostatic interactions between NH_3^+ groups from PAH and PO_4^- groups from DPPG without significant increase of roughness. These interactions are sufficiently strong to break the liposomes adsorbed on each layer, as we shall see from the adsorbed amounts calculated below from the VUV spectra data. The amount of DPPG adsorbed per bilayer was calculated by taking the intensity of the 136±4 nm peak in the VUV spectra for PAH/DPPG LbL films, since it is due only to adsorption of DPPG molecules (Table 4.6). From the absorbance intensity using the Lambert-Beer law, one obtains the adsorbed amount per layer per unit area (Γ_{DPPG}) using the partial absorption coefficient at 138 nm calculated from aqueous solutions and cast films in figure 4.16 a):

$$\Gamma_{DPPG} = \frac{Abs_{p138\,nm}}{2\varepsilon_{p_{138\,nm}}} \tag{4.2}$$

The factor 2 in the denominator appears because the PAH/DPPG film was deposited on both sides of the substrate. The mass of a DPPG adsorbed layer per unit area was calculated 6±1 mg/m^2 per layer, as shown in table 4.7, corresponding to 3.8×10^{18} (=2×1.9×10^{18}) molecules/m^2. This is a reasonable value if one considers that the surface density of DPPG molecules in a Langmuir monolayer is 2.1×10^{18} molecules/m^2 [237, 289-292]. The latter density was obtained for a condensed monolayer with surface pressure of 30 mN/m and mean molecular area of 45 Å^2. The good agreement indicates that the vesicles collapsed forming a lipid bilayer in the LbL film, which would lead to a mass of 5.5 mg/m^2, which is very closed to the measured value of 6±1 mg/m^2. Moreover, this value is totally in accordance with the DPPG amount per unit of area adsorbed onto a PAH layer of 4.93±0.09 mg/m^2 measured by QCM [111]. The amount of PAH adsorbed can be calculated from the absorbance at 168 nm peak, for which both DPPG and PAH molecules contribute, since the adsorbed amount of DPPG was already calculated, by using a simple absorbance values relation:

$$\Gamma_{PAH} = \frac{\frac{Abs_{168\,nm}}{2} - \Gamma_{DPPG} \times \varepsilon_{DPPG168nm}}{\varepsilon_{PAH168nm}} \tag{4.3}$$

where Γ_{PAH} is the adsorbed amount per layer per unit area, Abs_{168nm} is the absorbance at 168 nm per bilayer and the $\varepsilon_{PAH168nm}$ and $\varepsilon_{DPPG168nm}$ where the absorption coeficients at 168 nm of PAH and DPPG, respectively. Using the absorption coeficients at 168 nm presented in Figure 4.17 a), Γ_{PAH} was estimated as ~ 0.9 mg/m^2, consistent with 0.4 mg/m^2 obtained by Baba *et al* [130] for a dried PAH layer measured with a quartz crystal microbalance.

Table 4.7. Properties of PAH/DPPG LbL films, where Γ is the adsorbed amount per layer.

Layer	**Γ (mg/m^2)**	**Γ from literature (mg/m^2)**	**Molecules(or monomers) per Area (m^{-2})**	**Roughness (nm)**
DPPG	6±1	5.5 (lipid bilayer)	3.8×10^{18}=2×1.9x10^{18} (Langmuir layer =2.1×10^{18} [287-290, 293])	0.3[i)]
PAH	~0.9	0.4 [1]	9×10^{15}- 12×10^{15}	---

[i)] Measured by atomic force microscopy.

Because the LbL films were dried in between the adsorption process for each bilayer and submitted to vacuum, changes may have occurred in the adsorbed amounts and in the surface roughness [181]. In order to better analyze the DPPG layer, its surface morphology after drying was characterized by atomic force microscopy.

4.5.3 Surface Characterization of a DPPG layer

The surface of one bilayer PAH/DPPG film adsorbed onto silicon substrate was characterized by AFM. A topographic image in Figure 4.18 a) points to a quasi-flat surface with a root-mean-square roughness (Rq) of only 0.3 nm. The values of 3.24 and 20.9 for Skewness and Kurtosis functions, respectively, obtained from a statistical and frequency analysis of the topographic data, indicate that the surface has more peaks than valleys. The valleys can be explained by adsorption of liposomes on the PAH surface which were then ruptured and formed a lipid bilayer. In these regions the roughness was lower than the average for the whole sampled area. The valleys are surrounded by regions (peaks) that are two-bilayer thick, then leading to one-bilayer thick peaks in the AFM image of figure 4.18 b). The unfolding of liposomes to form lipid bilayers was proposed by Reimhult *et al.* [169]. The sites where liposomes were adsorbed could be determined from the distance between peaks varying from 80 to 150 nm and from 200 to 300 nm in figure 4.18 b). The largest diameters correspond to twice the original diameter of the extrused liposomes, suggesting that the entire liposome spreads on the substrate. It should be referred that AFM topographies of DPPG cast films revealed intact liposomes. The small valleys with the dimensions of twice liposome diameter, see figure 4.18 b), are surrounded by several peaks caused by an increased roughness when liposomes at the edges do not have space to spread completely into a bilayer or even to surface irregularities due to PAH adsorption. This explanation is consistent with models [67, 77, 169] for the formation of supported lipid bilayers onto solid substrates. An important requirement for the rupture of DPPG liposomes is a high adhesion strength between PAH and DPPG regions, which is expected as the PAH molecules were almost fully ionized for the film fabrication at pH 4 [129].

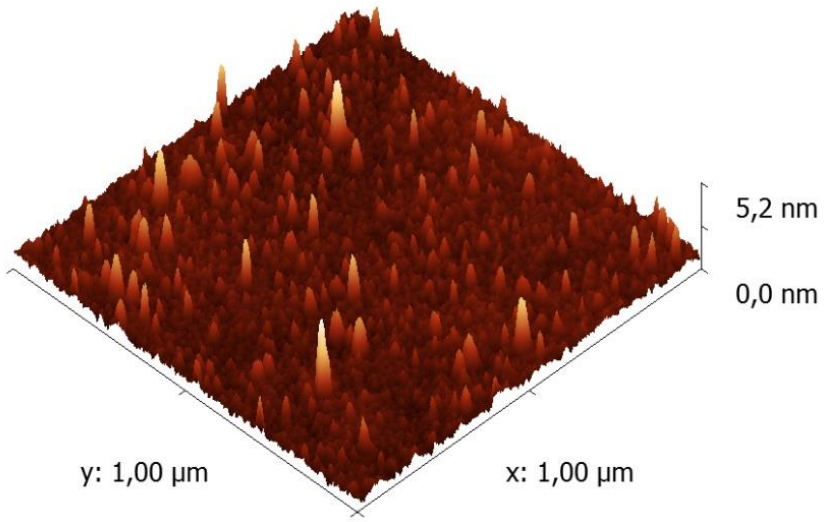

a)

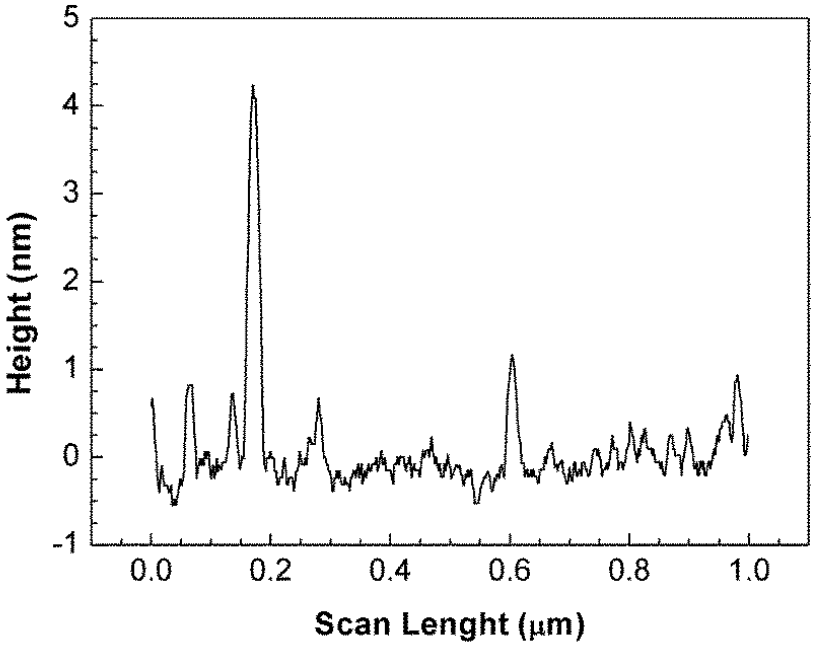

b)

Figure 4.18. a) AFM topographic image and b) A topographic profile of a 1-bilayer PAH/DPPG LbL film.

4.5.4 Effects from ultraviolet (UV) irradiation on a PAH/DPPG film

Since UV irradiation is known to affect biological systems, with effects being noted at the molecular level for cell membrane models, we verified whether damages on the PAH/DPPG LbL films could bring artifacts to the VUV data. No significant changes were noted in the spectra upon irradiating the films with UV at a fixed wavelength (140 nm) during one hour, as shown in figure 4.19. This result allows us to conclude that the VUV technique can be used for characterization of this type of heterostructures since the measurements were performed with the samples in vacuum and no noticeable damage caused by radiation occurs for the duration (ca. 20 min.) of the experiment.

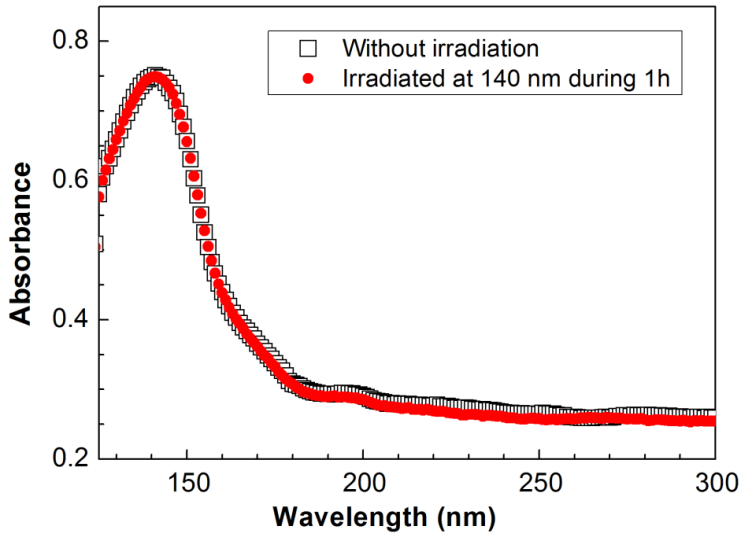

Figure 4.19.VUV spectra of a $(PAH/DPPG)_{10}$ biomimetic membrane before and after being irradiated at 140 nm during 1 h in vacuum.

4.5.5 XPS characterization of $(PAH/DPPG)_5$ and $(PEI/DPPG)_5$ LbL films

The $(PAH/DPPG)_5$ and $(PEI/DPPG)_5$ XPS spectra taken at a take-off angle of 0◦ and 60◦ of relative to the surface normal revealed the presence of carbon (C), oxygen (O), nitrogen (N) and phosphorous (P). Atomic percentages of these elements and respective binding energies (BEs) are summarized in table 4.8.

Both samples were fitted with three peaks in C 1s regions assigned to an aliphatic carbon, a carbon single bonded to an oxygen (C-O) or to a nitrogen (C-N), and a carbon bonded to oxygen through a double bond (C=O), respectively, from lower to higher BEs [213]. O 1s region of PEI/DPPG LbL film exhibit three components centered at 531.4, 532.6 and 535.0 (± 0.2) eV at a take-off angle of 0°. The first one is assignable to an oxygen single bonded to a phosphate and to a carbon and the oxygen double bonded to a carbon [213] and the third to water molecules aggregates entrapped in the film [6, 253]. At a take-off angle of 60° the BE of this third peak is higher. The second peak is assignable to a carbon linked to an oxygen by a single bond [213]. For PAH/DPPG LbL film at O 1s region could only be fitted with one peak centered at 532.2 eV. This finding is due to some constraints during the plots fitting however, it may reflect a different position of the polar head of the DPPG phospholipids and also the absence of water inside the heterostructure. Figure 4.20 shows the O 1s XPS spectra obtained at a take-off angle of 0° for both samples, where a clearly shift to higher BE is observable for the $(PEI/DPPG)_5$ LbL film due to the contribution of water molecules in the heterostructure. The region of the P 2p of both samples comprises one doublet. The most intense component P $2p_{3/2}$ centered at 133.2 ± 0.2 eV is typical of a phosphorous with a neighborhood rich in oxygen [254]. The N 1s spectrum is adjustable, for $(PEI/DPPG)_5$ LbL films, with three components centered at 399.1±0.2, 400.9±0.3 and 402.3±0.5 eV assignable, respectively, to imine (N), amine (NH) and to ionized nitrogen

[253], but only two peaks centered at 399.7±0.2 and 401.5±0.1 eV where found for the $(PAH/DPPG)_5$ LbL films with analogous correspondence for the two last PEI/DPPG assignments.

Table 4.8. Element composition in percentage and the respective Binding energies (eV), obtained from XPS spectra taken at 0◦ and 60 °of ejection relative to the normal surface of $(PAH/DPPG)_5$ and $(PEI/DPPG)_5$ LbL films. Relative error not exceed ±10%.

	$(PAH/DPPG)_5$				**$(PEI/DPPG)_5$**				**Assignment**
	Atomic (%)		**BE (eV)**		**Atomic (%)**		**BE (eV)**		
	0°	**60°**	**0°**	**60°**	**0°**	**60°**	**0°**	**60°**	
C 1s1	53.2	58.1	285.0	285.0	56.0	67.8	285.0	285.0	C-C, C-H
C 1s2	9.9	8.1	286.6	286.5	13.6	8.7	286.3	286.6	C-O, C-N
C 1s3	3.7	3.6	288.7	288.5	3.3	2.1	288.7	288.8	O=C-O
O 1s1					4.4	2.9	531.0	531.0	O-P, O=C
O 1s2	27.8	19.2	532.2	532.2	8.0	6.8	532.6	532.5	O-C
O 1s3					0.4	0.2	535.0	535.7	Water
N 1s1					6.1	4.3	399.1	399.0	N-C
N 1s2	0.5	0.6	399.7	399.6	1.6	1.1	400.9	400.6	N-H
N 1s3	1.8	1.4	401.5	401.5	0.3	0.5	402.3	401.7	N^+
P $2p_{3/3}$	2.0	6.0	133.4	133.6	4.2	3.7	133.2	133.1	P-O
P $2p_{1/2}$	1.0	3.0	134.3	134.4	2.1	1.8	134.1	134.1	P-O
[P]/[N]	1.3	4.5			0.77	0.91			
[N^+]/[Ntotal]	0.78	0.72			0.20	0.19			

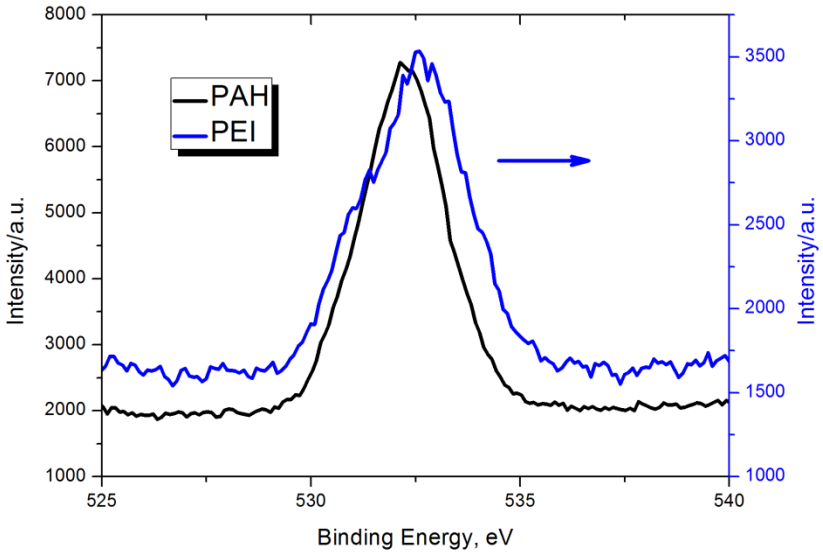

Figure 4.20. O 1s XPS spectra obtained at 0◦ of incidence for PAH/DPPG and PEI/DPPG LbL films.

Quantitative analysis can offer information about the inner structure of LbL films. The $(PAH/DPPG)_5$ LbL film atomic ratio [P]/[N] increases significantly from 0° to 60° reflecting the fact that we are dealing with a highly stratified heterostructure and a flat uniform lipid bilayer is covering the entire surface. On the other hand, the $(PEI/DPPG)_5$ LbL film presents atomic ratio [P]/[N] which slightly increases from 0° to 60° indicating that interdigitation is taking place and probably both situations, closed liposomes and lipid bilayers exist on the heterostructure. Previous studies (see section 4.3), have shown the frequency shift of sonicated liposomes when deposited onto a PEI surface and a value of ~50 Hz was obtained by QCM using the SVC system. This value can be converted in mass per unit area using the equation 3.1, where a value of ~9 mg/m^2 for a DPPG layer adsorbed on PEI is achieved. However, this value is lower than the 16 mg/m^2 predicted by theoretical calculations for a hexagonal close packing spheres adsorbed onto the quartz crystal. This difference suggests that after the DPPG liposomes immobilization on surface, vesicles disruption starts to happen leading to a release of the water molecules from liposomes, but it can also express some flattening of the liposomes on the surface. The ratio [N+]/[Ntotal] allows quantifying the ionization degree for both polyelectrolytes in the film. A higher value of net electrical charge for films prepared with PAH was found, pointing to stronger PAH/DPPG electrostatic interactions which contribute to vesicles rupture after the deposition. Therefore, two main questions arise from this result: *Is the PEI low ionization degree contributing to the adsorption of intact DPPG liposomes and will it be enough to create a biological heterostructure totally covered by liposomes with entrapped water? Although the PAH surface is highly ionized if the surface roughness is incremented is it possible to adsorb closed DPPG vesicles?* So far it is known that when the surface hydrophobicity increases that allows the counterions anchorage near the ionic groups and then electrostatic forces become lower [253], leading to a release of water molecules from surface. Recently, Herminghaus *et al* [294] demonstrated theoretically that some self-affine profiles of rough surfaces can induce hydrophobicity. Hence, for truly realize the DPPG liposomes dynamic growth during and after adsorption, more studies of polymer cushions surfaces properties must be taken in order to better characterize such heterostructures.

4.6 Conclusions

Aqueous dispersions of DPPG small unilamellar vesicles (SUVs) produced by two different processes such as extrusion and sonication were characterized by DLS. DPPG sonicated liposomes showed a polymodal distribution, however, after a careful analysis, a mean hydrodynamic diameter of 25 nm was considered for the most SUVs. The dispersion with extrused SUVs showed a monomodal distribution with a mean hydrodynamic diameter of 169±3 nm. Though, this value was considered to be much higher than the expected because extrusion procedure was performed with polycarbonate membranes with a pore diameter of 100 nm. DPPG cast films produced with extrused vesicles were analyzed by optical and spectroscopies techniques. Topographic images of the DPPG cast films probed by AFM allowed to understand that when vesicles are immobilized on smooth surface they break and spread all over originating a lipid bilayer. Nevertheless, and due to the fact that we were dealing with a concentrated suspension, this process is repeated until the entire surface is covered by

more lipid bilayers levels contributing to the increase of the surface roughness leading to the adsorption of intact SUVs on top. The integrity of the vesicles was confirmed by SEM. By combining these optical techniques, a mean diameter of 120 nm was found for DPPG vesicles produced by extrusion. The absorption spectra in the infrared region of cast films have shown the vibration levels corresponding to the chemical bonds of the DPPG molecules. The cast films were also characterized by XPS technique which has enable to calculate the atomic percentages of the detected elements such as carbon, oxygen, sodium and phosphorous and the respective binding energies that were assigned to the organic groups of the DPPG phospholipid molecules, confirming the FTIR assignments. The FTIR and XPS techniques have detected the presence of structural water on the cast films considered to be storage in the sealed DPPG liposomes.

Five different QCM experimental configurations were addressed to study the adsorption kinetics curves in liquid phase measurements, taking into account parameters such as mechanical vibration, acoustic vibrations and thermal fluctuations. Analysis of the kinetics curves of PEI polyelectrolyte and DPPG liposome revealed that horizontal modes create conditions to a higher frequency shift, due to the measurement of non-adsorbed molecules which are deposited on the quartz crystal caused by gravity force and to an increase of the kinetic curves instability of the measurements as a result of a fostering noise due to the mechanical vibrations. The vertical (CVC and SVC) systems proved to be more reproducible presenting much less instability in their kinetic curves.

Calculations for a close-packed DPPG liposome layer adsorbed onto the quartz crystal resonator showed that the DPPG mass amounts adsorbed onto PEI layer, attained by the SVC setup should be higher. Statistical analysis of the amplitude parameters calculated from AFM topographic images of PEI and PEI/DPPG LbL film surfaces have justified the measurement of a lower amount of DPPG showing that this weak and smooth polyelectrolyte layer creates conditions to the adsorption of intact flattened DPPG vesicles probably neighboring lipid bilayers domains.

After QCM improvements at solid/liquid interface, this technique was used to monitor the growth of a $(PEI/DPPG)_{10}$ LbL film onto a rough polyelectrolyte cushion. The results demonstrated that PEI and DPPG adsorbed amounts are in function of the number of bilayers already adsorbed, suggesting that the initial roughness of the surface controls the quasi-equilibrium adsorbed amount. The smaller mass amounts attained for the first DPPG layers suggests the following statements: i) a few intact vesicles are adsorbed while others spread on surface; and ii) by the fact that after PEI layer adsorption, rinse process leads to desorption of PSS molecules from the cushion, with the consequently formation of positive and negative charged surface islands where DPPG molecules can or cannot adsorb. Both cases lead to an increase of the surface roughness creating conditions to higher adsorbed amount for the next layers. Hence, it is expected that along the growth $(PEI/DPPG)_{10}$ LbL film, the roughness increases until a maximum, afterwards decreasing to a constant value which explains the DPPG and PEI adsorbed amount values. Therefore, it is expected that the last DPPG layers have a higher level of organization. The adsorption kinetic curves treatment has attested that the liposomes adsorption is governed by two processes. The first process, with adsorbed amounts and characteristic time parameters independent of the number of bilayers, is associated to fast adhesion of liposomes onto surface. The second is related to reorganization of liposomes and present characteristics times and

adsorbed amounts dependent of the number of bilayers. The high values found for the adsorption characteristic times parameters for this second process is an indicative of liposomes organization.

VUV measurements of DPPG in aqueous solutions and in cast and LbL films were reported. From the spectra we could assign the electronic transitions responsible for the light absorption and determine the amount of DPPG adsorbed on LbL films with PAH. Significantly, the adsorbed amounts pointed to adsorption as a lipid bilayer, which means that the DPPG liposomes have broken after the adsorption process. The final structure of the LbL films was reflected on the film topography investigated with AFM, for the images showed terraces with thicknesses again corresponding to lipid bilayers. The LbL films were not affected by prolonged UV irradiation in the absence of water molecules indicating that the VUV technique can be used for characterization of lipid heterostructures. We therefore propose VUV spectroscopy as a new powerful tool for LbL film characterization which we hope will be useful in, among others, cell membrane modeling and drug delivery studies based on phospholipids. It was shown that the surface roughness influences the adsorption of DPPG liposomes onto surfaces covered by an electrically charged PAH polyelectrolyte layer giving rise to its rupture or maintenance of its integrity. Low roughness was shown to induce liposome rupture while high roughness induces adsorption of whole liposomes.

XPS spectra of PAH/DPPG LbL films revealed that the PAH layer cushion is greatly ionized which promotes DPPG vesicles rupture and a polymer-supported phospholipid bilayers is formed, giving rise to a highly stratified heterostructure; while the XPS spectra of PEI/DPPG LbL film demonstrated that the lower ionization degree PEI has contributed to the adsorption of intact DPPG vesicles with entrapped water.

5 STORAGE OF WATER MOLECULES ON LbL FILMS

This chapter presents a thorough discussion of the dynamic processes occurred when DPPG liposomes are adsorbed on smooth and rough PEM surfaces, in order to understand the role of the surface roughness to maintain water molecules storage inside the intact vesicles with the aim of such heterostructures being used for application in sensors. Surface topographies of PEMs and PEMs/DPPG were characterized and models for adsorption and evolution of the growth surfaces are proposed. A statistical analysis of thin films morphologies is offered in terms of roughness amplitude and power spectral density (PSD) parameters. PSD curves were fitted with different models in order to obtain information about correlation lengths and mean grain size of the features, scaling exponents, fractal dimension and growth mechanisms. A detailed description of DPPG liposomes rupture phenomena onto surfaces with different values of roughness, i.e. surfaces prepared with a different number of polyelectrolyte layers, with the capacity to promote or to avoid this process is also reported. Adsorbed amounts and specific kinetic characteristic parameters of DPPG liposomes onto these different surfaces are presented and the adsorption phenomena of the liposomes inferred.

5.1 Adsorption of intact DPPG liposome layer on rough polyelectrolyte multilayers (PEMs)

The PEI/$(PSS/PAH)_5$ polyelectrolyte multilayer (PEM) cushion, comprising a last layer electrically charged, was assembled onto Au-quartz crystal resonators aiming to adsorbed and immobilize closed liposomes. The DPPG adsorption was supervised *in situ* by QCM using the SVC setup. AFM topographic images of PEM and DPPG surfaces were acquired *ex situ* and the 1D statistical parameters were analyzed in order to infer if confined vesicles were immobilized onto a PAH rough layer.

5.1.1 QCM measurements

The DPPG liposome adsorption kinetic curves were obtained by QCM at solid/liquid interface using the SVC experimental configuration. The QCM gives the oscillation frequency variation as a function of immersion time and using equation 3.1 it is possible to convert frequency shift in adsorbed amount per unit of area [112]. DPPG suspension, obtained by sonication, was adsorbed on PEI/$(PSS/PAH)_5$ cushion, assembled *ex situ* onto Au-quartz crystal support by the LbL technique, and the frequency variation of DPPG suspension adsorption was recorded with an appropriate software. Figure 5.1 shows the DPPG liposome adsorption kinetic curve onto this cushion.

The DPPG adsorption kinetic curves were fitted with equation 4.1 maintaining n_{JMA} equal to the unit [112]. However, in the present case, the kinetic curve can only be adapted to one exponential, meaning that only one adsorption process is taking place. The adsorption characteristic time and the maximum adsorbed amount per unit of area parameters found from are 22.05±0.03 minutes and 40±3 mg/m^2,

respectively. The existence of a unique adsorption process can be easily explained by two motifs: i) this kinetic curve was obtained after adding a concentrated DPPG liposome suspension into the QCM holder cell with the PEM+crystal already plugged and filled with ultrapure water. In the first seconds the DPPG vesicles do not adsorb onto PEM, since they are obliged to spread in the QCM holder cell and only then the adsorption occurs. This means that the nucleation process, common in LbL films literature [16, 295] is omitted, occurring only the diffusion process; ii) liposomes adsorbed onto PEM maintain the structural integrity. When the vesicles rupture occurred during the adsorption process, mechanisms such as adhesion, disruption, spreading and fusion of lipid membranes will be present and the kinetic curves will have more than one process [67].

The DPPG total adsorbed amount obtained by QCM suggests that liposomes should have a diameter of 60 nm, which is far from the mean value of 25 nm found by DLS measurements for the hydrodynamic diameter of DPPG liposomes, results showed in section 4.1. Assuming a compact distribution of spherical vesicles with 25 nm of diameter, it is expected to find 16 mg/m^2 of adsorbed amount per unit of area which is about a half of the experimental value. This result suggests that the surface morphology of PEM and of DPPG liposomes adsorbed on PEM should be carefully analyzed since a high roughness leads to a higher DPPG adsorbed amount.

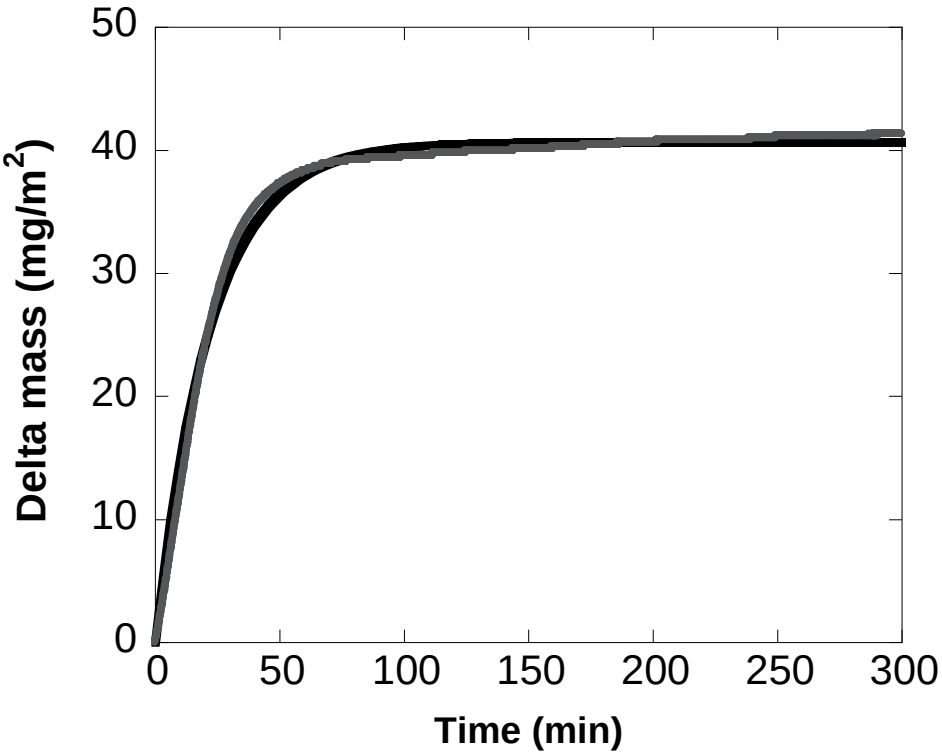

Figure 5.1**.** Adsorbed DPPG-liposome amount on a LbL film PEI/(PAH/PSS)$_5$ as a function of immersion time (grey) and the fit (black) obtained using equation 4.1, where n_{JMA} is equal to the unit.

.

5.1.2 AFM characterization

AFM topographic images showing surface morphologies of 2x2μm^2 scan area obtained from PEI/(PSS/PAH)$_5$ and PEI/(PSS/PAH)$_5$/DPPG LbL films are shown in Fig. 5.2. Surface profile parameters as root-mean-square roughness (Rq), correlation length and skewness were calculated and the obtained values are displayed in table 5.1.

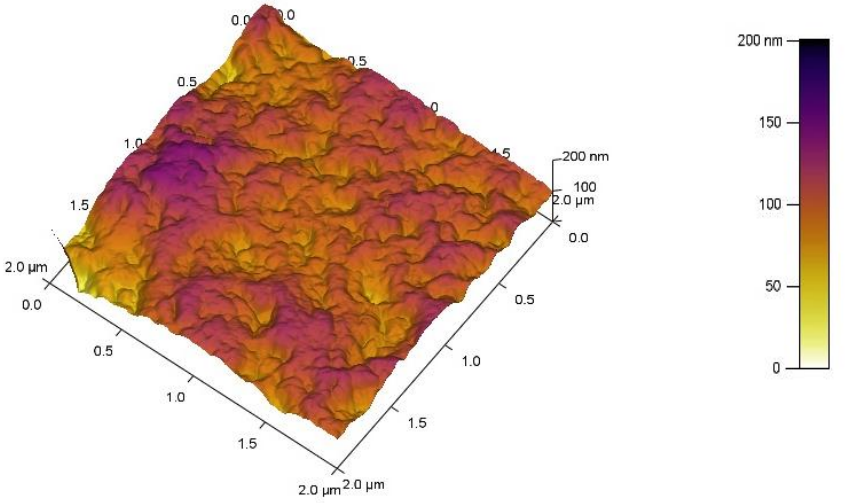

a)

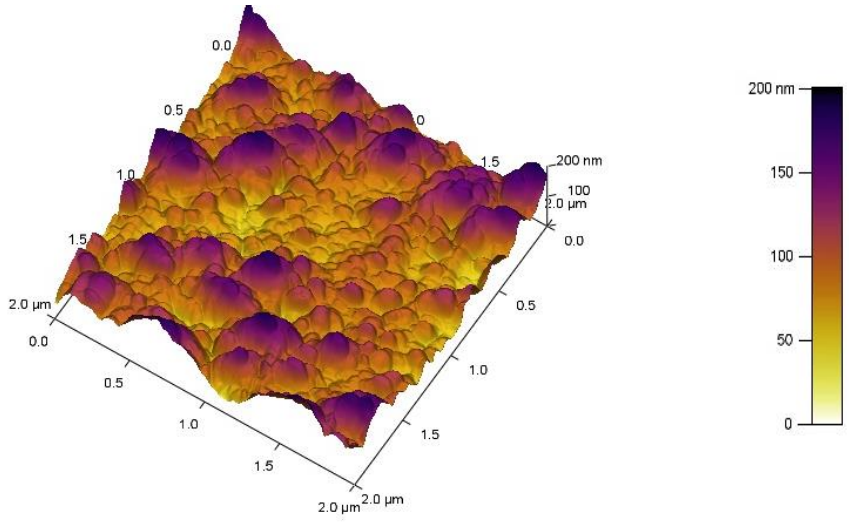

b)

Figure 5.2. AFM 3D topographic images of 2x2μm2 areas obtained from the a) template PEI(PSS/PAH)$_5$ and b) PEI(PSS/PAH)$_5$/DPPG LbL films.

Rq values reveal that when liposomes adsorbed on the rough cushion, roughness surface increases meaning that liposomes are immobilized in an intact form. Moreover, in the present case the roughness of the PEM surface is an order of magnitude plus than the values measured for the smooth PAH cushion, where the liposomes disrupted creating a supported-polymer phospholipid bilayer.

The correlation length indicates the distance that shows the position of the neighbors. Moreover, points of the surface profile that are separated by more than a correlation length may be considered as uncorrelated. The correlation length of PEM/DPPG has a small value than PEM; this indicates a random liposome distribution on the surface, according to the Langmuir adsorption model which usually has a first kinetic order curve as it was found in figure 5.1.

Skewness (Rsk) is the third moment of profile amplitude probability density function and is used to measure the profile symmetry about a mean line. When the height distribution is symmetrical, Rsk is zero. If the height distribution is asymmetrical, and the surface has more peaks than valleys the Skewness moment is positive, and if the surface is more planar and valleys are predominant, the Skewness is negative. As we can see in Table 5.1, the PEM has a negative Rsk and the PEM/DPPG has a positive Rsk, demonstrating that the valleys of the PEM are filled with DPPG liposomes.

Statistically analyzing figure 5.2 b) and measure the profile diameter of the intact liposomes, a mean diameter of 55 nm can be calculated. This value reveals that the adsorbed liposomes can be flattened if we compare it with DLS measurements.

In fact, grain size measurements of PEM/DPPG topographies indicate that the small grains (78%) have a mean width of 55±19 nm while the bigger (22%) have a value of 129±44 nm. The later suggests that some liposomes are aggregated.

Valuable information can be obtained also from the height distribution curves obtained from topographic data of the two surfaces which are plotted in figure 5.3. Both distribution plots were fitted with Guassian curves and the obtained characteristics peaks are displayed in table 5.1. In PEM height distribution one can see two types of characteristics heights, one with a value of 69±2 nm and other with 80.1±0.5 nm. These values justify the DPPG adsorbed amount per unit of area measured by QCM since the adsorption area is significantly higher than the quartz crystal surface which is used in the theoretical adsorbed amount calculation. The height distribution associated to PEM/DPPG reveals the presence of three structure types, while the data can be fitted with three Gaussian curves, namely 32.2±0.3 nm and 42.4±0.07 nm assigned to liposome mean diameter and 69±2 nm indicating that the original structure is maintained after adsorption of the liposome layer. The decrease of the mean heights in the case of PEM/DPPG surfaces indicates that the vesicles are adsorbed in the PEM valleys as already have been demonstrated by skewness values.

Table 5.1. AFM statistical parameters obtained from topographic images of PEI/(PSS/PAH)$_5$ and PEI(PSS/PAH)$_5$/DPPG surfaces with 2x2μm^2 scan area.

LbL films	AFM 1D Statistical parameters (rows)											
	Rq (nm)	*T (nm)*	*Rsk*	*Height distribution Gaussian fit parameters*								
				P1 (nm)	*W1 (nm)*	*A1*	*P2 (nm)*	*W2 (nm)*	*A2*	*P3 (nm)*	*W3 (nm)*	*A3*
PEM	13±5	297±3	-0.3±0.4	69±2	24±1	0.8±0.1	80.1±0.5	16±2	0.2±0.1	---	---	---
PEM/ DPPG	26±5	128±2	0.8±0.3	32.2±0.3	13.7±0.8	0.10±0.02	42.43±0.07	28±1	0.38±0.05	69±2	58±3	0.53±0.05

PEM – PEI/(PSS/PAH)$_5$; Rq – root-mean-square roughness; T – correlation length; RSk – Skewness; P1 – peak 1 position; W1 – width peak 1; A1 – area peak 1; P2 – peak 2 position; W2 – width peak 2; A2 – area peak 2; P3 – peak 3 position; W3 – width peak 3; A3 – area peak 3.

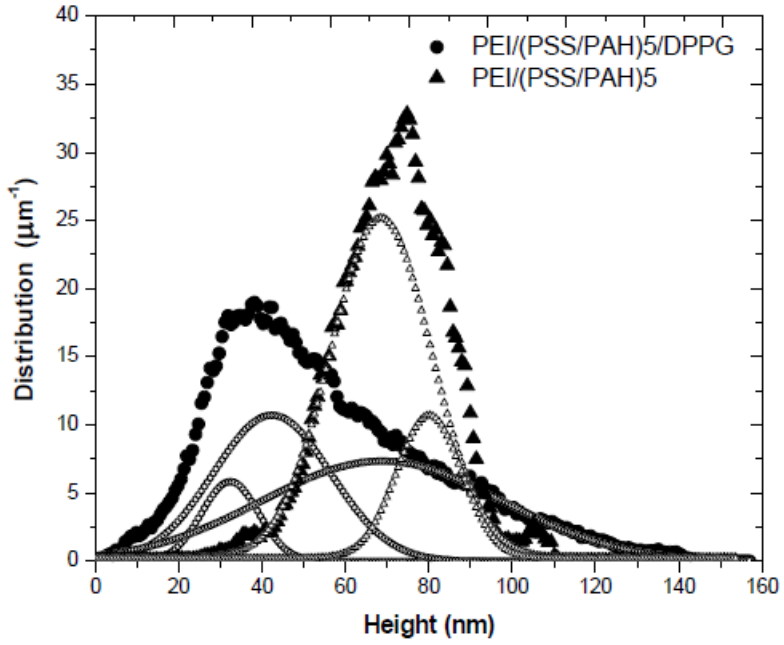

Figure 5.3. Height distribution of PEI/(PSS/PAH)$_5$ (closed triangles) and PEI(PSS/PAH)$_5$/DPPG (closed circles) obtained from the AFM images. The respective Gaussian fits of the height distributions are represented with open symbols.

5.2 AFM *in situ* surface analysis of Au/DPPG and Au/PAH/DPPG films

This section is dedicated to the analysis of topographic surfaces imaged by AFM *in situ,* i.e. at solid/liquid interface, of DPPG liposomes, obtained by the sonication method, deposited on Au-quartz crystal and on PAH surfaces. Roughness amplitude parameters of the surfaces, including root-mean-square roughness as well as height distribution functions are presented. A PSD analysis of the features, treated as self-affine structures, was infer and parameters including mean grain size, correlation lengths, fractal geometry, growth regimes and scaling concepts were found by applying a combination of three PSD models namely, the conventional, the fractal and the ABC or K-correlation.

5.2.1 Amplitude parameter analysis

Figure 5.4 shows AFM *in situ* images with 2 μm of scan length of DPPG suspension deposited on Au surface at room temperature: a) and b) Au surface in ultra-pure water; c) and d) Au/DPPG at 3 minutes; e) and f) Au/DPPG at 5 minutes; g) and h) Au/DPPG at 10 minutes; and finally i) and j) Au/DPPG at 120 minutes, heights and phases, respectively. The time t=0 minutes corresponds to the instant before the injection of DPPG suspension into the AFM liquid cell. A topographic view of the height Au surface (figure 5.4 a)) suggests that considerable constrains may hinder the AFM analysis since the gold surface is not a flat surface and its grain diameter has the same size order of magnitude than the DPPG vesicles [111]. Like most of AFM studies of liposomes adsorption found in literature were carried out onto flat surfaces, it will be a huge challenge to understand the surface evolution when vesicles adsorb on a non-smooth surface. Various statistical quantities applied to characterize the surface topography such as, roughness amplitude parameters and height distribution gaussian fit parameters are presented in table 5.2.

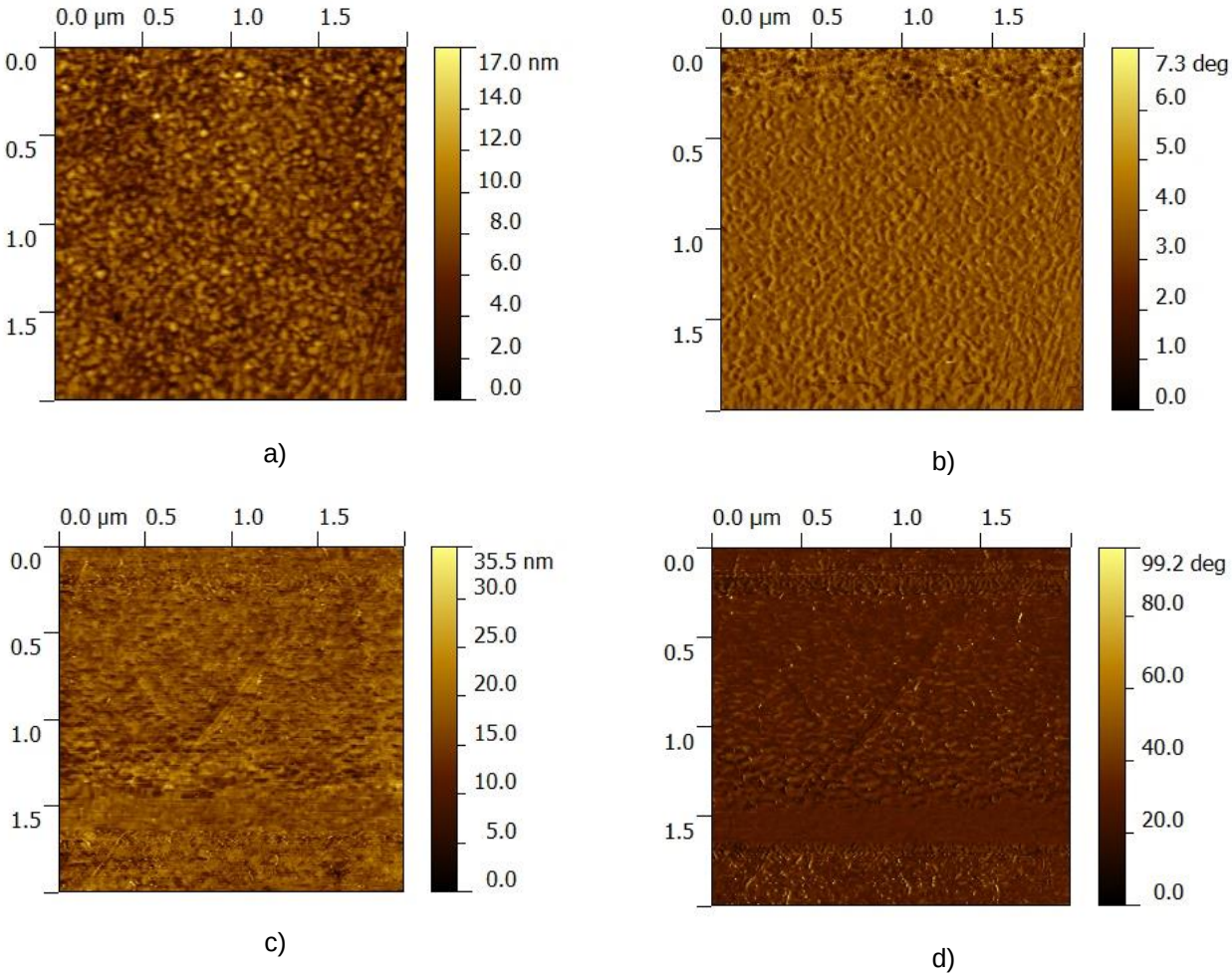

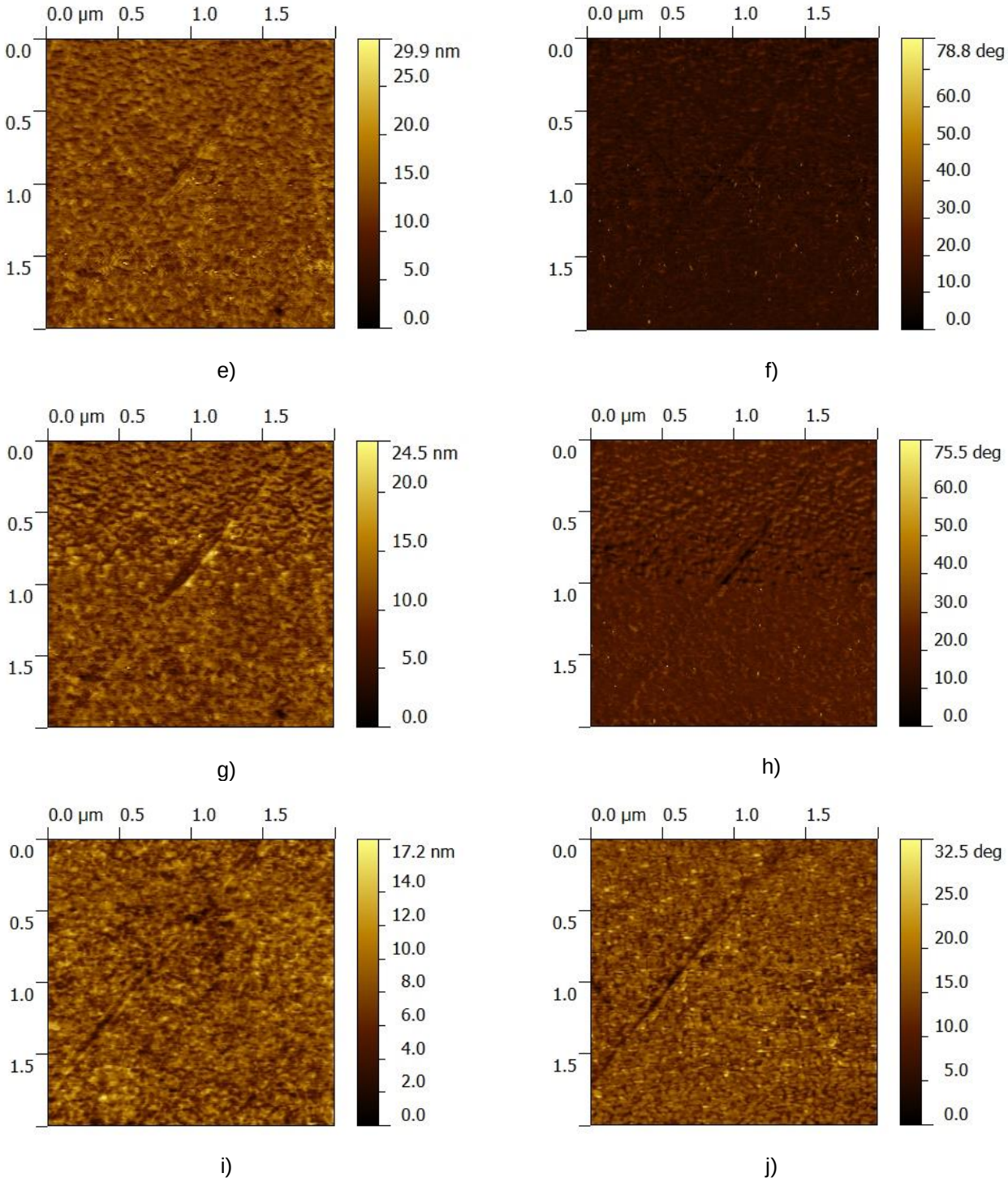

Figure 5.4. AFM *in situ* images with 2µm of scan size of DPPG suspension deposited on Au surface obtained in ultra-pure water at room temperature: a) and b) Au surface; c) and d) Au/DPPG at 3 minutes; e) and f) Au/DPPG at 5 minutes; g) and h) Au/DPPG at 10 minutes; and finally i) and j) Au/DPPG at 120 minutes, of heights and phases, respectively.

The heights and phases dynamic morphological changes of DPPG liposomes suspension deposited on a PAH-gold quartz crystal are shown in figures 5.5 a) and b), c) and d), e) and f), g) and h), and lastly i) and j) for 0, 3, 5, 10 and 60 minutes of adsorption time, respectively. The calculated surface parameters such as, roughness amplitude parameters and height distribution gaussian fit parameters are presented in table 5.3.

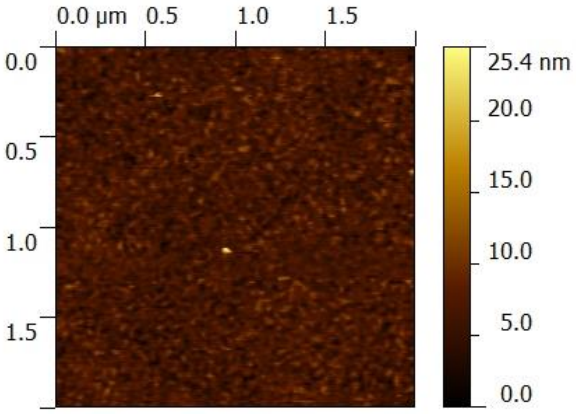

a)

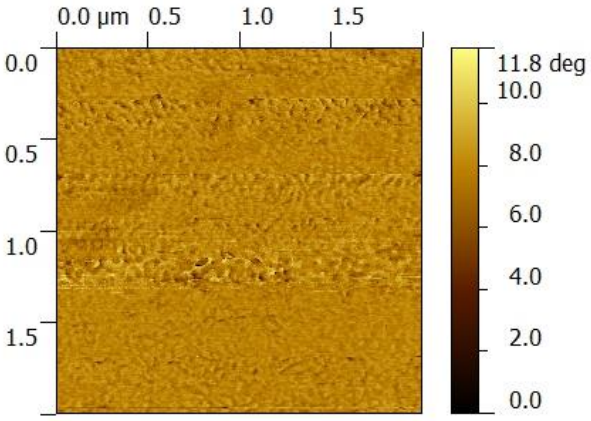

b)

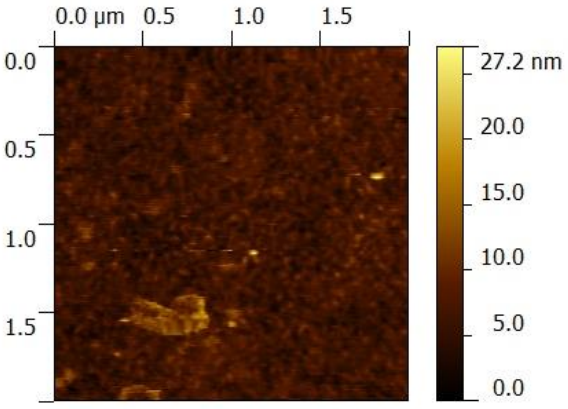

c)

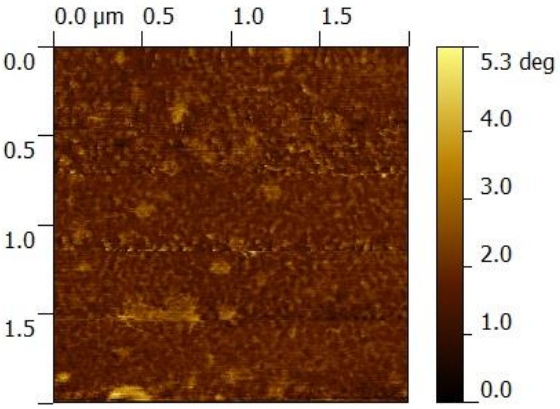

d)

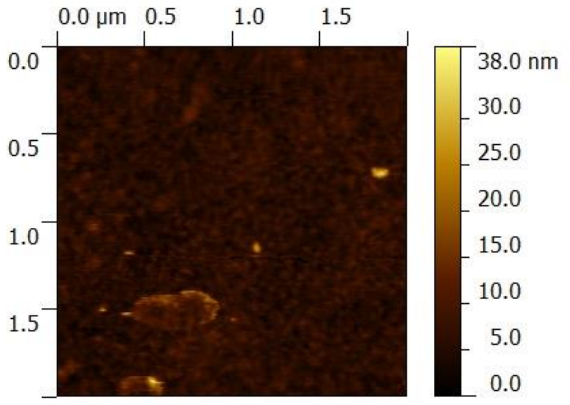

e)

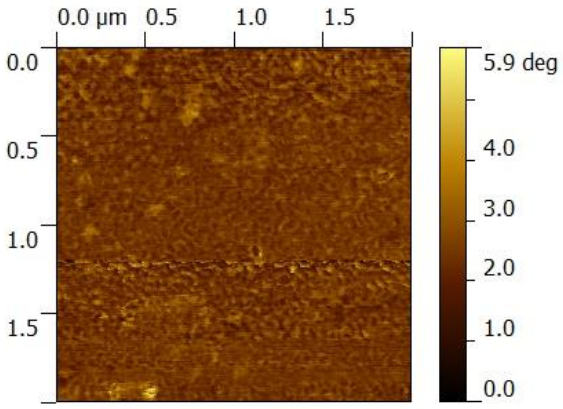

f)

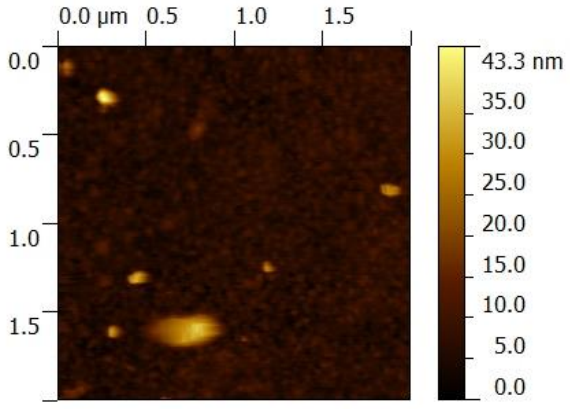

g)

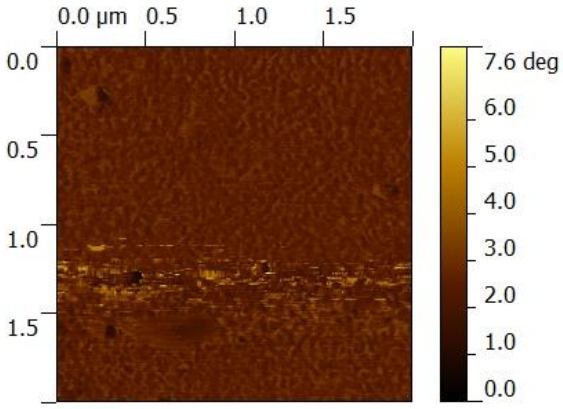

h)

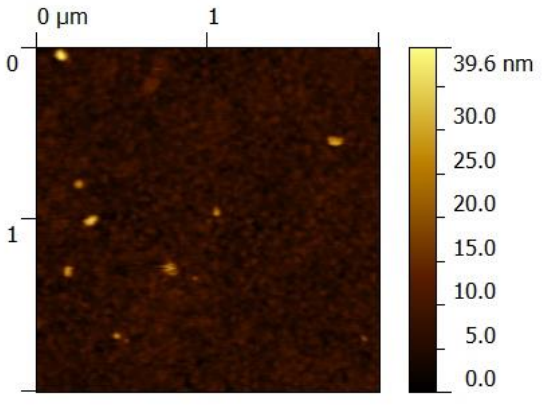

i)

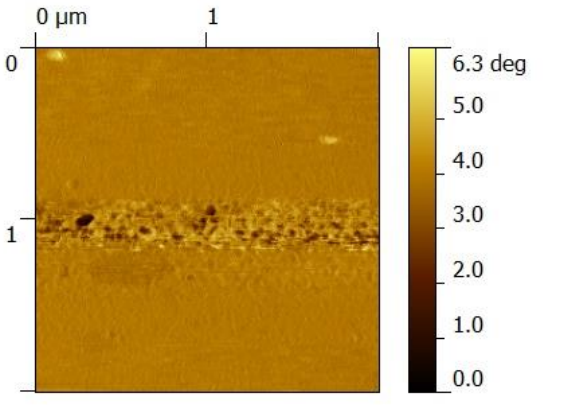

j)

Figure 5.5. AFM *in situ* images with 2µm of scan size of kinetics adsorption of DPPG liposome deposited on a Au/PAH surface, at room temperature: a) and b) 0 seconds (Au/PAH surface); c) and d) 3 minutes; e) and f) 5 minutes; g) and h) 10 minutes; and i) and j) 60 minutes. The first and seconds images correspond to heights and phases, respectively.

According table 5.2, the gold substrate revealed a kurtosis (Rku) moment of 3.1±0.6 which means that the surface has a normal distribution of peaks and valleys, indicating that we are dealing with a non-flat surface, as expected. After 3 and 5 minutes of DPPG injection into the liquid AFM cell, the Rku slightly increased to 4±1. This value suggests that the surface has more peaks than valleys which can be attributed to liposomes adsorption onto gold surface. Subsequently, Rku reduced to 3.3±0.9 and 3.1±0.6 at t=10 and t=120 minutes, respectively, which are values that resemble those that were found before vesicles assembly. Analyzing Rq values listed in table 5.2, one can see that after the first 3 minutes of DPPG adsorption the root-mean-square roughness rises from 1.5±0.3 to 2.7±0.6 nm, decreasing to 2.3±0.3 nm two minutes later. Five minutes after DPPG injection, this parameter was preserved decreasing again, at t=120 minutes, to a value close to the gold surface. This Rq behavior suggests that at 3 minutes the anionic DPPG vesicles are closed. But, as time passes, they interact electrostatically with the hydrophilic and oxidized gold surface, since the substrate had a specific treatment with UV/ozone during one hour [296]. Afterwards, vesicles start to open and deploy through the substrate creating a supported-lipid bilayer (SLB) as described by Israelachvilli [77]. Thus, surface evolution for SLB development presents two regimes: i) initially, there is a surface roughness variation as a function of time; ii) then a stabilization stage of the surface roughness which corresponds to a saturation time or crossover time is attained.

Table 5.2. AFM 1D Statistical parameters calculated from topographic images with $2\times2\mu m^2$ areas of Au surface (t=0) and DPPG deposited on Au at t = 3, 5, 10 and 120 minutes.

Time (min)	**AFM 1D Statistical parameters (rows)**								
	Rq (nm)	***Ra (nm)***	***Rtm (nm)***	***Rvm (nm)***	***Rpm (nm)***	***R_{KU}***	***Height distribution Gaussian fit parameters***		
							P1 (nm)	***W1 (nm)***	***A1***
0	1.5±0.3	1.2±0.2	11±1	3.0±1.0	6.8±0.1	3.1±0.6	7.064±0.006	3.42±0.01	0.981±0.004
3	2.7±0.6	2.1±0.4	25±3	9±2	16.9±0.3	4±1	16.79±0.01	5.13±0.02	0.959±0.005
5	2.3±0.3	1.8±0.3	21±2	7±1	13.6±0.2	4±1	13.410±0.007	4.45±0.02	0.970±0.003
10	2.3±0.3	1.8±0.3	17±2	5±1	10.8±0.2	3.3±0.9	10.596±0.008	4.53±0.02	0.977±0.004
120	1.9±0.2	1.4±0.2	13.4±0.9	3±1	8.1±0.2	3.2±0.6	7.984±0.008	3.61±0.02	0.973±0.005

Rq – root-mean-square roughness; Ra – Roughness average; R_{KU} – Kurtosis; Rtm - Average Maximum Height of the Profile; Rvm - Average Maximum Profile Valley Depth; Rpm - Average Maximum Profile Peak Height; P1 – peak 1 position; W1 – width peak 1; A1 – area peak 1.

Table 5.3. AFM 1D Statistical parameters calculated from topographic images with $2\times2\mu m^2$ areas of Au/PAH surface (t=0 min) and DPPG deposited on Au/PAH at t= 3, 5, 10 and 60 minutes.

Time (min)	AFM 1D Statistical parameters (rows)								
	Rq (nm)	*Ra (nm)*	*Rtm (nm)*	*Rvm (nm)*	*Rpm (nm)*	R_{KU}	*Height distribution Gaussian fit parameters*		
							P1 (nm)	*W1 (nm)*	*A1*
0	1.6±0.2	1.3±0.2	12±4	2.8±0.7	6.7±0.1	4	6.478±0.007	3.23±0.01	0.984±0.004
3	1.9±0.6	1.4±0.3	13±3	2.7±0.7	6.6±0.3	4	6.284±0.009	3.45±0.02	0.963±0.006
5	2.0±0.8	1.5±0.4	14±2	2.3±0.6	6.3±0.3	5	5.813±0.009	3.66±0.02	0.967±0.005
10	2.8±2*	1.9±1.0	17±9	2.6±0.8	7.2±0.9	6	6.433±0.008	4.06±0.02	0.958±0.004
60	2.1±0.8	1.5±0.3	15±6	2.4±0.7	6.7±0.2	6	6.357±0.007	3.89±0.02	0.988±0.004

Rq – root-mean-square roughness; Ra – Roughness average; R_{KU} – Kurtosis; Rtm - Average Maximum Height of the Profile; Rvm - Average Maximum Profile Valley Depth; Rpm - Average Maximum Profile Peak Height; P1 – peak 1 position; W1 – width peak 1; A1 – area peak 1.
* The large error is due to the fact that some DPPG vesicles have attached on surface after lipid bilayer formation.

Table 5.3 shows the one-dimensional height statistical parameters obtained from topographic images with 2 μm of scan length of DPPG liposomes deposited on Au/PAH polyelectrolyte surface at 0, 3, 5, 10 and 60 minutes. The Au/PAH substrate revealed a kurtosis moment (Rku) of 4 meaning that the surface has more peaks than valleys which can be associated to PAH layer adsorption onto the gold surface. After DPPG suspension deposition at t=3 min, the Rku remains unchanged suggesting that a DPPG lipid bilayer is already formed. Although, as the time passes the Rku moment slightly increase probably due to the presence of some aggregates of liposomes that have attached on Au/PAH/DPPG, see figure 5.5 g). The root-mean-square roughness (Rq) of the first and second topographic images took after DPPG dispersion deposition, at 3 and 5 minutes, are marginally higher than the PAH surface, being an evidence of liposomes disruption and subsequent formation of a phospholipid bilayer. At 10 minutes it is possible to observe an increment of Rq which presents a large error; this is due to the presence of some liposomes aggregates immobilized onto the cushion layer as already mentioned above. After one hour, Rq values decreased revealing liposomes desorption. Nevertheless, we must consider the preservation of the Rq values at 3 and 5 minutes. This Rq conservation are in accordance with adsorption studies of DPPG liposomes onto PAH which revealed that kinetics is ruled by three processes: i) the first with a small characteristic time ($\tau_1 = 2.19 \pm 0.02\ min$) during which the liposomes adsorb onto the PAH surface and break releasing the water stored; ii) followed by a long characteristic time with approximately 23 min corresponding to the end of the diffusion-controlled process; iii) and after another characteristic time, ~60 minutes, associated to a minor fraction of phospholipid desorption from the surface [111].

Generally, comparing the root-mean-square roughness of the Au/DPPG and Au/PAH/DPPG surfaces (see tables 5.2 and 5.3), it is possible to realize that after DPPG injection onto PAH the Rq value is smaller, representing a fast DPPG adsorption followed by vesicles disruption due to the electrostatic forces between both molecules. It is well known that at pH ~ 4 PAH is highly ionized [129] and, therefore, the electrostatic interactions between NH_3^+ and PO_4^- groups of PAH and DPPG,

respectively, are strong, as indicated by XPS data (see section 4.5.5). On the other hand, interactions between the polar head groups of the DPPG and the nonpolar PAH chains (hydrophobic interactions) might be weak.

To better understand the processes that occur during liposomes adsorption, the DPPG kinetic curve onto PAH and the Rq *in situ* values were plotted together, and are presented in Figure 5.6 a). The DPPG frequency shift measured by QCM was converted into adsorbed amount per unit area using equation 3.1 and a value of 5±1 mg/m^2 was attained corresponding to a planar DPPG bilayer [297].

The height distribution curves obtained by treatment of the AFM *in situ* topographic images of Au/DPPG and Au/PAH/DPPG at different DPPG adsorption times are shown in figures 5.6 b) and c), respectively. The parameters achieved by fitting the height distribution gaussian curves, as well as the average maximum height of the profile (Rtm), the average maximum profile valley depth (Rvm) and the average maximum profile peak height (Rpm) are listed in tables 5.2 and 5.3 for Au/DPPG and AU/PAH/DPPG samples, respectively.

For the adsorption of DPPG vesicles onto the gold surface, the peak positions of the height gaussian distributions at 0, 3 and 120 minutes are centered at 7.064±0.006 nm, 16.79 ±0.01nm and 7.984±0.008 nm, respectively, assigned to the height of the Au surface, closed DPPG vesicles attached to the Au surface and to a supported-lipid bilayer (SPB), correspondingly. Thus, the height profiles revealed a substantial increase in the first three minutes of DPPG deposition, but afterwards decreasing to values close to the gold surface. Therefore, these height parameters are in accordance with the Rq, Ra and Rku values confirming the adsorption of closed DPPG liposomes onto the Au solid support in the first minutes, followed by vesicles break and scattering of the lipid bilayer on the surface.

Concerning the DPPG adsorption onto PAH, the estimated height parameters obtained by fitting the gaussian curves of figure 5.6 c) are listed in table 5.3. Similar peak position values at different adsorption times, such as 0, 3, 5, 10 and 60 minutes, reveals that the DPPG phospholipid bilayer has already been formed at 3 minutes which is in accordance with the small characteristic time, $\tau_1 = 2.19 \pm 0.02\ min,$ estimated by fitting the QCM kinetic curve of figure 5.6 a). The height residual peaks (that could not be fitted) with a range between 15-40 nm and presented in figure 5.6 c) are related to some DPPG vesicles that have attached onto the Au/PAH/DPPG surface.

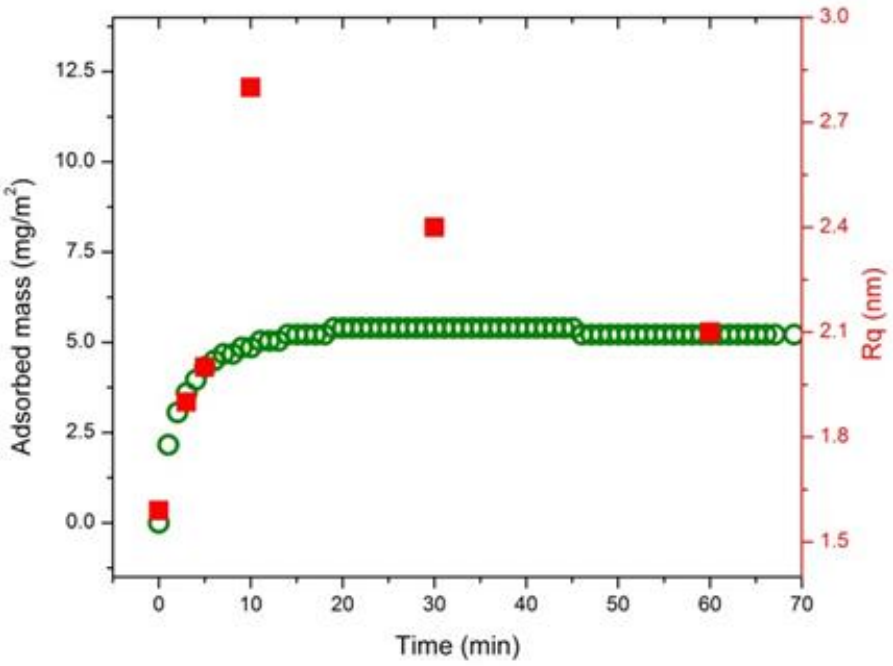
Adsorbed mass (mg/m²)
Rq (nm)
Time (min)
12.5
10.0
7.5
5.0
2.5
0.0
3.0
2.7
2.4
2.1
1.8
1.5
0
10
20
30
40
50
60
70

a)

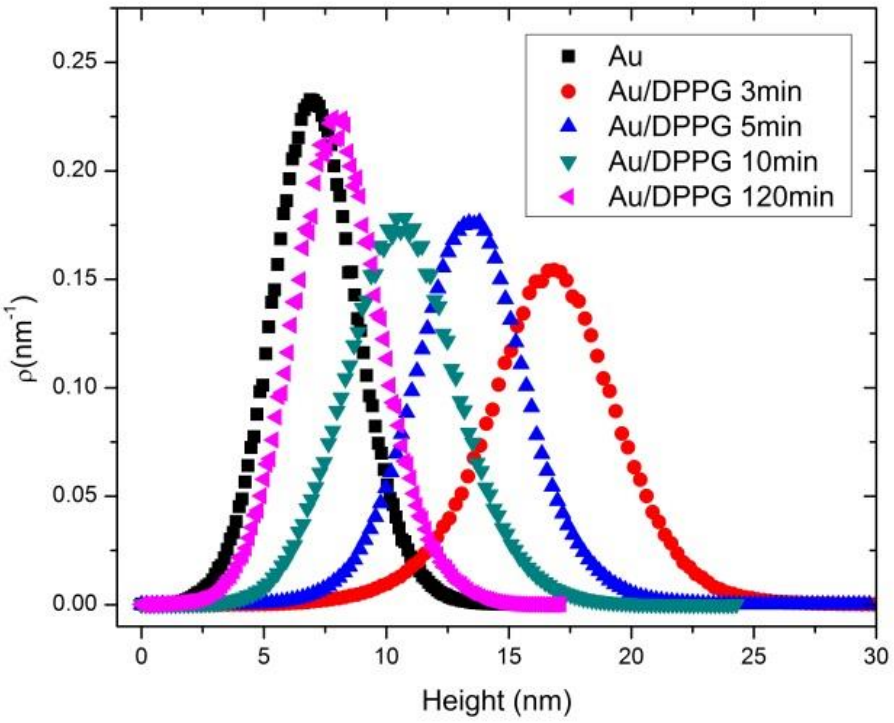
Au
Au/DPPG 3min
Au/DPPG 5min
Au/DPPG 10min
Au/DPPG 120min
ρ(nm⁻¹)
Height (nm)
0.25
0.20
0.15
0.10
0.05
0.00
0
5
10
15
20
25
30

b)

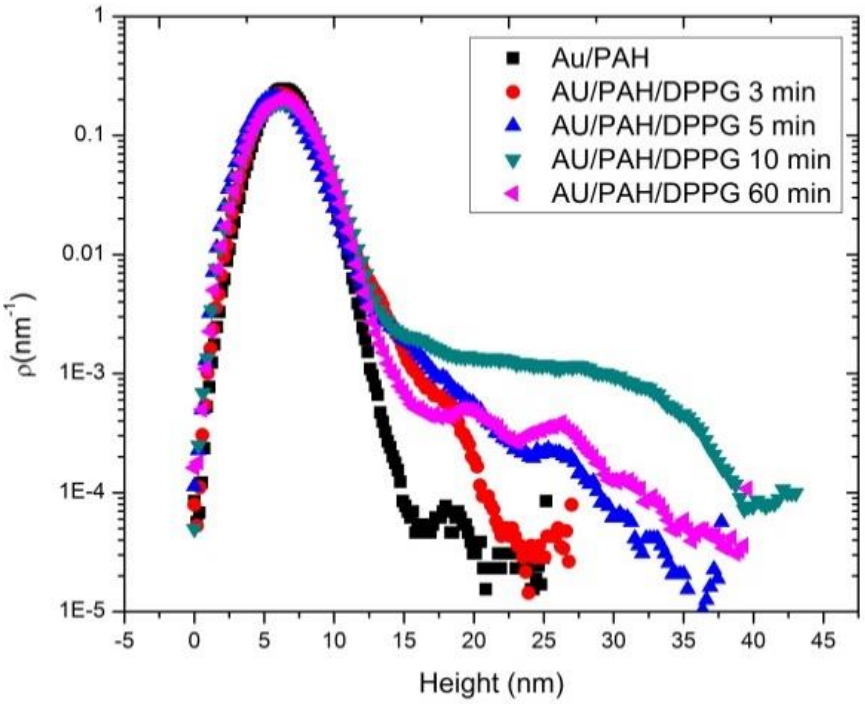

c)

Figure 5.6. a) DPPG adsorbed amount per unit of area onto a PAH layer measured by QCM (green circles) and Rq values obtained from 2×2μm^2 topographic images of DPPG liposomes adsorbed onto PAH at 3, 5, 10, 30 and 60 minutes (red squares). b) Height distribution curves obtained by treatment of 1D AFM topographic images *in situ* of Au and Au/DPPG films at 3, 5, 10 and 120 minutes and c) Au/PAH and Au/PAH/DPPG at 3, 5, 10 and 60 minutes.

The *ex situ* (in air) ellipsometry technique allows to measure the polarization state of an elliptically polarized light when it is reflected at a surface and was used to quantify optical parameters changes of the gold surface before and after a $(PAH/DPPG)_4$ LbL film build up. From the changes in the ellipsometric angles (Δ,Ψ) the refractive index and the thickness of the film can be deduced [298]. The results showed that there is a small increase of the amplitude angle (Ψ) from 43.65±0.025 to 44.2±0.3 and a significant decrease of the phase difference (Δ) from 105.89±0.06 to 90±3, which agrees with the presence of a thin nearly transparent layer, as expected for the formation of a $(PAH/DPPG)_4$ LbL film. According to the optical parameters, of the gold surface before and after $(PAH/DPPG)_4$ assembly, and assuming a linear PAH/DPPG growth as bilayers are added [289], the PAH/DPPG bilayer thickness was estimated in 5±1 nm. It should be referred that a comparable result was found by Schönherr *et al* [299] for a continuous phosphatidylcholine (PC) lipid bilayer.

5.2.2 Fractal Analysis

In order to characterize the surface topography of Au/DPPG and Au/PAH/DPPG, one must rely on the amplitude parameters; however, they only provide vertical information. PSD analysis, which offers both lateral and longitudinal information, was used to study the kinetics behavior of DPPG liposomes deposited on Au solid support and Au/PAH polymer surface as a function of time.

Figures 5.7 a) and b) show the one-dimensional PSD spectra of the AFM morphological images of figures 5.4 and 5.5, respectively, collected at discrete times for DPPG liposomes assemble on Au-quartz crystal surface and Au/PAH. This one-dimensional spectral analysis provides a representative description of the overall surface roughness.

All power spectra exhibit three distinct regions represented as parts I, II and III: (I) the plateau at low frequencies which is related to the height of the rough surface. This section has an absence of correlation (it does not change with the scale) and of characteristic length; (II) the region of the medium frequencies gives the correlation length, which defines the lateral extent of the rough surface, is strongly frequency dependent and it represents the power-law decay; and (III) the region at high frequencies, where the PSD is strongly influenced by tip artifacts, which was not considered for surface analysis [188]. PSD analysis de-convolutes the roughness as a function of surface lateral length scales, correlates the vertical amplitude with the spatial frequency of surface features and may also reveal the characteristics of the microstructure surface [189].

PSD spectra of figure 5.7 a) present a plateau at low spatial frequencies (region I) of $f < 7 \times 10^{7}$ m^{-1}, revealing a nearly constant value for roughness and an absence of any characteristic length beyond ca. 15 nm. The magnitude of PSD curves in this zone revealed that after 3 minutes of DPPG addition in the liquid AFM cell an increase occurs followed by a decrease 5 minutes later, which was maintained at t=10 minutes. When 120 minutes have elapsed, the magnitude at this section suffers a marginal reduction. The PSD spectra at region I complies with the roughness of the surface. The region II involves intermediate frequencies and characterizes the mechanism of the surface growth, where PSD is strongly frequency dependent. It also shows the surface self-affine behavior. Looking at this sector, it is possible to observe that after 3 minutes of DPPG vesicles injection in the liquid cell, there is a decrease of the slope value of the PSD curve. However, in the following measurements (t= 5, 10 and 120 minutes) the slope of the PSDs spectra in this region increased progressively, until reach a value close to the initial. So, at intermediate frequencies the PSD spectra reveals two regimes, strongly frequency dependent, with a constant slope (sub-regions IIa and IIb), representative of a combination of two mechanisms that are involved in surface growth. In the subzone IIa, the surface evolution corresponds to an anomalous dynamic scaling, i.e., roughening and smoothing mechanisms cannot reach equilibrium and the local surface changes with time. The subregion IIb is attributed to the balance between random fluctuations and diffusion processes, so the local structure remains unchanged [179]. As mentioned this region characterizes the surface self-affine behavior. The region III ($f > 3\times10^{8}$ m^{-1}) relates to the highest frequencies of the spectrum. This spatial frequencies range is associated with physical dimensions of the AFM tip. Thus, the convolution of the tip and surface features happens and consequently, the PSD is highly affected by AFM tip artefacts and it was not considered to surface analysis [185].

PSD spectra in Figure 5.7 b) at low frequencies ($f < 3 \times 10^7$ m^{-1}) have showed large changes probably due to the presence of some aggregates of DPPG vesicles that have attached on surface during growth surface evolution. Analyzing the first region frequency, we can detect a small increase of the PSD magnitude at 3 and 5 minutes, followed by an enhanced growth at 10 minutes revealing that some liposomes have aggregated. At an earlier stage (t=60 minutes) one can notice the typical behavior with the roll-off corner related to vesicles disruption promoted by electrostatic interactions between the anionic DPPG vesicles and the cationic PAH surface, leading to a decay of the power law. However, at the region II the PSD spectra of PAH and PAH/DPPG are quite similar leading us to conclude that the formation of the lipid bilayer have been occurred at 3 minutes of DPPG liposomes adsorption. The region III ($f > 3 \times 10^8$ m^{-1}) was not considered to surface analysis.

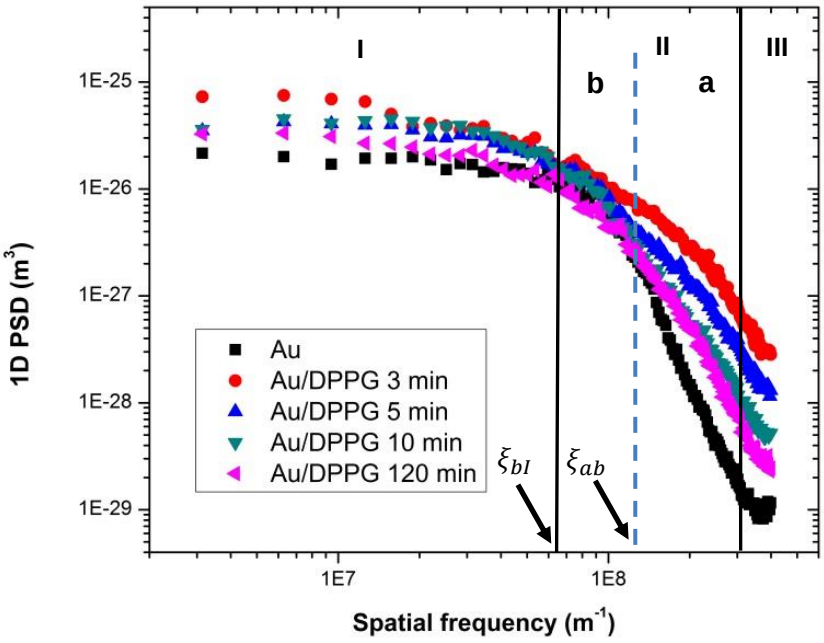

a)

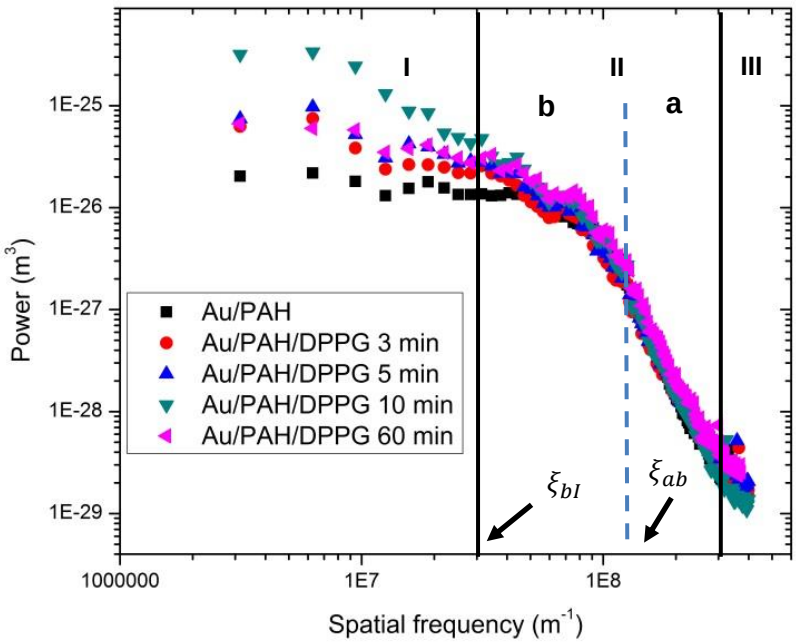

b)

Figure 5.7. Power spectra density evolution of the of the a) Au/DPPG and b) Au/PAH/DPPG LbL films.

The conventional mode to calculate the correlation length (ξ) involves determining the transition spatial frequency (f_t) of the intersection point between two fitted curves of two distinct regions of the PSD spectra. However, both PSD spectra (figures 5.7 a) and b)) showed that this medium-frequencies region is governed by two growth regimes which must be treated individually. The transition frequencies, marked with arrows in figures 5.7 a) and b), correspond to correlation lengths that define transitions between physical processes responsible for surface development. The first correlation length (ξ_{ab}) is defined by the inverse of the transition frequency (f_t) between the high-frequency and the self-affine intermediate frequency regions (transition between subregions IIa and IIb) and the second correlation length (ξ_{bI}) by the inverse of f_t among the low-frequency random roughness plateau and the intermediate-frequency self-affine region (transition between the section I and the subregion IIb). The first (ξ_{ab}) and second (ξ_{bI}) correlation lengths of the PSD spectra for DPPG adsorption onto Au and PAH at different adsorption times were calculated and are listed in tables 5.4 and 5.5, respectively.

The first (ξ_{ab}) and second (ξ_{bI}) correlation lengths estimated for the gold-quartz crystal show values of ~13 nm and ~9 nm, respectively, related to the mean grain diameter of the surface resonator and are depicted in table 5.4. Probably the presence of two different values is related with the fact that the quartz crystal resonator is coated with an under layer of chromium and an upper layer of gold. Therefore, the fact that these correlation length values are maintained during DPPG adsorption, lead us to conclude that the rupture of the vesicles on the Au surface arises. Similar correlation length

values can be found in table 5.5 for the DPPG vesicles deposition onto PAH. However, the first and second correlation lengths have a mean value higher which can be attributed to the PAH assemble onto the quartz crystal sensor.

The roughness exponents (α) were determined by the relation,

$$\alpha = \frac{\gamma - 1}{2} \tag{5.1}$$

where γ is the value of slope of the fitted PSD at two separate establishments and the obtained results are presented in tables 5.4 and 5.5. The α_a and α_b roughness exponents describe a combination of two processes that control the surface morphologies during growth and the mechanism responsible for the particles deposition [179].

The α_b scaling exponent value, α_b = 0.68, for DPPG liposomes adsorbed onto Au surface at 5 minutes is consistent with Villain model. This model predicts that the deposition of particles is preferentially driven by interactions with neighboring particles. This rough exponent shows the balance between random fluctuations and diffusion processes, i.e. the mechanism is far-from-equilibrium. At 10 minutes of liposomes adsorption α_b = 1, meaning that the stabilization of the process has occurred and a presence of a smooth DPPG lipid bilayer covering the surface is formed.

Roughness exponents estimated from region IIb for the deposition of DPPG onto PAH show values close to the unit, signifying that the surface is totally covered by a lipid bilayer after 3 minutes of phospholipid adsorption, i.e. the solid-liquid interface reached the steadiness. In addition, the fast adsorption and rupture of the liposomes is due to a strong interaction between the liposome and the completely charged PAH surface [6]. The explanation for this behavior has been also reported in literature, whereby the spread of the lipid membrane over a planar surface is favored at low pH, regardless to the net charge of the bilayer, process which is driven by van der Waals forces [70].

Although it was proved that the DPPG adsorption mechanism and consequent formation of a lipid bilayer reached its balance before t=3 minutes [111], afterwards (t=10 minutes) the rough exponent increased, due to the accumulation of aggregates of liposomes onto the Au/PAH/DPPG-bilayer surface; being $\alpha_a \gg 1$ which implies a locally rough surface and a decrease of the fractal dimension. After 3 minutes of DPPG adsorption the rough exponent, α_b, is close to the unit, which are in good agreement with the linear growth equation of the diffusion Villain model [192].

Scaling exponents calculated from region IIa for both (Au and PAH) surfaces have a similar anomalous dynamic behavior, shown by the increase of rough exponent as time passes; it became $\alpha_a \gg 1$, which is more evident in the Au/PAH/DPPG film. In this last situation, the roughening fluctuations and the smoothing effects cannot reach a balance, and the local surface slope increases and changes with time, as it is possible to observe by the large error of the Rq at 10 minutes of DPPG adsorption.

By plotting the Rq roughness evolution of Au/PAH/DPPG surface films as a function of time and fitting the power law behavior to the Rq roughness as $Rq(L,t) \propto t^{\beta}$, we can obtain the growth exponent β. However, as described above, at 3 minutes of DPPG adsorption onto PAH layer a lipid bilayer has already been formed and thus the growth exponent cannot be estimated.

Table 5.4. Slopes (γ) and the respective scaling exponents (α) acquired from the subregions *a* and *b* and the correlation lengths (ξ) attained for the transition of the *ab* and *bI* zones of the PSD curves of figure 5.7 a).

DPPG time adsorption (min)	γ_b	α_b	γ_a	α_a	ξ_{ab} **(nm)**	ξ_{bI} **(nm)**
0	3.1±0.2	**1.05**	5.53±0.07	**2.26**	8.6	13.3
3	1.69±0.05	**0.3425**	2.89±0.07	**0.943**	5.9	13.3
5	2.48±0.08	**0.678**	3.09±0.06	**1.043**	5.3	12.7
10	3.2±0.1	**1.0848**	3.69±0.06	**1.346**	6.5	12.7
120	2.4±0.1	**0.7183**	4.34±0.07	**1.6723**	6.8	13.8

Table 5.5. Slopes (γ) and the respective scaling exponents (α) acquired from the subregions *a* and *b* and the correlation lengths (ξ) attained for the transition of the *ab* and *bI* zones of the PSD curves of figure 5.7 b).

DPPG time adsorption (min)	γ_b	α_b	γ_a	α_a	ξ_{ab} **(nm)**	ξ_{bI} **(nm)**
0	2.5±0.1	**0.75**	4.63±0.06	**2.815**	9.9	15.9
3	3.1±0.1	**1.05**	4.09±0.05	**1.545**	11.8	14.5
5	3.0±0.1	**1**	4.12±0.05	**1.56**	11.8	15.2
10	3.0±0.1	**1**	4.72±0.05	**1.86**	10.6	14.5
60	2.8±0.2	**0.9**	4.43±0.08	**1.715**	10.6	15.2

More valuable information can be extracted from PSD spectra, e.g. mean grain diameter and fractal dimensions, by applying PSD models, such as the Fractal model ($PSD_{fractal}$) and the ABC or K-correlation model (PSD_{ABC}).

To determine surface fractal components the medium-frequency region (region II) of the PSD of Figures 5.7 a) and b) were fitted with the $PSD_{fractal}$ model given by equation 3.8. The spectral index found (ν) and the fractal dimensions (*Df*) obtained by the equation 3.9 are listed in table 5.6. Initially, the Au/DPPG surface has stronger fractal components than the Au/PAH/DPPG film. But as time passes, fractal components of the Au/DPPG surface decrease and the final *Df* reaches a value close

to the Au/PAH/DPPG surface. Both films have a *Df* nearly 2; so the surfaces can be described as fractal marginal/smooth.

Table 5.6. Spectral index (ν) obtained by fitting the PSD curves of figures 5.7 a) and b) with equation 3.8, and the respective fractal dimension calculated using the equation 3.9.

DPPG adsorption time	**Fractal contribution ($PSD_{fractal}$ model)**		**DPPG adsorption time**	**Fractal contribution ($PSD_{fractal}$ model)**	
	Au/DPPG			**Au/PAH/DPPG**	
(min)	ν	**DF**	**(min)**	ν	**DF**
0	4.00±0.08	1.00	**0**	2.7±0.1	1.65
3	1.16±0.05	2.42*	**3**	2.54±0.07	1.73
5	1.64±0.03	2.18	**5**	2.60±0.08	1.70
10	2.39±0.03	1.80	**10**	2.96±0.09	1.52
120	2.48±0.06	1.76	**60**	2.67±0.09	1.67

* At *Df*~2.5 the surface reveals a Brownian fractal.

Another model can be applied to extract information retained in these PSD curves. Tables 5.7 and 5.8 present the PSD_{ABC} model parameters obtained by fitting the region II of the PSD curves of figures 5.7 a) and b) with the equation 3.10. In this model the correlation length is given by the parameter B, which is related to the mean grain diameter of the surface. The results showed values similar to those obtained by the frequency inverse mode (ξ_{bI}), see tables 5.4 and 5.5. The exception falls on the Au/PAH/DPPG at 10 minutes where the correlation length shows a value close to the mean vesicle diameter, ~27 nm. Probably the real value is under masked by some vesicles that have been stuck on the Au/PAH/DPPG surface after formation of the DPPG bilayer, as mentioned above in analyses of figure 5.5 g). The magnitude at low spatial frequencies (A parameter) is related to the height of the rough surfaces. In tables 5.4 and 5.5 it is possible to observe that the A parameter generally remains constant in 1D PSD at low frequencies for Au/DPPG and Au/PAH/DPPG LbL films, however and because of the formation of vesicles aggregated on both surfaces at 3 and 10 minutes, for the first and second films respectively, there is an increase of the A parameter. The C parameter, corresponding to the inverse slop of the PSD curve, gives the nature of the roughness and is associated to growth mechanisms. Looking at the major periods of DPPG adsorption, both samples present a C~3 revealing that the film growth corresponds to bulk diffusion.

The final fractal dimension (*Df*) values for DPPG liposomes immobilization on both surfaces were also attained by the K-correlation or ABC model using the equation 3.11. At 3 and 10 minutes of DPPG

deposition on Au and PAH, respectively, the *Df* values increased to a value close to 3, which is representative of liposomes aggregation on surface. However at the end, the *Df* trends to values close to 2 proper of a marginal fractal surface.

Table 5.7. PSD_{ABC} model parameters given by equations 3.10 and 3.11 applied to the region II of the PSD curves of Figures 5.7 a). The correlation coefficient (CC) was obtained from the fit of experimental data to equation 3.10.

LbL films	**DPPG adsorption time (min)**	**Intrinsic contributions (PSD_{ABC} or K-correlation model)**				
		A (nm^3)	**B (nm)**	**C**	**CC**	***Df_{ABC}***
Au	0	19.7±0.4	6.8±0.2	5.6±0.3	0.98458	0.7
Au/DPPG	3	46±2	17±2*	1.2±0.3	0.98637	2.9
Au/DPPG	5	36.8±0.8	11±1	3.1±0.6	0.99401	1.95
Au/DPPG	10	46.1±0.9	11±1	3.9±0.1	0.9959	1.5
Au/DPPG	120	25.5±0.9	12±2	2.8±0.8	0.98604	2.1

***** Value close to the mean diameter of the DPPG liposomes.

Table 5.8. PSD_{ABC} model parameters given by equations 3.10 and 3.11 applied to the region II of the PSD curves of Figures 5.7 b). The correlation coefficient (CC) was obtained from the fit of experimental data to equation 3.10.

LbL films	**DPPG adsorption time (min)**	**Intrinsic contributions (PSD_{ABC} or K-correlation model)**				
		A (nm^3)	**B (nm)**	**C**	**CC**	***Df_{ABC}***
Au/PAH/DPPG	0	17.0±0.5	7.5±0.2	4.8±0.3	0.9758	1.1
Au/PAH/DPPG	3	31±2	15±3	2.7±0.2	0.98063	2.15
Au/PAH/DPPG	5	39±2	15±3	2.8±0.8	0.98858	2.1
Au/PAH/DPPG	10	82±8	27±5*	1.6±0.4	0.98645	2.7
Au/PAH/DPPG	60	39±2	12±3	3.1±0.2	0.97846	1.95

***** Value close to the mean diameter of the DPPG liposomes.

5.3 AFM *in situ* surface analysis of Au/PEI/(PSS/PAH)$_4$ and Au/PEI/(PSS/PAH)$_4$/DPPG films

The surface analysis performed in last section, such as amplitude roughness parameters and the conventional, fractal and ABC or K-correlation PSD models were applied to Au/PEI/(PSS/PAH)$_4$ and Au/PEI/(PSS/PAH)$_4$/DPPG-liposomes topographic surfaces imaged by AFM *in situ*, in order to extract information of surface morphology, microstructure and growth mechanisms. However, and bearing in mind that this PEM is rough and leads to the formation of aggregates or superstructures after DPPG-liposomes adsorption, another PSD model (PSD$_{sh}$) must be implemented in order to make available the size of these features.

5.3.1 Amplitude parameter analysis

Heights and phases of topographic images of Au/PEI/(PSS/PAH)$_4$ and Au/PEI/(PSS/PAH)$_4$/DPPG LbL films were obtained by AFM *in situ* and are displayed in figure 5.8. The DPPG suspension was obtained by the sonication method and the time adsorption onto PEM was 60 min.

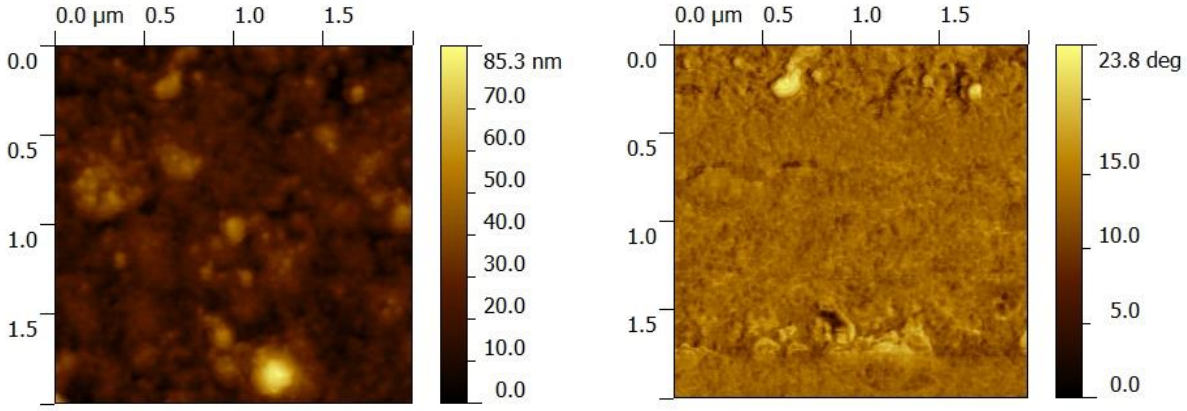

a) b)

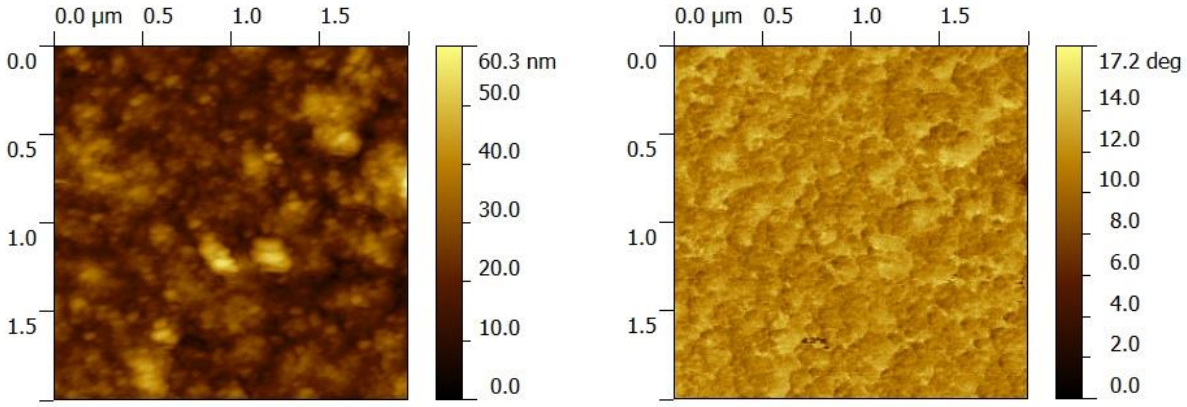

c) d)

Figure 5.8. AFM *in situ* topographic images with 2×2 μm^2 of a) and b) Au/PEI/(PSS/PAH)$_4$ and c) and d) Au/PEI/(PSS/PAH)$_4$/DPPG LbL films, heights and phases, respectively.

Table 5.9 displays the height amplitude parameters obtained from Au/PEI/(PSS/PAH)$_4$ (PEM) and Au/PEI/(PSS/PAH)$_4$/DPPG topographic images. The Ra roughness values are equal in both cases, being the Rq roughness slightly lower after DPPG adsorption. Furthermore, it can be detected a reduction of the mean peak-to-valley roughness (Rtm) and a growth of the height peaks (Rpm) justified by the adhesion of closed vesicles onto PEM surface, as we can see in PEM and PEM/DPPG profiles exhibited in figure 5.9 a). Although, the Rku is higher than 3 for both surfaces, i.e. the surface has more peaks than valleys, it slightly decreases after the adsorption of DPPG liposomes onto PEM, meaning a reduction of the surface sharpness due to the fact that intact vesicles have been immobilized. Height distributions for both surfaces are accessible in figure 5.9 b) and the parameters obtained after fitting the gaussian curves are displayed in table 5.9. Both surfaces present two maximum values of height centered at 17.7±0.2 and 26±3 nm for Au/PEI/(PSS/PAH)$_4$ and 20.6±0.2 and 33±3 nm for Au/PEI/(PSS/PAH)$_4$/DPPG. The largest area of the obtained fitted curves is the one centered at 20.6±0.2 nm proving that liposomes are adsorbed onto the PEM surface maintaining its own structure, i.e., being not flattened.

Table 5.9. AFM 1D Statistical parameters calculated from topographic images with 2×2μm^2 areas of Au/PEI/(PSS/PAH)$_4$ and Au/PEI/(PSS/PAH)$_4$/DPPG.

Time (min)	AFM 1D Statistical parameters (rows)											
							Height distribution Gaussian fit parameters					
	Rq (nm)	***Ra (nm)***	***Rtm (nm)***	***Rvm (nm)***	***Rpm (nm)***	R_{KU}	***P1 (nm)***	***W1 (nm)***	***A1***	***P2 (nm)***	***W2 (nm)***	***A2***
0	8±3	5±1	45±12	7±3	21±3	5±1	17.7±0.2	10.4±0.6	0.6±0.1	26±3	17±2	0.3±0.1
60	7±2	5±1	40±7	10±2	23±2	4±1	20.6±0.2	10.9±0.2	0.88±0.06	33±3	16±4	0.15±0.06

Rq – root-mean-square roughness; Ra – Roughness average; Rku – Kurtosis; Rtm - Average Maximum Height of the Profile; Rvm - Average Maximum Profile Valley Depth; Rpm - Average Maximum Profile Peak Height; P1 – peak 1 position; W1 – width peak 1; A1 – area peak 1; P2 – peak 2 position; W2 – width peak 2; A2 – area peak 2.

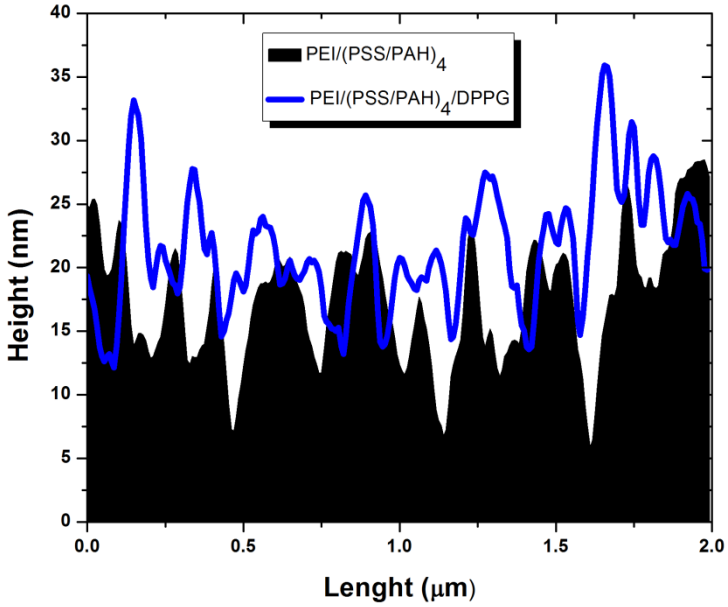

a)

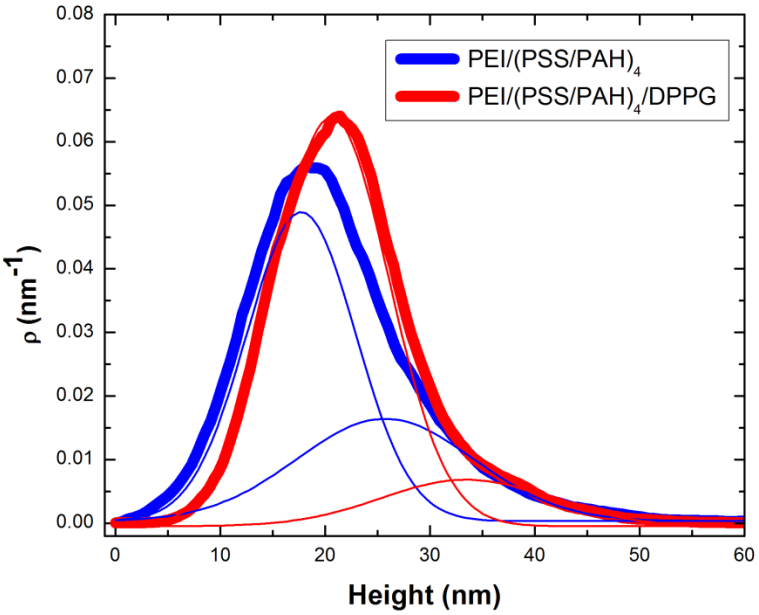

b)

Figure 5.9. a) Au/PEI/(PSS/PAH)$_4$ and Au/PEI/(PSS/PAH)$_4$/DPPG height profiles with 2 μm of scan length obtained from the topographic images showed in figures 5.9 a) and c). b) Height distribution curves and respective gaussian fitted curves obtained by treatment of 1D AFM topographic images *in situ* of Au/PEI/(PSS/PAH)$_4$ and Au/PEI/(PSS/PAH)$_4$/DPPG.

5.3.2 Fractal analysis

Figure 5.10 presents the PSD spectra of Au/PEI/(PSS/PAH)$_4$ and Au/PEI/(PSS/PAH)$_4$/DPPG surfaces profiles. The plateau at low spatial frequencies (region I) $f < 2.2\times10^7$ m^{-1} of the PSD spectra reveals an absence of any characteristic length beyond ca. 45 nm. This region can also give information about height profiles deviations of the surface. Thus, a rather decrease of the magnitude of the power spectra at low frequencies, after DPPG liposomes connection onto the PEM, means that vesicles have contributed to a small reduction of the surface roughness. The region II of PSD spectra obeys to two regimes that are frequency dependent and have a constant slope (sub-regions IIa and IIb). This region characterizes the surface self-affine behavior and involves intermediate frequencies at 2.2×10^7 m^{-1} $< f < 3.1\times10^8$ m^{-1}, representative of a combination of two mechanisms in the course of growth evolution. The region III ($f > 3.1\times10^8$ m^{-1}) of the PSD spectra was not considered for surface analysis as explained above in subsection 5.2.2. At subregion IIb, these PSD spectra have a more smooth corner than the one obtained for DPPG vesicles immobilization on Au or PAH (see figure 5.7 a) and b)) meaning a surface with a higher thickness.

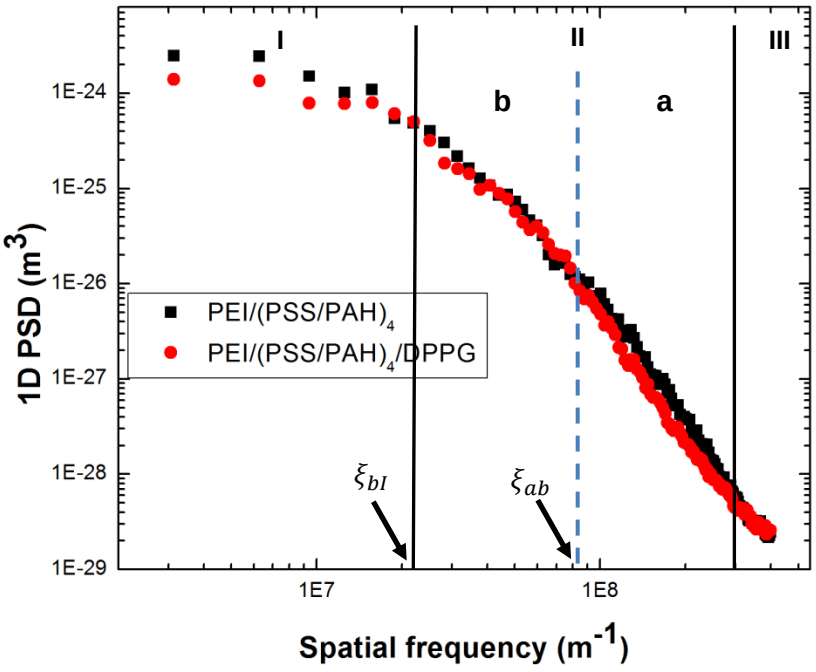

Figure 5.10. Power spectra density of the Au/PEI/(PSS/PAH)$_4$ and Au/PEI/(PSS/PAH)$_4$/DPPG surfaces.

The first (ξ_{ab}) and second correlation length (ξ_{bI}) having each a specific transition frequency and marked with arrows in figure 5.10, can express the mean grain diameter of a self-affine surface, in this case containing two different arrangements. Table 5.10 shows the found values for the two correlation lengths, 9 and 42 nm for Au/PEM, and 13 and 45 nm for Au/PEM/DPPG assigned to the mean grain diameter of gold and PEM surfaces, respectively. Using this model it isn't possible to determine the mean grain diameter of the DPPG vesicles attached to the PEM.

The roughness exponents (α) were estimated by equation 5.1 of the fitted PSD in the two regimes and the found parameters are listed in table 5.10. For both systems the α_b is equal to one, meaning that the growth surface as reached the equilibrium following the diffusion Villain model and the grain morphology approaches to the ideal circular shape. The fact that α_a decreased after the deposition of the DPPG vesicles reveals a reduction of the number of the aggregates on the surface.

Table 5.10. Slopes (γ) and the respective scaling exponents (α) acquired from the subregions a and b and the correlation lengths (ξ) attained for the transition of the *ab* and *bI* zones of the PSD curves of figure 5.10.

LbL film	γ_b	α_b	γ_a	α_a	ξ_{ab} **(nm)**	ξ_{bI} **(nm)**
Au/PEI/(PSS/PAH)$_4$	3.03±0.07	**1.015**	4.42±0.05	**1.71**	9	42
Au/PEI/(PSS/PAH)$_4$/DPPG	3.0±0.1	**1.0**	4.19±0.05	**1.595**	13	45

The region II of the PSD spectra showed in figure 5.10 were also fitted with the $PSD_{fractal}$ model which takes into account the substrate influence and provides the information about the relative amounts of the surface irregularities at different scales. The spectral parameters and *Df* values were estimated using equations 3.8 and 3.9, respectively, and the found values are listed in table 5.11 The spectral indices (ν) for both films are similar. This is also evident in the high-frequency region were the slope of the PSD curves are almost the same. However, the spectral strength (*K*) is higher for the surface with DPPG liposomes. This outcome suggests that this heterostructure has stronger fractal components. Both films have a *Df* almost 2 which indicates that they belong to the category of marginal fractal, being the PEM/DPPG surface more smooth and with less irregularities on its topography than the PEM cushion.

Table 5.11. Spectral index (ν), spectral strength (K) and correlation coefficient (CC) parameters obtained by fitting the PSD curves of figure 5.10 with equation 3.8 and the respective fractal dimensions calculated by equation 3.9.

Fractal contribution ($PSD_{fractal}$ model)							
Au/PEI/$(PSS/PAH)_4$				**Au/PEI/$(PSS/PAH)_4$/DPPG**			
K	***ν***	***Df***	**CC**	***K***	***ν***	***Df***	**CC**
2.5±0.4	2.60±0.05	1.7	0.9945	4.4±0.4	2.86±0.05	1.57	0.99296

Conventional PSD analysis method reveals the correlation lengths for PEM and gold surfaces, but it does not allow the detection of DPPG vesicles on surface. So, a further examination using the ABC or k-correlation model was applied to medium frequencies of the PSD plots of figure 5.10. The PSD plots feature of the samples Au/PEM and Au/PEM/DPPG were characterized using the ABC model and the found A, B and C parameters are shown in table 5.12. The A parameter which is the magnitude at low spatial frequency, has shown to decreases after the DPPG vesicles deposition onto PEM indicating a diminution of the height of the rough surface. The B parameter determines the position of the 'knee', which is defined as the slope of a line connecting two points of the surface and corresponds to the mean grain diameter of the features of a rough surface. The obtained values for this parameter were 50±9 nm and 21.0±0.5 nm corresponding to the mean grain size of PEM and of PEM/DPPG, respectively. It is interesting to observe that the attained mean grain size value for PEM is approximately equal to the ξ_{bI} parameter (42 and 45 nm) calculated by the conventional correlation length method and it is assigned to the PAH polymer domains. The mean grain size of 21.0±0.5 nm found for PEM/DPPG surface approaches to the mean grain hydrodynamic diameter of the DPPG liposomes measured by DLS. Once enhancing the idea that DPPG vesicles immobilize onto PEM surface maintaining its own structure, i.e. without being flattened. Besides, this is a proof of consistence of the ABC analysis method, since it is able to separate correctly the DPPG vesicles component from the total roughness of the sample, in this case the PEM domains. The results attained from this method allow to access observations that would not be possible from the conventional PSD examination. The intrinsic contribution obtained from C parameter outlines the growth mechanisms of the surface under analysis. The value found for the PEM LbL was 2.5±0.4 lying between the condensation mechanism and the bulk diffusion, and for the PEM/DPPG was 4.1±0.1 referring to a surface diffusion. The fractal dimension of the surface can be obtained from the C parameter of the k-correlation model. The *Df* found for PEM was around 2.25 standing between the Brownian fractal and the marginal fractal. The PEM/DPPG reveals a *Df* of 1.46, a value nearly to the marginal fractal. Since *Df* value determines the roughness nature one can conclude that the PEM cushion has a more irregular structure than the PEM/DPPG surface, which is composed by an organized layer of close-packed DPPG vesicles.

Table 5.12. PSD_{ABC} model parameters given by equations 3.10 and 3.11 applied to the region II of the PSD curves of figure 5.10. The correlation coefficient (CC) was obtained from the fit of experimental data to equation 3.10.

LbL films	**Intrinsic contributions (PSD_{ABC} or K-correlation model)**					
	f **(m^{-1})**	**A (nm^3)**	**B (nm)**	**C**	**CC**	***Df_{ABC}***
Au/PEI/$(PSS/PAH)_4$	$[2.2\times10^7:8.8\times10^7]$	2000±418	50±9	2.5±0.4	0.99771	2.25
Au/PEI/$(PSS/PAH)_4$/DPPG	$[2.8\times10^7:1.5\times10^8]$	392±17	21.0±0.5	4.1±0.1	0.99568	1.46

Although the ABC model has proved to be a good tool to apply to the plateau of medium frequencies (subregion IIb of figure 5.10), the PSD spectra is not adapted to this model at the low frequency region (I). It is well known that the low frequency components of the PSD spectra represent the aggregates or superstructures. The presence of such superstructures (or grain clusters) can be extracted from the PSD spectra of these films using the PSD_{sh} model (see equation 3.12). This model was applied to the region I of the PSD plots of figure 5.10 and the found values are listed in table 5.13. The lateral size of the superstructures is given by the τ_{sh} parameter. The results showed values of 43 nm and 87 nm for the τ_{sh} parameter of the PEM and PEM/DPPG surfaces, respectively. This observation leads us to assume that if vesicles with 25 nm of mean hydrodynamic diameter are densely immobilized onto PEM surface, comprising 43 nm of length size, a final value of 87 nm for the superstructures is reliable. This is also a proof that DPPG vesicles are disposed onto PEM domains. However, another superstructure located in the PSD curve at $1.6\text{x}10^7$ m^{-1} frequency (63 nm) could not be fitted due to the reduced number of points. Concluding, after diffusion processes the DPPG vesicles joined to the PEM leading to a duplication of the length size of the PEM mounds and the surface morphology becomes more regular with a lower fractal dimension. Figure 5.11 outlines the ideal model obtained for the Au/PEI/$(PSS/PAH)_4$/DPPG heterostructure.

Table 5.13. Superstructure contribution components (PSD_{sh}). Parameter τ_{sh} describes the mean size of aggregates (superstructures). CC is the correlation coefficient.

LbL films	**Superstructure contributions (PSD_{sh} model)**		
	f_{sh} **(m^{-1})**	τ_{sh} **(nm)**	**CC**
Au/PEI/$(PSS/PAH)_4$	4.4×10^6	43	0.838*
Au/PEI/$(PSS/PAH)_4$/DPPG	4.4×10^6	87	0.917*

* The second superstructure located at f= $1.6\text{x}10^7$ m^{-1} was not taken into account for the PSD_{sh} model.

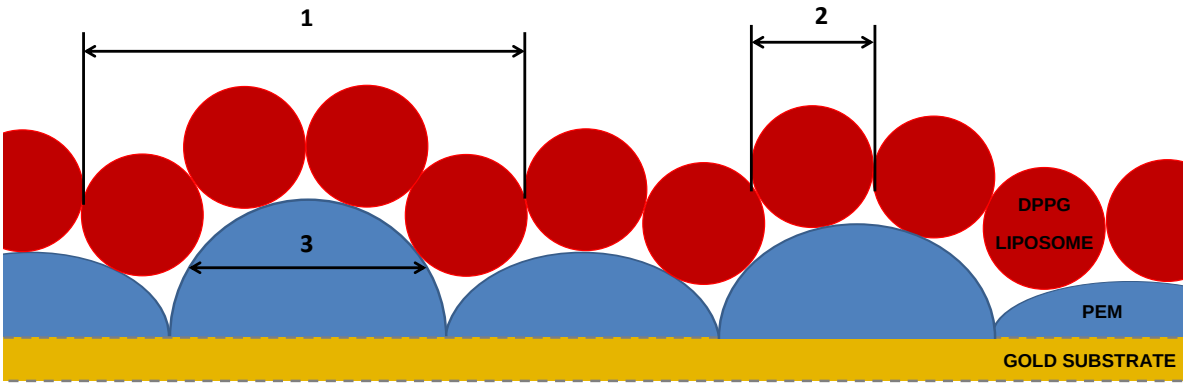

Figure 5.11. Schematic representation of the proposed model for Au/PEI/$(PSS/PAH)_4$/DPPG-liposomes heterostructure, where Au substrate, PEI/$(PSS/PAH)_4$ cushion and DPPG liposomes are displayed in yellow, blue and red colors, respectively. The arrows symbolize the size obtained for each surface feature represented by numbers: 1) lateral size of the superstructures or aggregates of DPPG liposomes achieved by the PSD_{sh} model; 2) size of the DPPG liposomes acquired by the PSD_{ABC} model; 3) size of the PEM grains obtained by the PSD-conventional, PSD_{ABC} and PSD_{sh} models.

5.4 Adsorption Kinetics of DPPG Liposome Layers: A Quantitative Analysis of Surface Roughness

This section provides a quantitative analysis of the adsorption of DPPG liposomes, obtained by sonication, adsorbed onto flat and rough PEMs surfaces containing the same upper layer. The kinetic adsorption parameters obtained by fitting the QCM curves are presented and compared to root-mean-square roughness and mean grain size values extracted from topographic surfaces imaged *ex situ* by AFM, at discriminated DPPG adsorption times.

5.4.1 QCM measurements

DPPG liposomes adsorption kinetics onto PAH and PEI$(PSS/PAH)_4$ polymer cushions with different roughness were obtained from QCM measurements using the SVC system and the adsorbed amounts per unit area were calculated by equation 3.1 [300].

Figure 5.12 shows the DPPG adsorbed amount kinetic curves onto PAH and PEI/$(PSS/PAH)_4$ polymer cushions. The total DPPG adsorbed amount measured onto a PAH cushion was 5±1 mg/m^2, which is in accordance with the value calculated for a planar DPPG bilayer [297].

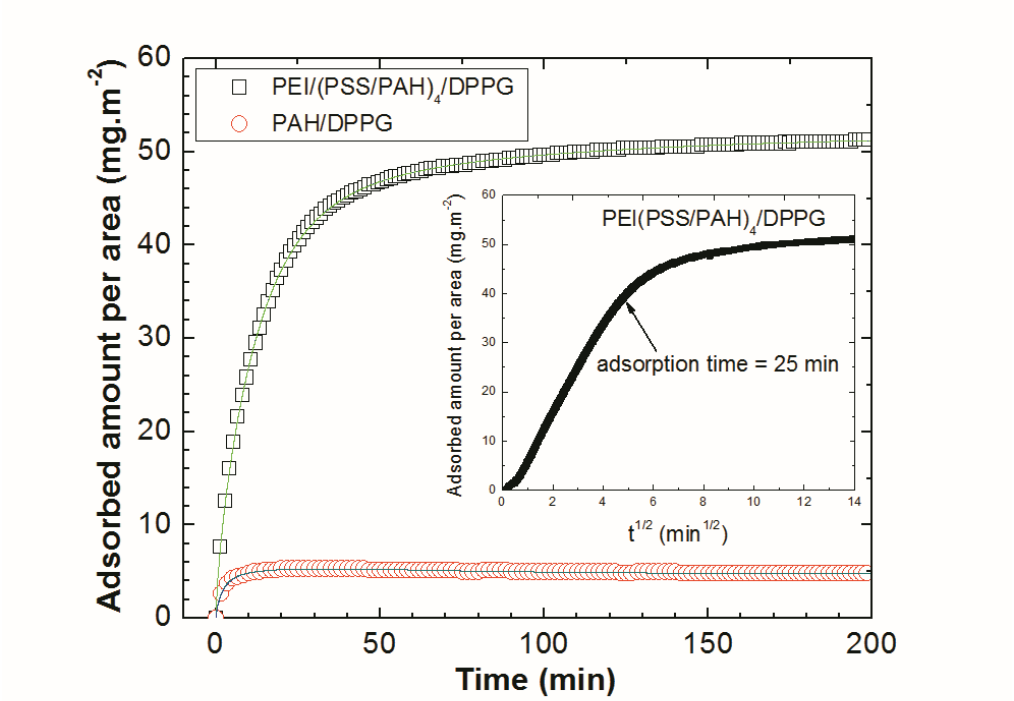

Figure 5.12. Adsorbed amount kinetics of DPPG-liposomes onto PAH and PEI/(PAH/PSS)$_4$ cushions. The inset displays the DPPG adsorbed amount kinetics plotted as a function of $t^{1/2}$.

The DPPG adsorbed amount onto PEI/(PSS/PAH)$_4$ was 51±1 mg/m^2, which is higher than the predicted value for a planar DPPG bilayer, suggesting that most of the DPPG liposomes remained intact. Supposing a layer of close-packed intact DPPG liposomes adsorbed onto a flat surface having the crystal diameter, a mean value of 80 nm for the diameter size for intact liposomes is achieved. This value is however far from the one obtained from the DLS measurements, which indicates a large number of liposomes with 25 nm of diameter size. Even if some large liposomes are being adsorbed, their mass cannot justify the obtained adsorbed amount for DPPG onto PEI/(PSS/PAH)$_4$. However, if the polymer-cushion surface roughness is higher than that of quartz crystal an adsorbed amount of DPPG-liposomes of 51 mg/m^2 is plausible. Assuming 25 nm diameter DPPG liposomes, the surface area would have to be about 3 times larger than the flat support, to be able to adsorb a complete layer of intact liposomes, value that can be easily attained in a rough surface.

Generally, the adsorption kinetics of layers onto LbL films is seen to follow a two processes mechanism as described by the equation 4.1. In the case of polyelectrolyte adsorption, the process with short characteristic time, or the first process, is associated to a nucleation process in which the adsorbed amount is proportional to polyelectrolyte concentration in solution. The second process, or the process with longer characteristic times, is related with diffusion of the polyelectrolyte molecules onto the double layer and due to the replacement of counterions by the polyelectrolyte [266]. The DPPG onto PEI/(PSS/PAH)$_4$ cushion adsorption kinetics data was fitted to this equation and the obtained parameters are displayed in Table 5.14.

Table 5.14. Kinetics parameters for DPPG liposomes adsorption onto PAH and PEM (PEI/(PSS/PAH)$_4$) cushions. The correlation coefficient (CC) parameter was obtained from the fit of experimental data to equation 4.1.

LbL films	Γ_1 (mg/m^2)	τ_1 (min)	Γ_2 (mg/m^2)	τ_2 (min)	n	Γ_3 (mg/m^2)	τ_3 (min)	CC
PAH	2.29±0.02	2.19±0.02	6.45±0.05	22.73±0.06	0.5	-3.81±0.02	64.3±0.2	0.9890
PEM	30.75±0.03	12.87±0.01	21.57±0.03	22.73±0.06	0.5	---	---	0.9999

Regarding the adsorption of DPPG onto PAH, the data was better fitted when a second first order process is added to equation 4.1. The result parameters from fitting the adsorption of DPPG onto PAH are also displayed in table 5.14, where Γ_3 represents the adsorbed amount per unit area and τ_3 is the characteristic time related with this third process.

Parameters listed in table 5.14 reveal that the adsorption of DPPG liposome onto PEI/(PSS/PAH)$_4$ cushion is taking place in two stages. In an initial stage, liposomes migrate to the crystal-PEM surface, being the adsorption governed by both diffusion phenomena and attractive electrostatic forces between the positive PAH layer surface and the DPPG liposomes negatively charged. As the liposomes are being adsorbed, both concentration gradient and electrostatic forces intensity decrease contributing for the establishment of a constant DPPG adsorbed amount. By plotting the adsorbed amount as a function of $t^{1/2}$ as shown in the inset of figure 5.12, a linear behavior can be observed, which confirms diffusion controlled adsorption as follows from Langmuir-Schaeffer equation [301].

Analyzing the parameters displayed in table 5.14, one can infer about the processes that are occurring during the adsorption. For the process with n taking a value of 0.5, process 2, the characteristic time parameter τ_2 obtained is about ~23 minutes, matching with the end of the diffusion controlled process as shown in the inset of figure 5.12. The maximum adsorbed amount associated to this process allows to conclude that about 2/5 of the DPPG liposomes adsorbed are caused by the liposome diffusion to the crystal-PEM surface. Process 1, with a characteristic time of about 13 minutes, is driven by the electrostatic interactions, having its intensity decreased as the liposomes are being adsorbed onto the surface.

The DPPG liposome adsorbed amount data onto PAH cushion was fitted to two first order process plus a process having n equal to 0.5 and a characteristic time of 23 minutes. This latter process was imposed since it is expected that liposomes have a similar diffusion behavior for both cases of presented adsorption. However, experimental data revealed that the maximum adsorbed amount is attained in about 30 minutes, decreasing slightly after that. Such behavior can only be explained by the two other processes: the process having a smaller characteristic time, during which the liposomes adsorb on the PAH surface, and another process associated to phospholipid desorption from the

surface, having larger characteristic time. These processes are in accordance, respectively, with the liposome rupture and desorption of lipids which are in the spatial regions where lipid bilayers edges overlap. This has already been mentioned in literature [67, 75]. Moreover, adsorbed amounts around 5 mg/m^2 indicate a complete coverage by a lipid bilayer as a result of liposome rupture. In addition, it suggests that the liposome rupture is induced by a strong interaction between the liposome and the completely charged PAH surface [6]. The explanation for this behavior has been also reported in literature, whereby the spread of the lipid membrane over a planar surface is favored at low pH, regardless the net charge on the bilayer, process which is driven by van der Waals forces [70]. However, in the present case the difference between the PAH layer deposited on gold and that on the PEM surface, is the surface morphology itself, as one expects the PEM surface is rougher than the PAH single layer. To conclude about the roughness, the topographies of these surfaces were measured and its characterization will be described in next section.

5.4.2 AFM topographic images

Topographic images from PAH and $PEI/(PSS/PAH)_4$ cushions deposited onto Au-coated quartz crystal surfaces both with DPPG adsorbed at different times, were obtained by AFM. Topographic images with an area of 2×2 μm^2 of a) Au/PAH, b) Au/PAH/DPPG, c) $Au/PEI/(PSS/PAH)_4$ and d) $PEI/(PSS/PAH)_4$/DPPG are shown in figure 5.13 a), b), c) and d), respectively. The DPPG adsorption time was 5 minutes. Table 5.15 displays the root-mean-square roughness (Rq) and the mean grain size quantities. Grain size values were obtained from statistical treatment of the topography by the method described by Itoh *et al* [193]. One must to be aware that Rq calculations for rough surfaces, in cases of large polyelectrolytes aggregates and/or liposomes, leads to large error bars which in certain samples attains values of 40%. It should be referred that the error bars correspond to Rq standard deviation calculated from all individual row/column values of a unique topographic image data.

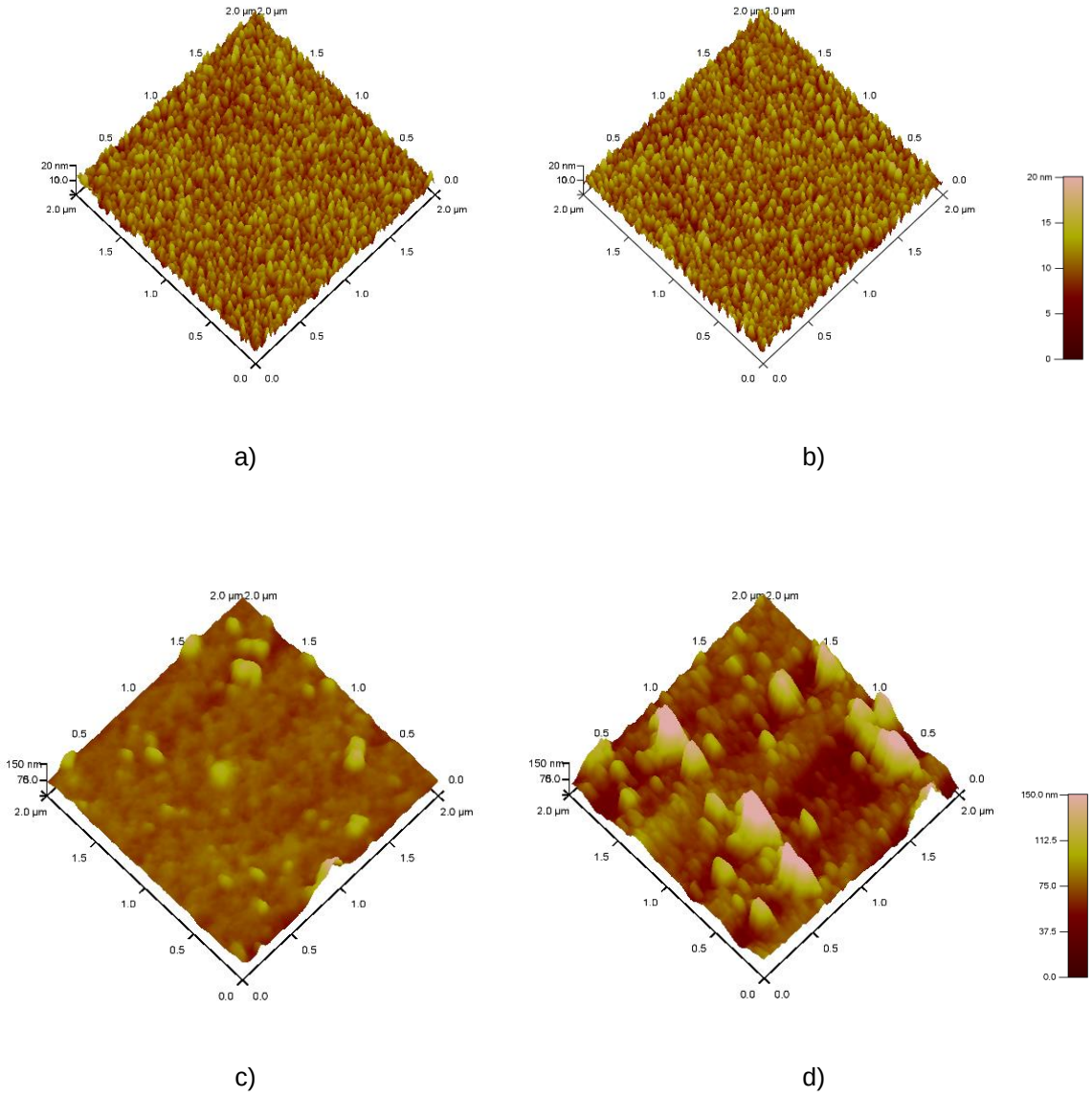

Figure 5.13. Topographic images with $2\times2\mu m^2$ area of a) Au/PAH, b) Au/PAH/DPPG c) Au/PEI/(PSS/PAH)4 and d) PEI/(PSS/PAH)4/DPPG surfaces. The adsorption time of DPPG in b) and d) was 5 minutes.

From table 5.15, the Rq values, considering 0.5x0.5 μm^2 scan areas, indicate that roughness of PAH layer adsorbed onto Au-coated quartz crystal is 0.2 nm higher than that of the gold surface, while the PEI/$(PSS/PAH)_4$ PEM is 2.6 nm higher. This result is consistent since as the number of layers increases the roughness also increase, as a result of coil-like conformation polyelectrolyte during adsorption which results in nonlinear buildup behavior [262].

Table 5.15. Surface parameters obtained from statistical treatment of the AFM images. Topographic data was obtained from a measured area of 2×2 μm^2 and the roughness was also calculated in scan areas of 0.5×0.5 μm^2.

Surface	**DPPG time adsorption (s)**	**Rq (nm)**		**Mean grain Size (nm)**
Scanned Area	---	0.5×0.5 μm^2	2.0×2.0 μm^2	2.0×2.0 μm^2
Au	---	1.4±0.2	1.5±0.2	8±1
Au/PAH	0	1.6±0.3	1.7±0.2	5.4±0.6
	5	1.9±0.4	1.9±0.3	4.8±0.7
	30	1.8±0.3	1.8±0.2	4.0±0.8
	60	2.0±0.6	2.1±0.9	5.8±0.6
	300	1.8±0.3	1.9±0.2	5.0±0.7
	900	1.5±0.3	1.6±0.2	5 ±2
	1800	1.5±0.3	1.5±0.2	6.5±0.9
Au/PEI(PSS/PAH)$_4$	0	4±1	7±4	31±4
	5	7±1	19±6	42±2
	30	7±2	17±9	42±13
	60	7±2	14±4	31±5
	300	9±2	22±8	40±3
	900	9±5	29±11	49±5
	1800	8±2	22±7	24±3

5.4.3 Adsorbed amount and roughness kinetics – a comparison

The Rq values obtained for different DPPG adsorption times were plotted together with the respective QCM kinetics curves, as shown in figure 5.14 a) and b). For the case of PAH cushion, the roughness increases during the first few minutes, which coincides with the first fast process, with a smaller characteristic time. Afterwards the roughness decreases to a constant value, revealing that the liposomes are being disrupted at the surface and the lipids re-organized, in accordance with desorption as revealed by the third adsorption kinetics process. The Rq of PEI/(PSS/PAH)$_4$ cushion surface as a function of adsorption time, as seen in figure 5.14 b), increases up to a constant value which is consistent with liposomes structural integrity preservation. The Rq values attained in both cases, 1.5 nm and 22 nm, respectively, for liposomes adsorption on PAH and on PEI/(PSS/PAH)$_4$

cushions can be now compared with liposome sizes values of table 4.15, allowing to conclude that the liposomes disrupt on PAH layer while in PEI(PSS/PAH)$_4$ cushion structure integrity is maintained.

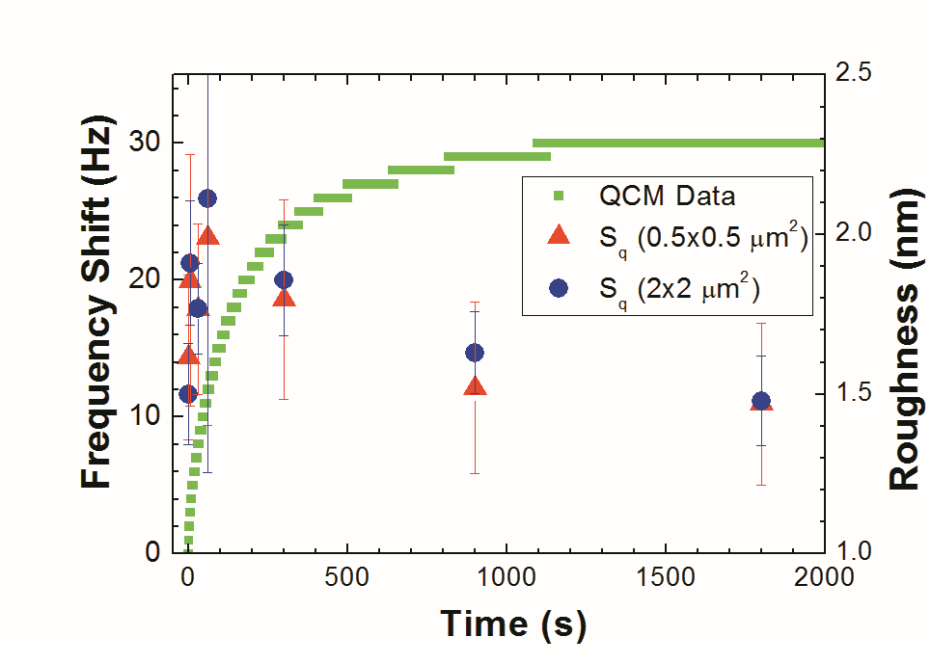

a)

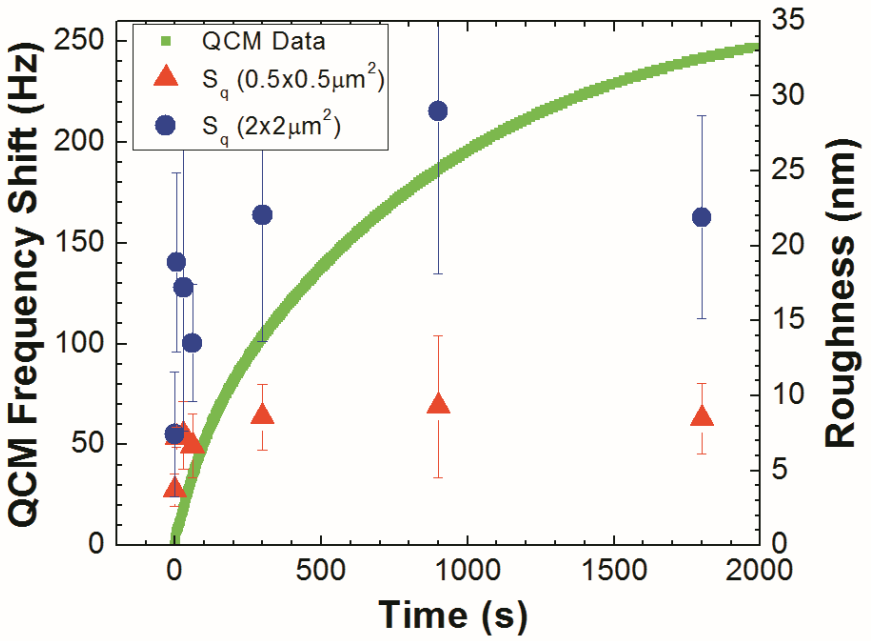

b)

Figure 5.14. DPPG adsorbed amount per unit of area and roughness values obtained from 0.5×0.5μm^2 (triangles) and 2×2μm^2 (circles) topographic images of DPPG liposomes adsorbed during different periods of time onto: a) PAH and b) PEI/(PSS/PAH)$_4$ cushions.

This conclusion is also consistent with the mean grain size values for the case of DPPG-liposomes adsorption onto the PEM cushion as a function of adsorption time as shown in figure 5.15, which reveals grain sizes values close to the liposome diameter, however the mean value is somewhat higher indicating that, in certain cases, the liposomes are immobilized on surface in a flattened arrangement. The liposomes flattening can occur during its deposition onto solid supports, by vesicles deformation during topography measurements as a result of interactions with the tip and by irregular distribution of liposomes on surfaces due to physical interactions [263].

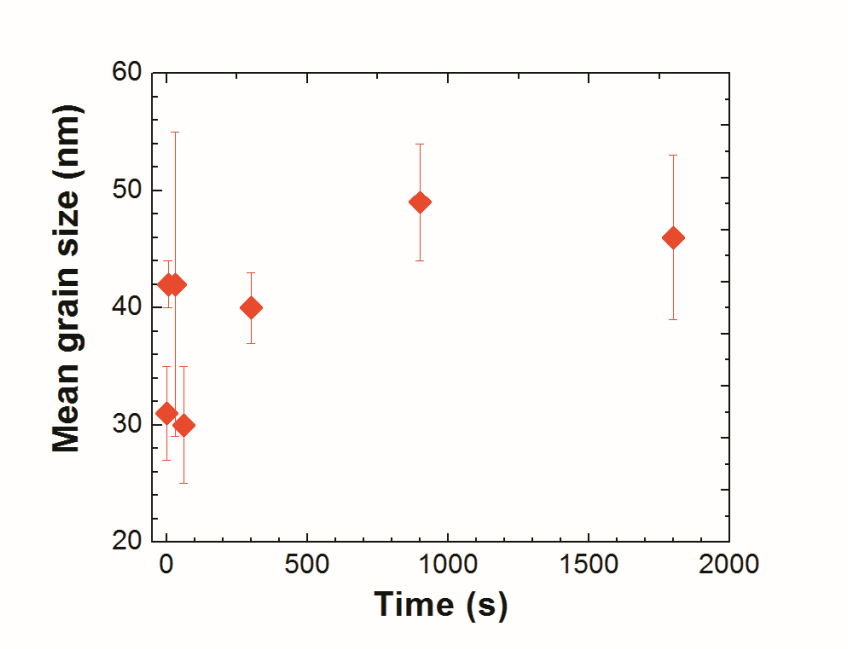

Figure 5.15. Mean grain size values of topographic images PEI/(PSS/PAH)$_4$/DPPG with 2×2μm^2 area versus DPPG time adsorption on PEI/(PSS/PAH)$_4$.

Roughness data obtained as a function of DPPG adsorption time onto PAH cushions show an increase in roughness within the first 2 min, which can be associated with the first liposomes adsorbed on the surface without rupture, followed by a decrease in roughness as a result of liposome rupture. In addition, the grain size seems to follow the grains of the gold surface, indicating once more rupture of liposomes. The fact that the values calculated from different scan areas follow similar behavior should be taken into consideration.

5.4.4 Roughness as a measure of surface hydrophobicity at its contribution for rupture or maintenance of intact liposomes

Adsorption of DPPG liposomes onto the PEI/(PSS/PAH)$_4$ cushion suggests that the surface morphology evolution arises from adsorption of particles with self-organization behavior which, leads to a fractal surface as already observed in polyelectrolytes adsorption [179, 302-304]. For those self-affine surfaces, the Rq is dependent of both scan length and adsorption time parameters. A relation

between roughness and roughness scaling parameters describing self-affine surfaces has been introduced by Family and Vicsek [305] by considering two parameters to give information about processes involved in surface creation in terms of topography and growth. These parameters are the spatial scaling exponent, α, and the temporal growth exponent, β, obtained by the equations 3.14 and 3.13, respectively.

Roughness data obtained as a function of adsorption time of DPPG onto PEI/$(PSS/PAH)_4$ cushion allows to determine a growth exponent of 0.19±0.07 and a value of about 0.84 for the roughness exponent. This last value is presented without error because it was calculated only from roughness calculated in two scanned areas. Comparing these values with those obtained for different self-affine fractal models, it is possible to conclude that the adsorption follows the Villain's model [306]. This model considers a simple growth process where particles are randomly deposited onto a substrate and subsequently relax into a nearby position, where the binding is strongest. This mechanism is consistent with the prevalent electrostatic interactions between the DPPG liposomes and the last PAH layer of the PEM.

However, roughness per se cannot explain the phenomena underlying liposomes adsorption onto rough surfaces which guarantees liposome integrity. With respect to this issue, in the 90's hydrophobicity and roughness concepts began to be related [307] and in 2000 Herminghaus [294] demonstrated theoretically that certain class of self-affine profiles of surface roughness can induce hydrophobicity. Moreover, an increase of roughness was shown to give rise to an increase of surface hydrophobicity, as demonstrated by Jung and Bhushan [308-310]. In fact, water contact angle measurements of PAH/PSS films indicate [6] that rough films present higher contact angle and consequently are more hydrophobic. Recently, Herminghaus [311] presented an analytic theory which allows calculation of the wetting-phase diagram, adsorption isotherms, and percolation threshold of the adsorbed liquid film, for isotropic randomly rough substrates with arbitrary lateral correlation function and height distribution. As a result, it has been demonstrated that the roughness influences the adsorption phenomena and is associated to surface hydrophobicity. Consequently, liposome rupture can be controlled by the surface hydrophobicity. An increase in hydrophobicity reduces the number of water molecules on the PAH surface, contributing for counterions anchorage near PAH ionic groups, thus reducing the electrostatic forces between the liposome and the PAH layer and consequently preventing the liposome rupture.

5.5 Adsorption of DPPG liposome on different roughness cushions: analysis of adsorbed amount, surface composition and topography

Various polyelectrolyte multilayers (PEMs) with different number of layers and roughness, having as upper layer the charged PAH polyelectrolyte, were assembled onto Au-quartz crystal resonators. The assembly of intact DPPG vesicles, obtained by sonication procedure, onto these PEMs was monitored by QCM using the SVC setup and kinetic adsorption parameters were inferred. Surface topographies of the samples were *ex situ* imaged by AFM in non-contact mode and the amplitude parameters were

extracted. Grain values of the surface features were attained from PSD spectra of these surfaces using a combination of three PSD models, such as fractal, ABC or K-correlation and superstructures. Moreover, the elemental compositions of PEM and PEM/DPPG LbL films as well as binding energies of organic groups of the molecules were achieved by XPS analysis.

5.5.1 DPPG Adsorption Kinetics

Adsorption kinetic curves of DPPG liposomes onto PEI/$(PSS/PAH)_b$ polymer cushions with different number of bilayers, *b*, are shown in Figure 5.16 a). The curve of DPPG liposome adsorption kinetics onto a PAH layer is also included in this figure for comparison. It was shown that the total amount of DPPG adsorbed onto a PAH layer is 5±1 mg/m^2 which is in accordance with the theoretical value calculated for a planar DPPG bilayer. The final amount of DPPG adsorbed per unit of area onto PEI/$(PSS/PAH)_3$ and PEI/$(PSS/PAH)_4$ is close to 51±1 mg/m^2, a value higher than that one predicted for a planar DPPG bilayer, suggesting that the most of the immobilized DPPG liposomes remained intact. Supposing a layer of DPPG liposomes close-packed adsorbed onto a flat surface, a value of 16 mg/m^2 is achieved for the adsorbed amount per unit of area, for vesicles with a diameter of 25 nm. However, if the surface roughness of the polymer-cushion is higher than that of the quartz crystal, an adsorbed amount of DPPG-liposomes of 51 mg/m^2 is plausible. Assuming a 25 nm diameter of the liposomes, in order to be able to adsorb a complete layer of intact liposomes the surface area should be 3 times larger than that of the flat quartz crystal, a value easily attained in a rough surface.
Generally, the adsorption kinetics of layers assembled onto LbL films are seen to follow two or three processes as described in ref. [16]. Though, the adsorption behavior described by the kinetic curves can be interpreted by fitting the experimental data with a general theoretical curve such as:

$$\Gamma = \Gamma_{max}\left(1 - exp\left(-\left(\frac{t}{\tau}\right)^{n}\right)\right) \qquad (5.1)$$

where Γ is the adsorbed amount per unit area, Γ_{max} is the maximum amount adsorbed at the end of the process, τ is the characteristic time of adsorption and n is the exponent of time which is related with the type of adsorption process that is taking place. The adsorption parameters obtained from fitting the kinetic data of the DPPG liposomes to equation 5.1 are listed in table 5.16. To identify the general trends for the different number of adsorbed cushion bilayer, b, the maximum adsorbed amounts and characteristic times, were plotted in figure 5.16 b). In Figure 5.16 c), the n parameter was also plotted as a function of the cushion number of bilayers, b.

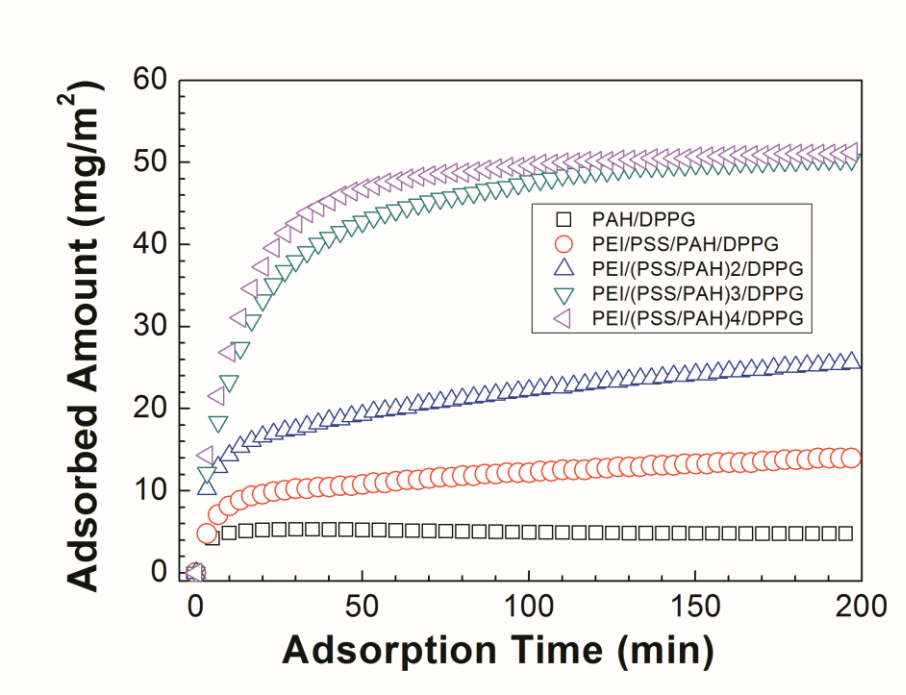
Adsorbed Amount (mg/m^2)
Adsorption Time (min)
PAH/DPPG
PEI/PSS/PAH/DPPG
PEI/(PSS/PAH)2/DPPG
PEI/(PSS/PAH)3/DPPG
PEI/(PSS/PAH)4/DPPG

a)

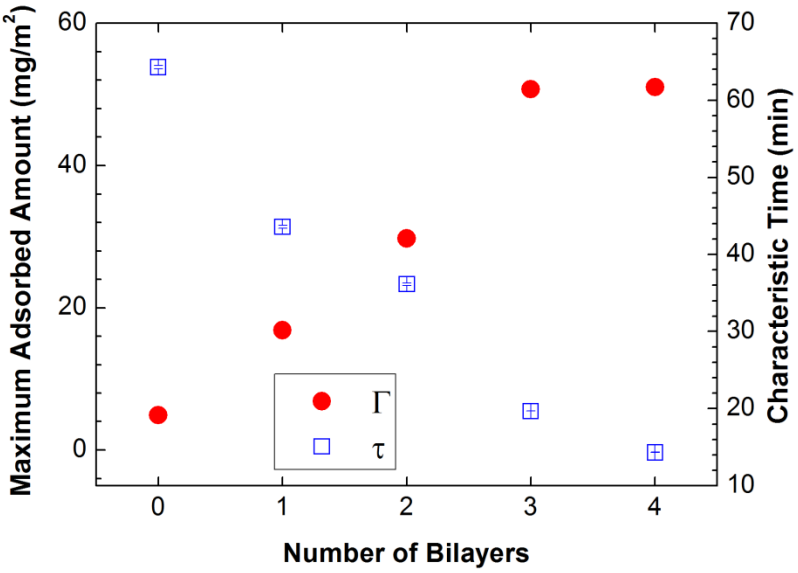
Maximum Adsorbed Amount (mg/m^2)
Characteristic Time (min)
Number of Bilayers
Γ
τ

b)

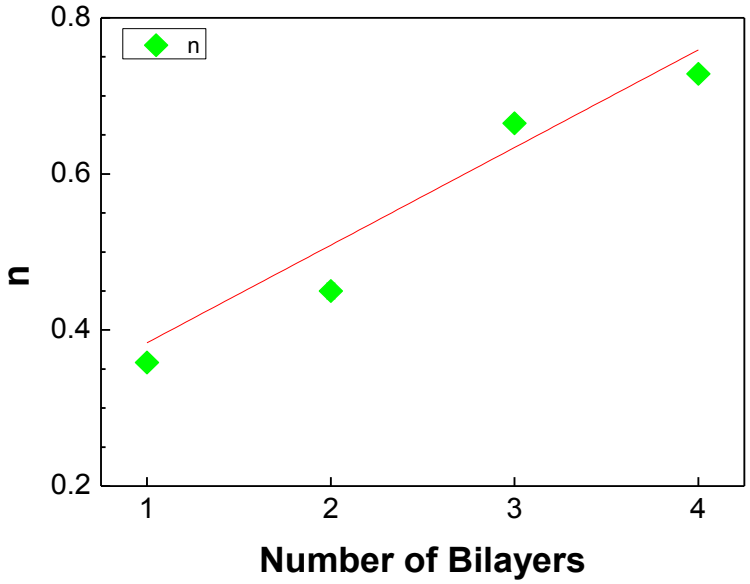

c)

Figure 5.16. a) Kinetics of the adsorbed amount Γ of DPPG-liposomes onto PEI/(PAH/PSS)$_b$ cushions. b) Maximum adsorbed amount Γ_{max} and characteristic time τ as a function of the number of bilayers in the cushion, b. c) The evolution of parameter n with the number of bilayers in the cushion.

Table 5.16. Adsorption parameters obtained from the fitting of DPPG liposome kinetics curves.

LbL films	DPPG Kinetic Parameters			
	Γ_{max} (mg/m^2)	τ (min)	n	CC
PEI/PSS/PAH	16.87±0.02	43.6±0.7	0.3583±0.0008	0.98647
PEI/(PSS/PAH)$_2$	29.74±0.02	36.1±0.2	0.45±0.01	0.98449
PEI/(PSS/PAH)$_3$	50.713±0.005	19.69±0.02	0.6648±0.0005	0.99852
PEI/(PSS/PAH)$_4$	51.029±0.004	14.33±0.01	0.7281±0.0006	0.99842

5.5.2 XPS Characterization

Quantitative information may be extracted from XPS data, even if in the present case of systems that are stratified in nature, the obtained values should be considered as just a qualitative indication [253]. Nevertheless, all the BE and elemental composition values resulting from XPS are listed in Table 5.17. The XPS survey spectrum of PEI/(PSS/PAH)$_4$ LbL films revealed the presence of carbon, oxygen, nitrogen, sulfur, chlorine and sodium, as expected. However, for PEI/(PSS/PAH)$_4$/DPPG the presence of sulphur, chlorine and sodium is just residual; but phosphorus, absent in the first one, is now clearly seen. Since sulfur, chlorine and sodium are constituents of the LbL cushion and phosphorus is only present on DPPG, this first result shows clearly that DPPG covered the entire cushion surface.

The analysis of the detailed regions was also performed. The N 1s spectrum was fittable, for PEI/(PSS/PAH)$_4$ sample, with two components (constrained to the same FWHM = 1.9±0.2 eV and the same Gaussian-Lorentzian percentage) centered at 399.5±0.2 and 401.6±0.1 eV and assignable to amine (>NH) and protonated amine (>NH_3^+), respectively [312]. In the sample with DPPG, the nitrogen signal is much weaker and only the second component could be fitted.

The S 2p presents a single doublet for PEI/(PSS/PAH)$_4$ sample: the component S 2p$_{3/2}$ centered at 168.1±0.2 eV and the component S 2p$_{1/2}$ is centered at 169.5±0.2 eV. This doublet is assignable to the SO_3^- group in PSS; it is perfectly defined for the PEI/(PSS/PAH)$_4$ sample and just residual for the PEI/(PSS/PAH)$_4$/DPPG one, as already verified in the survey spectrum. Cl 2p, in the PEI/(PSS/PAH)$_4$ sample, presented two doublets with a spin-orbit split of 1.6±0.1 eV, the components Cl 2p$_{3/2}$ being centered at 198.0±0.1 eV and 200.1±0.2 eV. The presence of these two doublets is most likely related to a differential charging in the sample, due to the different location of the Cl^- ion (next to the polyelectrolyte chain or integrated into NaCl nanocrystals) [63]. In the presence of DPPG, Cl 2p became so weak that a detailed fitting was not possible. Na 1s was centered at 1071.7±0.2 eV and, once again, it was just residual in the sample covered with DPPG. Spectra of the sample with DPPG adsorbed onto the cushion presented the peak associated to phosphorus, P 2p, which is also a single doublet: the component P 2p$_{3/2}$ centered at 133.5±0.2 eV and the component P 2p$_{1/2}$ centered at 134.3±0.2 eV.

For the case of PEI/(PSS/PAH)$_4$ sample, the O 1s peak was fitted with two components, one centered at 531.6±0.2eV, assigned to oxygen in PSS sulphonate groups and another one centered at 533.3±0.1eV, tentatively, assigned to water entrapped in the film. For the case of the PEI/(PSS/PAH)$_4$/DPPG sample, the O 1s peak was also fitted with two components, but one is centered at 531.3±0.2eV, assigned to the oxygen of phosphate and another centered at 532.8±0.1 eV that can be attributed to a mixture of ether and carbonyl oxygen in DPPG.

Concerning the sodium, the Na 1s spectrum was fitted with a single peak centered at 1071.7±0.2 eV.

Carbon, in the cushion, could be fitted with the components assignable to PSS and PAH groups, centered in the expected BE and in the expected quantitative proportions. In the DPPG covered sample, peaks corresponding to DPPG were adequate to fit the C 1s region; namely, $\pi \rightarrow \pi^*$ loss, due to the PSS π system not being detected.

Table 5.17. Binding energies and XPS elemental composition in atomic percentage, for PEI/(PSS/PAH)$_4$ and PEI/(PSS/PAH)$_4$/DPPG films. Relative error do not exceed ±10%.

	PEI/(PSS/PAH)$_4$			**PEI/(PSS/PAH)$_4$/DPPG**		
	BE(eV)	**Atomic %**	**Assignment**	**BE(eV)**	**Atomic %**	**Assignment**
C 1s 1 (PSS)	284.7	24.0	C-C,C-H (sp^2)			
C 1s 2 (PSS)	285.0	9.6	C-C,C-H (sp^3)	285.0	66.8	C-C, C-H (sp^3)
C 1s 3 (PSS)	285.2	4.8	C-S	286.6	10.1	C-O, C-N^+
C 1s 4 (PAH)	285.3	17.3	C-C, C-H	289.0	3.7	O-C=O^-
C 1s 5 (PAH)	286.5	8.7	C-N+			
C 1s 6 (PSS)	291.3		π-π*			
O 1s 1	531.6	13.6	O-S	531.3	5.7	O-P, O=C
O 1s 2	533.3	1.9	Entrapped H_2O	532.8	10.5	O-C
N 1s 1	399.5	0.5	>N-			
N 1s 2	401.6	5.8	>N^+<	401.4	1.6	>N^+<
Cl 2p$_{3/2}$ 1	198.0	3.2	see text		nq	
Cl 2p$_{1/2}$ 1	199.5	1.6				
Cl 2p$_{3/2}$ 2	200.1	1.5				
Cl 2p$_{1/2}$ 2	201.6	0.7				
S 2p$_{3/2}$	168.1	2.8	SO_3^-		nq	
S 2p$_{1/2}$	169.5	1.4				
Na 1s	1071.7	2.6	Na^+		nq	
P 2p$_{3/2}$				133.5	1.2	P-O
P 2p$_{1/2}$				134.3	0.6	

From the above results, we can conclude that the DPPG covers the LbL cushion very efficiently and that the charge compensation occurs between the phosphate group in the DPPG and the protonated amine in the PAH and does not involve (or it does to only a much lower extent) the sodium ion.

5.5.3 AFM analysis

AFM *ex situ* topographic images with an area of 2×2 μm^2 from PEI(PSS/PAH)$_b$ cushions, with b varying from 1 to 4 before and after adsorption of DPPG for 15 hours are presented in fig 5.17. From the analysis of the topographic data we calculated the root-mean-square roughness (Rq) parameters which are displayed in Table 5.18.

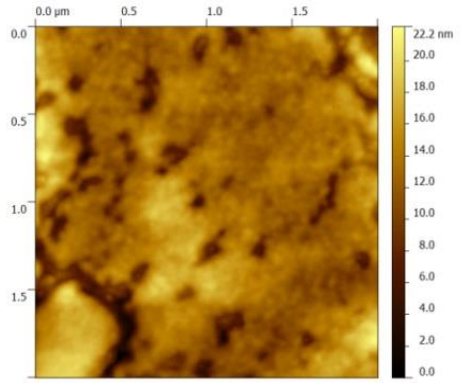
0.0 µm
0.5
1.0
1.5
22.2 nm
20.0
18.0
16.0
14.0
12.0
10.0
8.0
6.0
4.0
2.0
0.0

a)

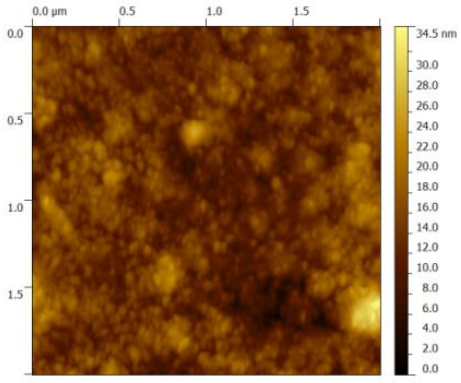
0.0 µm
0.5
1.0
1.5
34.5 nm
30.0
28.0
26.0
24.0
22.0
20.0
18.0
16.0
14.0
12.0
10.0
8.0
6.0
4.0
2.0
0.0

b)

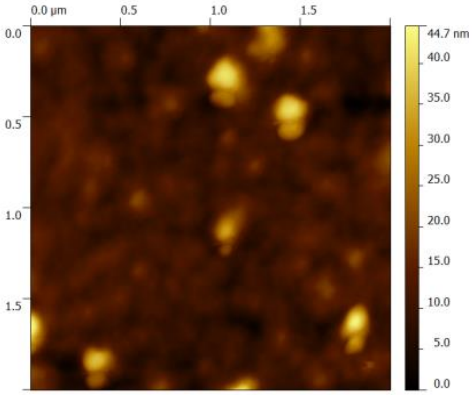
0.0 µm
0.5
1.0
1.5
44.7 nm
40.0
35.0
30.0
25.0
20.0
15.0
10.0
5.0
0.0

c)

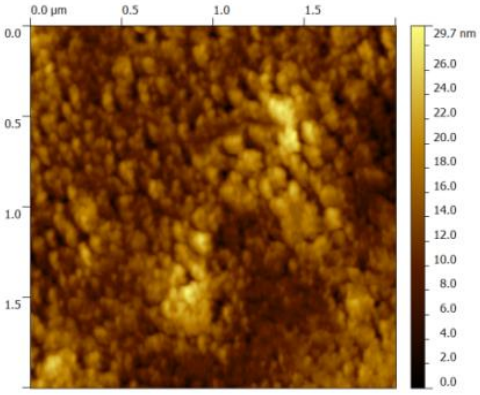
0.0 µm
0.5
1.0
1.5
29.7 nm
26.0
24.0
22.0
20.0
18.0
16.0
14.0
12.0
10.0
8.0
6.0
4.0
2.0
0.0

d)

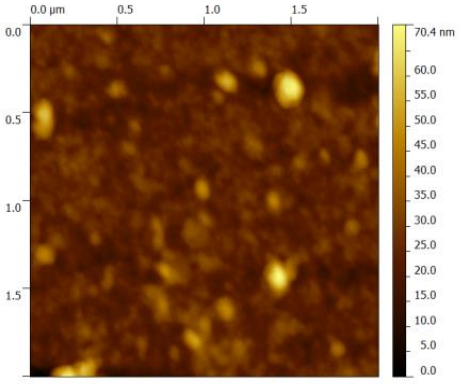
0.0 µm
0.5
1.0
1.5
70.4 nm
60.0
55.0
50.0
45.0
40.0
35.0
30.0
25.0
20.0
15.0
10.0
5.0
0.0

e)

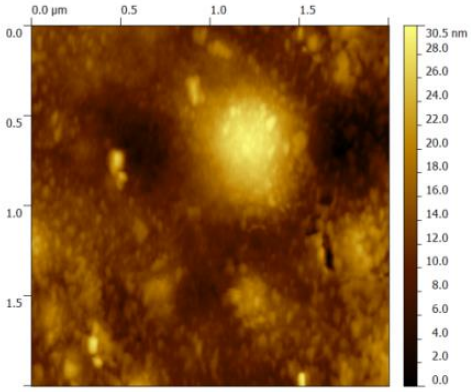
0.0 µm
0.5
1.0
1.5
30.5 nm
28.0
26.0
24.0
22.0
20.0
18.0
16.0
14.0
12.0
10.0
8.0
6.0
4.0
2.0
0.0

f)

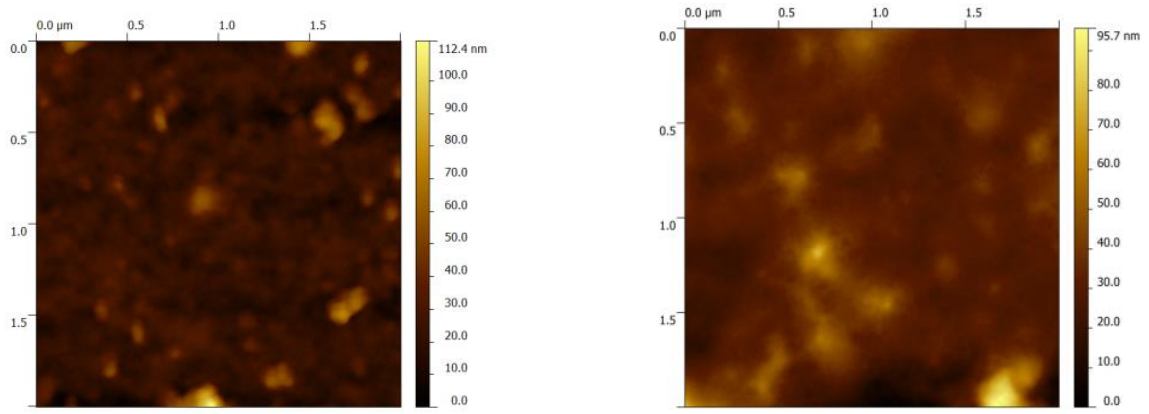

g) h)

Figure 5.17. Topographic images with $2\times2\mu m^2$ area of a) $PEI/(PSS/PAH)_1$; b) $PEI/(PSS/PAH)_1$/DPPG; c) $PEI/(PSS/PAH)_2$; d)$PEI/(PSS/PAH)_2$/DPPG; e) $PEI/(PSS/PAH)_3$; f) $PEI/(PSS/PAH)_3$/DPPG; g) $PEI/(PSS/PAH)_4$ and h) $PEI/(PSS/PAH)_4$/DPPG surfaces. The adsorption time of DPPG was of 15 hours.

Table 5.18 Root-mean-square roughness (Rq) values obtained from surface topographies of $PEI/(PSS/PAH)_{1<b<4}$ and $PEI/(PSS/PAH)_{1<b<4}$/DPPG imaged by AFM. Topographic data was obtained from a measured area of 2×2 μm^2.

PEM	**Rq (nm)**
PEI/PSS/PAH	2.9±0.3
$PEI/(PSS/PAH)_2$	5.0±0.5
$PEI/(PSS/PAH)_3$	6.0 ±0.6
$PEI/(PSS/PAH)_4$	8.5±0.3
DPPG onto PEM	**Rq (nm)**
PEI/PSS/PAH/DPPG	3.2±0.2
$PEI/(PSS/PAH)_2$/DPPG	4.0±0.8
$PEI/(PSS/PAH)_3$/DPPG	4.6 ±0.5
$PEI/(PSS/PAH)_4$/DPPG	9.0±0.4

The topographic images also allow to determine the curves of height distributions (HD) before and after DPPG liposomes adsorption onto PEI/(PSS/PAH)$_b$ cushion. In figure 5.18 the HDs are plotted for the cases of b=1 and b=4, for comparison. As the number of layers, b, in the cushion increases, these distributions show an increase of the maximum height. When comparing the cushions PEI/(PSS/PAH)$_1$ and PEI/(PSS/PAH)$_1$/DPPG, only a small increase of the maximum height is observed (a couple of nm), while an increase of ~10 nm is found when one compares the HDs associated to PEI/(PSS/PAH)$_4$ and PEI/(PSS/PAH)$_4$/DPPG. A similar increase is found when heights are compared at maxima for the DPPG-free cushions with number of layers between 1 and 4. This value can be easily explained if one considers that the liposomes have hydrodynamic diameter of ~25 nm as measured by DLS, and then they are being adsorbed intact.

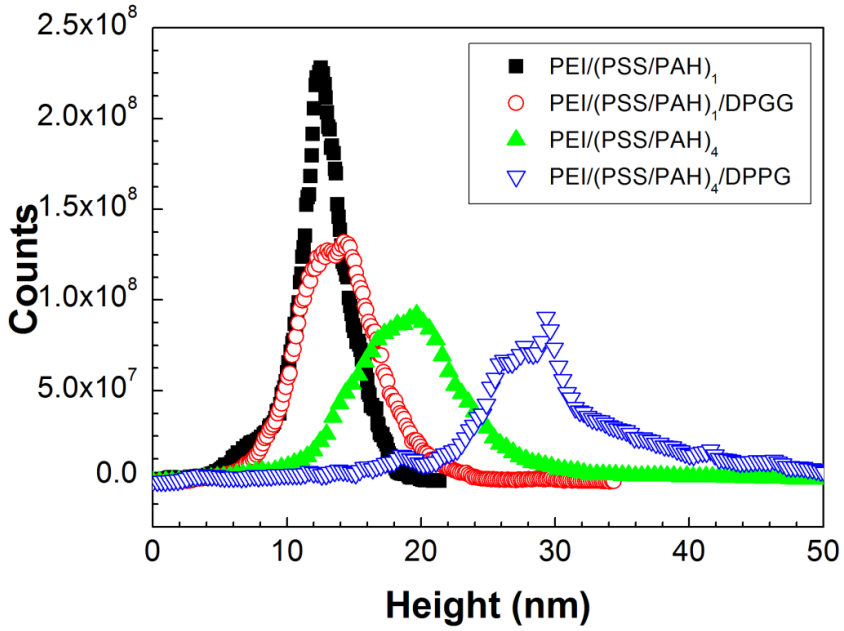

Figure 5.18. Height distribution of AFM topographies before and after adsorption of DPPG onto PEI/(PSS/PAH)$_b$ cushion; with b=1 and b=4.

5.5.4 Grain analysis

The power spectral density (PSD) curves can provide improvement in grain analysis of the characterized surfaces. These spectra were calculated from topographies images of figure 5.17. In the present case the studies were done using the one-dimensional (1D) power spectral density which takes into account the surface profiles measured along the AFM fast-scan direction and because of this the units are in m^3. The obtained PSD curves are plotted in Figure 5.19 a) and b) for the surfaces of PEI/(PSS/PAH)$_b$ cushions and for the same cushions with DPPG liposomes adsorbed, respectively.

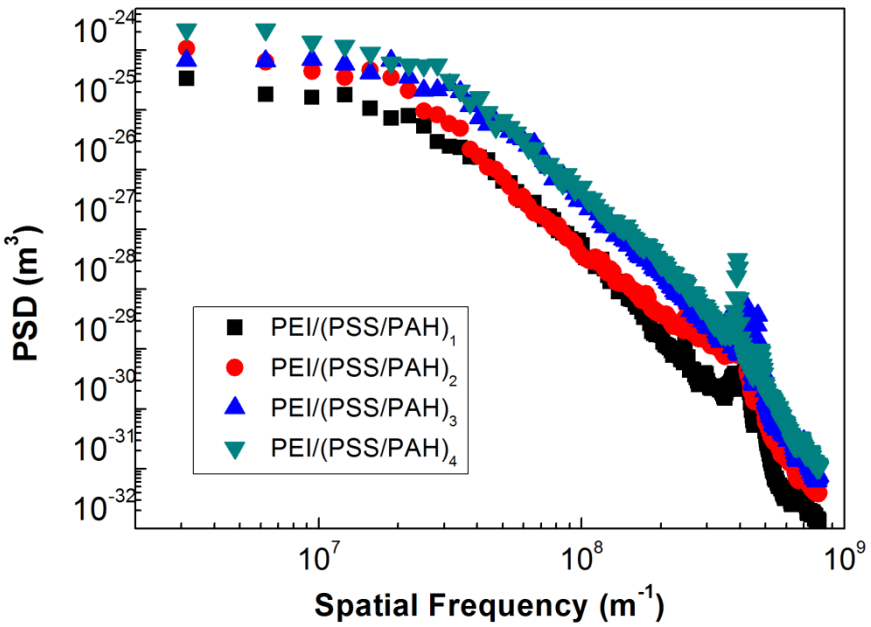

a)

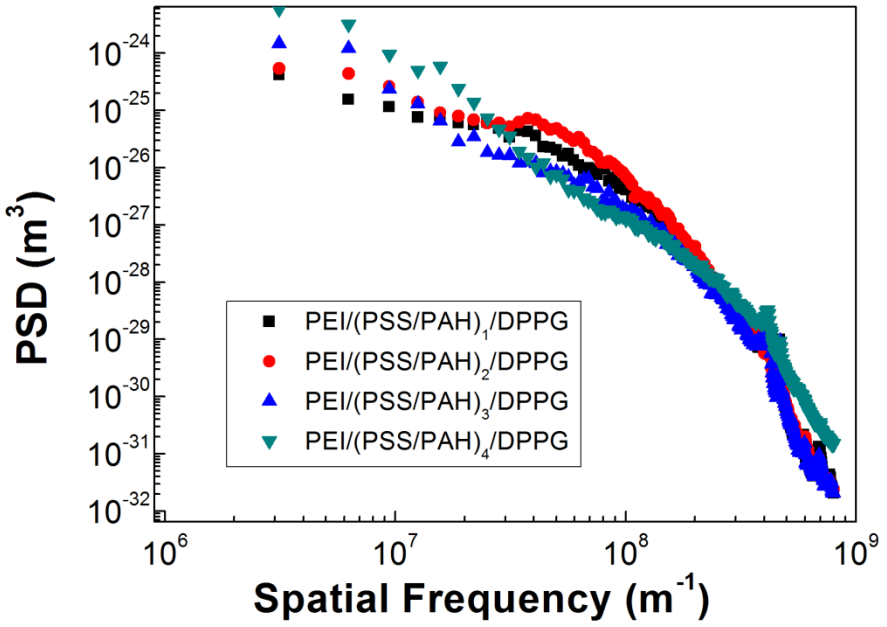

b)

Figure 5.19. Plot of the PSD functions versus spatial frequency, corresponding to: a) cushions with different number of bilayers, b, and b) same cushions as in a), but after adsorption of DPPG.

The PSD plots can be analyzed by a combination of different models applied to extract information retained in these curves. An overview of models applied in surface characterization can be found in ref. [190]. In accordance with these models one can interpret the obtained data in different regions. Therefore in the case of PSD curves of figure 5.19 a), one can find two well defined regions. For high spatial frequencies the PSD function reflects the roughness contribution from all features of the surface and in this case the PSD follows the inverse power law decay (equation 3.8). The ν index allows determining the fractal dimension (D_f) which in turn can be used to quantify the surface morphology. The D_f values can be calculated in the case of PSD at one dimension by equation 3.9. For medium-low spatial frequencies, the PSD curve can be explained by the ABC model or the k-correlation model and allows determining the mean grain size. This model, is a generalization of the fractal behavior, and presents a flat response below a cut-off frequency, followed by a decrease of the PSD values with the increase of spatial frequency, as described by the equation 3.10. This would permit the comparison of different methods of measuring the same morphological parameter.

By analyzing the PSD data associated to samples with the DPPG adsorbed onto cushions, figure 5.19 b), one can find that these curves cannot be associated only to those models. It is necessary to consider the superstructure PSD model, PSD_{sh}, which makes possible characterize aggregates or superstructures formed on the surface, and it's represented by the equation 3.12.

These models were used to fit the PSD curves present in Figure 5.19 a) and b) and the calculated parameters are displayed in Table 5.19. The analysis of data listed in Table 5.19 reveals that the surfaces of all samples follow the fractal model for higher spatial frequency, revealing that the fractal dimension Df, parameter which provides information about the surface irregularities, increases as the number of bilayers of the cushions rises. In the case of the PEI/$(PSS/PAH)_b$ cushions, the changes in *Df* are not significant. However, in the case of DPPG adsorbed on the cushion, the evolution of the *Df* is significant and indicates that for cushions with few layers the surface is flat, suggesting the rupture of the liposomes. Nonetheless, for the case of cushions with higher number of bilayers, *Df* is approaching a value of 2, indicating that the surface is rough and therefore liposomes are being adsorbed intact.

The parameter A calculated from fitting the 1D PSD data to ABC model is associated to the height of the low spatial frequency plateau. A generally increases for the case of cushions with DPPG, and decreases for the case of DPPG adsorbed to the cushion. The parameter B, which is related to correlation length and consequently represents the mean grain size, a mean value of 42 nm was found for the cushions, while in the case of DPPG adsorbed onto these cushions a mean grain size value of 17 nm was achieved, which is close to hydrodynamic diameter for DPPG liposomes measured by DLS. However, these last samples present other features, DPPG aggregates, exhibiting a superstructure size, given by the superstructures PSD model (eq. 3.12), and dependent of the cushion bilayers number. In fact, this parameter takes a value of 149 nm for the PEM with one bilayer decreasing, with the growth of the PEM bilayers number, to 43 nm which is similar to the grain size values found for the cushions. But in the case of the DPPG adsorbed onto PEM containing four bilayers, superstructures with size of 78 nm were also found. This value can be easily justified if closed DPPG vesicles, with 25 nm of diameter, are hexagonal-packed onto the PEM grains, with a

size of 43 nm. The 149 nm value attributed to the grain size of the PEM containing one bilayer was obtained due to the unfold of the DPPG vesicles onto the cushion, consequently creating a lipid bilayer that covers the surface, making it more uniform and thus increasing the grain size. These results allows us to conclude that cushions with higher roughness leads to larger quantities of intact liposomes adsorbed on surface, while flat cushions causes the vesicles rupture creating lipid bilayers on surface. Figure 5.20 outlines the ideal model obtained for the Au/PEI/$(PSS/PAH)_4$/DPPG heterostructure

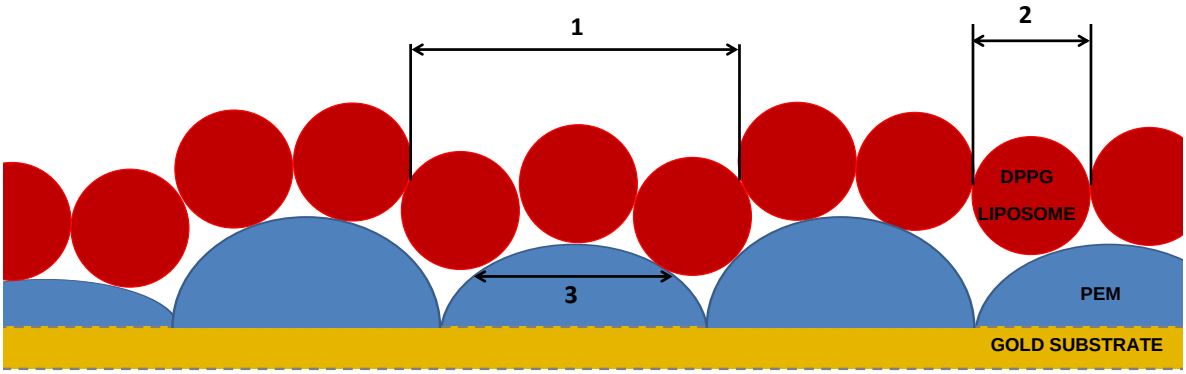

Figure 5.20. Schematic representation of the proposed model for Au/PEI/$(PSS/PAH)_4$/DPPG-liposomes heterostructure, where Au substrate, PEI/$(PSS/PAH)_4$ cushion and DPPG liposomes are displayed in yellow, blue and red colors, respectively. The arrows symbolize the size obtained for each surface feature represented by numbers: 1) lateral size of the superstructures or aggregates of DPPG liposomes achieved by the PSD_{sh} model; 2) size of the DPPG liposomes acquired by the PSD_{ABC} model; 3) size of the PEM grains obtained by the PSD_{ABC} and PSD_{sh} models.

Table 5.19. Data calculated from $PSD_{fractal}$, PSD_{ABC} and PSD_{sh} models.

	Fractal Model				**ABC model**				**Sh model**			
	lnK	**γ+1**	***Df***	**CC**	**A (nm^3)**	**B (nm)**	**(C+1)/2**	**CC**	**k_{sh} (nm^3)**	**τ_{sh} (nm)**	**f_{sh} (×10^6) (m^{-1})**	**CC**
PEM												
$PEI/(PSS/PAH)_1$	16.4±0.9	4.20±0.05	1.40±0.03	0.997	740±30	29±2	2.10±0.05	0.979				
$PEI/(PSS/PAH)_2$	17±2	4.36±0.07	1.32±0.04	0.994	220±10	38±1	2.18±0.07	0.989				
$PEI/(PSS/PAH)_3$	4±1	3.63±0.05	1.69±0.03	0.996	990±30	61±3	1.82±0.05	0.957				
$PEI/(PSS/PAH)_4$	10±1	3.82±0.05	1.59±0.03	0.996	1800±100	39±3	1.92±0.05	0.946				
DPPG onto PEM												
$PEI/(PSS/PAH)_1$/DPPG	29±1	4.87±0.06	1.02±0.03	0.995	100±5	18.5±0.5	2.44±0.08	0.988	5.5±0.1	149±(1)	1.6±0.2	0.996
$PEI/(PSS/PAH)_2$/DPPG	33±2	5.03±0.09	1.00±0.05	0.994	157±5	15.8±0.3	2.52±0.09	0.997	320±20	59±(0.6)	3.2±0.1	0.969
$PEI/(PSS/PAH)_3$/DPPG	17±2	4.3±0.1	1.35±0.05	0.990	16.7±0.7	12.9±0.3	2.15±0.8	0.988	1340±40	61±(0.3)	3.1±0.1	0.975
$PEI/(PSS/PAH)_4$/DPPG	6.4±1.3	3.00±0.07	2.00±0.04	0.991	16±2	22±1	1.50±0.07	0.991	5500±0.100 480±60*	78±(0.4) 43±(0.5)*	3.2±0.1 15.8±0.01*	0.995

* A second superstructure was also included.

5.5.5 Initial roughness - the key for opening the charged liposomes

As the degree of ionization of the last layer of polyelectrolyte of the cushion is equal for all cushions, the last layer is PAH, prepared from similar conditions. Therefore, it is expected that the effect of adsorption of open or intact liposomes is not controlled by hydrophobicity. Thus, it is possible to verify if the roughness is influencing the liposomes adsorption by normalizing the QCM data in accordance with the equation:

$$F_{ol} = \frac{\Gamma_{DPPG\max} - \Gamma}{\Gamma_{DPPG\max} - \Gamma_{DPPG\min}} \tag{5.2}$$

where Γ is the DPPG adsorbed amount and $\Gamma_{DPPG\max}$ and $\Gamma_{\min}$ are the DPPG adsorbed amount onto the cushion with four bilayers and one bilayer, respectively. These last values were chosen because in the first case the adsorbed amount reveals that the liposomes are open while in the second case the liposomes are intact. Therefore, this normalization represents the fraction of open liposomes, F_{ol}. By plotting the fraction of open liposomes as a function of the cushion roughness, as shown in figure 5.21, it is observed that the fraction of open liposomes decreases with increasing cushion roughness. This result leads us to conclude that the surface roughness is a fundamental variable for control the fraction of intact liposomes adsorbed onto a surface, important parameter for the development of well-design sensors based on functional biomolecules encapsulated in liposomes.

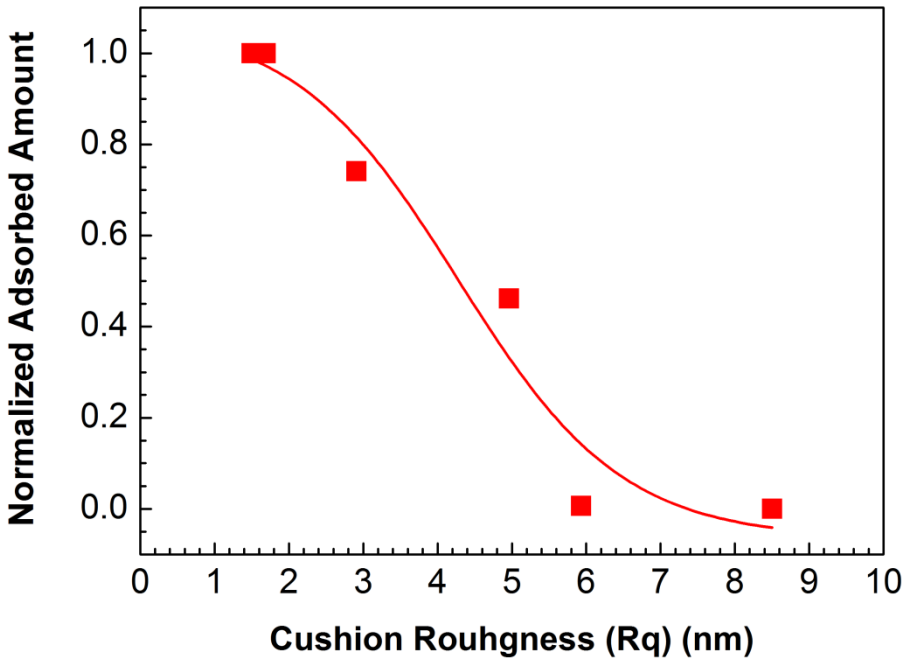

Figure 5.21. Normalized adsorbed amount as a function of the cushion roughness where the liposomes are adsorbed.

5.6 $(PAH/DPPG)_3$, $(PEI/DPPG)_3$ and $(PEI/(DPPG+melanin))_3$ LbL films used as sensors

Aiming to verify the functionality and ability of the supramolecular heterostructures investigated in this work, a multisensory systems constructed with three different LbL films, namely $(PAH/DPPG)_3$, $(PEI/DPPG)_3$ and $(PEI/DPPG+melanin)_3$ combined with seven electrodes of silver (Ag), gold (Au), copper (Cu), glassy carbon (GC), palladium (Pd), nickel (Ni) and platinum (Pt) was developed in order to obtain geographical classification of olive oils samples from different Portuguese and Moroccan regions. The DPPG+melanin designation means DPPG vesicle with melanin encapsulated inside it aqueous “bag”.

5.6.1 XPS characterization of PEI/(DPPG+melanin) LbL films

The $(PEI/DPPG+melanin)_8$ LbL film was characterized by XPS at of 0◦ and 60◦ of take-off angle. To better understand this heterostructure the PEI and DPPG+melanin cast films deposited onto silicon substrates were also analyzed by XPS at 0° of ejection. The PAH/DPPG and PEI/DPPG LbL films have been previously analyzed by XPS in section 4.5.5. The XPS spectra of the $(PEI/DPPG+melanin)_8$ LbL film revealed the presence of carbon (C), oxygen (O), nitrogen (N) and phosphorous (P). The atomic percentages of these elements and the respective binding energies are summarized in table 5.20. The XPS spectra of this LbL film was fitted with three peaks in C 1s regions assigned to an aliphatic carbon, a carbon single bonded to an oxygen (C-O) or to a nitrogen (C-N) and a carbon in a ester group (O-C=O), respectively, from lower to upper binding energies [213]. At the O 1s core level the XPS spectra exhibit only two components centered at 531.0±0.2 and 532.6±0.2 eV of binding energies. The first one is assignable to an oxygen in a phosphate or double bonded to a carbon [213] and the second to a carbon singly bonded to an oxygen [6, 253]. The N 1s spectrum shows three components centered at 399.1±0.2, 400.7±0.3 and 402.1±0.5 eV assignable, respectively, to imine (N), amine (NH) and ionized nitrogen [253]. The P 2p region contains one doublet centered at 133.3±0.2 eV and 134.1±0.2 eV. The first BE is typical of a phosphorous surrounded by oxygen atoms [254].

The $(PEI/DPPG+melanin)_8$ LbL film atomic ratio [N]/[P] presents a small decrease from the 0° to 60°, proving the low stratification of the heterostructure meaning that probably intact DPPG+melanin vesicles are dispersed throughout the surface while others have disrupted originating a lipid bilayer with melanin intra-layered. To notice that to perform XPS measurements the samples are submitted to high vacuum for several hours. Although these results have proved the presence of intact DPPG+melanin liposomes in the heterostructure, the presence of water could not be confirmed by XPS measurements. However, Marli *et al* have detected the presence of water molecules in DPPG+melanin cast films by FTIR spectroscopy [4].

Table 5.20. Elemental composition in percentage and the respective Binding energies (eV), obtained from XPS spectra taken at 0° and 60° of electron ejection relative to the normal surface of the $(PEI/DPPG+melanin)_8$ LbL films. Also atomic percentage and BE of PEI and DPPG+melanin casted films are displayed. Relative error do not exceed ±10%.

	Cast films				**LbL film**				
	PEI		**DPPG+melanin**		**$(PEI/DPPG+melanin)_8$**				
	Atomic (%)	**BE (eV)**	**Atomic (%)**	**BE (eV)**	**Atomic (%)**		**BE (eV)**		**Assignments**
					0°	**60°**	**0°**	**60°**	
C 1s1	66.8	285.6	61.5	285.0	56.9	67.3	285.0	285.0	C-C, C-H
C 1s2			9.9	286.6	14.1	9.5	286.4	286.5	C-O, C-N
C 1s3			3.7	289.0	4.4	2.7	288.7	288.7	O=C-O
O 1s1	2.8	531.5	5.2	531.3	5.2	4.0	531.0	530.8	O-P, O=C
O 1s2			16.4	532.8	10.1	9.2	532.6	532.6	O-C
N 1s1	29.6	399.1			5.4	4.2	399.1	399.2	N
N 1s2	0.9	401.1	0.32	400.7	2.1	1.5	400.7	400.7	N-H
N 1s3					0.72	0.60	402.1	401.9	N^+
P $2p_{3/3}$			1.2	133.7	0.75	0.70	133.3	133.1	P-O
P $2p_{1/2}$			0.58	134.7	0.38	0.35	134.1	134.1	P-O
Na			1.1	1071.3					Na

5.6.2 Geographical classification of olive oils by a portable hybrid electronic tongue

The $(PAH/DPPG)_3$, $(PEI/DPPG)_3$ and $(PEI/(DPPG+melanin))_3$ LbL films were used to be applied in a multisensory system for the classification of olive oils collected from different Moroccan and Portuguese regions. Gallo Classico, Fio Dourado, Oliveira da Serra, Paladin, Gallo Reserva and SOS Pobreza were the Portuguese olive oils selected; and Moulay Idriss, M'rirt, Ouarzazate, Ouazzane and Taounate were the Moroccan olive oils picked out. The proposed system, called Hybrid Electronic tongue (HE-tongue), consists of a hybrid sensor array formed by two families of sensors; three LbL films with different PEMs and seven voltammetric sensors (Copper (Cu), Glassy Carbon (GC), Gold (Au), Nickel (Ni), Palladium (Pd), Platinum (Pt) and Silver (Ag)). The voltammetric signals provided by the sensors have been evaluated using the Principal Component Analysis (PCA). The HVE-tongues may comprise two or more sensor families and are frequently a combination of potentiometric, voltammetric and/or conductimetric sensors. After getting signals from all types of sensors, data processing is performed by chemometric methods to extract useful information. The HVE-tongue allows to obtain varied information about the sample giving the opportunity for a more accurate characterization, rising the probability of correct samples classification [233].

5.6.3 HE-tongue responses and radar plots

The electrochemical measurements were carried out by dipping, simultaneously, in different olive oil solutions, three different LbL films with the seven electrodes. It is recognized, that the electrochemical response of a given compound depends on the intrinsic chemical nature of both the electrode and the redox behavior of the product itself. As a result, the reaction between the redox active compositions and sensors would be expected to produce specific cyclic voltammograms. Besides, adsorption of redox inactive compositions present in the sample matrices may also be expected to affect current signals. Therefore, the differences between samples in cyclic voltammograms yield an overall fingerprint which can be interpreted with the use of appropriate mathematical techniques.

Figure 5.22 shows the cyclic voltammograms obtained from the immersion of PEI/DPPG sensor in Moroccan and Portuguese olive oil samples. The response of the electrodes to different olive oils origins directly affects causing shifts in the shapes and changes in the current intensities at the ends of the voltammograms. The highest current for Portuguese olive oils was observed in “Gallo Classico” (≈ 20 µA) and the lowest current was obtained for “Gallo Reserva” (≈ 5 µA) (Fig. 5.22 a)). Although the obtained voltammograms present similar shape, we succeed to distinguish them from the current values attained at the ends of the curves.

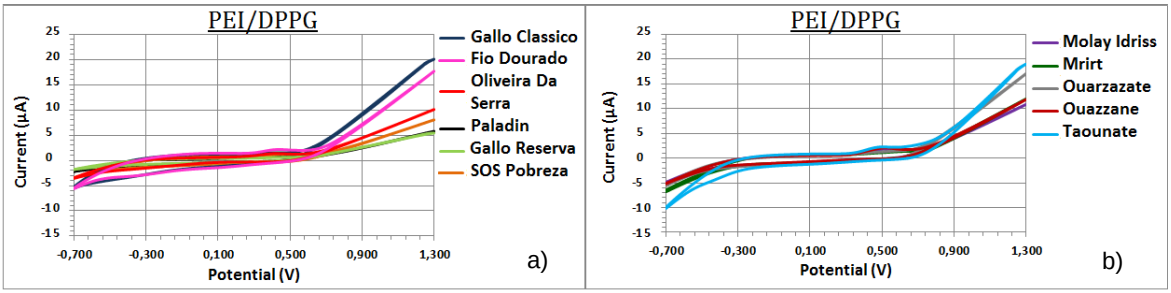

Figure 5.22. Voltammetric responses of PEI/DPPG electrode immersed in (a) Portuguese olive oil samples, and in (b) Moroccan olive oil samples.

To better visualize the differences amongst products, a radar plot of sensor responses was performed in which the vertices are the sensor arrays used in the HE-tongue, as shown in Fig. 5.23. From these plots, one can conclude that the use of ΔI feature allowed obtain patterns that clearly discriminate olive oil samples.

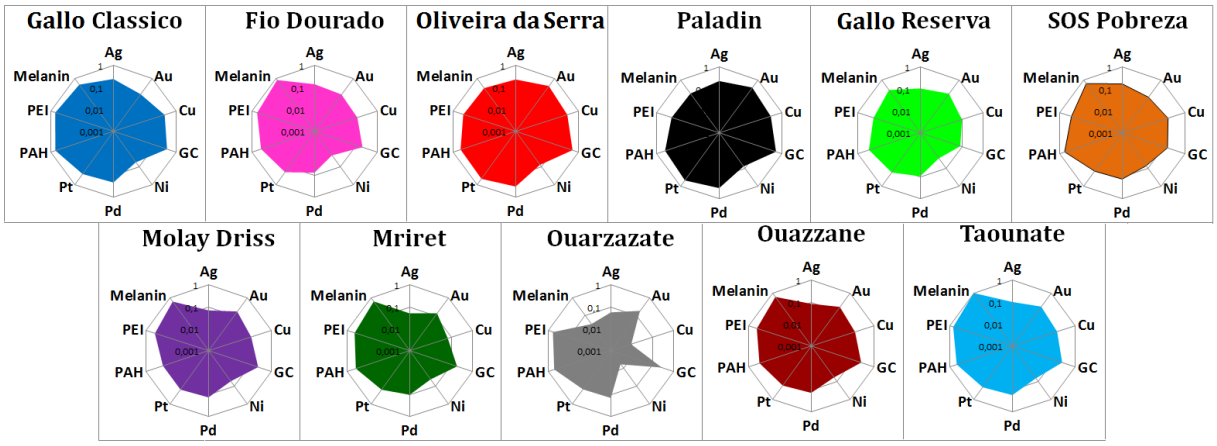

Figure 5.23: Radar plots of the response of the HE-tongue for the Moroccan and Portuguese olive oil samples (expressed as the current change ΔI).

5.6.4 Principal Component Analysis

For the discrimination of the different olive oils, the Principal Component Analysis (PCA) procedure was carried out using the three variables (ΔI, S_{ox} and S_{red}). To reduce the variability associated with possible fluctuations in the HE-tongue signals, and to minimise other sources of variance also affecting the total signal of the sensors, normalised rather than absolute signals were used to conduct PCA analysis. Hence, to normalise the variables, the autoscaled pre-processing technique was applied to a dataset of 66 measurements×30 features. The first three principal components accounted 85.15 % of the total variance (PC1 = 55.68 %; PC2 = 16.97 %; PC3 = 12.50 %). As observed in the score plot of Fig. 5.24, the three PC axes contribute for separating the olive oils in such way that the eleven different classes were well described by all components. However on this plot, the regions associated to “Oliveira da Serra” and “Paladin” overlap into some extent, making difficult to distinguish between this two oils. However, it should be referred that these oils are manufactured by the same producer.

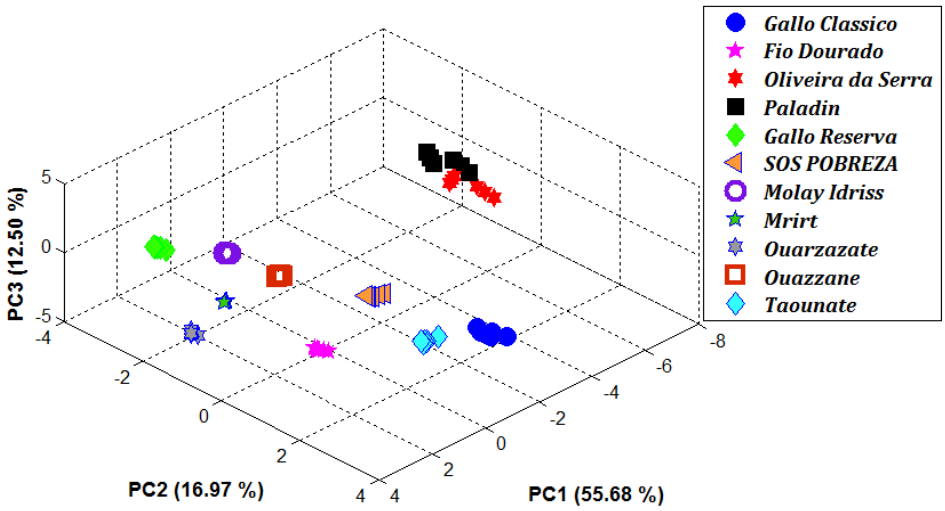

Figure 5.24 : PCA plot performed on the 11-studied Portuguese and Moroccan olive oil measurements gathered using the HE-tongue.

5.7 Conclusions

It was proved that DPPG liposomes layer adsorbed onto a rough PEI/$(PSS/PAH)_5$ surface maintains its integrity. The adsorbed amount obtained from adsorption kinetics curves revealed that the liposomes are covering the entire surface but with an effective surface higher than the QCM crystal quartz area which is consistent with a rough surface. The kinetic curves were obtained by QCM using the SVC system, where a concentrated DPPG suspension was injected in a homemade cell, with water filled and a PEI/$(PSS/PAH)_5$+Au-quartz crystal resonator already plugged. It was verified that the adsorption kinetic is governed by a unique process with a characteristic time of approximately 20 minutes which can be explained through the migration of liposomes to the surface during the diffusion phenomenon and also because vesicles are being adsorbed without rupture. The analysis of the surface topographies of PEM and PEM with DPPG liposomes, reveal that the intact DPPG liposome are randomly adsorbed on the PEM surface, filling the PEM valleys and thus decreasing the height parameters. The results of the height distribution functions demonstrated that the height of the adsorbed liposome ranges 30-40 nm. A mean diameter of 55 nm was calculated from the profile length of the DPPG vesicles, which is higher than the hydrodynamic diameter attained by DLS measurements, showing that liposomes are flattened.

The evolution of surface morphology and microstructure of the LbL films growth, when DPPG liposomes are deposited on Au-quartz crystal resonator and Au/PAH surfaces was monitored by AFM *in situ* at discriminated adsorption times. An amplitude statistical analysis of Au/DPPG showed that after the DPPG liposomes addition, the height parameters have increased considerably in the first 3 minutes which was attributed to intact vesicles immobilized on Au surface, decreasing after 5 minutes showing that liposomes collapse and spread all over the substrate creating a SPB, due to electrostatic interactions between the DPPG vesicles and the Au surface. Moreover, the peak position parameters obtained from the height distribution Gaussian fits centered at 16.79±0.01 nm for 3 minutes and

7.984±0.008 nm for 120 minutes, were assigned to closed DPPG vesicles and to supported-lipid bilayer (SPB), respectively, attached on Au surface. In the case of adhesion of DPPG vesicles on highly charged PAH surface, the statistical amplitude analysis showed that after 3 minutes, generally, the height parameters have maintained its values signifying that, at this adsorption time, a SPB is already formed. This assumption was confirmed by QCM measurements which revealed a characteristic time of 2.19±0.02 min for the first kinetic adsorption process associated to DPPG vesicles adsorption and consequent disruption on PAH surface. By converting the frequency shift in adsorbed mass per unit of area a value of 5 mg/m^2 was calculated corresponding to a DPPG lipid bilayer mass. The PAH/DPPG bilayer thickness obtained by ellipsometry measurements showed a value of 5±1 nm. The only exception of the amplitude parameters analysis is situated at t=10 min of DPPG adsorption where an increase of the roughness is found, due to the presence of DPPG vesicles aggregates attached to the Au/PAH/DPPG-bilayer surface. Concluding, the disruption of DPPG vesicles and consequent creation of a DPPG-lipid bilayer on PAH is faster than on Au surface because the polyelectrolyte cushion is more ionized. Quantitative surface characterization of both Au/DPPG and Au/PAH/DPPG LbL films provided by 1D PSD analysis allowed to identify three distinct regions located at low, medium and high frequencies in all power spectra. The plateau at low frequencies behaves similarly to the height amplitude parameters obtained for both experiments. The correlation lengths of the two regimes found at medium and high frequencies of the PSD spectra of the Au/DPPG and Au/PAH/DPPG LbL films were calculated by determining its frequency transition and the found values were assigned to the grain size of the Au/Cr quartz crystal coverage and to the Au/PAH, respectively. The calculation of the roughness exponents revealed that DPPG-liposomes adsorbed onto Au and Au/PAH surfaces follow, respectively, the non-linear and linear Villain self-affine model. The region of medium frequencies of the PSD spectra of the Au/DPPG and Au/PAH/DPPG samples were also analyzed by the fractal model, revealing final *Df* values nearly 2, which means that both samples have fractal smooth/marginal surfaces. The medium and high frequencies regions of the PSD curves of both samples were successfully fitted with the ABC nonlinear parametrical model which allowed determining the roughness behavior, thus validating the amplitude analysis, and the mean grain size of the surface features. Besides, the *Df* results obtained from this model were ~2 for both samples confirming the values attained by the fractal model.

It was proved by amplitude analysis of Au/PEI/$(PSS/PAH)_4$ and Au/PEI/$(PSS/PAH)_4$/DPPG topographic images, obtained by AFM *in situ* experiments, that after DPPG vesicles adsorption onto rough PEM there is a reduction of the sharpness of the surface because closed vesicles are mostly immobilized on PEM valleys. Besides, the found height characteristic parameters at 20.6±0.2 nm and 33±3 nm, related to the PEM/DPPG surface, were assigned to the DPPG liposomes mean diameter. Both surfaces revealed similar PSD spectrum comprising three distinct regions situated at low, medium and high frequencies. Since, the found values for the two correlation lengths, positioned at the transition frequencies, were only assigned to the mean grain diameter of the PEM and the gold surface, a further PSD analysis have been made. Thus, fractal PSD analysis revealed *Df* values close to 2 for both samples, although for the PEM/DPPG surface the *Df* is smaller which is an evidence of less irregularities on its topography. The ABC model was also applied for both PSD spectra displaying

the following sentences: i) after DPPG vesicles adsorption there is a reduction of the magnitude at medium-low frequencies showing a decrease of the roughness parameters; ii) the grain size values attained are 50±9 and 21.0±0.5 nm attributed to PAH domains of the PEM cushion and to intact DPPG vesicles immobilized onto PAH, respectively; iii) the growth mechanisms for the PEM proved to be between condensation and bulk diffusion processes and the adsorption of DPPG liposomes onto PEM revealed to be by surface diffusion; iv) *Df* values for both topographies are close to 2; having the PEM/DPPG surface a lower value which is a prove of a more regular microstructure due to the adsorption of close-packed DPPG vesicles. However, the ABC model could not be adapted to the low frequencies region of the PSD spectra due to the presence of superstructures on surface. So, lateral sizes of the grain clusters of both samples were extracted using the PSD_{sh} model, which have shown similar value for PEM features, although for PEM/DPPG surface a much higher value was achieved, proving the hexagonal packing of the DPPG liposomes onto PEM. Moreover, the roughness exponents achieved set forth that the DPPG adsorption onto PEM was governed by the diffusion Villain model. Concluding, the combination of these PSD models offers exhaustive information not only of the accessible surface of the sample but also of its inner structural properties. The fractal model describes self-affine properties of the surface providing its fractal dimension. Whereas k-correlation (or ABC) and superstructures models provide information about growth mechanisms of thin films and give quantitative description of vertical and lateral dimensions of the surface features and their aggregates.

Roughness of a positively charged PAH polyelectrolyte surface was shown to strongly influence the adsorption of DPPG liposomes on it. Adsorption kinetics curves of DPPG liposomes onto a low roughness PAH layer reveal an adsorbed amount of 5 mg/m^2, pointing to liposome rupture while, high roughness surface leads to adsorbed amounts of 51 mg/m^2, signifying adsorption of intact liposomes. Adsorption kinetic parameters calculated from adsorption kinetics curves, allow us conclude that the adsorption process is due to electrostatic interactions and also depends on processes such as diffusion and re-organization of lipids on surface. Analysis of the roughness kinetics enabled to calculate a growth exponent of 0.19±0.07 and a roughness exponent around 0.84 revealing that DPPG-liposomes adsorbed onto rough surfaces follow the Villain self-affine model. By relating self-affine surfaces with hydrophobicity, the liposomes integrity was explained by the reduction of the number of water molecules on the PAH surface, contributing for counterions anchorage near PAH ionic groups, reducing the liposome/PAH layer electrostatic forces and, consequently, avoiding the liposome rupture.

The maintenance of DPPG liposome integrity is conditioned by the surface roughness of the cushion used to adsorb liposomes. Low roughness was shown to induce liposome rupture while high roughness causes the adsorption of whole liposomes. In fact, the adsorption kinetics of DPPG layers onto LbL films revealed that the adsorbed amount increases from a value of 5±1 mg/m^2 to a value of 51 mg/m^2. The first value is easily explained by a planar DPPG bilayer adsorbed while values higher than 16 mg/m^2 can be only explained if DPPG liposomes with 25 nm of diameter, i.e. intact liposomes, are being adsorbed onto a rough surface. Also, the decrease of the adsorption characteristic time with the increase of the bilayers number also points to a higher adsorption of whole liposomes. Moreover,

the XPS characterization allowed us to conclude that the LbL cushion is covered efficiently by the DPPG liposomes and that the charge compensation occurs between the phosphate group of the DPPG molecule and the protonated amine of the PAH molecule without involving (or involving in a much lower extent) the sodium ion. The relation between the increase of PEI/$(PSS/PAH)_b$ cushions roughness with the growth of the bilayers number was confirmed by AFM topographies. In addition, a maximum height sequential growth, obtained from the height distribution (HD) curves, was observed as the number of bilayers of the cushion increase. Furthermore, a small shift of the height associated to the maximum of occurrences of PEI/$(PSS/PAH)_1$ cushion and PEI/$(PSS/PAH)_1$/DPPG was detected, while a value of ~10 nm was found when comparing the HD associated to PEI/$(PSS/PAH)_b$ and PEI/$(PSS/PAH)_b$/DPPG, being $2 \leq b \leq 4$. The height difference of 10 nm can be easily explained if liposomes, with hydrodynamic diameter of about 25 nm, are adsorbed intact. The grain analysis carried out by exploration of power spectral density curves using the fractal, ABC and superstructures models, allowed to conclude that the cushions grain size takes a mean value of 42 nm, while in the case of DPPG vesicles adsorbed onto the cushion it presents a mean value of 17 nm which is close of the liposomes hydrodynamic diameters values. In addition, the fractal dimension values obtained from these models are in accordance with the values calculated from roughness parameters. The fraction of open liposomes calculated from the normalized maximum adsorbed amounts and plotted as a function of the initial surface roughness, decrease with the cushion roughness growth. This result leads us to conclude that surface roughness is a fundamental variable that can be used in order to control the adsorption of intact liposomes. This finding is of particular importance for the development of sensors based on liposomes with molecules encapsulated.

In this sense, LbL films of $(PAH/DPPG)_3$, $(PEI/DPPG)_3$ and $(PEI/DPPG+melanin)_3$ were prepared to be tested as sensors. The elemental composition of the LbL film $(PEI/DPPG+melanin)_3$ and respective binding energies were obtained by XPS technique. The atomic ratio [N/P] have proved that this heterostructure possess a low stratification probably due to the existence of intact DPPG+melanin vesicles and lipid bilayers with melanin intra-layered. The presence of water could not be confirmed by XPS measurements. A Hybrid Electronic-tongue consisting of a liquid sensor array formed by those three different LbL films combined with seven electrodes, has been developed for the discrimination of Moroccan and Portuguese olive oil samples. The HE-tongue combined with chemometric techniques demonstrated high ability to distinguish between eleven olive oil clusters. Although for two Portuguese olive oils, the PCA analysis exhibited a slight overlap which mainly arises from its linear characteristics. As a final conclusion, it can be said that portable HE-tongue device coupled with chemometric techniques can be extended too many other products towards quality control.

6 CONCLUSION

6.1 Conclusions

This work shows that the roughness has a crucial role in the adsorption of whole liposomes on a surface. This main conclusion comes from the achievements described below.

Cast films produced with DPPG liposomes suspensions deposited onto flat substrates were characterized by optical and spectroscopies techniques, which have confirmed the adsorption of DPPG molecules. Topographic images obtained by AFM showed several terraces of lipid bilayers, caused by the unfolding of the DPPG vesicles, and intact vesicles upon the bilayers. The integrity of these closed vesicles was confirmed by SEM. FTIR and XPS techniques confirmed the presence of structural water in these films.

A commercial QCM was tested at solid/liquid interface using five specific experimental configurations with the quartz crystal resonator vertically or horizontally positioned. The kinetics curves analysis of the assembled aqueous solutions of PEI, weak polyelectrolyte, and DPPG liposomes revealed that horizontal modes lead to a higher resonance frequency shift, due to the measurement of non-adsorbed molecules which are deposited on the quartz crystal and to an increase of the kinetic curves instability of the measurements as a result of a fostering noise due to the mechanical vibrations. The vertical modes proved to be more reliable. Topographic images obtained by AFM technique showed a smooth PEI polyelectrolyte surface covered by intact DPPG vesicles adjacent to lipid bilayers domains, explaining the lower measured mass compared to theoretical calculations due to the release of the entrapped water after the vesicles breakdown.

Aiming to create heterostructures with intact liposomes, the LbL film growth of DPPG vesicles alternated with the PEI polyelectrolyte assembled upon a rough cushion were characterized *in situ* using QCM. The QCM data analysis allowed to infer that DPPG adsorbed amount is dependent of the bilayers number already adsorbed. This dependence was interpreted by roughness evolution with the number of bilayers which increases until a maximum, being followed by a decrease until attains a constant value. Kinetic curves reveal that the DPPG adsorption is justified by two processes: i) the first associated to DPPG liposomes adsorption with a small constant time independent of the bilayers number; ii) the second dependent of the bilayers number is associated to a structural rearrangement of DPPG liposomes on the surface.

DPPG emulsions and PAH/DPPG LbL films were characterized by VUV spectroscopy. Measurements in the 6.0–9.5 eV range allowed us to identify the electronic transitions responsible for the spectra, which were assigned to carboxyl, hydroxyl and phosphate groups in DPPG while the PAH spectra is governed by electronic transitions in the amino groups. The surface mass density of the LbL films could be determined, proving that a DPPG lipid bilayer has been created. This liposomes rupture into bilayers was confirmed by AFM measurements. In subsidiary experiments we ensured that the UV irradiation in vacuum had negligible damage in the DPPG liposomes during the course of the VUV measurements. In addition to demonstrate the usefulness of VUV spectroscopy, the results presented here may be exploited in biological applications of liposome-containing films. The assembly of the PAH/DPPG LbL films, characterized by XPS spectroscopies and AFM, have confirmed the

development of a DPPG lipid bilayer. The PAH polyelectrolyte layer proved to be a smooth highly ionized cushion with strong electrostatic interactions thus leading to the vesicles disruption. The PEI/DPPG LbL film monitored by QCM, AFM and XPS techniques showed that DPPG vesicles immobilization onto PEI polyelectrolyte layer, having a low ionization degree and a smooth surface, leads to the adsorption of intact vesicles adjacent to lipid bilayers patches. Structural water was found in this heterostructure proving the integrity of the DPPG liposomes and its capacity to encapsulate functional molecules, e.g. proteins, to create sensors and devices.

It was demonstrated that DPPG liposomes can be adsorbed without rupture on a rough cushion, such as PEI/$(PSS/PAH)_5$. The *in situ* adsorption kinetic curves, obtained by QCM using a homemade aqueous cell, revealed that this process is governed by a diffusion phenomenon with a characteristic time of approximately 20 minutes. The total adsorbed amount per unit of area revealed that the integrity of the liposomes was maintained during adsorption. The analysis of the surface topographies of both surfaces revealed that intact vesicles are randomly adsorbed on cushion surface, filling its valleys leading to a decrease of the mean height.

Surface topographies obtained by AFM *in situ* of DPPG liposomes deposited onto two different smooth surfaces, such as Au-quartz crystal resonator and PAH polyelectrolyte layer, have proved that vesicles break, unfold and spread throughout the surfaces, creating a DPPG lipid bilayer. Amplitude parameters comparison between both experiments showed that the time needed to form a lipid bilayer is faster when a more ionized surface is used, such as PAH surface. Kinetic adsorption curves obtained by QCM of DPPG liposomes adsorbed onto this highly charged surface allowed to verify that at ~2 minutes a lipid bilayer is formed, testifying the statistical analysis. The PSD spectra of both surface topographies, when DPPG liposomes are being adsorbed, were analyzed by conventional correlation length method and by fractal and ABC or k-correlation models. Two types of correlation lengths for Au/DPPG and Au/PAH/DPPG LbL films were found and assigned to the grain size of Au/Cr quartz crystal coverage and to the Au/PAH, respectively. The scaling exponents revealed that DPPG-liposomes adsorbed onto Au and Au/PAH surfaces follow, respectively, the non-linear and linear Villain self-affine model. The ABC nonlinear parametrical model was well adapted to all PSD spectra allowing extracting the mean grain size of the surfaces and the roughness behavior thus validating the amplitude analysis. Both PSD models achieved *Df* values nearly 2, which means that both samples have fractal smooth/marginal surfaces.

It was demonstrated by amplitude analysis of AFM surface topographies obtained *in situ*, that DPPG vesicles are intact adsorbed onto rough cushion (Au/PEI/$(PSS/PAH)_4$) filling the valleys and consequently minimizing the surface acuity. The PSD spectra of both surface topographies were analyzed by the conventional correlation length method and by a combination of three PSD models, namely fractal, ABC or k-correlation and superstructure. The first method revealed to be inefficient because it could only found the grain size assigned to the PEM cushion and to the gold surface. The PSD analysis using the ABC model have shown that: i) surface roughness decreases after DPPG vesicles adsorption; ii) the attained grain size values of 50±9 and 21.0±0.5 nm are attributed to PAH cushion domains and to closed vesicles immobilized on cushion, respectively; iii) the adsorption of DPPG liposomes onto PEM revealed to be caused by diffusion. The PSD superstructure model

allowed obtaining the lateral sizes of the grain clusters, showing a value close to the size of the grain cushion, although for DPPG surface a much higher value was achieved, proving the hexagonal packing of the DPPG liposomes onto PEM. The fractal and ABC PSD models have shown *Df* close to 2, being the *Df* of the PEM/DPPG surface smaller manifesting less irregularities on its topography. The roughness exponents set forth that DPPG vesicles deposition is ruled by the diffusion Villain model. It is important to say that all these methods complete each other providing an exhaustive description not only of the accessible surface of the sample but also of its inner structural properties. So, the information that can be achieved from experimental AFM images depends on method used for surface analysis.

The surface roughness was shown to influence the adsorption of DPPG liposomes onto surfaces covered by an electrically charged PAH polyelectrolyte layer and also the conditions giving rise to its rupture or maintenance of its integrity. Low roughness was shown to induce liposome rupture while high roughness induces adsorption of whole liposomes. Whereas the roughness increase is leading to an increase of hydrophobicity, one can expect that the reduction of the number of water molecules on the PAH surface contributes for the counterions anchorage near PAH ionic groups and consequent reduce the electrostatic force between the liposome and the PAH layer and contributing to liposome integrity. Moreover, the adsorption kinetics curves, of both adsorbed amount and surface roughness, allowed to determine the adsorption kinetics parameters which were related with the adsorption processes namely, electrostatic forces, liposomes diffusion and of re-organization of lipids on the surface. It was possible also to conclude that the adsorption of whole liposomes follows the Villain fractal model.

The capacity to control the final structure of liposomes adsorbed onto surfaces with different roughness values was validated. Thus, flat surfaces have shown to induce vesicles rupture while surfaces roughness growing causes an increase of the adsorption amount of whole liposomes. The adsorption of DPPG liposomes onto cushions, having its surface highly charged and roughness changing from flat to rough by increasing the number of bilayers, was monitored by QCM. The adsorption kinetics parameters demonstrate an increasing of the DPPG adsorbed amount from a value of 5±1 mg/m^2, i.e. planar lipid bilayer, to a value of 51 mg/m^2, i.e. intact liposomes adsorbed onto a rough surface. Besides, the adsorption characteristic time decreases with the increasing of the bilayers number suggesting the adsorption of whole liposomes. Furthermore, the XPS characterization allowed to set effort that the rough cushion is well covered by DPPG liposomes being the charge compensation between the phosphate group of the DPPG phospholipid and the protonated amine of the PAH molecule without involving (or involving in a much lower extent) the sodium ion. AFM topographies confirmed that the PEI/(PSS/PAH)$_b$ cushions roughness increases with the growth of bilayers number as well as the maximum height of the distribution curves. Besides, the height distribution (HD) of the PEI/(PSS/PAH)$_1$ cushion and PEI/(PSS/PAH)$_1$/DPPG demonstrate a small shift, i.e. no intact liposomes on PEM surface, while a value of about 10 nm was found when HD of PEI/(PSS/PAH)$_b$ cushions and PEI/(PSS/PAH)n/DPPG with number of layers (b) between 2 to 4 are compared, i.e. with close liposomes immobilized on PEM surface. Grain analysis performed by extracting information of the PSD plots using the fractal, ABC and superstructures models, allowed to

found that the cushions have a mean grain size of 42 nm, while in the DPPG adsorbed onto the cushion have a mean value of 17 nm attesting its integrity. In addition, the roughness parameters behavior was confirmed by the fractal dimension values attained from these PSD models. The fraction of open liposomes, calculated from the normalized maximum adsorbed amounts, decreases as the cushion roughness increases, allowing us to conclude that the surface roughness is a crucial variable that governs the adsorption of open or whole liposomes. This conclusion is fundamental for the development of well-design sensors based on heterostructures comprising liposomes with functional biomolecules encapsulated.

The $(PAH/DPPG)_3$, $(PEI/DPPG)_3$ and $(PEI/DPPG+melanin)_3$ LbL films were prepared to be applied in sensors. The LbL film $(PEI/DPPG+melanin)_3$ was characterized by XPS technique evidencing that this heterostructure has a low stratification probably due to the existence of both intact DPPG vesicles with encapsulated melanin and lipid bilayers with melanin intra-layered. Those three LbL films were successfully applied in a multisensory system combined with chemometric techniques for the classification of olive oils collected from different Moroccan and Portuguese regions demonstrating good ability in discriminating and classifying among 11 olive oil samples on account of their region.

6.2 Future remarks

The results and conclusions obtained from this work have enabled essential advances in understanding the role of the surface roughness on the adsorption of intact liposomes without and with functional biomolecules incorporated, such as melanin. However, more adsorption studies are necessary in order to confirm the roughness' rules that lead to the adsorption of intact liposomes with any functional biomolecules incorporated. This study also demonstrated that roughness is associated to surface hydrophobicity. So, further research of surface hydrophobicity of self-affine rough surfaces, e.g. contact angle measurements, are required in order to verify experimentally if high roughness induce high hydrophobicity. Regarding LbL films assembly it is now known that an increase in hydrophobicity reduces the water molecules number on the surface, contributing for counterions anchorage near polyelectrolytes ionic groups, consequently reducing the electrostatic forces between the cationic and anionic polyelectrolyte layers. Hence, in order to prevent liposome rupture it becomes necessary systematic measurements to characterize the electrical charge of the surfaces.

6.3 Developed work

6.3.1 Papers published in international journals

- Duarte AA, Gomes PG, Ribeiro JHF, Ribeiro PA, Hoffmann SV, Mason NJ, Oliveira Jr. ON, Raposo M. "Characterization of PAH/DPPG Layer-by-Layer films by VUV spectroscopy", EPJ E-Soft Matter & Biological Physics, 36 9 (2013) 98.

- Duarte AA, Filipe SL, Abegão LM, Gomes PG. Ribeiro PA, Raposo M (2013). “Adsorption Kinetics of DPPG Liposome Layers: A Quantitative Analysis of Surface Roughness”. Microscopy and Microanalysis,7:1-9.

6.3.2 Papers published in proceedings

- Duarte, A.A.; Filipe, S.L.; Raposo, M., "Adsorption of intact DPPG liposome on rough polyelectrolyte multilayers" *Bioengineering (ENBENG), 2013 IEEE 3rd Portuguese Meeting in*, vol., no., pp.1,4, 20-23 Feb. 2013.
- Duarte, A.A.; Raposo, M., "Growth analysis of PEI/DPPG self-assembled films by quartz crystal microbalance" *Bioengineering (ENBENG), 2012 IEEE 2nd Portuguese Meeting in*, vol., no., pp.1,6, 23-25 Feb. 2012.

6.3.3 Submitted papers

- Tahri K., Duarte A.A., Saidi T., Bougrini M., Ribeiro P. A., El Bari N., Raposo M. and Bouchikhi B. “Discrimination of olive oils according to geographical origin by a portable hybrid electronic tongue combined with chemometric analysis”, submitted to Journal of Food Engineering.
- A.A. Duarte, L.M.G. Abegão, J.H.F. Ribeiro, J. P. Lourenço, P. A. Ribeiro and M. Raposo, “Study of adsorption kinetics *in situ* of polyelectrolytes and liposomes using quartz crystal microbalance: influence of experimental layout”, submitted to Review of Scientific Instruments.

6.3.4 Papers to be submitted

- A. A. Duarte, Ana Maria Botelho do Rego, Marco Salerno, Paulo A. Ribeiro, Nezha El Bari, Benachir Bouchikhi, and M. Raposo. “Adsorption of DPPG liposomes on different roughness polymer cushions with different roughness: analysis of adsorbed amount, surface composition and topography”.
- A. A. Duarte, Joaquim T. Marquês, Francisco Brasil, Ana S. Viana, Pedro Tavares, Maria Raposo. “Surface analysis of dipalmitoyl phosphatidyl glycerol liposomes adsorption by AFM *in situ*”.

6.3.5 Atas communications

- Duarte, A. A. and M. Raposo. "Surface roughness as rupture control factor of lipid vesicles." *Microscopy and Microanalysis*19.S4 (2013): 107-108.

6.3.6 Oral communications

- Duarte, A. A. *et al*, “Adsorption of intact DPPG liposome on rough polyelectrolyte Multilayers” proceedings book (Biomaterials, NanoBiotechnology, Biomolecular, BioProcess Engineering and BioInformatics: Oral 3) of 3rd Portuguese Bioengineering Meeting at University of Minho, Campus de Gualtar, CP2-B1, February 2013.
- DUARTE, A.A. & RAPOSO, M. “Surface roughness as rupture control factor of lipid vesicles”. In "Microscopy: A tool for the advancement of science" abstracts book (Materials Science: Oral 5) of XLVI Congress of the Portuguese Society for Microscopy (SPMicros) September 2012 at Centro Hospitalar de Lisboa Central - Hospital D. Estefânia.

6.3.7 Poster communications

- DUARTE, A.A. & RAPOSO, M. "Growth analysis of PEI/DPPG self-assembled films by quartz crystal microbalance". In Bioengineering (ENBENG), Coimbra February 2012 IEEE 2nd Portuguese Meeting in, pp. 1-6 (poster presentation).
- Duarte, P. Gomes, S. Hoffmann, M. Raposo. "Characterization of the VUV radiation effect on lipid emulsions". In Conference Proteção Radiológica na Saúde, Lisboa September 2013. Radiobiology Session (poster presentation).

References

[1] O.N. Oliveira Jr., M. Raposo, A. Dhanabalan, Langmuir-Blodgett (LB) and self-assembled (SA) polymeric films, in: H.S. Nalwa (Ed.) Handbook of Surfaces and Interfaces of Materials, Academic Press, New York, 2001, pp. 1-63.

[2] H. Haas, M. Raposo, P. Ribeiro, R. Steitz, P. Cavatorta, P. Riccio, Myelin model membranes on a soft polymer cushion, Biophysical Journal (Annual Meeting Abstracts), 80(1): Part 2 (Jan 2001).

[3] S. Gromelski, A.M. Saraiva, R. Krastev, G. Brezesinski, The formation of lipid bilayers on surfaces, Colloids Surf B Biointerfaces, 74 (2009) 477-483.

[4] M.L. Moraes, P.J. Gomes, P.A. Ribeiro, P. Vieira, A.A. Freitas, R. Kohler, O.N. Oliveira, Jr., M. Raposo, Polymeric scaffolds for enhanced stability of melanin incorporated in liposomes, J Colloid Interface Sci, 350 (2010) 268-274.

[5] V.P.N. Geraldo, M.L. Moraes, V. Zucolotto, O.N. Oliveira Jr., Immobilization of Ibuprofen-Containing Nanospheres in Layer-by-Layer Films, J Nanosci Nanotechnol, 11 (2011) 1167-1174.

[6] J.M. Lourenço, P.A. Ribeiro, A.M. Botelho do Rego, M. Raposo, Counterions in layer-by-layer films-influence of the drying process, J Colloid Interface Sci, 313 (2007) 26-33.

[7] T. Nomura, M. Okuhara, Frequency shifts of piezoelectric quartz crystals immersed in organic liquids, Analytica Chimica Acta, 142 (1982) 281-284.

[8] M. Lampin, R. Warocquier-Clérout, C. Legris, M. Degrange, M. Sigot-Luizard, Correlation between substratum roughness and wettability, cell adhesion, and cell migration, Journal of biomedical materials research, 36 (1997) 99-108.

[9] A. Brú, J.M. Pastor, I. Fernaud, I. Brú, S. Melle, C. Berenguer, Super-rough dynamics on tumor growth, Physical Review Letters, 81 (1998) 4008.

[10] W. Xia, W. DowHAN, In vivo evidence for the involvement of anionic phospholipids in initiation of DNA replication in Escherichia coli, Proceedings of the National Academy of Sciences, 92 (1995) 783-787.

[11] A. von Nahmen, M. Schenk, M. Sieber, M. Amrein, The structure of a model pulmonary surfactant as revealed by scanning force microscopy, Biophysical Journal, 72 (1997) 463-469.

[12] M.I.N. da Silva, S.N. Dezidério, J.C. Gonzalez, C.F.O. Graeff, M.A. Cotta, Synthetic melanin thin films: Structural and electrical properties, Journal of Applied Physics, 96 (2004) 5803-5807.

[13] M. Sugumaran, Comparative Biochemistry of Eumelanogenesis and the Protective Roles of Phenoloxidase and Melanin in Insects, Pigment Cell Research, 15 (2002) 2-9.

[14] Y.-C. Hung, V.M. Sava, S.Y. Makan, T.-H.J. Chen, M.-Y. Hong, G.S. Huang, Antioxidant activity of melanins derived from tea: comparison between different oxidative states, Food Chemistry, 78 (2002) 233-240.

[15] A. Pedicelli, F. Desiderio, G. Esposito, M. Rollo, A. Albanese, T. Verdolotti, F. D'Argento, L. Bonomo, G. Maira, C. Colosimo, Three-dimensional rotational angiography for craniotomy planning and postintervention evaluation of intracranial aneurysms, Radiol Med, (2012).

[16] M. Raposo, R.S. Pontes, L.H.C. Mattoso, O.N. Oliveira Jr., Kinetics of Adsorption of Poly(o-methoxyaniline) Self-Assembled Films, Macromolecules, 30 (1997) 6095-6101.

[17] S.J. Singer, G.L. Nicolson, The fluid mosaic model of the structure of cell membranes, Science, 175 (1972) 720-731.

[18] E.D. Robertis, E.M.D. Robertis Jr., Cell and Molecular Biology, 8th edition, International Copyright Union, (1987).

[19] http://www.goldiesroom.org/Note%20Packets/03%20Cytology/00%20Cytology--WHOLE.htm (accessed 08/10/13 at 09:55 a.m.).

[20] G. Vereb, J. Szollosi, J. Matko, P. Nagy, T. Farkas, L. Vigh, L. Matyus, T.A. Waldmann, S. Damjanovich, Dynamic, yet structured: The cell membrane three decades after the Singer-Nicolson model, Proc Natl Acad Sci U S A, 100 (2003) 8053-8058.

[21] C. Peetla, A. Stine, V. Labhasetwar, Biophysical interactions with model lipid membranes: applications in drug discovery and drug delivery, Mol Pharm, 6 (2009) 1264-1276.

[22] A.M. Seddon, D. Casey, R.V. Law, A. Gee, R.H. Templer, O. Ces, Drug interactions with lipid membranes, Chem Soc Rev, 38 (2009) 2509-2519.

[23] http://www.nature.com/scitable/ebooks/essentials-of-cell-biology-14749010/118240266 (accessed 20/06/14 at 17:05 a.m.).

[24] http://www.pharmainfo.net/reviews/overview-brain-targeting-drug-delivery-system (accessed 20/06/14 at 10:05 a.m.).

[25] V.P. Torchilin, Recent advances with liposomes as pharmaceutical carriers, Nature reviews. Drug discovery, 4 (2005) 145-160.

[26] D.D. Lasic, Novel applications of liposomes, Trends Biotechnol, 16 (1998) 307-321.

[27] A.D. Bangham, M.M. Standish, J.C. Watkins, Diffusion of univalent ions across the lamellae of swollen phospholipids, J Mol Biol, 13 (1965) 238-252.

[28] M.K. Jain, D.G. Touissaint, E.H. Cordes, Kinetics of water penetration into unsonicated liposomes. Effects of n-alkanols and cholesterol, J Membr Biol, 14 (1973) 1-16.

[29] D.A. Tyrrell, T.D. Heath, C.M. Colley, B.E. Ryman, New aspects of liposomes, Biochim Biophys Acta, 457 (1976) 259-302.

[30] M.J. Ostro, Liposomes, Sci Am, 256 (1987) 102-111.

[31] D. Lichtenberg, Y. Barenholz, Liposomes: preparation, characterization, and preservation, Methods Biochem Anal, 33 (1988) 337-462.

[32] A.D. Bangham, in Permeability and Function of Biological Membranes, in: L. edit. by Bolis, Katchalsky, A., Keynes, R. D., Loewenstein, W. R., and Pethica, B. A. (Ed.), North-Holland, Amsterdam, 1970.

[33] E. Sackmann, T. Feder, Budding, fission and domain formation in mixed lipid vesicles induced by lateral phase separation and macromolecular condensation, Mol Membr Biol, 12 (1995) 21-28.

[34] O.G. Mouritsen, K. Jorgensen, A new look at lipid-membrane structure in relation to drug research, Pharm Res, 15 (1998) 1507-1519.

[35] F. Szoka, Jr., D. Papahadjopoulos, Comparative properties and methods of preparation of lipid vesicles (liposomes), Annu Rev Biophys Bioeng, 9 (1980) 467-508.

[36] M.C. Woodle, D. Papahadjopoulos, Liposome preparation and size characterization, Methods Enzymol, 171 (1989) 193-217.

[37] D.D. Lasic, The mechanism of vesicle formation, Biochem J, 256 (1988) 1-11.

[38] D. Papahadjopoulos, S. Nir, N. Duzgunes, Molecular mechanisms of calcium-induced membrane fusion, J Bioenerg Biomembr, 22 (1990) 157-179.

[39] P.R. Cullis, M.B. Bally, T.D. Madden, L.D. Mayer, M.J. Hope, pH gradients and membrane transport in liposomal systems, Trends Biotechnol, 9 (1991) 268-272.

[40] G. Gregoriadis, The carrier potential of liposomes in biology and medicine (second of two parts), N Engl J Med, 295 (1976) 765-770.

[41] D. Papahadjopoulos, A. Gabizon, Targeting of liposomes to tumor cells in vivo, Ann N Y Acad Sci, 507 (1987) 64-74.

[42] L.D. Mayer, M.B. Bally, M.J. Hope, P.R. Cullis, Techniques for encapsulating bioactive agents into liposomes, Chem Phys Lipids, 40 (1986) 333-345.

[43] L.B. Margolis, Cell interaction with model membranes. Probing, modification and simulation of cell surface functions, Biochim Biophys Acta, 779 (1984) 161-189.

[44] G.F. Kersten, D.J. Crommelin, Liposomes and ISCOMS as vaccine formulations, Biochim Biophys Acta, 1241 (1995) 117-138.

[45] J.M. Sallovitz, M.I. Zonco Menghini, C.E. Lanusse, Impact of liposomes as delivery systems in veterinary medicine, Vet Res, 29 (1998) 409-430.

[46] R.M. Winslow, New transfusion strategies: red cell substitutes, Annu Rev Med, 50 (1999) 337-353.

[47] T.M. Chang, Future prospects for artificial blood, Trends Biotechnol, 17 (1999) 61-67.

[48] G. Gregoriadis, P.D. Leathwood, B.E. Ryman, Enzyme entrapment in liposomes, FEBS Lett, 14 (1971) 95-99.

[49] F. Le Caherec, P. Bron, J.M. Verbavatz, A. Garret, G. Morel, A. Cavalier, G. Bonnec, D. Thomas, J. Gouranton, J.F. Hubert, Incorporation of proteins into (Xenopus) oocytes by proteoliposome microinjection: functional characterization of a novel aquaporin, J Cell Sci, 109 (Pt 6) (1996) 1285-1295.

[50] M. Michel, A. Izquierdo, G. Decher, J.C. Voegel, P. Schaaf, V. Ball, Layer by layer self-assembled polyelectrolyte multilayers with embedded phospholipid vesicles obtained by spraying: integrity of the vesicles, Langmuir, 21 (2005) 7854-7859.

[51] N.C. Santos, M.A.R.B. Castanho, LIPOSSOMAS: A BALA MÁGICA ACERTOU?, Quim. Nova, Vol. 25 (2002) 1181-1185.

[52] V. Torchilin, V. Weissig, Liposomes: A Practical Approach, OUP Oxford, 2003.

[53] www.avantilipids.com (accessed 05/03/10 at 11:00 a.m.).

[54] Z. Tang, Y. Wang, P. Podsiadlo, N.A. Kotov, Biomedical Applications of Layer-by-Layer Assembly: From Biomimetics to Tissue Engineering, Adv Mater, 18 (2006) 3203-3224.

[55] O.N. Oliveira Jr., A. Riul Jr, M. Ferreira, V. Zucolotto, V.B.P. Leite, Polímeros na era da nanotecnologia: controle molecular em filmes nanoestruturados . In: EBEE-2004. (Org.). Material Didático da IX Escola Brasileira de Estrutura Eletrônica (2004).

[56] R.K. Banerjee, A.G. Datta, Proteoliposome as the model for the study of membrane-bound enzymes and transport proteins, Mol Cell Biochem, 50 (1983) 3-15.

[57] http://www.physics.uwo.ca/~smittler/surface.html (accessed 08/08/14 at 3:05 p.m.).

[58] J. Sagiv, Organized monolayers by adsorption. 1. Formation and structure of oleophobic mixed monolayers on solid surfaces, Journal of the American Chemical Society, 102 (1980) 92-98.

[59] E.E. Polymeropoulos, J. Sagiv, Electrical conduction through adsorbed monolayers, The Journal of Chemical Physics, 69 (1978) 1836-1847.

[60] http://nimet.ufl.edu/nanomed.asp (accessed 2/2/14 at 9:05 a.m.).

[61] G. Decher, J.D. Hong, J. Schmitt, Buildup of ultrathin multilayer films by a self-assembly process. 3. Consecutively alternating adsorption of anionic and cationic polyelecrolytes on charged surfaces, Thin Solid Films, 210 (1992) 831-835.

[62] O.N. Oliveira Jr., V. Zucolotto, S. Balasubramanian, L. Li, H.S. Nalwa, J. Kumar, S.K. Tripathy, *Layer-by-layer polyelectrolyte based thin films for electronic and photonic applications*, in: A.S. Publishers (Ed.) Handbook of Polyelectrolytes and Their Applications, S. K., Tripathy, J. Kumar, H. S. Nalwa, Los Angeles, 2002, pp. 1.

[63] J.M. Lourenço, P.A. Ribeiro, A.M. Botelho do Rego, F.M. Braz Fernandes, A.M. Moutinho, M. Raposo, Counterions in poly(allylamine hydrochloride) and poly(styrene sulfonate) layer-by-layer films, Langmuir, 20 (2004) 8103-8109.

[64] R. Richter, A. Mukhopadhyay, A. Brisson, Pathways of lipid vesicle deposition on solid surfaces: A combined QCM-D and AFM study, Biophys J, 85 (2003) 3035-3047.

[65] M. Malcher, D. Volodkin, B.a. Heurtault, P. André, P. Schaaf, H. Möhwald, J.-C. Voegel, A. Sokolowski, V. Ball, F. Boulmedais, B. Frisch, Embedded Silver Ions-Containing Liposomes in Polyelectrolyte Multilayers: Cargos Films for Antibacterial Agents, Langmuir, 24 (2008) 10209-10215.

[66] R.P. Richter, R. Bérat, A.R. Brisson, Formation of Solid-Supported Lipid Bilayers: An Integrated View, Langmuir, 22 (2006) 3497-3505.

[67] K.L. Weirich, J.N. Israelachvili, D.K. Fygenson, Bilayer Edges Catalyze Supported Lipid Bilayer Formation, Biophys J, 98 (2010) 85-92.

[68] I. Pfeiffer, S. Petronis, I. Köper, B. Kasemo, M. Zäch, Vesicle Adsorption and Phospholipid Bilayer Formation on Topographically and Chemically Nanostructured Surfaces, J Phys Chem B, 114 (2010) 4623-4631.

[69] S. Dante, T. Hauß, R. Steitz, C. Canale, N.A. Dencher, Nanoscale structural and mechanical effects of beta-amyloid (1–42) on polymer cushioned membranes: A combined study by neutron reflectometry and AFM Force Spectroscopy, BBA Biomembranes, 1808 (2011) 2646-2655.

[70] P.S. Cremer, S.G. Boxer, Formation and Spreading of Lipid Bilayers on Planar Glass Supports, J Phys Chem B, 103 (1999) 2554-2559.

[71] J.A. Zasadzinski, Novel approaches to lipid based drug delivery, Curr. Opin. Solid State Mat. Sci., 2 (1997) 345–349.

[72] E. Sackmann, Supported membranes: scientific and practical applications., Science, 271 (1996) 43-48.

[73] L.K. Tamm, H.M. McConnell, Supported phospholipid bilayers, Biophysical Journal, 47 (1985) 105-113.

[74] E.T. Castellana, P.S. Cremer, Solid supported lipid bilayers: From biophysical studies to sensor design, Surf Sci Rep, 61 (2006) 429-444.

[75] E. Reimhult, M. Zach, F. Hook, B. Kasemo, A multitechnique study of liposome adsorption on Au and lipid bilayer formation on SiO2, Langmuir, 22 (2006) 3313-3319.

[76] R.P. Richter, A.R. Brisson, Following the formation of supported lipid bilayers on mica: A study combining AFM, QCM-D, and ellipsometry, Biophys J, 88 (2005) 3422-3433.

[77] T.H. Anderson, Y. Min, K.L. Weirich, H. Zeng, D. Fygenson, J.N. Israelachvili, Formation of supported bilayers on silica substrates, Langmuir, 25 (2009) 6997-7005.

[78] S. Faiss, E. Luthgens, A. Janshoff, Adhesion and rupture of liposomes mediated by electrostatic interaction monitored by thickness shear mode resonators, European Biophysics Journal with Biophysics Letters, 33 (2004) 555-561.

[79] D. Stroumpoulis, A. Parra, M. Tirrell, A kinetic study of vesicle fusion on silicon dioxide surfaces by ellipsometry, AIChE J, 52 (2006) 2931-2937.

[80] J.T. Marques, A.S. Viana, R.F. De Almeida, Ethanol effects on binary and ternary supported lipid bilayers with gel/fluid domains and lipid rafts, Biochim Biophys Acta, 1808 (2011) 405-414.

[81] N. Kohli, S. Vaidya, R.Y. Ofoli, R.M. Worden, I. Lee, Arrays of lipid bilayers and liposomes on patterned polyelectrolyte templates, Journal of Colloid and Interface Science, 301 (2006) 461-469.

[82] I. Reviakine, A. Brisson, Formation of supported phospholipid bilayers from unilamellar vesicles investigated by atomic force microscopy, Langmuir, 16 (2000) 1806-1815.

[83] C.A. Keller, B. Kasemo, Surface specific kinetics of lipid vesicle adsorption measured with a quartz crystal microbalance, Biophys J, 75 (1998) 1397-1402.

[84] Y. Tang, Z. Wang, J. Xiao, S. Yang, Y.J. Wang, P. Tong, Studies of Phospholipid Vesicle Deposition/Transformation on a Polymer Surface by Dissipative Quartz Crystal Microbalance and Atomic Force Microscopy, The Journal of Physical Chemistry B, 113 (2009) 14925-14933.

[85] A.S. Angelatos, K. Katagiri, F. Caruso, Bioinspired colloidal systems via layer-by-layer assembly, Soft Matter, 2 (2006) 18-23.

[86] L.Q. Ge, J.Y. Ji, Fabrication and Stability Study of Multilayer Liposome, Asian J. Chem., 22 (2010) 66-78.

[87] M.L. Moraes, P.J. Gomes, P.A. Ribeiro, P. Vieira, A.A. Freitas, R. Kohler, O.N. Oliveira, M. Raposo, Polymeric scaffolds for enhanced stability of melanin incorporated in liposomes, Journal of Colloid and Interface Science, 350 (2010) 268-274.

[88] Y. Nakane, I. Kubo, Layer-by-layer of liposomes and membrane protein as a recognition element of biosensor, Thin Solid Films, 518 (2009) 678-681.

[89] Y. Fukui, K. Fujimoto, The Preparation of Sugar Polymer-Coated Nanocapsules by the Layer-by-Layer Deposition on the Liposome, Langmuir, 25 (2009) 10020-10025.

[90] D.V. Volodkin, P. Schaaf, H. Mohwald, J.C. Voegel, V. Ball, Effective embedding of liposomes into polyelectrolyte multilayered films: the relative importance of lipid-polyelectrolyte and interpolyelectrolyte interactions, Soft Matter, 5 (2009) 1394-1405.

[91] M.L. Moraes, M.S. Baptista, R. Itri, V. Zucolotto, O.N. Oliveira, Immobilization of liposomes in nanostructured layer-by-layer films containing dendrimers, Mater. Sci. Eng. C-Biomimetic Supramol. Syst., 28 (2008) 467-471.

[92] G. Decher, Fuzzy nanoassemblies: Toward layered polymeric multicomposites, Science, 277 (1997) 1232-1237.

[93] B.G. De Geest, N.N. Sanders, G.B. Sukhorukov, J. Demeester, S.C. De Smedt, Release mechanisms for polyelectrolyte capsules, Chemical Society Reviews, 36 (2007) 636-649.

[94] M. Michel, D. Vautier, J.C. Voegel, P. Schaaf, V. Ball, Layer by layer self-assembled polyelectrolyte multilayers with embedded phospholipid vesicles, Langmuir, 20 (2004) 4835-4839.

[95] M. Tanaka, E. Sackmann, Polymer-supported membranes as models of the cell surface, Nature, 437 (2005) 656-663.

[96] F. Yamauchi, Y. Koyamatsu, K. Kato, H. Iwata, Layer-by-layer assembly of cationic lipid and plasmid DNA onto gold surface for stent-assisted gene transfer, Biomaterials, 27 (2006) 3497-3504.

[97] Y. Min, N. Pesika, J. Zasadzinski, J. Israelachvili, Studies of bilayers and vesicle adsorption to solid substrates: development of a miniature streaming potential apparatus (SPA), Langmuir, 26 (2010) 8684-8689.

[98] T.H. Vu, T. Shimanouchi, H. Ishii, H. Umakoshi, R. Kuboi, Immobilization of intact liposomes on solid surfaces: a quartz crystal microbalance study, J Colloid Interface Sci, 336 (2009) 902-907.

[99] S. Morita, M. Nukui, R. Kuboi, Immobilization of liposomes onto quartz crystal microbalance to detect interaction between liposomes and proteins, Journal of Colloid and Interface Science, 298 (2006) 672-678.

[100] M.L. Moraes, M.S. Baptista, R. Itri, V. Zucolotto, O.N. Oliveira Jr, Immobilization of liposomes in nanostructured layer-by-layer films containing dendrimers, Mater Sci Eng C, 28 (2008) 467-471.

[101] C. Delajon, T. Gutberlet, R. Steitz, H. Mohwald, R. Krastev, Formation of polyelectrolyte multilayer architectures with embedded DMPC studied in situ by neutron reflectometry, Langmuir, 21 (2005) 8509-8514.

[102] N. Agmon, Liquid Water: From Symmetry Distortions to Diffusive Motion, Accounts of Chemical Research, 45 (2011) 63-73.

[103] J. Li, X. Gong, H. Lu, D. Li, H. Fang, R. Zhou, Electrostatic gating of a nanometer water channel, Proceedings of the National Academy of Sciences, 104 (2007) 3687-3692.

[104] M.D. Fayer, Dynamics of water interacting with interfaces, molecules, and ions, Accounts of chemical research, 45 (2011) 3-14.

[105] T. Farhat, G. Yassin, S.T. Dubas, J.B. Schlenoff, Water and ion pairing in polyelectrolyte multilayers, Langmuir, 15 (1999) 6621-6623.

[106] T. McIntosh, S. Simon, Area per molecule and distribution of water in fully hydrated dilauroylphosphatidylethanolamine bilayers, Biochemistry, 25 (1986) 4948-4952.

[107] M. Mezei, D.L. Beveridge, Theoretical studies of hydrogen bonding in liquid water and dilute aqueous solutions, The Journal of Chemical Physics, 74 (1981) 622-632.

[108] H. Watanabe, S. Iwata, Theoretical studies of geometric structures of phenol-water clusters and their infrared absorption spectra in the O–H stretching region, The Journal of chemical physics, 105 (1996) 420-431.

[109] M.L. Berkowitz, R. Vácha, Aqueous solutions at the interface with phospholipid bilayers, Accounts of chemical research, 45 (2011) 74-82.

[110] J. Skinner, P. Pieniazek, S. Gruenbaum, Vibrational spectroscopy of water at interfaces, Accounts of chemical research, 45 (2011) 93-100.

[111] A.A. Duarte, S.L. Filipe, L.M. Abegão, P.J. Gomes, P.A. Ribeiro, M. Raposo, Adsorption Kinetics of DPPG Liposome Layers: A Quantitative Analysis of Surface Roughness, Microsc Microanal, 19 (2013) 867-875.

[112] A.A. Duarte, M. Raposo, Growth analysis of PEI/DPPG self-assembled films by Quartz Crystal Microbalance, Bioengineering (ENBENG), 2012 IEEE 2nd Portuguese Meeting in, (Feb. 2012) 1-6.

[113] M. Campas, C. O'Sullivan, Layer-by-layer biomolecular assemblies for enzyme sensors, immunosensing, and nano architectures, Analytical Letters, 36 (2003) 2551-2569.

[114] K. Matsumoto, Dispensable nature of phosphatidylglycerol in Escherichia coli: dual roles of anionic phospholipids, Molecular microbiology, 39 (2001) 1427-1433.

[115] M. Hagio, I. Sakurai, S. Sato, T. Kato, S. Tabata, H. Wada, Phosphatidylglycerol is essential for the development of thylakoid membranes in Arabidopsis thaliana, Plant and cell physiology, 43 (2002) 1456-1464.

[116] J.T. Queenan, C.Y. Spong, C.J. Lockwood, Queenan's management of high-risk pregnancy: an evidence-based approach, John Wiley & Sons, 2012.

[117] S.P. Nighswander-Rempel, J. Riesz, J. Gilmore, J.P. Bothma, P. Meredith, Quantitative fluorescence excitation spectra of synthetic eumelanin, The Journal of Physical Chemistry B, 109 (2005) 20629-20635.

[118] V.M. Sava, S.-M. Yang, M.-Y. Hong, P.-C. Yang, G.S. Huang, Isolation and characterization of melanic pigments derived from tea and tea polyphenols, Food Chemistry, 73 (2001) 177-184.

[119] A.M. Karlsson, K. Bjuhr, M. Testorf, P.Å. Öberg, E. Lerner, I. Lundström, S.P.S. Svensson, Biosensing of opioids using frog melanophores, Biosensors and Bioelectronics, 17 (2002) 331-335.

[120] C. Breton, J.-F. Terral, C. Pinatel, F. Médail, F. Bonhomme, A. Bervillé, The origins of the domestication of the olive tree, Comptes rendus biologies, 332 (2009) 1059-1064.

[121] C.L. Huang, B.E. Sumpio, Olive oil, the mediterranean diet, and cardiovascular health, Journal of the American College of Surgeons, 207 (2008) 407-416.

[122] M.I. Gurr, Dietary lipids and coronary heart desease: Old evidence, new persspective, Progress in lipid research, 31 (1992) 195-243.

[123] N. Ouazzani, R. Lumaret, P. Villemur, Genetic variation in the olive tree (Olea europaea L.) cultivated in Morocco, Euphytica, 91 (1996) 9-20.

[124] L.T. Vaz-Freire, M. da Silva, A. Freitas, Comprehensive two-dimensional gas chromatography for fingerprint pattern recognition in olive oils produced by two different techniques in Portuguese olive varieties< i> Galega Vulgar, Cobrançosa</i> e< i> Carrasquenha</i>, Analytica chimica acta, 633 (2009) 263-270.

[125] A. Bakhouche, J. Lozano-Sánchez, R. Beltrán-Debón, J. Joven, A. Segura-Carretero, A. Fernández-Gutiérrez, Phenolic characterization and geographical classification of commercial Arbequina extra-virgin olive oils produced in southern Catalonia, Food Research International, 50 (2013) 401-408.

[126] C. Pizarro, S. Rodríguez-Tecedor, N. Pérez-del-Notario, J. González-Sáiz, Recognition of volatile compounds as markers in geographical discrimination of Spanish extra virgin olive oils by chemometric analysis of non-specific chromatography volatile profiles, Journal of Chromatography A, 1218 (2011) 518-523.

[127] M. Lerma-García, C. Lantano, E. Chiavaro, L. Cerretani, J. Herrero-Martínez, E. Simó-Alfonso, Classification of extra virgin olive oils according to their geographical origin using phenolic compound profiles obtained by capillary electrochromatography, Food research international, 42 (2009) 1446-1452.

[128] C. Capannesi, I. Palchetti, M. Mascini, A. Parenti, Electrochemical sensor and biosensor for polyphenols detection in olive oils, Food Chemistry, 71 (2000) 553-562.

[129] J. Choi, M.F. Rubner, Influence of the degree of ionization on weak polyelectrolyte multilayer assembly, Macromolecules, 38 (2005) 116-124.

[130] A. Baba, F. Kaneko, R.C. Advincula, Polyelectrolyte adsorption processes characterized in situ using the quartz crystal microbalance technique: alternate adsorption properties in ultrathin polymer films, Colloids and Surfaces a-Physicochemical and Engineering Aspects, 173 (2000) 39-49.

[131] J. Wegener, A. Janshoff, C. Steinem, The quartz crystal microbalance as a novel means to study cell-substrate interactions In situ, Cell Biochemistry and Biophysics, 34 (2001) 121-151.

[132] B. A. Cavic, M. Thompson, G. L. Hayward, Acoustic waves and the study of biochemical macromolecules and cells at the sensor-liquid interface, Analyst, 124 (1999) 1405-1420.

[133] S.-M. Chang, H. Muramatsu, C. Nakamura, J. Miyake, The principle and applications of piezoelectric crystal sensors, Materials Science and Engineering: C, 12 (2000) 111-123.

[134] B. Ding, J. Kim, Y. Miyazaki, S. Shiratori, Electrospun nanofibrous membranes coated quartz crystal microbalance as gas sensor for NH3 detection, Sensors and Actuators B: Chemical, 101 (2004) 373-380.

[135] D. Ballantine Jr, R.M. White, S.J. Martin, A.J. Ricco, E. Zellers, G. Frye, H. Wohltjen, Acoustic Wave Sensors: Theory, Design, & Physico-Chemical Applications, Academic press, 1996.

[136] V.M. Mecea, From Quartz Crystal Microbalance to Fundamental Principles of Mass Measurements, Analytical Letters, 38 (2005) 753-767.

[137] L.M.G. Abegão, Desenvolvimento de um sensor para detecção de nano e micro concentrações de deltametrina, in: Departamento de Física, Universidade Nova de Lisboa, 2012.

[138] Y. Okahata, O. Shimizu, H. Ebato, Detection of odorous substances by using a lipid-coated quartz-crystal microbalance in the gas phase, Bulletin of the Chemical Society of Japan, 63 (1990) 3082-3088.

[139] C. O'sullivan, R. Vaughan, G. Guilbault, Piezoelectric immunosensors-theory and applications, (1999).

[140] E.R. Kleinfeld, G.S. Ferguson, Rapid, reversible sorption of water from the vapor by a multilayered composite film: a nanostructured humidity sensor, Chemistry of materials, 7 (1995) 2327-2331.

[141] R. Bear, C. Blakemore, A.P. Instruments, Reducing the Detection Limits for a Process Moisture Analyzer, TECHNICAL PAPERS-ISA, 410 (2001) 21-30.

[142] J. Leskinen, J. Joutsensaari, A. Jakorinne, M. Laasanen, J. Jokiniemi, Diffusion based nanoparticle monitor using QCM-technology, in: Proc. European Aerosol Conf, 2009, pp. 247-250.

[143] D. McKeown, C. Claysmith, Quartz crystal microbalance systems for shuttle contamination measurements, in: Proc. of (he International Spacecraft Contamination Conference, USAF Academy, NASA/USAF Pub. NASA-CP-2039/AFML, 1978.

[144] D.A. Buttry, M.D. Ward, Measurement of interfacial processes at electrode surfaces with the electrochemical quartz crystal microbalance, Chemical Reviews, 92 (1992) 1355-1379.

[145] D. Yang, V. Ding, J. Luo, R.S. Currier, S. Obrey, Y. Zhao, Hydrogen Adsorption in Thin Films of Prussian Blue Analogues, in: The 2008 Annual Meeting, 2008.

[146] J.M. Jones, T. Coffey, Using the quartz crystal microbalance to study macro-and nanoscale bubbles at solid–liquid interfaces, in: Journal of Physics: Conference Series, IOP Publishing, 2008, pp. 072026.

[147] E. Calvo, C. Danilowicz, C. Lagier, J. Manrique, M. Otero, Characterization of self-assembled redox polymer and antibody molecules on thiolated gold electrodes, Biosensors and Bioelectronics, 19 (2004) 1219-1228.

[148] Z.L. Wang, J. Wiley, Characterization of nanophase materials, Wiley Online Library, 2000.

[149] P. Miečinskas, K. Leinartas, V. Uksienė, A. Lugauskas, R. Ramanauskas, E. Juzeliūnas, QCM study of microbially influenced corrosion of aluminium subjected to the influence of Aspergillus niger Tiegh, Chemija, 17 (2006) 30-34.

[150] P. Murphy, C. Boxall, R. Taylor, Investigation of water adsorption on metal oxide surfaces under conditions representative of PuO2 storage containers, in: Meeting Abstracts, The Electrochemical Society, 2013, pp. 699-699.

[151] M. Lazerges, H. Perrot, N. Zeghib, E. Antoine, C. Compere, In situ QCM DNA-biosensor probe modification, Sensors and Actuators B: Chemical, 120 (2006) 329-337.

[152] C. Ayela, F. Roquet, L. Valera, C. Granier, L. Nicu, M. Pugnière, Antibody–antigenic peptide interactions monitored by SPR and QCM-D: A model for SPR detection of IA-2 autoantibodies in human serum, Biosensors and Bioelectronics, 22 (2007) 3113-3119.

[153] M. Lee, S.K. Park, C. Chung, H. Kim, QCM study of beta-casein adsorption on the hydrophobic surface: Effect of ionic strength and cations, BULLETIN-KOREAN CHEMICAL SOCIETY, 25 (2004) 1031-1035.

[154] G.E. Rydell, A.B. Dahlin, F. Höök, G. Larson, QCM-D studies of human norovirus VLPs binding to glycosphingolipids in supported lipid bilayers reveal strain-specific characteristics, Glycobiology, 19 (2009) 1176-1184.

[155] D. Ivnitski, I. Abdel-Hamid, P. Atanasov, E. Wilkins, Biosensors for detection of pathogenic bacteria, Biosensors and Bioelectronics, 14 (1999) 599-624.

[156] J. Wegener, J. Seebach, A. Janshoff, H.-J. Galla, Analysis of the composite response of shear wave resonators to the attachment of mammalian cells, Biophysical journal, 78 (2000) 2821-2833.

[157] T. Hianik, V. Ostatná, Z. Zajacová, E. Stoikova, G. Evtugyn, Detection of aptamer–protein interactions using QCM and electrochemical indicator methods, Bioorganic & medicinal chemistry letters, 15 (2005) 291-295.

[158] L. Qingwen, G. Hong, W. Yiming, L. Guoan, M. Jie, Studies on Self-Assembly Monolayers of Cysteine on Gold by XPS, QCM, and Electrochemical Techniques, Electroanalysis, 13 (2001) 1342-1346.

[159] J. Alenus, A. Ethirajan, F. Horemans, A. Weustenraed, P. Csipai, J. Gruber, M. Peeters, T. Cleij, P. Wagner, Molecularly imprinted polymers as synthetic receptors for the QCM-D-based detection of l-nicotine in diluted saliva and urine samples, Analytical and bioanalytical chemistry, (2013) 1-9.

[160] K. Ariga, Y. Okahata, In situ characterization of Langmuir-Blodgett films during a transfer process. Evaluation of transfer ratio and water incorporation by using a quartz crystal microbalance, Langmuir, 10 (1994) 3255-3259.

[161] J. Pérez, B.R. Weiner, The laser ablation of gold films at the electrode surface of a quartz crystal microbalance, Applied surface science, 62 (1992) 281-285.

[162] X. Turon, O.J. Rojas, R.S. Deinhammer, Enzymatic kinetics of cellulose hydrolysis: A QCM-D study, Langmuir, 24 (2008) 3880-3887.

[163] A. Welle, A. Chiumiento, R. Barbucci, Competitive protein adsorption on micro patterned polymeric biomaterials, and viscoelastic properties of tailor made extracellular matrices, Biomolecular engineering, 24 (2007) 87-91.

[164] C. Lu, A.W. Czanderna, Applications of piezoelectric quartz crystal microbalances, Elsevier, 1984.

[165] E. Reimhult, F. Hook, B. Kasemo, Vesicle adsorption on SiO2 and TiO2: Dependence on vesicle size, Journal of Chemical Physics, 117 (2002) 7401-7404.

[166] E. Reimhult, F. Hook, B. Kasemo, Intact vesicle adsorption and supported biomembrane formation from vesicles in solution: Influence of surface chemistry, vesicle size, temperature, and osmotic pressure, Langmuir, 19 (2003) 1681-1691.

[167] T.H. Vu, T. Shimanouchi, H. Ishii, H. Umakoshi, R. Kuboi, Immobilization of intact liposomes on solid surfaces: A quartz crystal microbalance study, Journal of Colloid and Interface Science, 336 (2009) 902-907.

[168] T.H. Anderson, Y.J. Min, K.L. Weirich, H.B. Zeng, D. Fygenson, J.N. Israelachvili, Formation of Supported Bilayers on Silica Substrates, Langmuir, 25 (2009) 6997-7005.

[169] E. Reimhult, B. Kasemo, F. Hook, Rupture Pathway of Phosphatidylcholine Liposomes on Silicon Dioxide, Int J Mol Sci, 10 (2009) 1683-1696.

[170] M. Lösche, J. Schmitt, G. Decher, W.G. Bouwman, K. Kjaer, Detailed structure of molecularly thin polyelectrolyte multilayer films on solid substrates as revealed by neutron reflectometry, Macromolecules, 31 (1998) 8893-8906.

[171] G. Binnig, H. Rohrer, C. Gerber, E. Weibel, Surface Studies by Scanning Tunneling Microscopy, Physical Review Letters, 49 (1982) 57-61.

[172] G. Binnig, C.F. Quate, C. Gerber, Atomic Force Microscope, Physical Review Letters, 56 (1986) 930-933.

[173] P. Vermette, Liposome characterization by quartz crystal microbalance measurements and atomic force microscopy, Methods Enzymol, 465 (2009) 43-73.

[174] http://artsci.ucla.edu/artsci/SI_BLOG/?paged=38 (accessed 12/08/13 at 10.33 a.m.).

[175] P.J. Eaton, P. West, Atomic force microscopy, Oxford University Press New York, 2010.

[176] M. Raposo, P.A. Ribeiro, M.A. Pereira-da-Silva, O.N. Oliveira Jr., Current Issues on Multidiscipplinary Microsocpy Research and Education, in: A. Méndez-Vilas, L. Labajos-Broncano (Eds.) FORMATEX Microscopy Book Series N.2, 2004, pp. 224.

[177] M. Raposo, Q. Ferreira, P.A. Ribeiro, A Guide for Atomic Force Microscopy Analysis of Soft-Condensed Matter, in: A. Méndez-Vilas, J. Díaz (Eds.) Modern Research and Educational Topics in Microscopy, FORMATEX, 2007, pp. 758-769.

[178] S. Fang, S. Haplepete, W. Chen, C. Helms, H. Edwards, Analyzing atomic force microscopy images using spectral methods, Journal of applied physics, 82 (1997) 5891-5898.

[179] Q. Ferreira, G. Bernardo, A. Charas, L.s. Alcácer, J. Morgado, Polymer Light-Emitting Diode Interlayers. Formation Studied by Current-Sensing Atomic Force Microscopy and Scaling Laws., J Phys Chem C Nanomater Interfaces, 114 (2009) 572-579.

[180] N.C. de Souza, J.R. Silva, R. Di Thommazo, M. Raposo, D.T. Balogh, J.A. Giacometti, O.N. Oliveira, Influence of solution treatment on the adsorption and morphology of poly (o-methoxyaniline) layer-by-layer films, The Journal of Physical Chemistry B, 108 (2004) 13599-13606.

[181] N.C. de Souza, J.R. Silva, M.A. Pereira-da-Silva, M. Raposo, R.M. Faria, J.A. Giacometti, O.N. Oliveira, Jr., Dynamic scale theory for characterizing surface morphology of layer-by-layer films of poly(o-methoxyaniline), J Nanosci Nanotechnol, 4 (2004) 548-552.

[182] A. Calò, P. Stoliar, E. Bystrenova, F. Valle, F. Biscarini, Measurement of DNA morphological parameters at highly entangled regime on surfaces, The Journal of Physical Chemistry B, 113 (2009) 4987-4990.

[183] P. Viville, R. Lazzaroni, J.L. Brédas, P. Moretti, P. Samorí, F. Biscarini, The influence of thermal annealing on the morphology of sexithienyl thin films, Advanced Materials, 10 (1998) 57-60.

[184] C.J. Buchko, K.M. Kozloff, D.C. Martin, Surface characterization of porous, biocompatible protein polymer thin films, Biomaterials, 22 (2001) 1289-1300.

[185] M. Iazykov, Growth of pentacene on parylene and on BCB for organic transistors application, and DNA-based nanostructures studied by Amplitude: Modulation Atomic Force Microscopy in air and in liquids, in, Ecole Centrale de Lyon, 2011.

[186] P. Brault, P. Dumas, F. Salvan, Roughness scaling of plasma-etched silicon surfaces, Journal of Physics. Condensed Matter, 10 (1998) L27-L32.

[187] E.A. Eklund, E.J. Snyder, R.S. Williams, Correlation from randomness: quantitative analysis of ion-etched graphite surfaces using the scanning tunneling microscope, Surface science, 285 (1993) 157-180.

[188] P. Dash, P. Mallick, H. Rath, A. Tripathi, J. Prakash, D. Avasthi, S. Mazumder, S. Varma, P. Satyam, N. Mishra, Surface roughness and power spectral density study of SHI irradiated ultra-thin gold films, Applied Surface Science, 256 (2009) 558-561.

[189] M.W. Mitchell, D.A. Bonnell, Quantitative topographic analysis of fractal surfaces by scanning tunneling microscopy, Journal of Materials Research, 5 (1990) 2244-2254.

[190] J. Ferré-Borrull, A. Duparre, E. Quesnel, Procedure to characterize microroughness of optical thin films: application to ion-beam-sputtered vacuum-ultraviolet coatings, Applied optics, 40 (2001) 2190-2199.

[191] Z.-N. Fang, B. Yang, M.-G. Chen, C.-H. Zhang, J.-P. Xie, G.-X. Ye, Growth and morphology of ultra-thin Al films on liquid substrates studied by atomic force microscopy, Thin Solid Films, 517 (2009) 3408-3411.

[192] A.-L. Barabási, Fractal concepts in surface growth, Cambridge university press, 1995.

[193] T. Itoh, N. Yamauchi, Surface morphology characterization of pentacene thin film and its substrate with under-layers by power spectral density using fast Fourier transform algorithms, Appl Surf Sci, 253 (2007) 6196-6202.

[194] N. Sahoo, S. Thakur, R. Tokas, Fractals and superstructures in gadolinia thin film morphology: Influence of process variables on their characteristic parameters, Thin Solid Films, 503 (2006) 85-95.

[195] D.H. Li, J. Ganczarczyk, Fractal geometry of particle aggregates generated in water and wastewater treatment processes, Environmental science & technology, 23 (1989) 1385-1389.

[196] X. Li, B.E. Logan, Size distributions and fractal properties of particles during a simulated phytoplankton bloom in a mesocosm, Deep Sea Research Part II: Topical Studies in Oceanography, 42 (1995) 125-138.

[197] D.G. Lee, J.S. Bonner, L.S. Garton, A.N.S. Ernest, R.L. Autenrieth, Modeling coagulation kinetics incorporating fractal theories: comparison with observed data, Water Research, 36 (2002) 1056-1066.

[198] S. Walheim, M. Böltau, J. Mlynek, G. Krausch, U. Steiner, Structure formation via polymer demixing in spin-cast films, Macromolecules, 30 (1997) 4995-5003.

[199] A. Ballestad, B. Ruck, J. Schmid, M. Adamcyk, E. Nodwell, C. Nicoll, T. Tiedje, Surface morphology of GaAs during molecular beam epitaxy growth: Comparison of experimental data with simulations based on continuum growth equations, Physical Review B, 65 (2002) 205302.

[200] J. Villain, Continuum models of crystal growth from atomic beams with and without desorption, Journal de physique I, 1 (1991) 19-42.

[201] Q. Ferreira, Estudo da formação de filmes nanoestruturados para aplicação em fotónica, in, Tese de Doutoramento, Universidade Nova de Lisboa, Lisboa, 2007.

[202] http://chemwiki.ucdavis.edu/Analytical_Chemistry/Instrumental_Analysis/Microscopy/Dynamic_Light_Scattering (accessed at 07/07/13 at 14.05 a.m.).

[203] R. Pecora, Dynamic light scattering: applications of photon correlation spectroscopy, Springer, 1985.

[204] B.J. Berne, Dynamic light scattering: with applications to chemistry, biology and physics, DoverPublications. com, 1976.

[205] C.N.R. Rao, Ultra-violet and visible spectroscopy, (1975).

[206] R. Silverstein, F. Webster, Spectrometric identification of organic compounds, John Wiley & Sons, 2006.

[207] Michael K. Denk, CHEM 2070. (Online) UV-Vis & PES, 2005 (accessed 10/02/14 at 10:10 a.m.).

[208] S. Eden, P. Limão-Vieira, S.V. Hoffmann, N. Mason, VUV photoabsorption in CF< sub> 3</sub> X (X= Cl, Br, I) fluoro-alkanes, Chemical physics, 323 (2006) 313-333.

[209] http://en.wikipedia.org/wiki/File:ASTRID-schematic.png (accessed 15/08/13 at 15:15 a.m.).

[210] D.A. Skoog, D.M. West, Principles of instrumental analysis, Saunders College Philadelphia, 1980.

[211] http://www.chem.queensu.ca/people/faculty/horton/research.html, (11.30 A.M., 05/08/2013).

[212] A.B. do Rego, L.V. Ferreira, H. Nalwa, Handbook of Surfaces and Interfaces of Materials, (2001).

[213] G. Beamson, D. Briggs, High resolution XPS of organic polymers, (1992).

[214] H.W. Siesler, Y. Ozaki, S. Kawata, H.M. Heise, Near-infrared spectroscopy: principles, instruments, applications, John Wiley & Sons, 2008.

[215] W. Perkins, Fourier transform-infrared spectroscopy: Part I. Instrumentation, Journal of Chemical Education, 63 (1986) A5.

[216] http://www.tappsa.co.za/archive/APPW2002/Title/Analytical_techniques/analytical_techniques.html, (18.18 P.M., 05/09/2013).

[217] T. Naes, T. Isaksson, T. Fearn, T. Davies, A user friendly guide to multivariate calibration and classification, NIR publications, 2002.

[218] D. McMullan, An improved scanning electron microscope for opaque specimens, Proceedings of the IEE-Part II: Power Engineering, 100 (1953) 245-256.

[219] K. Smith, C. Oatley, The scanning electron microscope and its fields of application, British Journal of Applied Physics, 6 (1955) 391.

[220] C.W. Oatley, W.C. Nixon, R.F.W. Pease, Scanning Electron Microscopy, in: L. Marton (Ed.) Advances in Electronics and Electron Physics, Academic Press, 1966, pp. 181-247.

[221] D. McMullan, Scanning electron microscopy 1928–1965, Scanning, 17 (1995) 175-185.

[222] N. Aslam, Neuron cell survival on positively charged surface bound gold nanoparticles over gold and silicon substrate in: Department of Microelectronics and Applied Physics KTH, Royal Institute of Technology, Stockholm, Sweden 2010, pp. 83.

[223] http://www.tcd.ie/Physics/Surfaces/ellipsometry2.php (accessed 14/12/13 at 09:45 a.m.).

[224] Y. Vlasov, A. Legin, A. Rudnitskaya, C. Di Natale, A. D'amico, Nonspecific sensor arrays (" electronic tongue") for chemical analysis of liquids (IUPAC Technical Report), Pure and Applied Chemistry, 77 (2005) 1965-1983.

[225] J. Rabe, S. Buttgenbach, J. Schroder, P. Hauptmann, Monolithic miniaturized quartz microbalance array and its application to chemical sensor systems for liquids, Sensors Journal, IEEE, 3 (2003) 361-368.

[226] J.J. Lavigne, S. Savoy, M.B. Clevenger, J.E. Ritchie, B. McDoniel, S.-J. Yoo, E.V. Anslyn, J.T. McDevitt, J.B. Shear, D. Neikirk, Solution-based analysis of multiple analytes by a sensor array: toward the development of an “electronic tongue”, Journal of the American Chemical Society, 120 (1998) 6429-6430.

[227] I.M. Apetrei, C. Apetrei, Voltammetric e-tongue for the quantification of total polyphenol content in olive oils, Food Research International, 54 (2013) 2075-2082.

[228] L.G. Dias, A. Fernandes, A.C. Veloso, A.A. Machado, J.A. Pereira, A.M. Peres, Single-cultivar extra virgin olive oil classification using a potentiometric electronic tongue, Food chemistry, 160 (2014) 321-329.

[229] M. Gutiérrez, S. Alegret, R. Cáceres, J. Casadesús, O. Marfà, M. del Valle, Nutrient solution monitoring in greenhouse cultivation employing a potentiometric electronic tongue, Journal of agricultural and food chemistry, 56 (2008) 1810-1817.

[230] A. Rudnitskaya, A. Ehlert, A. Legin, Y. Vlasov, S. Büttgenbach, Multisensor system on the basis of an array of non-specific chemical sensors and artificial neural networks for determination of inorganic pollutants in a model groundwater, Talanta, 55 (2001) 425-431.

[231] M. Gutiérrez, S. Alegret, M. del Valle, Bioelectronic tongue for the simultaneous determination of urea, creatinine and alkaline ions in clinical samples, Biosensors and Bioelectronics, 23 (2008) 795-802.

[232] A. Gutés, D. Calvo, F. Céspedes, M. del Valle, Automatic sequential injection analysis electronic tongue with integrated reference electrode for the determination of ascorbic acid, uric acid and paracetamol, Microchimica Acta, 157 (2007) 1-6.

[233] F. Winquist, S. Holmin, C. Krantz-Rülcker, P. Wide, I. Lundström, A hybrid electronic tongue, Analytica Chimica Acta, 406 (2000) 147-157.

[234] J.M. Gutiérrez, Z. Haddi, A. Amari, B. Bouchikhi, A. Mimendia, X. Cetó, M. del Valle, Hybrid electronic tongue based on multisensor data fusion for discrimination of beers, Sensors and Actuators B: Chemical, 177 (2013) 989-996.

[235] K. Tahri, A.A. Duarte, T. Saidi, M. Bougrini, P.A. Ribeiro, N.E. Bari, M. Raposo, B. Bouchikhi, Discrimination of olive oils according to geographical origin by a portable hybrid electronic tongue combined with chemometric analysis, Journal of Food Engineering, (2014) Submitted.

[236] Z. Haddi, H. Alami, N. El Bari, M. Tounsi, H. Barhoumi, A. Maaref, N. Jaffrezic-Renault, B. Bouchikhi, Electronic nose and tongue combination for improved classification of Moroccan virgin olive oil profiles, Food Research International, 54 (2013) 1488-1498.

[237] J. Pimthon, R. Willumeit, A. Lendlein, D. Hofmann, All-atom molecular dynamics simulation studies of fully hydrated gel phase DPPG and DPPE bilayers, J Mol Struct, 921 (2009) 38-50.

[238] M.J. Shultz, T.H. Vu, B. Meyer, P. Bisson, Water: A responsive small molecule, Accounts of chemical research, 45 (2011) 15-22.

[239] A. Dicko, H. Bourque, M. Pézolet, Study by infrared spectroscopy of the conformation of dipalmitoylphosphatidylglycerol monolayers at the air–water interface and transferred on solid substrates, Chemistry and physics of lipids, 96 (1998) 125-139.

[240] P. Aoki, D. Volpati, F. Cabrera, V. Trombini, A. Riul Jr, C. Constantino, Spray layer-by-layer films based on phospholipid vesicles aiming sensing application via e-tongue system, Materials Science and Engineering: C, 32 (2012) 862-871.

[241] T.E. Goto, L. Caseli, Understanding the Collapse Mechanism in Langmuir Monolayers through Polarization Modulation-Infrared Reflection Absorption Spectroscopy, Langmuir, 29 (2013) 9063-9071.

[242] A. Blume, W. Hübner, G. Messner, Fourier transform infrared spectroscopy of 13C: O labeled phospholipids hydrogen bonding to carbonyl groups, Biochemistry, 27 (1988) 8239-8249.

[243] C. Schwieger, A. Blume, Interaction of poly (L-lysines) with negatively charged membranes: an FT-IR and DSC study, European Biophysics Journal, 36 (2007) 437-450.

[244] M. Paolorossi, G.G. Montich, Conformational changes of β2-human glycoprotein I and lipid order in lipid–protein complexes, Biochimica et Biophysica Acta (BBA)-Biomembranes, 1808 (2011) 2167-2177.

[245] W.K. Surewicz, H.H. Mantsch, New insight into protein secondary structure from resolution-enhanced infrared spectra, Biochimica et Biophysica Acta (BBA)-Protein Structure and Molecular Enzymology, 952 (1988) 115-130.

[246] R. El-Jastimi, M. Lafleur, Structural characterization of free and membrane-bound nisin by infrared spectroscopy, Biochimica et Biophysica Acta (BBA)-Biomembranes, 1324 (1997) 151-158.

[247] S. Morandat, M. Bortolato, G. Anker, A. Doutheau, M. Lagarde, J.-P. Chauvet, B. Roux, Plasmalogens protect unsaturated lipids against UV-induced oxidation in monolayer, Biochimica et Biophysica Acta (BBA)-Biomembranes, 1616 (2003) 137-146.

[248] S. Ortial, S. Morandat, M. Bortolato, B. Roux, A. Polidori, B. Pucci, G. Durand, PBN derived amphiphilic spin-traps. II/Study of their antioxidant properties in biomimetic membranes, Colloids and Surfaces B: Biointerfaces, 113 (2014) 384-393.

[249] K.O. Kwon, M.J. Kim, M. Abe, T. Ishinomori, K. Ogino, Thermotropic behavior of a phospholipid bilayer interacting with metal ions, Langmuir, 10 (1994) 1415-1420.

[250] B. Stuart, Infrared spectroscopy, Wiley Online Library, 2005.

[251] C. Mestres, A. Ortiz, I. Haro, F. Reig, M. Alsina, Influence of phospholipidic charge on the interaction of a multiple antigenic peptide from Hepatitis A virus with monolayers and bilayers, Langmuir, 13 (1997) 5669-5673.

[252] http://www.rsc.org/suppdata/jm/c1/c1jm13790e/c1jm13790e.pdf (accessed 05/12/12 at 16:00 a.m.).

[253] M. Raposo, J. Lourenco, A.M. Botelho do Rego, A.M. Ferraria, P.A. Ribeiro, Counterions–A new approach to control the degree of ionization of polyelectrolytes in layer-by-layer films, Colloids and Surfaces A: Physicochemical and Engineering Aspects, 412 (2012) 1-10.

[254] C. Wagner, C.J. Powell, J. Allison, J. Rumble, NIST X-ray Photoelectron Spectroscopy Database (Version 2.0), Retrieved from NIST Standard Reference Data Program website: http://www. nist. gov/srd, (1997).

[255] M.A. Fontecha-Cámara, M.V. López-Ramón, L.M. Pastrana-Martínez, C. Moreno-Castilla, Kinetics of diuron and amitrole adsorption from aqueous solution on activated carbons, Journal of Hazardous Materials, 156 (2008) 472-477.

[256] A.A. Duarte, P.J. Gomes, J.H. Ribeiro, P.A. Ribeiro, S.V. Hoffmann, N.J. Mason, O.N. Oliveira Jr, M. Raposo, Characterization of PAH/DPPG layer-by-layer films by VUV spectroscopy, The European Physical Journal E, 36 (2013) 1-8.

[257] M. Kolasińska, R. Krastev, P. Warszyński, Characteristics of polyelectrolyte multilayers: Effect of PEI anchoring layer and posttreatment after deposition, Journal of Colloid and Interface Science, 305 (2007) 46-56.

[258] A. Trybała, L. Szyk-Warszyńska, P. Warszyński, The effect of anchoring PEI layer on the build-up of polyelectrolyte multilayer films at homogeneous and heterogeneous surfaces, Colloids and Surfaces A: Physicochemical and Engineering Aspects, 343 (2009) 127-132.

[259] Y. Li, S.M. Ghoreishi, J. Warr, D.M. Bloor, J.F. Holzwarth, E. Wyn-Jones, Binding of Sodium Dodecyl Sulfate to Some Polyethyleneimines and Their Ethoxylated Derivatives at Different pH Values. Electromotive Force and Microcalorimetry Studies, Langmuir, 16 (2000) 3093-3100.

[260] X. Zhu, F. Tang, T.S. Suzuki, Y. Sakka, Role of the initial degree of ionization of polyethylenimine in the dispersion of silicon carbide nanoparticles, Journal of the American Ceramic Society, 86 (2003) 189-191.

[261] R. Lobo, M. Pereira-da-Silva, M. Raposo, R. Faria, O. Oliveira Jr, The morphology of layer-by-layer films of polymer/polyelectrolyte studied by atomic force microscopy, Nanotechnology, 14 (2003) 101.

[262] P.A. Ribeiro, R. Steitz, I.E. Lopis, H. Haas, N.C. Souza, O.N. Oliveira, M. Raposo, Thermal stability of poly(o-methoxyaniline) layer-by-layer films investigated by neutron reflectivity and UV-VIS spectroscopy, J Nanosci Nanotechnol, 6 (2006) 1396-1404.

[263] A.P. Serro, A. Carapeto, G. Paiva, J.P.S. Farinha, R. Colaço, B. Saramago, Formation of an intact liposome layer adsorbed on oxidized gold confirmed by three complementary techniques: QCM-D, AFM and confocal fluorescence microscopy, Surf Interface Anal, 44 (2012) 426-433.

[264] J.J.I. Ramos, S. Stahl, R.P. Richter, S.E. Moya, Water Content and Buildup of Poly(diallyldimethylammonium chloride)/Poly(sodium 4-styrenesulfonate) and Poly(allylamine hydrochloride)/Poly(sodium 4-styrenesulfonate) Polyelectrolyte Multilayers Studied by an in Situ Combination of a Quartz Crystal Microbalance with Dissipation Monitoring and Spectroscopic Ellipsometry, Macromolecules, 43 (2010) 9063-9070.

[265] J.M.C. Lourenço, Presença e influência dos contraiões em filmes automontados, in: Física, FCT - UNL, Monte da Caparica, 2008, pp. 187.

[266] Q. Ferreira, P.J. Gomes, Y. Nunes, M.J.P. Maneira, P.A. Ribeiro, M. Raposo, Atomic force microscope characterization of PAH/PAZO multilayers, Microelectron. Eng., 84 (2007) 506-511.

[267] J. Pimthon, R. Willumeit, A. Lendlein, D. Hofmann, All-atom molecular dynamics simulation studies of fully hydrated gel phase DPPG and DPPE bilayers, Journal of Molecular Structure, 921 (2009) 38-50.

[268] M. Edvardsson, S. Svedhem, G. Wang, R. Richter, M. Rodahl, B. Kasemo, QCM-D and reflectometry instrument: applications to supported lipid structures and their biomolecular interactions, Analytical chemistry, 81 (2008) 349-361.

[269] J. Radler, H. Strey, E. Sackmann, Phenomenology and kinetics of lipid bilayer spreading on hydrophilic surfaces, Langmuir, 11 (1995) 4539-4548.

[270] Y. Lvov, K. Ariga, M. Onda, I. Ichinose, T. Kunitake, A careful examination of the adsorption step in the alternate layer-by-layer assembly of linear polyanion and polycation, Colloids and Surfaces a-Physicochemical and Engineering Aspects, 146 (1999) 337-346.

[271] M. Kolasinska, R. Krastev, P. Warszynski, Characteristics of polyelectrolyte multilayers: Effect of PEI anchoring layer and posttreatment after deposition, Journal of Colloid and Interface Science, 305 (2007) 46-56.

[272] T. Ari, M. H.Güven, Valence-shell electron energy-loss spectra of formic acid and acetic acid, J Electron Spectrosc Relat Phenom, 106 (2000) 29-35.

[273] E.E. Barnes, W.T. Simpson, Correlations among Electronic Transitions for Carbonyl and for Carboxyl in the Vacuum Ultraviolet, J Chem Phys, 39 (1963) 670.

[274] K. Xu, G. Amaral, J. Zhang, Photodissociation dynamics of ethanol at 193.3 nm : The H-atom channel and ethoxy vibrational distribution, J Chem Phys, 111 (1999) 6271.

[275] S. Satyapal, J. Park, R. Bersohn, B. Katz, Dissociation of methanol and ethanol activated by a chemical reaction or by light, J Chem Phys, 91 (1989) 6873.

[276] Y. Wen, J. Segall, M. Dulligan, C. Wittig, Photodissociation of methanol at 193.3 nm: Translational energy release spectra, J Chem Phys, 101 (1994) 5665.

[277] S. Harich, J.J. Lin, Y.T. Lee, X. Yang, Competing atomic and molecular hydrogen pathways in the photodissociation of methanol at 157 nm, J Chem Phys, 111 (1999) 5.

[278] S.-H. Lee, H.-I. Lee, Y.T. Lee, Distributions of angular anisotropy and kinetic energy of products from the photodissociation of methanol at 157 nm, J Chem Phys 121 (2004) 11053.

[279] R. Mota, R. Parafita, A. Giuliani, M.-J. Hubin-Franskin, J.M.C. Lourenço, G. Garcia, S.V. Hoffmann, N.J. Mason, P.A. Ribeiro, M. Raposo, P. Limão-Vieira, Water VUV electronic state spectroscopy by synchrotron radiation, Chem Phys Lett, 416 (2005) 152-159.

[280] Z.-J. Zhang, H.-H. Chen, X.-X. Yang, J.-T. Zhao, G.-B. Zhang, C.-S. Shi, , *VUV spectroscopic properties of rare-earth (RE3+ = Eu, Tb, Tm)-doped AZr2(PO4)3 (A+ = Li, Na, K) type phosphate*, J Phys D Appl Phys, 41 (2008) 105503.

[281] M. Kaneyoshi, Luminescence of some zirconium-containing compounds undervacuum ultraviolet excitation, J Lumin, 121 (2006) 102-108.

[282] R.J. Thompson, A.B.F. Duncan, Intensities of Electronic Transitions in Ammonia, J Chem Phys, 14 (1946) 574-577.

[283] A. Osted, J. Kongsted, O. Christiansen, Theoretical study of the electronic gas-phase spectrum of glycine, alanine, and related amines and carboxylic acids., J Phys Chem A, 109 (2005) 1430-1440.

[284] W.R. Harshbarger, Identification of C state of ammonia by electron impact spectroscopy., J Chem Phys, 54 (1971) 2504-2509.

[285] W.R. Harshbarger, A. Skerbele, E.N. Lassettre, Generalized oscillator strength of the A-X transition of ammonia, J Chem Phys, 54 (1971) 3784-3789.

[286] E. Tannenbaum, E.M. Coffin, A.J. Harrison, The Far Ultraviolet Absorption Spectra of Simple Alkyl Amines, J Chem Phys, 21 (1953) 311.

[287] M.-J. Hubin-Franskin, J. Delwiche, A. Giuliani, M.-P. Ska, F. Motte-Tollet, I.C. Walker, N.J. Mason, J.M. Gingell, N.C. Jones, *Electronic excitation and optical cross sections of methylamine and ethylamine in the UV-VUV spectral region*, J Chem Phys, 116 (2002) 9261.

[288] L. Chantranupong, G. Hirsch, R. J. Buenker, M. Kimura, M.A. Dillon, Theoretical study of the electronic spectrum of ammonia: Generalized oscillator strength calculations for the A-X transition Chem Phys Lett, 154 (1991) 13-21.

[289] P.H.B. Aoki, D. Volpati, A. Riul Jr., W. Caetano, C.J.L. Constantino, Layer-by-layer Technique as a new approach to produce nanostrutured films containing phospholipids as a transducers in sensing applications, Langmuir, 25 (2009) 2331-2338.

[290] P.H.B. Aoki, P. Alessio, M.L. Rodríguez-Méndez, J.A.D.S. Saez, C.J.L. Constantino, Taking Advantage of Electrostatic Interactions To Grow Langmuir-Blodgett Films Containing Multilayers of the Phospholipid Dipalmitoylphosphatidylglycerol, Langmuir 25 (2009) 13062-13070.

[291] T.F. Schmidt, L. Caseli, T. Viitala, O.N. Oliveira Jr, Enhanced activity of horseradish peroxidase in Langmuir–Blodgett films of phospholipids, Biochimica et Biophysica Acta (BBA)-Biomembranes, 1778 (2008) 2291-2297.

[292] R.I.S. Romão, Q. Ferreira, J. Morgado, J.M.G. Martinho, A.M.P.S.G. Silva, Microphase Separation in Mixed Monolayers of DPPG with a Double Hydrophilic Block Copolymer at the Air-Water Interface: A BAM,LSCFM, and AFM Study, Langmuir, 26 (2010) 17165-17177.

[293] T.F. Schmidt, L. Caseli, T. Viitala, O.N. Oliveira Jr., Enhanced activity of horseradish peroxidase in Langmuir-Blodgett films of phospholipids, Biochim Biophys Acta, 1778 (2008) 2291–2297.

[294] S. Herminghaus, Roughness-induced non-wetting, Europhys. Lett, 52 (2000) 165–170.

[295] Q. Ferreira, P.J. Gomes, M.J.P. Maneira, P.A. Ribeiro, M. Raposo, Mechanisms of Adsorption of an Azo-polyelectrolyte onto Layer-by-Layer Films, Sensors and Actuators B-Chemical, 126 (2007) 311-317.

[296] D.E. King, Oxidation of gold by ultraviolet light and ozone at 25 C, Journal of Vacuum Science & Technology A, 13 (1995) 1247-1253.

[297] A.A. Duarte, M. Raposo, Growth analysis of PEI/DPPG self-assembled films by quartz crystal microbalance, in: Bioengineering (ENBENG), 2012 IEEE 2nd Portuguese Meeting in, 2012, pp. 1-6.

[298] P. Ying, A.S. Viana, L.M. Abrantes, G. Jin, Adsorption of human serum albumin onto gold: a combined electrochemical and ellipsometric study, Journal of Colloid and Interface Science, 279 (2004) 95-99.

[299] H. Schönherr, J.M. Johnson, P. Lenz, C.W. Frank, S.G. Boxer, Vesicle adsorption and lipid bilayer formation on glass studied by atomic force microscopy, Langmuir, 20 (2004) 11600-11606.

[300] G.Z. Sauerbrey, Use of the vibrating quartz for thin film weighing and microweighing, Phys, 155 (1959) 206-222.

[301] J. Lyklema, Fundamentals of Interface and Colloid Science, Academic Press; 1 edition, 1991.

[302] N.C. de Souza, J.R. Silva, C.A. Rodrigues, L.d.F. Costa, J.A. Giacometti, O.N. Oliveira Jr, Adsorption processes in layer-by-layer films of poly(o-methoxyaniline): the role of aggregation, Thin Solid Films, 428 (2003) 232-236.

[303] N.C. de Souza, V. Zucolotto, J.R. Silva, F.R. Santos, D.S. dos Santos Jr, D.T. Balogh, O.N. Oliveira Jr, J.A. Giacometti, Morphology characterization of layer-by-layer films from PAH/MA-co-DR13: the role of film thickness, J Colloid Interface Sci, 285 (2005) 544-550.

[304] N.C. de Souza, F. Marystela, K. Wohnrath, J.R. Silva, J. Oliveira, O.N., J.A. Giacometti, Morphological characterization of Langmuir–Blodgett films from polyaniline and a ruthenium complex (Rupy): influence of the relative concentration of Rupy, Nanotechnology, 18 (2007) 075713 - 075719

[305] F. Family, T. Vicsek, Scaling of the active zone in the Eden process on percolation networks and the ballistic deposition model, J. Phys. A: Math. Gen., 18 (1985) L75.

[306] D.E. Wolf, J. Villain, Growth with Surface Diffusion, J. Europhys. Lett. , 13 (1990) 389-394.

[307] H. Takahashi, W.J. Finger, Dentin surface reproduction with hydrophilic and hydrophobic impression materials, Dental Materials, 7 (1991) 197-201.

[308] Y.C. Jung, B. Bhushan, Contact angle, adhesion and friction properties of micro- and nanopatterned polymers for superhydrophobicity, Nanotechnology 17 (2006) 4970-4980.

[309] B. Bhushan, Y.C. Jung, K. Koch, Micro-, nano- and hierarchical structures for superhydrophobicity, self-cleaning and low adhesion, Philos Transact A Math Phys Eng Sci, 367 (2009) 1631-1672.

[310] B. Bhushan, Y.C. Jung, Natural and biomimetic artificial surfaces for superhydrophobicity, self-cleaning, low adhesion, and drag reduction, Progress in Materials Science, 56 (2011) 1-108.

[311] S. Herminghaus, Wetting, spreading, and adsorption on randomly rough surfaces, The European Physical Journal E, 35 (2012) 1-10.

[312] Z. Li, E. Kang, K. Neoh, K. Tan, Effect of thermal processing conditions on the intrinsic oxidation states and mechanical properties of polyaniline films, Synthetic metals, 87 (1997) 45-52.